

Computational modeling of thermal transport in low-dimensional materials

DISSERTATION

zur Erlangung des akademischen Grades

Doktoringenieur (Dr.-Ing.)

vorgelegt

der Fakultät Maschinenwesen

der Technischen Universität Dresden

von

M. Sc. Leonardo Rafael Medrano Sandonas

geboren am 23. November 1988 in Lima, Peru

Tag der Einreichung: 18. Juli 2018

Tag der Verteidigung: 22. Oktober 2018

Vorsitzender: Prof. Dr.rer.nat.habil. C. Breitkopf

Gutachter: Prof. Dr. G. Cuniberti

Prof. Dr.-Ing.habil. M. Kästner

Prof. Dr. V. Mujica

Mitglied: Prof. Dr.rer.nat.habil. S. Gemming

Printed and published with the support of the German Academic Exchange Service.

CONTENTS

ABSTRACT	4
ZUSAMMENFASSUNG	6
LIST OF ABBREVIATIONS	8
LIST OF FIGURES	11
LIST OF TABLES	13
1 Introduction	15
1.1 Nanophononics: a route for thermal management	15
1.2 Thermal transport in low-dimensional materials	17
1.3 Objectives and outline	22
2 Two-dimensional thermal rectifiers	25
2.1 Classical molecular dynamics	25
2.1.1 Empirical interatomic potentials	28
2.1.2 Heat bath	30

2.1.3	Nonequilibrium molecular dynamics	32
2.1.4	Vibrational modes analysis	33
2.2	Tuning the properties of thermal rectifiers	35
2.2.1	Structural asymmetry	36
2.2.2	Substrate deposition	47
2.3	Summary	54
3	Quantum phonon transport	55
3.1	Theoretical background	55
3.1.1	Ballistic phonon transport	55
3.1.2	Density functional tight-binding method	63
3.2	Thermal transport in low-dimensional systems	68
3.2.1	Structural anisotropy	68
3.2.2	Nanoscale grain boundaries	71
3.2.3	Molecular functionalization	76
3.2.4	Uniaxial strain	79
3.2.5	Doping distribution	84
3.3	Summary	88
4	Time-dependent quantum phonon transport	89
4.1	Nonequilibrium Green's functions	89
4.1.1	Theoretical model	89
4.1.2	Equation of motion for the Green's functions	91
4.1.3	Auxiliary-mode approach	94
4.2	Time-dependent thermal current in nanojunctions	101
4.2.1	One-dimensional atomic chain	101

4.2.2	Carbon-based molecular junctions	108
4.3	Summary	111
5	Conclusions and Outlook	113
A	NEMD simulations	117
A.1	Benchmarking of the heat bath parameters	117
A.2	Real-space vibrational mode analysis	119
B	NEGF-DFTB implementation	123
B.1	Basic concepts of DFTB	123
B.2	PHONON tool	128
C	Time-dependent NEGF	131
	BIBLIOGRAPHY	137
	SCIENTIFIC OUTPUT	159
	ACKNOWLEDGMENTS	162

ABSTRACT

Over the past two decades, controlling thermal transport properties at the nanoscale has become more and more relevant. This is mostly motivated by the need of developing novel energy-harvesting techniques based on thermoelectricity and the necessity to control the heat dissipation in semiconductor devices. In this field, two major research lines can be identified: On one side "phononics", which aims at developing devices such as thermal diodes, thermal transistors, and thermal logic gates, among others, and on the other side, phonon engineering aiming at controlling heat transport by producing or structurally modifying heterostructures made of novel nanomaterials (e.g., two-dimensional (2D) materials, nanotubes, organic systems). In order to gain insight into the factors controlling nanoscale heat flow and to be able to design highly-efficient thermal devices, the development of new computational approaches is crucial.

The primary goal of the present thesis is the implementation of new methodologies addressing classical and quantum thermal transport at the nanoscale. We will focus on three major issues: (i) We will study thermal rectification effect in nanodevices made of novel 2D materials by means of nonequilibrium molecular dynamics simulations. The influence of structural asymmetry and substrate deposition on the thermal rectification will be investigated. (ii) To address quantum ballistic thermal transport in nanoscale systems, we will implement a nonequilibrium Green's functions (NEGF) treatment of transport combined with a density-functional based approach. Here, we will explore the dependence of the thermal transport properties of 2D materials and nanotubes on different intrinsic (structural anisotropy and grain boundaries) and external (molecular functionalization, strain engineering, and doping) factors. Finally, (iii) a time-dependent NEGF formalism will be developed and implemented to probe the transient and steady thermal transport in molecular junctions.

In short, our results show that the mechanisms governing the thermal rectification effect in the 2D thermal rectifiers proposed in this work are shape asymmetries, interface material (planar stacking order), and changes in the degree of spatial localization of high-frequency modes (under

nonequilibrium heat transport conditions). The rectification effect can be also controlled by substrate engineering. Moreover, we found that quantum ballistic thermal transport in 2D puckered materials displays an anisotropic behavior. The presence of structural disorder in the form of grain boundaries in graphene reduces overall its thermal transport efficiency. Dynamical disorder induced by coupling to a thermostat has however a weaker effect, suggesting that structural defects are playing a major role. External factors have a noticeable influence on the heat transport in new 2D materials and BNC heteronanotubes. On the other hand, we have also been able to characterize, from a quantum point of view, the phonon dynamics in carbon-based molecular junctions. We expect that the results obtained within this thesis will yield new insights into the thermal management of low-dimensional materials, and thus open new routes to the design of thermoelectric and phononic devices.

ZUSAMMENFASSUNG

In den letzten zwei Jahrzehnten hat die Kontrolle der thermischen Transporteigenschaften im Nanobereich immer mehr an Bedeutung gewonnen. Dies ist vor allem auf die Notwendigkeit zurückzuführen, neue Energiegewinnungstechniken zu entwickeln, die auf Thermoelektrizität basieren, sowie auf die Problematik, die Wärmeabfuhr in Halbleiterbauelementen kontrollieren zu müssen. In diesem Bereich lassen sich zwei große Forschungslinien identifizieren: Auf der einen Seite "Phononik", die unter anderem auf die Entwicklung von Bauelementen wie thermischen Dioden, Transistoren und Logikgattern abzielt, und auf der anderen Seite die Phonontechnik, die den Wärmetransport durch Herstellung oder strukturelle Modifikation von Heterostrukturen aus neuartigen Nanomaterialien (z.B. zweidimensionalen (2D) Materialien, Nanoröhren, organischen Systemen) steuert. Um einen Einblick in die Faktoren zu erhalten, die den Wärmefluss im Nanobereich steuern, und um hocheffiziente thermische Bauteile entwickeln zu können, ist die Entwicklung neuer Berechnungsansätze entscheidend.

Das Hauptziel der vorliegenden Arbeit ist die Implementierung neuer Methoden, die sich mit dem klassischen und dem quantenthermischen Transport auf der Nanoskala befassen. Wir werden uns auf drei Hauptthemen konzentrieren: (i) Wir werden den thermischen Rektifikationseffekt in Nanobauteilen aus neuartigen 2D-Materialien mit Hilfe von Nichtgleichgewichts-Molekulardynamiksimulationen studieren. Der Einfluss von Strukturasymmetrie und Substratablagerung auf die thermische Rektifikation wird untersucht. (ii) Um den quantenballistischen Wärmetransport in nanoskaligen Systemen anzugehen, werden wir eine NEGF-Behandlung (Nichtgleichgewichts-Greensche Funktionen) des Transports in Kombination mit einem dichte-funktionalen Ansatz implementieren. Hier wird die Abhängigkeit der thermischen Transporteigenschaften von 2D-Materialien und Nanoröhrchen von verschiedenen intrinsischen (strukturelle Anisotropie und Korngrenzen) und externen (molekulare Funktionalisierung, Stammtechnik und Dotierung) Faktoren untersucht. Schließlich wird (iii) ein zeitabhängiger NEGF-Formalismus entwickelt und implementiert, um den transienten und stetigen Wärmetransport in molekularen Verbindungen zu untersuchen.

Unsere Ergebnisse zeigen, dass die wesentlichen Mechanismen für die thermische Gleichrichtung in 2D thermischen Gleichrichtern durch Asymmetrien der Bauteilform, das Interface-Material (planare Stapelung Reihenfolge), und Änderungen im Grad der räumlichen Lokalisierung von Hochfrequenz-Modi (unter Nicht-Gleichgewicht Wärmetransport-Bedingungen) gegeben sind. Der Gleichrichteffekt kann auch durch die Wahl des Substrats gesteuert werden. Darüber hinaus haben wir festgestellt, dass der quantenballistische Wärmetransport in 2D-Puckered-Materialien ein anisotropes Verhalten zeigt. Das Vorhandensein von strukturellen Störungen in Form von Korngrenzen in Graphen reduziert insgesamt die Effizienz des Wärmetransports. Dynamische Störungen, die durch die Ankopplung an einen Thermostaten hervorgerufen werden, haben jedoch eine schwächere Wirkung, was darauf hindeutet, dass strukturelle Defekte eine große Rolle spielen. Externe Faktoren haben einen nachweislichen Einfluss auf den Wärmetransport in neuen 2D-Materialien und BNC-Heteronanotubes. Weiterhin konnten wir auch die Phonondynamik in kohlenstoffbasierten molekularen Verbindungen quantitativ charakterisieren. Wir erwarten, dass die Ergebnisse dieser Arbeit neue Erkenntnisse über das Wärmemanagement von niedrigdimensionalen Materialien liefern und damit neue Wege für das Design von thermoelektrischen und phononischen Bauelementen eröffnen.

LIST OF ABBREVIATIONS

1D	One-dimensional
2D	Two-dimensional
AC	Armchair
BNC	Boron-nitride-carbon
BTE	Boltzmann transport equation
CNT	Carbon nanotube
DFT	Density functional theory
DFTB	Density functional tight-binding
DOS	Density of states
EMD	Equilibrium molecular dynamics
EOM	Equation of motion
GB	Grain boundary
GF	Green's function
GK	Green-Kubo
hBN	Hexagonal boron-nitride
LD	Lattice dynamics
LJ	Lennard-Jones
MD	Molecular dynamics
NEGF	Nonequilibrium Green's functions
NEMD	Nonequilibrium molecular dynamics
NH	Nose-Hoover
NVE	Microcanonical ensemble
NVT	Canonical ensemble
PR	Participation ratio
TD	Time-dependent
TMD	Transition metal dichalcogenides
TR	Thermal rectification
VDOS	Vibrational density of states
ZT	Figure of merit
ZZ	Zigzag

LIST OF FIGURES

1.1	Thermal management of low-dimensional materials.	18
2.1	Schematic representation of the NEMD method.	32
2.2	Rectification response of asymmetric MoS ₂ nanoribbons.	37
2.3	Real-space vibrational mode analysis for the T-shaped MoS ₂ nanoribbon.	39
2.4	Projections of the polarization vectors on the T-shaped MoS ₂ nanoribbon.	40
2.5	Phase quotient for the T-shaped MoS ₂ nanoribbon.	41
2.6	Spatial distributions of vibrational modes for T-shaped MoS ₂ nanoribbons.	42
2.7	Dependence of M parameter with the asymmetry degree for the T-shaped and trapezoidal MoS ₂ nanoribbons.	43
2.8	Rectification response of coplanar hBN-G heterojunctions with zigzag interface (B-C bridge bonding).	44
2.9	Real-space vibrational mode analysis of asymmetric coplanar hBN-G heterojunctions.	46
2.10	Temperature profiles and vibrational density of states for deposited heterojunctions.	48
2.11	Vibrational density of states of the heat baths in symmetric hBN-G and G-hBN nanoribbon heterojunctions after substrate deposition.	50
2.12	Interface thermal transport properties of deposited hBN-G and G-hBN nanoribbon heterojunctions.	51

2.13	Substrate temperature dependence of the in-plane mode contribution to the total vibrational density of states.	52
2.14	Heat flux values in the forward and backward directions for symmetric hBN-G nanoribbons after substrate deposition.	53
3.1	Scheme of Schwinger/Keldysh-contour in the imaginary time plane.	57
3.2	Schematic representation of the partition scheme for transport calculation using Green's function technique.	59
3.3	2D puckered materials and their phonon dispersion.	69
3.4	Phonon transmission function and thermal conductance 2D puckered materials.	71
3.5	Structures of linear and curved graphene grain boundaries.	72
3.6	Phonon transmission and thermal conductance for graphene grain boundaries.	73
3.7	Influence of atomic defects (structural disorder) on the thermal transport properties of GBs.	74
3.8	Influence of dynamical disorder on the thermal transport properties of GBs.	76
3.9	Atomistic representation and thermal transport properties of graphene grain boundaries.	77
3.10	Temperature dependence of the phonon thermal conductance in graphene GBs upon functionalization with H- and O-atoms.	77
3.11	Phonon transmission and phonon thermal conductance for molecular functionalized grain boundaries.	78
3.12	Schematic representation of the partition scheme for transport calculation in two-dimensional materials.	79
3.13	Bond lengths at first and second neighbors as a function of the applied strain for 2D materials.	80
3.14	Variation of the thermal conductance as a function of the applied strain in 2D materials.	81
3.15	D parameter as a function of the applied strain for 2D materials.	82
3.16	Variation of in-plane and out-of-plane mode contributions to the the thermal conductance as a function of the applied strain for 2D materials.	83

3.17	Atomistic view of BNC heteronanotubes with different doping distribution pattern.	84
3.18	Phonon transport properties of BNC heteronanotubes.	85
3.19	Phonon density of states analysis for helical BNC heteronanotubes.	86
3.20	Phonon density of states analysis for BNC heteronanotubes with different doping distribution pattern.	86
4.1	Schematic representation of the target molecular junctions in the present study. .	90
4.2	Comparison of obtained results for a 1D atomic chain by using different self-energy spectral density.	102
4.3	Variation of the total energy of a dimer as a function of the number of atoms in the 1D atomic chain.	103
4.4	Analysis of spectral density parameters by using Landauer approach.	104
4.5	Variation of the heat flux in the steady state as a function of the number of atoms in the 1D atomic chain.	105
4.6	Cut-off frequency dependence of the steady state heat flux for the dimer at different temperatures bias.	106
4.7	Thermal conductance as a function of the mean temperature for an 1D atomic chain with 8 atoms.	106
4.8	Energy of a diatomic chain vs number of poles of the auxiliary-mode approach . .	107
4.9	Time-evolution of the thermal transport properties for the 1D atomic model. . .	108
4.10	Time-evolution of the thermal transport properties for the carbon-based molecular junctions.	109
A.1	Benchmarking of the heat bath length.	118
A.2	Benchmarking of the relaxation time in the heat bath.	119
A.3	Spatial distributions of vibrational modes for T-shaped MoS ₂ nanoribbons. . . .	120
A.4	Spatial distributions of vibrational modes for trapezoidal MoS ₂ nanoribbons. . .	121

LIST OF TABLES

2.1	LJ parameters for the interaction between the nanoribbon heterojunctions and the different substrates.	47
3.1	Calculated lattice constants of 2D puckered materials.	70
A.1	Values of the heat flux and thermal rectification for different length of the heat bath	118
A.2	Values of the heat flux and thermal rectification for different relaxation time of the heat bath	119

1 INTRODUCTION

1.1 NANOPHONONICS: A ROUTE FOR THERMAL MANAGEMENT

Over the past half-century, the drive for faster, cheaper computing and its long-associated requirements of increasing device density and progressive device miniaturization have served to push scientists and engineers to continually develop new and ever-improving materials, tools, processes, and design methodologies [1]. However, these exciting technological advances and emerging applications are also creating thermal management challenges that may serve to ultimately limit their effectiveness, scope of implementation, or overall feasibility. Consequently, the novel field of nanophononics has emerged and a wealth of new physics and applications has been demonstrated [2–5]. Nanophononics aims at developing efficient strategies to control the heat flow in organic and inorganic nanostructures, and it arose with the goal of realizing thermal (or phononic) devices such as diodes, transistors, and logic gates [2, 6]. Recent efforts in nanophononics have stimulated completely new applications in the fields of nanoelectronics [7, 8], renewable energy harvesting [9, 10], nano- and optomechanics [11], quantum technologies [12, 13], and medical therapy, imaging and diagnostics [14].

An important breakthrough in the field was the theoretical prediction [15] and subsequent observation in a mesoscopic nanostructure [16] of the quantization of the phononic thermal conductance at low temperatures in analogy to the conductance quantization for charge transport. Recently, it was also shown that the thermal conductance of gold metallic wires down to single-atom junctions is quantized at room temperature and that the Wiedemann-Franz law relating thermal and electrical conductance is satisfied even in single-atom contacts [17, 18]. In contrast to the electrical conductance quantization (with conductance quantum= e^2/h), the quantum of thermal conductance κ_0 is not a constant, but depends on the temperature T : $\kappa_0 = \pi^2 k_B^2 T/3h$, with k_B being the Boltzmann's constant and h the Planck's constant. This already demonstrates a fundamental difference between charge and phonon transport. Another basic difference relies on the different energy ranges determining the corresponding transport properties: in the case of

electrons the relevant energy window lies around the Fermi level, while for phonons the thermal conductivity is formally an integral result of the whole vibrational spectrum. The difficulty of working with a broad spectrum of excitations naturally possesses major challenges in designing thermal devices such as cloaks and rectifiers [2, 4], or processing information with phononic computing [6].

From the experimental point of view, it is considerably more difficult to control the heat flow in a nanostructure than it is to control the flow of charges. Unlike electrons, the quantum carriers of heat (phonons for periodic systems or vibrons in the case of finite-size structures) are not particles with defined properties but bundles of energy that have neither mass nor charge and can therefore not be influenced by electromagnetic fields in a straightforward way. Also, while in nanoscale electronics considerable progress has been achieved in designing and implementing local electrodes and gates over very short length scales, establishing well-defined temperature gradients –the most natural way to control heat flow– at the nanoscale still remains a major experimental challenge. In this sense, the characterization of thermal devices has promoted the development of new sophisticated experimental techniques (e.g., 3ω method [19, 20] and frequency domain thermoelectance [21]) pioneered by D. Cahill et al. [22]. As a result, this has led to the modification of atomic force microscopes for thermometry [17, 23] and the use of Scanning Thermal Microscopy [18, 24].

Thus, to turn nanophononics from a dream into reality different approaches are required based on nanoscale engineering of the transport properties, i.e., tailoring the material’s structure to gain control over its thermal response. This strategy has already been successfully implemented in nanostructured thermoelectric materials. Although the fundamental tool to understand nanophononics, i.e., non-equilibrium thermodynamics, has been well established in the macroscopic scale, there are many open questions in the nanoscale. These questions have deep implications on how to transport and control heat over such length scales. The fact that low-dimensional materials have finite cross sections and a large surface-to-volume ratio, can induce strong modifications of the vibrational spectrum as well as of the heat transport mechanisms. Results related to these issues have been summarized in recent comprehensive reviews, see Refs. [2–4]. These differences to macroscopic heat transport can lead to new devices which require a new theoretical understanding and new experiments to characterize them. There have been many theoretical/computational methods to study heat transport in nanostructures [4, 25]. These methods can be largely grouped into three categories. The first category includes methods based on molecular dynamics (MD) simulations such as equilibrium MD (EMD) which is based on the Green-Kubo formula [26] and nonequilibrium MD (NEMD) which is related to the Fourier’s law [27, 28]. The second category includes methods based on the Boltzmann transport equation (BTE) [29, 30] and the lattice dynamics (LD) [31]. Finally, the third category includes methods based on the Landauer formula or more generally the nonequilibrium Green’s functions (NEGF) formalism [32–35]. These methodologies have been already successfully applied to predict the thermal transport properties of a variety of low-dimensional materials, providing the correct trend and comparable results with respect to experimental investigations [36–38]. Hence,

it has been shown that the thermal conductivity is sensitively affected by different factors such as geometry, doping, and defects [37, 39–41]. Moreover, the spatial confinement of phonons is further influenced by the rigidity of the boundaries, which in turn affects the phonon group velocity, the phonon relaxation time and ultimately may lead to a reduction of the thermal conductivity [42, 43].

Additionally, in non-stationary situations, where time-dependent (TD) external parameters can strongly affect a nanoscale system, the dynamics of the vibrational system becomes crucial. For example, a time-varying temperature bias [44, 45] or strong local heating by laser fields [46, 47] can be used to exert additional control over thermal transport. In this context, novel nonequilibrium effects like molecular heat pumping [48, 49], cooling [50], and rectification [51, 52] have been proposed. The description of such phenomena often requires working directly in the time domain, which is very challenging from a numerical point of view. In this respect, noticeable progress has been achieved in the description of TD transport of spins [53, 54] and electrons [55–60]. However, less attention has been paid to a similar treatment of vibrational degrees of freedom. Thus, only recently new approaches, only focusing on simple model systems, have been developed to deal with TD thermal phenomena in molecular scale nanojunctions [61–63], which are the ultimate level achievable regarding device miniaturization [64–66].

Despite this promising progress in the development of methodologies to understand thermal transport at the nanoscale, there are still many fundamental questions about the thermal management of, e.g., thermoelectric materials, phononic devices, and integrated circuits, that need to be addressed. In this sense, to achieve an optimal thermoelectric response (high figure of merit (ZT)), a given material should simultaneously have very good electronic properties and low thermal conductance, ideally implementing an electron crystal and a phonon glass [9]. Regarding to phononic devices, the main building-block of phononics is the thermal rectifier, which aims to control heat current similar to electronic rectifiers in microelectronics [67]. Similarly, when applying a temperature bias across a thermal rectifier, the thermal resistance is small when the bias is applied in one direction, while the thermal resistance becomes large in the other direction. In short, the field of nanophononics is currently providing several routes for thermal management which will lead to design and improve novel nanoscale technological applications.

1.2 THERMAL TRANSPORT IN LOW-DIMENSIONAL MATERIALS

The outcomes produced by the studies on thermal management have promoted the rise of novel low-dimensional systems such as two-dimensional (2D) materials, nanotubes, and molecular nanojunctions (see Fig. 1.1). Several works have already been performed to explore the applicability of these materials for the development of potential thermoelectric and phononic devices. For instance, the first solid-state active three-terminal thermal device based on VO_2 with large rectification of the heat current has recently been demonstrated [68]. Other successful experimental findings are thermal rectifiers based on carbon or boron-nitride nanotubes with

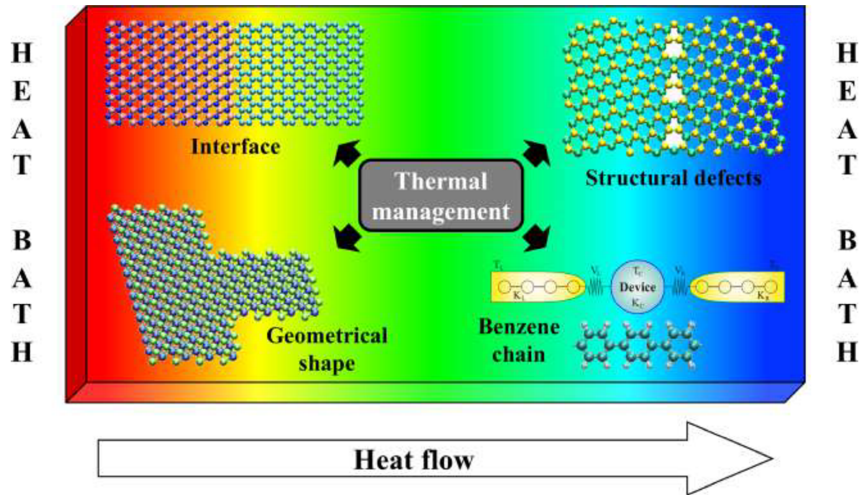


Figure 1.1: Schematic representation of the different possibilities to study and control thermal transport in low-dimensional systems such as two-dimensional materials (hBN-graphene interface, structural defects in MoS₂ monolayer, and T-shaped WSe₂ monolayer) and carbon-based molecular junctions (benzene chain).

asymmetric mass loading [69], and reduced graphene oxide [70]. From a theoretical point of view, it has been found that thermal rectification in nanostructured systems sensitively depends on several parameters such as heat bath features [71, 72], the device geometry [37, 73], and on the interface properties between different materials inside the device [74, 75]. Most of these investigations have been focused on carbon-based nanomaterials like carbon nanotubes and graphene nanoribbons [37, 40, 73, 76–78]. In particular, graphene has drawn much attention due to its extremely high thermal conductivity and the system has also been intensively studied for nano-electronic applications [37, 41, 70, 79]. However, graphene has a basic problem: the low-energy electronic structure is dominated by two linear bands due to the peculiarities of its lattice structure. For electronic applications, a tunable band gap is however quite important and, as a result, new 2D materials have been recently proposed, which could become real alternatives to graphene electronics (and phononics): hexagonal boron-nitride (hBN), phosphorene, silicene, and transition metal dichalcogenides (TMD, e.g., MoS₂, WS₂, Bi₂Te₃, among others), all of which have the same honeycomb structure like graphene [80–82]. These materials are expected to display different physical properties due to the differences in their chemical composition, and thus offer a new broad playground to explore and develop nanoscale devices with tailored electrical, optical, and thermal properties (see recent reviews in Refs. [80–83]). In the following, a brief description of the relevant properties of the 2D materials studied in the present thesis will be presented, giving emphasis to the thermal transport properties.

Phosphorene (or black phosphorene), one of the newest member from the family of 2D materials, has been successfully produced by mechanical exfoliation from bulk black phosphorous [84, 85]. The main feature of phosphorene is its puckered honeycomb structure, which leads to electronically relevant properties such as a non-zero bandgap of $\sim 1.4\text{eV}$, large current on-off ratios, high charge mobility, and fast photo-response [86, 87]. Moreover, anisotropic behavior of

its physical properties has been demonstrated [88–94]. In this respect, Luo et al. have reported anisotropic in-plane thermal conductivity of suspended few-layer black phosphorus measured by micro-Raman spectroscopy [88]. Here, it was also found that, independent of the number of layers, the thermal conductivity for the zigzag (ZZ) direction is larger than for the armchair (AC) direction; for black phosphorus films thicker than 15 nm values of ~ 40 W/mK and ~ 20 W/mK for ZZ and AC directions, respectively, were reported. This effect has been theoretically described by using BTE [89, 90] and NEGF techniques [91]. Electronic anisotropy has also been experimentally observed in layered black phosphorous [92, 93]. The results indicate that the AC direction is the most preferable electron transport direction. Taking advantage of these anisotropic properties, Fei et al. have shown, by performing first-principles band structure calculations, that the thermoelectric performance of phosphorene can indeed be enhanced for transport in the AC direction, with values of $ZT \sim 1.0$ at room temperature [94].

Materials analogous to phosphorene have been also recently discovered, e.g., arsenene (a single layer of arsenic) and monolayer tin sulphide (SnS). They all may exist, like in phosphorene, orthorhombic puckered structures and semiconducting band gaps and, more interestingly, they all display anisotropic features in their physical properties [95–100]. Unlike arsenene, SnS nanosheets have been successfully synthesized by several techniques [99, 101]. It has also been found that SnS thin films display a strong angle-dependent Raman response, indicative of anisotropy in their optical properties [101]. The large Seebeck coefficient and the low thermal conductivity theoretically found in SnS bulk produce comparative thermoelectric performance compared to SnSe bulk [102], which has been proclaimed to be an excellent candidate for thermoelectric devices [103]. Moreover, Guo et al. have shown that the thermal conductivity for SnS bulk is very low compared to other 2D materials and is also anisotropic [102]. Based on the studies performed in other phosphorene analogues [94, 98], it is expected that the anisotropic effect remains in monolayer form of SnS. However, to the best of our knowledge, this statement has not been yet verified.

Inside the fascinating group of TDM materials, molybdenum disulphide (MoS_2) monolayer has been shown as the most promising material for implementing field effect transistors (FET) and optical devices due to its sizable electronic band gap [104, 105]. Moreover, its thermoelectric properties suggested potential applications for thermal energy harvesting and thermopower generation [106, 107]. Experimental studies of thermal transport have reported that the thermal conductivity of MoS_2 monolayer depends on the number of layers (34.5 ± 4 W/mK for a monolayer [108] and 52 W/mK for an 11-layer sample [109]) and it is lower than that of bulk MoS_2 [110] and of graphene [111]. In addition to the suspended sample, a relatively higher thermal conductivity 62 W/mK was observed in supported MoS_2 monolayer [112]. There have also been several theoretical investigations to study intrinsic thermal conduction of this novel material. For instance, Cepellotti et al. claimed that the room temperature thermal conductivity of MoS_2 sheet reaches a values of around ~ 300 W/mK after using the exact solution of the BTE [113]. Besides, it has been found, by combining the NEGF approach with first-principles, that the

thermal conductivity for armchair and zigzag MoS₂ nanoribbons at 300 K is about 674 W/mK and 841 W/mK, respectively [114]. On the other hand, Li et al. found that the thermal conductivity for a typical sample size of 1 μ m is 83 W/mK using ab-initio calculations [115]. Very close values were also found by using BTE combined with a relaxation time approximation [116] and NEGF [117]. Consequently, comparing these results to those from the experimental results, the exact intrinsic thermal conductivity of MoS₂ monolayer remains almost unclear. It is also worth mentioning that similar to carbon based materials, nowadays, the transport properties of the nanoscale allotropes of MoS₂ [118] and phosphorene [119] like nanorods, nanoribbons, nanotubes, and fullerenes are being discussed as possible candidates for designing thermoelectric phononic devices.

Heterostructures made of 2D materials have also drawn tremendous attention since they offer additional tunability of the electrical and thermal response [120, 121]. Although most of these investigations have naturally focused on the study of electronic properties due to potential applications in next generation electronic devices, engineered heterostructures also offer a new avenue for engineering thermal transport properties [122–124]. Thus, graphene/hexagonal boron-nitride (G/hBN) heterojunctions have been extensively studied due to the small lattice mismatch (2%) of the precursors [125–128], and the synthesis of coplanar hybrid graphene and hBN monolayers has been successfully reported in several studies [125, 126]. In particular, it has been shown that hBNC nanoribbons can be half-metallic or semiconducting depending on how graphene nanoribbons are embedded in the hBN matrix [129]. Interesting electrical rectifying effect and negative differential resistance have been theoretically predicted for graphene/hBN nanoribbon heterojunctions by using NEGF-DFT [130]. Moreover, the electron transport properties of BNC heteronanotubes have been widely investigated [131–133], finding that these materials have tunable electronic bandgap and exhibit negative differential resistance and rectifying behavior.

On the other hand, an increasing interest in the thermal transport properties in such heterojunctions is also taking place [134, 135]. Hong et al. [136] have found, by using NEMD simulations, that the interface thermal resistance decreases with increasing length of the G/hBN heterojunction and increases with increasing tensile strain independently of the heat flux direction. However, Chen et al. [137] have recently demonstrated that heat current runs preferentially from the hBN to G domain, which enhances the thermal rectification in this heterostructure. Thermal conductivity in symmetric G/hBN heterojunctions has also been found, by using a normal mode decomposition approach, to depend on the periodicity and interface configuration of the superlattices [138, 139]. A minimum in the thermal conductivity at a critical pitch in G/hBN superlattices was reported in Refs. [140, 141]. By using Green's function techniques, it has been shown that the bond type (C-N or C-B) along the interface sensitively controls the probability of scattering between the available phonon transport channels [142]. Barrios-Vargas et al. [127] showed by a finite-element based model that the thermal conductivity of polycrystalline structures of graphene and hBN is minimized for a hBN grain density of 70%, while this minimum was previously reported to occur at a density of 50% and 40% by using a real-space

Kubo approach [143] and EMD [139], respectively. MD simulations were used to study thermal transport in planar BNC heterostructures, finding that BC_2N monolayer displays a strong anisotropy of the in-plane thermal transport [144]. Combining the phonon and electron transport properties of armchair BNC nanoribbons, Yang et al. [145] have shown that, in comparison to pristine graphene ribbons, ZT for these systems gets enhanced 10-20 times, while for zigzag nanoribbons, ZT could be increased by a factor of 2-3. All these novel effects reported in BNC heterostructures strongly depend on their structure and configuration, which can be controlled with by the dimension of BN and C domains.

It is well-known that many of these novel 2D materials have a high potential for nanoelectronics and energy applications [81, 113]. Therefore, currently, it is of great interest to reveal how their physical properties can be tailored by varying different control parameters. Here, besides altering the geometrical shape and chemical composition to build phononic devices, strain engineering has been proved to be a powerful tool to manipulate and control both electron and thermal transport properties of 2D materials [89, 91, 134, 146–153]. In experiments, several straining techniques have been developed, but due to the challenge of manipulating nanoscale matter, only few of them have already been proved to be feasible [154, 155]. For instance, Wang et al. [148], by employing in-situ strained Raman spectroscopy, found that the influence of strain on the vibrational modes in few-layer black phosphorus is anisotropic. This effect was also recently observed by using a modified bending technique to apply uniaxial strain in ultrathin black phosphorous [156]. A reduction of the band gap in single- and bilayer MoS_2 has also been reported, induced by bending the flexible substrate in which they are supported [149] and by considering cylindrical cavities [146]. Strain-induced phonon softening has been observed in MoS_2 [149] and WS_2 [157] monolayers, which may alter their thermal behavior. From the modelling point of view, NEMD simulations have been widely used to study the influence of strain on the thermal conductivity of 2D materials [134, 147], revealing clear differences in their thermal response. While the thermal conductivity in silicene [150] and hBN [134] first increases with the tensile strain and then decreases, for other materials like graphene [147] and MoS_2 [158] it decreases with increasing strain, similar to their bulk phase. It has also been shown, by employing first-principle calculations, that the thermal anisotropy in phosphorene is strain dependent, increasing under uniaxial strain [89]. Moreover, using NEGF technique, it has been shown that tensile strain leads to a semiconducting-to-metal transition in single layer MoS_2 for elongations of the order of 11% [153] and to an anomalous strain dependence of the thermal conductance in phosphorene [91].

Besides inorganic materials, thermal management of nanojunctions has become a very relevant issue in the field of nanophononics. This is mainly due to the uncontrollable generation of high levels of heating when electron current goes through the junctions, affecting the nature of the transmission and possibly undermining its structural integrity [64, 65]. In general, heat transfer in molecular junctions has been addressed mostly as special case in connection to electron transport [3, 159]. Thermoelectric properties and energy conversion in molecular junctions has also

been become feasible to probe in recent experimental works [66, 160, 161]. Nevertheless, some direct studies have looked at toy models with quantum mechanical effects, and noticed that the steady state heat transport is equivalent to classical heat transport with temperature relaxation [162], leaving open many questions about the properties of heat flow far away from equilibrium. Additionally, it has been found, by atomistic simulations, that the thermal conductance strongly depends on the contact-molecule coupling [163, 164]. Other studies on the non-equilibrium dissipation of heat in molecular devices have been performed, reporting an energy dependence of their electronic transmission characteristics [66, 165]. New experiments have also found that ultrafast effects are crucial for heat transport over these length scales [166]. Hence, thermal management of novel low-dimensional materials shown in this section has become a relevant issue for the future of nanoelectronics and nanophononics, confirming the necessity for more profound experimental and theoretical investigations of their electron and thermal transport properties.

1.3 OBJECTIVES AND OUTLINE

The main topic of this thesis is the theoretical study of classical and quantum heat transport in low-dimensional materials. Two major issues will be (i) to rationalize the factors influencing heat transport in such nanosystems in a systematic way and from both the classical and quantum points of view, and based on it, (ii) to propose appropriate material design strategies allowing for the control of heat flow in realistic nanomaterial structures. Main targets of the thesis will be novel two-dimensional materials and molecular nanojunctions. The 2D materials that we will deal with have different numbers of atomic layers perpendicular to the plane: hBN is a single atom layer material like graphene, phosphorene contains two atomic layers, and MoS₂ monolayer consist of three atomic layers, with the outer layers being the S-species and the inner layer includes the Mo atoms [82]. In this way, we can explore the influence of these atomic scale differences in systems which are globally two-dimensional. While nanojunctions will be formed by carbon-based molecules such as polyethylene and polyacetylene.

Initially, items (i) and (ii) will be addressed using nonequilibrium molecular dynamics simulation which is already available in several simulation softwares. On the other hand, from the methodological point of view, this thesis is aiming at (a) implementing nonequilibrium Green's function formalism to study quantum ballistic transport, this will be combined with a DFT method to ensure a realistic description of the transport properties, and (b) developing the necessary formalism to treat the influence of phonon dynamics on the quantum thermal transport properties at the atomistic level. Due to the novelty of this last item, we will first demonstrate the method, as a proof of concept, in simple nanoscale junctions based on polyethylene and polyacetylene dimers.

The present thesis is structured as follows. In Chapter 2, nonequilibrium molecular dynamics is described and employed to study heat transport in thermal rectifiers made of novel two-dimensional materials. Here, the influence of substrate deposition on the thermal transport

properties of these devices is also discussed. This is an attempt to understand the long existing controversy over the device-substrate relationship. Consequently, phonon ballistic transport in low-dimensional materials is engineered by varying various control parameters. A brief description of the NEGF-DFT method and the outcomes of its application are presented in Chapter 3. In Chapter 4, a new atomistic framework for time-dependent quantum thermal transport is developed and, then, applied to study carbon-based molecular junctions. Finally, the conclusions and outlook of the work are displayed in Chapter 5.

2 TWO-DIMENSIONAL THERMAL RECTIFIERS

In general, the heat energy is transmitted through a material by electrons, phonons or other excitations as spin waves, depending on the type of material. The present chapter will be only focused on energy transferred by lattice dynamics, which is the dominant mechanism in semiconductors. Specially, the main goal will be the search and control of the thermal rectification effect in nanodevices made of novel 2D materials. As it was mentioned in Chapter 1, to have an optimal thermal rectifier, the device should provide a large heat flow for a certain temperature gradient, but ideally be insulating when the direction of the gradient, and thus of the heat flow, is reversed [2].

To understand heat transport across these novel nanodevices, molecular dynamics (MD) simulations are carried out. This is a powerful tool for materials modeling at the nanoscale and it allows us to have atomic scale resolution observations which is, most of the times, not possible in experiments. Moreover, when dealing with rectification effects, a special kind of MD has to be used, i.e., nonequilibrium molecular dynamics (NEMD), which has been widely used for the study of carbon-based thermal rectifiers [2, 37]. NEMD method is already implemented in the LAMMPS code [167] and, hence, this will be the software used to perform all MD simulations in the present chapter. In the following, the main concepts of NEMD simulations are discussed.

2.1 CLASSICAL MOLECULAR DYNAMICS

It is known that to study the dynamical properties of a many-body problem, numerical simulations are necessary because of the limitations of analytic approaches. Starting from the Born-oppenheimer approximation which assumes a separability of time scales for nuclear and electron motion and, consequently, the total Hamiltonian of the system can be split into two parts, electron and nuclei Hamiltonian [168]. As a result, the electron Hamiltonian parametrically

depends on the nuclear positions which can be obtained by using, e.g., molecular dynamics (MD) simulations [169, 170]. MD is a deterministic method in which the electronic structure information of the system is contained in the interatomic potential U , as it will be discussed in the following sections. This method has been successfully used to investigate both equilibrium and nonequilibrium state of materials at different length scales. Thus, besides the goal of the thesis (i.e., thermal rectification effect), applications of MD simulations have covered a wide range of research topics, such as liquids, defects, fatigue, clusters, and biomolecules [170].

Molecular dynamics is a method based on the numerical integration of Newton's equation of motion, i.e.,

$$m_i \frac{d^2 \mathbf{r}_i}{dt^2} = \sum_{j=1, j \neq i}^N \mathbf{F}_{ij} \quad (i = 1, 2, \dots, N), \quad (2.1)$$

where N is the number of particles in the system and \mathbf{F}_{ij} denotes the force exerted on particle i by particle j and corresponds to the gradient of the interatomic potential between such particles given by

$$\mathbf{F}_{ij} = -\frac{\partial U}{\partial r_{ij}}. \quad (2.2)$$

The summation is carried out over all other particles in the system. Eq. (2.1) represents $3N$ equations due to the three Cartesian components of \mathbf{r}_{ij} . The major task of an MD simulation is to solve these $3N$ equations and then analyze the simulation results to obtain the information of interest.

MD simulation is a statistical mechanics approach, which relates the microscopic behavior in a system with its thermodynamics. According to statistical mechanics, physical quantities can be evaluated by averaging over configurations distributed according to a certain statistical ensemble. For the N -particle system, MD simulation calculates the trajectory in a $6N$ -dimensional phase space ($3N$ positions and $3N$ momenta) at each instantaneous time. This trajectory obtained from MD simulation provides such a set of configurations. Thus, to get the thermodynamic variables such as temperature, it relies on the ergodicity hypothesis of statistical mechanics, which asserts that the phase space can be fully recovered in the long-time limit and the time average is equivalent to the ensemble average. Therefore, thermodynamic variables of interest can be obtained by the time average along the trajectory in an MD simulation [171].

Nevertheless, to get the MD trajectory, the equations of motion have first to be numerically solved. Indeed, various techniques have been developed to integrate the equations of motion [172], e.g., Runge-Kutta model, predictor-corrector method, Verlet method, etc. For our purpose, the simplest, stable, and time-reversible is the Verlet algorithm [173], which can be derived through a series of Taylor expansions. In the first place, let's expand the position vector,

$$\mathbf{r}(t + \Delta t) = \mathbf{r}(t) + \mathbf{v}(t)\Delta t + \frac{\mathbf{F}(t)}{2m}\Delta t^2 + \frac{\Delta t^3}{3!}\ddot{\mathbf{r}} + O(\Delta t^4). \quad (2.3)$$

Similarly,

$$\mathbf{r}(t - \Delta t) = \mathbf{r}(t) - \mathbf{v}(t)\Delta t + \frac{\mathbf{F}(t)}{2m}\Delta t^2 - \frac{\Delta t^3}{3!}\ddot{\mathbf{r}} + O(\Delta t^4). \quad (2.4)$$

Summing up these two equations,

$$\mathbf{r}(t + \Delta t) = 2\mathbf{r}(t) - \mathbf{r}(t - \Delta t) + \frac{\mathbf{F}(t)}{2m}\Delta t^2 + O(\Delta t^4). \quad (2.5)$$

Hence, the estimate of the new positions contains an error that is of order Δt^4 , where Δt is the time step in the MD simulation. Then, the velocity can be derived from knowledge of the trajectory as:

$$\mathbf{v}(t) = \frac{\mathbf{r}(t + \Delta t) - \mathbf{r}(t - \Delta t)}{2\Delta t} + O(\Delta t^2). \quad (2.6)$$

This expression for the velocity is only accurate of order Δt^2 . To obtain more accuracy in the calculations, velocity-Verlet algorithm has been developed, in which the positions are calculated as [174]

$$\mathbf{r}(t + \Delta t) = \mathbf{r}(t) + \mathbf{v}(t)\Delta t + \frac{\mathbf{F}(t)}{2m}\Delta t^2, \quad (2.7)$$

and the velocities by

$$\mathbf{v}(t + \Delta t) = \mathbf{v}(t) + \frac{\mathbf{F}(t + \Delta t) + \mathbf{F}(t)}{2m}\Delta t. \quad (2.8)$$

Notice that in this algorithm, the new velocities can only be computed after the new positions are known and from these, the new forces. Eq. (2.8) is accurate to order Δt^4 and it can be proven rigorously that Eqs. (2.7) and (2.8) are equivalent to the original Verlet algorithm. Thus, it is obvious that in any integration algorithm, the time step is always an important factor. Too large time step may give problems in the integration algorithm due to high energy overlaps between atoms and, then, lead to a program failure. Too small time step will result in much more computer time. Usually, in one time step, the motion of the particle should be approximately one order of magnitude smaller than the atom-atom bond length. For most solid state materials, the suggested time step at room temperature is from 0.1 fs to 1 fs (1 fs = 10^{-15} s).

Furthermore, the atomic positions and velocities must be initialized to start with an MD simulation. In crystalline solids, for example, the starting positions will be defined by the crystal symmetry and the positions of the atoms within the unit cell of the crystal. Then, periodic boundary conditions are considered to simulate a large system. Whereas, for amorphous solids, the particles can be randomly distributed in the simulation cell. The initial velocities are set by assuming a Maxwell-Boltzmann distribution for velocities along the three dimensions. This can be done using Gaussian-distributed random numbers, with the condition that the total momentum of the particles is equal to zero and specifying the temperature and total energy of the system. Notice that another crucial input to start the MD simulation is the interatomic potential (or force field), in which lies the accuracy of the simulation results (see section below).

2.1.1 Empirical interatomic potentials

The investigation of the physical properties of any material by means of molecular dynamics simulations strongly depends on how the interactions among the constituent atoms are described. Nowadays, first-principle methods are available to carry out these kind of studies [175], but they are time consuming when dealing with large systems (hundred of nanometers) and become practically impossible most of the time. In these situations, empirical interatomic potentials are desirable because they do not require tedious quantum mechanical calculations. However, their accuracy and transferability need to be proved. Consequently, tremendous efforts have been done to develop reliable force fields for many material systems that can accurately describe the interatomic interactions and easily be applied to a large system size. Generally speaking the total potential can be decomposed in the following sum,

$$U = \sum_i U_1(\mathbf{r}_i) + \sum_{i<j} U_2(\mathbf{r}_i, \mathbf{r}_j) + \sum_{i<j<k} U_3(\mathbf{r}_i, \mathbf{r}_j, \mathbf{r}_k) + \dots, \quad (2.9)$$

where the first term represents the one-body contribution to the potential and is often associated to an external field, e.g., an electric field. The second and third terms represent two-body and three-body interatomic potentials, respectively. The choice of the interatomic potential depends on the problem at hand (type of atomic structure and on the properties to be studied), and on the necessity of modeling experimental findings.

One of the simplest and most popular two-body potential used in condensed matter physics is the Lennard-Jones (LJ) potential, where the total potential decomposes in a sum of pair potentials

$$U = \sum_i \sum_{j>i} U_{ij}, \quad (2.10)$$

with,

$$U_{ij} = \begin{cases} 4\epsilon \left[\left(\frac{\sigma}{r_{ij}} \right)^{12} - \left(\frac{\sigma}{r_{ij}} \right)^6 \right] & \text{if } r_{ij} < 2.5\sigma \\ 0 & \text{otherwise.} \end{cases} \quad (2.11)$$

Here, ϵ and σ are the LJ energy and length scales, corresponding to the zero-energy pair-separation distance and the potential well depth. The first term in Eq. (2.11) models the strong repulsive interaction between atoms at small separation distances, while the second term models the attractive van der Waals interaction between electrically neutral molecules or atoms. The values ϵ and σ are chosen to reproduce thermodynamic properties of the gas phase [169]. For this work, the LJ potential has been truncated by imposing a cut-off radius of 2.5σ . So when calculating the potential felt by a particle, one only needs to consider particles within this cutoff distance. This can be used to speed up the simulations avoiding unnecessary force calculations.

Despite not being able to fully account of the physical and chemical properties in current relevant materials (e.g., nanoparticles, nanotubes, two-dimensional materials), LJ potential can not be underestimated as it represents an important model to describe the vdW interaction. For instance, LJ potential has been widely used to model graphene-substrate interaction and inter-layer interaction in multi-layer graphene [176]. This approach will be also used for studying the influence of substrate on the thermal transport properties of coplanar graphene/BN nanoribbons (see Sec. 2.2.2). Accordingly, because of the limitations of LJ potential, in some situations, it is required to use more sophisticated semi-empirical potentials whose parameters are chosen to reproduce either microscopic or macroscopic properties of a model system. These semi-empirical potentials are usually no longer pair potentials like the LJ potential but many-body, where the many-body terms describes how does the potential energy of an atom depends on its coordination. One such example is the Tersoff potential, which was first proposed for Silicon [177] and later for Carbon [178]. J. Tersoff abandoned the use of N-body potential form and proposed a new approach by effectively coupling two-body and higher multi-atom correlations into the model. As for the Biswas and Hamann potential, the Morse form is adopted, related to the exponential decay dependence of the electronic density. Thus, the potential is written in the following form:

$$U = \sum_i E_i = \frac{1}{2} \sum_{i \neq j} U_{ij}, \quad (2.12)$$

with

$$U_{ij} = f_C(r_{ij}) [f_R(r_{ij}) + b_{ij} f_A(r_{ij})], \quad (2.13)$$

where the potential energy is decomposed into a site energy E_i which is expressed then as a bonding energy U_{ij} . r_{ij} is the distance between the atoms i and j . f_A and f_R are the attractive and repulsive pair potentials, respectively; and f_C is a smooth cut-off function. These functions are given by

$$f_R(r_{ij}) = A e^{-\lambda_1 r_{ij}}, \quad (2.14)$$

$$f_A(r_{ij}) = -B e^{-\lambda_2 r_{ij}}, \quad (2.15)$$

$$f_C(r_{ij}) = \begin{cases} 1 & \text{if } r < R - D \\ \frac{1}{2} - \frac{1}{2} \sin \left[\frac{\pi}{2} (r - R) / D \right] & \text{if } R - D < r < R + D \\ 0 & \text{if } r > R + D. \end{cases} \quad (2.16)$$

Notice that the parameters R and D are not systematically optimized but are chosen so as to include the first-neighbor shell (mainly for high-symmetry bulk structure). The f_C function, thus, decreases from 1 to 0 in the range $R - D < r < R + D$. The main feature of this potential is the presence of the b_{ij} term. As explained before, the basic idea is that the strength of each bond depends upon the local environment and is lowered when the number of neighbors is relatively high. This dependence is expressed by b_{ij} , which can increase or reduce the attractive force

relative to the repulsive force, according to the environment, such that

$$b_{ij} = \frac{1}{\left(1 + \beta^n \zeta_{ij}^n\right)^{1/2n}}, \quad (2.17)$$

$$\zeta_{ij} = \sum_{k \neq i, j} f_C(r_{ij}) g(\theta_{ijk}) e^{[\lambda_3^3 (r_{ij} - r_{ik})^3]}, \quad (2.18)$$

$$g(\theta_{ijk}) = 1 + \frac{c^2}{d^2} - \frac{c^2}{[d^2 + (h - \cos \theta)^2]}. \quad (2.19)$$

The term ζ_{ij} defines the effective coordination number of atom i , i.e., the number of nearest neighbors, taken into account the relative distance of two neighbors $r_{ij} - r_{ik}$ and the bond angle θ . The function $g(\theta)$ has a minimum for $h = \cos \theta$, the parameter d determines how sharp the dependence on angle is, and c expresses the strength of the angular effect. This potential and the parameters were chosen to fit theoretical and experimental data obtained for realistic and hypothetical silicon configurations, namely the cohesive energy of several high-symmetry bulk structures, the lattice constant and bulk modulus of the silicon lattice in the diamond configuration.

Additionally, as it was mentioned above, the force field parameters are usually developed for individual element only. However, besides single element materials, alloys offer a continuously variable system with a wide range of crystal lattices and band gaps, leading to various new physical and chemical properties. To model the interatomic interaction in multi-component system, the force field parameters are approximated by a combination of single-element parameters. The most frequently used mixing rules are the arithmetic average (Lorentz rule) for length parameters [179]

$$\sigma_{ij} = \frac{\sigma_i + \sigma_j}{2}, \quad (2.20)$$

and the geometric average (Berthelot rule) for energy parameters

$$\epsilon_{ij} = \sqrt{\epsilon_i \epsilon_j}. \quad (2.21)$$

2.1.2 Heat bath

Conventional MD generates a microcanonical ensemble (NVE), in which the total number of particles, the volume, and the energy are conserved. The conservation of energy allows the numerical stability of the simulation to be tested. However, to compare the simulations with experiments, it is better to use the canonical ensemble (NVT), in which the temperature, instead of the energy, is controlled. The temperature of a system, based on the equipartition theorem, is defined as

$$T = \frac{2}{3Nk_B} \left\langle \sum_{i=1}^N \frac{m_i \mathbf{v}_i \cdot \mathbf{v}_i}{2} \right\rangle, \quad (2.22)$$

where N is total number of atoms in the system, k_B is Boltzmann constant, m_i and \mathbf{v}_i is the mass and velocity vector of atom i , respectively. The angular bracket denotes the ensemble average.

Thus, for a NVT simulation, it is essential the definition of a heat bath, which is also called thermostat. The heat bath maintains a fixed temperature for a particular part of the system. It works by adding an additional force term to the system's Hamiltonian. This additional force interacts with the particles in the system. Hence, the momentum of the particles is adjusted corresponding to the target temperature. If the momentum is too large, the temperature will be reduced, otherwise, it will be increased. Depending on the nature of the extra force (excitation), there are two kinds of heat baths widely used in MD simulations [180]. One is the deterministic type, such as Berendsen and Nose-Hoover (NH) heat baths, and the other is the stochastic type, such as Langevin heat bath.

In general, a deterministic heat bath is preferred as it is time reversible and the results are reproducible. Here, the Berendsen heat bath is the simplest thermostat to implement due to that it modifies the bath temperature by only scaling the particle velocities [181]. However, because of its inability to reproduce a fully canonical ensemble, this thermostat has been reported to cause artifacts in various studies [182]. Consequently, in the present work, NH heat bath will be used for all temperature equilibration and NEMD simulations.

In the scheme of the NH thermostat, the equation of motion for a particle i in the heat bath is:

$$\frac{d\mathbf{r}_i}{dt} = \frac{\partial H}{\partial \mathbf{p}_i}, \quad \frac{d\mathbf{p}_i}{dt} = -\frac{\partial H}{\partial \mathbf{r}_i} - \zeta \mathbf{p}_i, \quad (2.23)$$

where H is the Hamiltonian of the system, $\mathbf{p}_i = m_i \mathbf{v}_i$ and \mathbf{r}_i are the momentum and coordinate of particle i , respectively, and ζ is an auxiliary variable modeling the microscopic action of the heat bath. The dynamics of ζ is governed by the following equation:

$$\frac{d\zeta}{dt} = \frac{1}{\tau^2} \left[\frac{T(t)}{T_0} - 1 \right], \quad T(t) = \frac{2}{3Nk_B} \sum_i \frac{\mathbf{p}_i \cdot \mathbf{p}_i}{2m_i}, \quad (2.24)$$

where T_0 and τ are the aimed temperature and the relaxation time of the heat bath, respectively, and N is the total number of particles that is in contact with heat bath. The relaxation time τ should be properly chosen to avoid unrealistically low-temperature fluctuations with small τ , and the inactive sampling with large τ (e.g. $\tau \rightarrow \infty$) [183].

On the other hand, with Langevin heat bath, the equation of motion can be written as

$$\frac{d\mathbf{p}_i}{dt} = -\frac{\partial H}{\partial \mathbf{r}_i} + \xi - \lambda \mathbf{p}_i, \quad (2.25)$$

where the random force ξ and the dissipation rate λ are introduced into the system simultaneously. This kind of stochastic excitation is consistent with the microscopic picture of Brownian motion. The random force ξ follows the Gaussian distribution with zero mean value and variance of $2m\lambda k_B T$ according to the fluctuation-dissipation theorem.

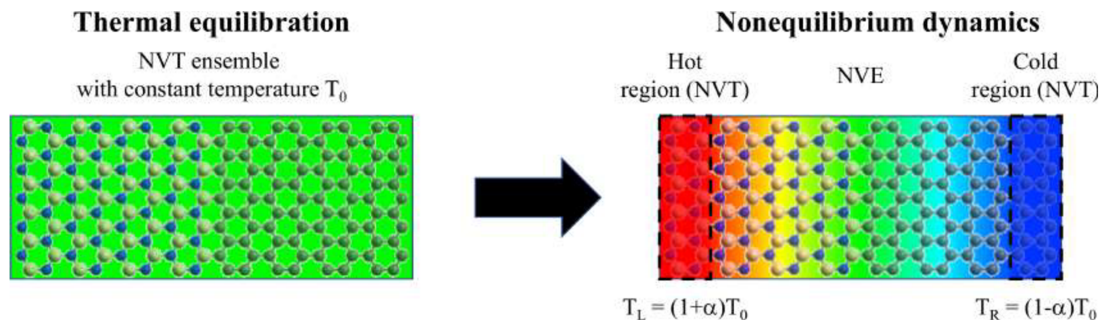


Figure 2.1: Schematic representation of the procedure used to perform the nonequilibrium molecular dynamics simulations. Firstly, thermal equilibration at a constant temperature T_0 is carried out and, hence, a temperature bias $\Delta T = 2\alpha T_0$ is imposed until the system reaches the steady state. Then, the thermal transport properties are calculated.

2.1.3 Nonequilibrium molecular dynamics

During the last decades, with the development of technology to synthesize and characterize materials at the nanoscale, there has been a great demand to understand and control their thermal transport properties. As it is well-known, thermal transport at this scale needs to be thought differently from that at the macroscale, namely in terms of the size effect of the intrinsic heat conduction and the importance of interfaces. Hence, besides characterizing thermal transport properties in macroscale systems, nonequilibrium molecular dynamics (NEMD) method also offers a straightforward route to calculate these properties at length scale smaller than the phonon mean free path of the material. Moreover, it can be an alternative choice to equilibrium molecular dynamics (EMD) method, also known as Green-Kubo (GK) method, which is based on the linear response theory and widely used to calculate thermal conductivity in periodic systems (or macroscale systems) [184]. The general strategy of NEMD method is to calculate thermal conductivity by applying a perturbation to the system and measuring the response. Indeed, NEMD-based methods utilize perturbations to realize faster convergence compared to the GK method. NEMD simulations are also closer in realization to experimental measurements, and are suitable to prove the onset of nonlinear effects due to large temperature gradients.

A typical NEMD simulation begins by equilibrating the system at a certain temperature, typically the mean target temperature. Then, one defines two regions at the ends of the simulation cell as heat source and heat sink, and generates an energy heat flow between which perturbs the dynamics in the central region (acting as a NVE ensemble). This phenomenon is schematically represented in Fig. 2.1. Eventually, the system converges to a steady state with linear temperature gradient and constant heat flux. The required time to reach convergence generally grows with the system size due to increase in the degrees of freedom. Notice that when the system size is comparable to the mean free path of phonons, further increasing of the size makes the heat conduction more diffusive, which helps the system to reach the steady state. Once steady state is achieved, from the temperature gradient ∇T and heat flux J , thermal conductivity can be

calculated through the Fourier's Law,

$$\kappa = -\frac{J}{\nabla T}. \quad (2.26)$$

There are several ways of controlling the temperature in the thermal reservoirs. An option, which will be used in the present work, is to apply thermostat, e.g., velocity scaling, Nosé-Hoover, Langevin, as described above. Alternatively, one can apply the reverse-NEMD approach, in which the stationary heat flux is induced by swapping the momenta of particles between the heat source and sink [27, 185]. Although it has been pointed out that the choice can alter the convergence speed or conservation of momentum and energy, these appear to have little influence to the calculated values of thermal conductivity [184, 185].

Despite the simplicity of the simulation, there are several methodological issues that are worth addressing. For instance, for the linear response theory to be applicable, the temperature gradient needs to be sufficiently small. Since it is not possible to prove a priori, it needs to be checked by performing multiple simulations with different temperature gradients and heat fluxes [186]. Moreover, on carrying out NEMD simulations by locally applying the thermostat at the ends of the system, the interface between the temperature-controlled part and the central region often gives rise to a nonlinear temperature profile near the thermostats [187]. This appears due to the mismatch of lattice-vibrational spectra between the heat bath and the rest of the system. This mismatch causes reflection of vibrational modes and alters the scattering dynamics at the boundary, and thus, give rise to local nonequilibrium phonon distribution, which can significantly alter the overall heat conduction when the system length is smaller than the characteristic phonon mean free path. The most intuitive approach to minimize this effect is by choosing the appropriate thermostat parameters [187]. In the present work, a benchmark of the parameters for Nose-Hoover thermostat has been performed for MoS₂ nanoribbons, see Appendix A.

2.1.4 Vibrational modes analysis

To rationalize the process of thermal rectification in the studied nanoscale systems, a vibrational mode analysis in real space is performed [188, 189]. Here, it is assumed that the normal-mode solution of the atom i takes the form of $u_{i\alpha,\lambda} = (1/\sqrt{m})\varepsilon_{i\alpha,\lambda} \exp(i\omega_\lambda t)$. Hence, to find the normal-mode frequencies ω_λ and their corresponding vector components $\varepsilon_{i\alpha,\lambda}$ of the vibrational modes, the lattice dynamical equations must be solved [189]:

$$\omega_\lambda^2 \varepsilon_{i\alpha,\lambda} = \sum_{j\beta} \Phi_{i\alpha,j\beta} \varepsilon_{j\beta,\lambda}, \quad (2.27)$$

where Φ is the mass-weighted force constant matrix and its elements are given by

$$\Phi_{i\alpha,j\beta} = \frac{1}{\sqrt{m_i m_j}} \frac{\partial^2 U}{\partial u_{i\alpha} \partial u_{j\beta}}. \quad (2.28)$$

Here $u_{i\alpha}$ is the displacement of ion i in the α Cartesian direction, m_i is the mass of ion i , and U is the total potential energy employed for the molecular dynamics simulation. The dynamical matrix can be thought of as representing the connection between the forces acting on the atoms and the displacements from their equilibrium positions of those atoms. Then, the atomic forces are calculated numerically using a finite-difference approach. The vibrational modes of a system with N atoms are calculated by diagonalizing the $3N \times 3N$ matrix given by Eq. (2.28). In the present study, time and configurational averages are performed for all the quantities related to this analysis.

The first important characteristic of the vibrational properties is the vibrational density of states (VDOS) which measures number of vibrations within a given frequency range. Considering the presence of edges and interfaces in nanostructures, it is useful to examine the relative contribution of a given group of atoms to the total VDOS. Thus, the partial VDOS (PVDOS) is defined as [189]:

$$S(\omega) = \sum_{j_A} \sum_{\lambda} \sum_{\alpha} |\varepsilon_{j_A\alpha,\lambda}|^2 \delta(\omega - \omega_{\lambda}), \quad (2.29)$$

where $\varepsilon_{j_A\alpha,\lambda}$ is the vibrational eigenvector component of mode λ with polarization $\alpha = X, Y, Z$, and ω_{λ} is the frequency of the corresponding mode. Notice that the sum over j_A only includes atoms of a given type. Summing then over the index A gives the total VDOS. On the other hand, Dickey and Paskin [190] found that $S(\omega)$ is also equal to the Fourier transform of the velocity autocorrelation function of the system $f(t)$, i.e.,¹

$$\bar{S}(\omega) = \int f(t) \cos \omega t dt, \quad (2.30)$$

where $f(t)$ describes correlations between velocities at different times along an equilibrium trajectory and it is calculated as [191]:

$$f(t) = \frac{\langle \sum_{i=1}^N \mathbf{v}_i(t_0) \cdot \mathbf{v}_i(t) \rangle}{\langle \sum_{i=1}^N \mathbf{v}_i^2(t_0) \rangle}. \quad (2.31)$$

Nevertheless, the information provided by the VDOS analysis does not reveal the degree of localization or delocalization of the vibrational modes in different spectral ranges. Hence, to characterize each mode λ with respect to these features, the participation ratio (PR) has been calculated, which is defined according to:

$$P_{\lambda}^{-1} = N \sum_i \left(\sum_{\alpha} \varepsilon_{i\alpha,\lambda}^* \varepsilon_{i\alpha,\lambda} \right)^2. \quad (2.32)$$

Here, $\varepsilon_{i\alpha,\lambda}$ is the vibrational eigenvector component of atom i and N is the number of atoms in the system. The PR measures the fraction of atoms participating in a mode and hence varies between 1 for delocalized modes to $O(1/N)$ for localized modes.

¹Here, the notation $\bar{S}(\omega)$ has been used to distinguish the vibrational density of states computed by using the velocity autocorrelation function from this one calculated within the real-space vibrational mode analysis, $S(\omega)$.

To complement the previous analysis, the spatial distribution of the vibrational modes located within a specific spectral range (Λ) was analyzed by defining the quantity $\phi_{i\alpha,\Lambda}$, which is computed as: [192]

$$\phi_{i\alpha,\Lambda} = \frac{\sum_{\lambda \in \Lambda} \varepsilon_{i\alpha,\lambda}^* \varepsilon_{i\alpha,\lambda}}{\sum_{1 \leq j \leq N} \sum_{\lambda \in \Lambda} \varepsilon_{j\alpha,\lambda}^* \varepsilon_{j\alpha,\lambda}}. \quad (2.33)$$

A large value of $\phi_{i\alpha,\Lambda}$ indicates a strong contribution of the i th atom to vibrational modes belonging to the spectral region defined by Λ . Moreover, while the participation ratio only gives information about the degree of localization, there are extra quantities that describe additional features of the vibrational modes in the system. Thus, the polarization vector $e_{i\alpha,\lambda}$ of an atom i , for a given mode λ , is defined as:

$$e_{i\alpha,\lambda} = \frac{\varepsilon_{i\alpha,\lambda}}{\sum_{\alpha} \varepsilon_{i\alpha,\lambda}^* \varepsilon_{i\alpha,\lambda}}. \quad (2.34)$$

In a crystal without defects, the normal modes are all modes with well-defined polarization vectors [193]. For example, for an LA mode, if the polarization vector is parallel to \mathbf{k} (say, the Z direction), then each ion has a unit polarization vector component of ± 1 in the Z direction and 0 in the X and Y directions.

Another relevant quantity is the phase quotient Ψ_{λ} of a mode λ , which is given by [188]:

$$\Psi_{\lambda} = \frac{\sum_{\langle i,j \rangle} (\sum_{\alpha} \varepsilon_{i\alpha,\lambda} \varepsilon_{j\alpha,\lambda})}{\sum_{\langle i,j \rangle} |\sum_{\alpha} \varepsilon_{i\alpha,\lambda} \varepsilon_{j\alpha,\lambda}|}, \quad (2.35)$$

where i and j are nearest neighbors. Ψ_{λ} is a discriminant of the acoustic versus optical nature of the mode. Ψ_{λ} values near 1.0 indicate that nearest-neighbors atoms vibrate mostly in-phase like an acoustic mode, while, values near -1 indicate that they vibrate out-of-phase in a manner characteristic of an optical mode.

2.2 TUNING THE PROPERTIES OF THERMAL RECTIFIERS

It has been proved that equilibrium thermal transport properties (e.g., thermal conductivity) of nanomaterials can be tuned by modifying some features of the material. However, regarding to nonequilibrium effects such as thermal rectification, there is only information about carbon-based materials [37, 40, 73, 76–78]. Hence, in this section, thermal rectifiers made of MoS₂ [194] and coplanar graphene/hBN [195] nanoribbons will be proposed. The main idea is to study the influence of two relevant factors: the geometry of the nanomaterial and the substrate type on which they are deposited. To know the efficiency of a material as a rectifier, the heat flux in forward J_f and backward J_b directions have to be measured. The backward direction of the heat flux is computed by reversing the temperature gradient direction. To quantify the performance as rectifier, a thermal rectification (TR) ratio η is defined as:

$$\eta[\%] = \left(\frac{|J_f - J_b|}{J_b} \right) \times 100. \quad (2.36)$$

The heat currents $J_{f,b}$ induced by the temperature bias ΔT are computed as

$$J_{f,b} = \frac{1}{2} \left(\frac{\partial E_L^{f,b}}{\partial t} + \frac{\partial E_R^{f,b}}{\partial t} \right), \quad (2.37)$$

where $E_L^{f,b}$ and $E_R^{f,b}$ are the total energies that have been added to or subtracted from the atoms in the left (L) and right (R) heat baths, respectively. Notice that once the system reaches the steady state, the absolute values of the time derivatives have to be almost the same for left and right baths. As it is shown in Appendix A, a wrong choice of thermostat parameters may lead to an improper interpretation of the simulation results.

2.2.1 Structural asymmetry

Here, the influence of the geometry on the thermal rectification is first studied. Based on previous works, it is known that symmetric nanoribbons made of a single material do not display thermal rectification effect [2]. In fact, the geometry of the material must present a structural asymmetry in order to produce this effect. Thus, to improve the performance of the material as thermal rectifiers the degree of structural asymmetry has to increase. This geometrical factor is quantified using the dimensionless quantity $W_{LR} = W_{\text{Left}}/W_{\text{Right}}$ with W_{Left} and W_{Right} are the widths of the left and right ends of the nanoribbon, respectively (see Fig. 2.2(a)). The case $W_{LR} = 1.0$ corresponds to a fully symmetric rectangular structure. The length (L) and width (W) of the central region of the nanoribbon change by the same scale, $W_{\text{Left}} = \sqrt{3}L/2$, when its size increases. Only W_{Right} is reduced to generate the structural asymmetry.

In this section, for all NEMD simulations, the temperatures for left and right heat baths are defined as $T_L = (1+\alpha)T_0$ and $T_R = (1-\alpha)T_0$ for the forward direction of the heat flux (heat flows left-to-right or wider-to-narrower) and the opposite case for the backward direction (heat flows right-to-left or narrower-to-wider). Then, the temperature bias is equal to $\Delta T = |T_L - T_R| = 2\alpha T_0$ ($\alpha > 0$). To avoid spurious effects related to the specific choice of initial velocities, an average over five random choices of the initial velocity distribution is additionally performed. Nanoribbons are simulated with free boundary conditions in all directions. The ends in X-direction (one layer) have been fixed to avoid global rotations of the system during the simulation. The standard velocity Verlet algorithm is used to integrate Newton's equations of motion, and the MD time step depends on the study, for MoS₂ nanoribbons is set to 0.5 fs, while for coplanar graphene/hBN nanoribbons is 0.1 fs. All investigated nanostructures have been initially relaxed using a quickstep method.

MoS₂-based thermal rectifier

Besides graphene, there are meanwhile a variety of novel two-dimensional materials which are expected to display different transport properties due to the differences in their chemical

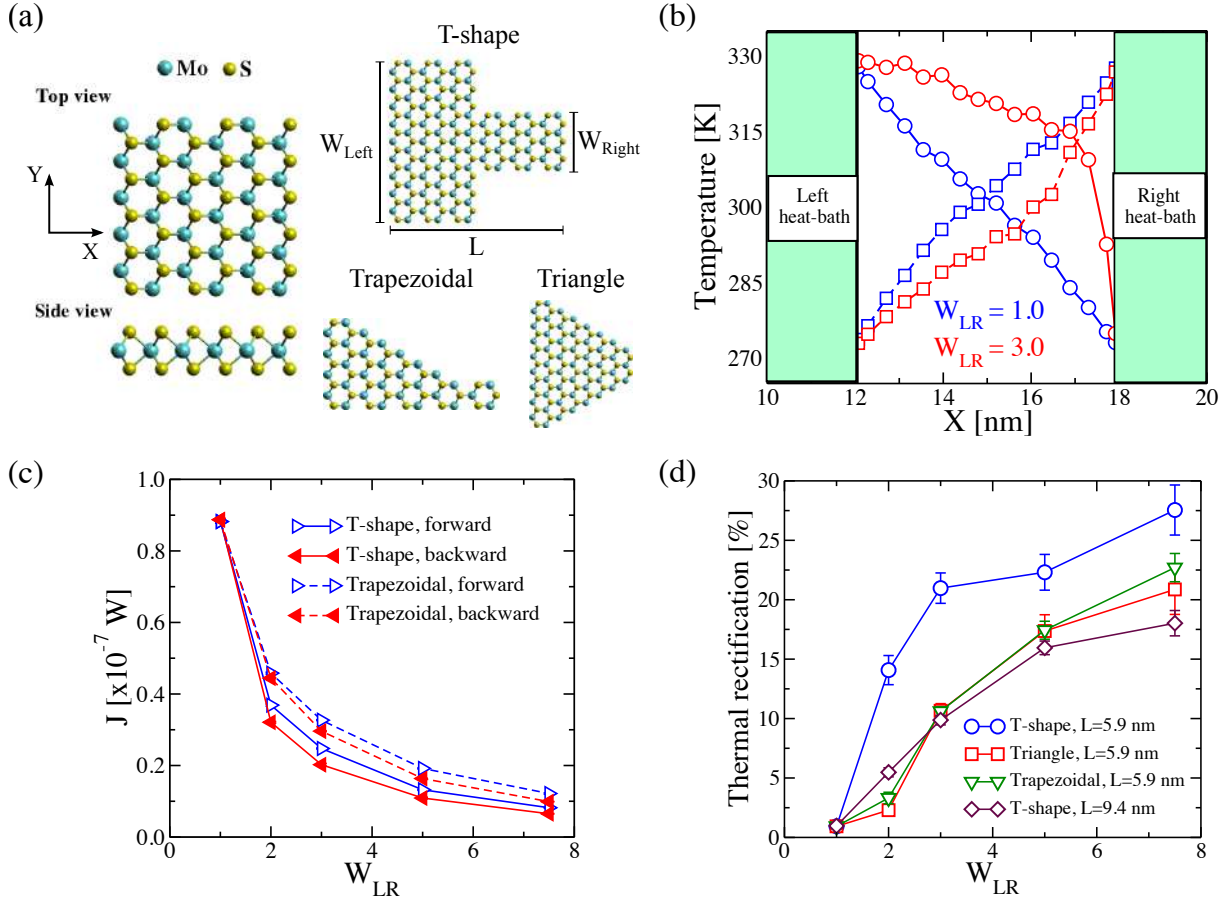


Figure 2.2: (a) Schematic of MoS₂ monolayer. Top and side view in armchair direction. Asymmetrical geometrical shapes selected for the MoS₂ nanoribbons ($W_{Left} = \sqrt{3}L/2$). (b) Temperature profile for trapezoidal nanoribbons of length equal to 5.9 nm with $W_{LR} = 1.0$ (blue lines) and $W_{LR} = 3.0$ (red lines). Both, forward (○) and backward (□) directions of the heat flux are shown. Variation of the (c) heat flux and (d) thermal rectification after increasing W_{LR} parameter for each geometrical shape. For these calculations, $T_0 = 300$ K and $\alpha = 0.1$ have been considered.

composition (see Chapter 1), and thus offer a new broad playground to explore and develop nanoscale devices, e.g., thermal rectifiers. One of these materials is molybdenum disulphide (MoS₂) monolayer, which has attracted considerable attention mainly because of its sizable electronic bandgap and lower thermal conductivity compared to graphene [104, 105, 107]. Although a variety of theoretical studies has been published, addressing the phonon dispersion and thermal conductivity of MoS₂ layers and ribbons [114, 115, 117, 151, 158, 196–198], less attention has yet been devoted to the possibility of engineering the thermal response of MoS₂ nanostructures via structural asymmetries. Thus, in the present section, three geometrical shapes of MoS₂ nanoribbons have been considered to study possible thermal rectification effects: T-shaped, trapezoidal, and triangular (see Fig. 2.2a). Hence, as it was mentioned above, a crucial issue in all MD simulation is the choice of the appropriate force field. In the case of MoS₂ several force fields have recently been developed [158, 197]. However, they turned out to have different problems when applying them to simulate systems with open boundary conditions (e.g., nanoribbons) at

room temperature. Consequently, after careful checks, a force field developed on the basis of tight-binding quantum chemistry calculations by Onodera et al. [199] has been used to perform the NEMD simulations. This force field includes ionic, covalent, and van der Waals interactions among Mo and S atoms. This interatomic potential has already been successfully applied to study mechanical [199, 200] and thermal [106] properties of MoS₂ monolayer.

After geometry optimization, the lattice constant for MoS₂ obtained is $a = 3.38 \text{ \AA}$. This value is close to the one reported in previous works [158, 197]. Then, equilibration MD in the NVT ensemble is first run for 2 ns and at $T_0 = 300 \text{ K}$ with a Nosé-Hoover thermostat using a relaxation time equal to 0.1 ps. The choice of thermostat is a sensitive issue in NEMD simulations, but as discussed in Ref. [71], different algorithms in NEMD simulations only led to negligible differences in the computed heat flows². Once the temperature reached the required value, the thermostat was removed, and the NEMD simulations were carried out for 20 ns. Each heat bath extended over four atomic layers corresponding to a length of roughly $\sim 2.3 \text{ nm}$. Time averages of the temperature and the heat current were carried out over the last 10 ns of the simulation.

Fig. 2.2(b) shows the temperature profiles at a bias of $\alpha = 0.1$ for trapezoidal MoS₂ nanoribbons of length $L = 5.9 \text{ nm}$ with $W_{\text{LR}} = 1.0$ (symmetric) and $W_{\text{LR}} = 3.0$ (asymmetric). For symmetric nanoribbons, the temperature profile has a symmetric and nearly linear behavior for both directions, forward and backward, of the applied temperature bias, so that no rectification of the thermal current can take place, as expected. Whereas, for $W_{\text{LR}} = 3.0$, the temperature gradient along the nanoribbon becomes non-linear and displays a different dependence on the spatial distance from the heat baths for forward and backward heat flows. Notice that the mean temperature is mainly controlled by the wider heat bath (left bath), and this shows up in the strong non-linear evolution of the temperature profile after increasing distance from the wider bath. As a consequence, the corresponding thermal currents are also different and heat rectification can take place, see Fig. 2.2(c). In other words, the heat flux runs preferentially from the wider to the narrower region, so that the device behaves as a “good” thermal conductor in that direction. This behavior is improved when the temperature bias is increased, as shown in the inset of Fig. 2.5. In Fig. 2.2(d), one can see that for the different nanoribbon shapes, the qualitative trends are rather similar: with increasing structural asymmetry the degree of rectification increases and can achieve rather high values of roughly 30 %, values which are comparable with those found in more complex engineered graphene nanoribbons [37, 78]. This is related to the increasing difference in the number of atoms involved in the nanoribbon-heat bath interaction at both ends with increasing W_{LR} , which increasingly breaks the heat flux symmetry as the temperature bias is reversed. These effects have been also reported for graphene ribbons [37, 40, 73]. There is however a clear quantitative difference in the heat rectification efficiency of T-shaped ribbons when compared to the triangular and trapezoidal ones. Namely, the former has a larger TR ratio for the same length L . This is largely related to how the transition from the wider to the narrower region is built in: in the triangular and trapezoidal nanoribbons the transition

²See Appendix A for a discussion of the thermostat parameters used in these simulations

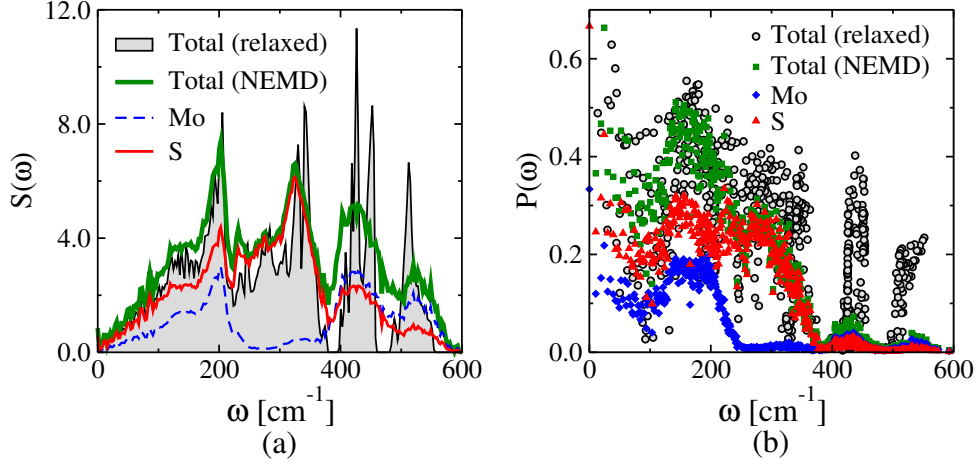


Figure 2.3: Total and partial (a) vibrational density of states and (b) participation ratio for the T-shaped MoS₂ nanoribbon with length $L = 5.9$ nm and $W_{LR} = 3.0$ as obtained from NEMD simulations in the forward temperature bias direction ($\alpha = 0.1$). For reference, the corresponding total VDOS for the structurally relaxed (i.e. before starting the NEMD simulation) T-shaped MoS₂ nanoribbon with $W_{LR} = 3.0$ is also shown.

is smooth (it can be called adiabatic as done with quantum point contacts [201]), while for the T-shaped ribbon there is a narrow interface region where an abrupt transition from wider to narrower sections takes place. Hence, heat flow differences resulting from the global asymmetry of the nanoribbon will be enhanced due to this sharp interface. Notice that upon increasing the system size, the effect of the structural asymmetry in the thermal rectification weakens and eventually disappears, i.e. $\eta \rightarrow 0$ for $L(\text{or } W) \rightarrow \infty$. Fig. 2.2(d) shows this tendency for T-shaped ribbons with two different lengths: $L = 5.9$ nm and $L = 9.4$ nm and highlights the fact that, besides structural asymmetry, another major factor influencing thermal rectification is the transversal finite size of the nanostructures [2, 37, 73].

Next, to rationalize the process of thermal rectification in asymmetrically structured MoS₂ nanoribbons, a real-space mode analysis is performed [202] (see Sec. 2.1.4). For the sake of clarity, this part is only focused on T-shaped nanoribbon with $L = 5.9$ nm and $W_{LR} = 3.0$, since the results for the other geometries are qualitatively similar [194]. In Fig. 2.3(a), the total and partial vibrational density of states (PVDOS) of the T-shaped ribbon are displayed. Here, the VDOS of the structurally relaxed T-shaped nanoribbon before running the NEMD simulation (black solid line) is showed as reference. The major difference to the VDOS obtained from the NEMD simulation (green solid line) is the spectral broadening, which manifests more clearly for the high-frequency vibrational modes above 400 cm^{-1} . Regarding to the PVDOS for Mo and S atoms in the nanoribbon, it can be roughly identified three different spectral regions [197]: a low frequency range (up to 200 cm^{-1}) where both S and Mo atoms carry similar spectral weights, although the contributions of the S atoms are slightly larger; an intermediate range ($\sim 200\text{-}380 \text{ cm}^{-1}$), where the spectral weight is carried almost exclusively by S atoms; a high frequency range ($> 380 \text{ cm}^{-1}$) where again both atom types contribute similarly to the total VDOS, although

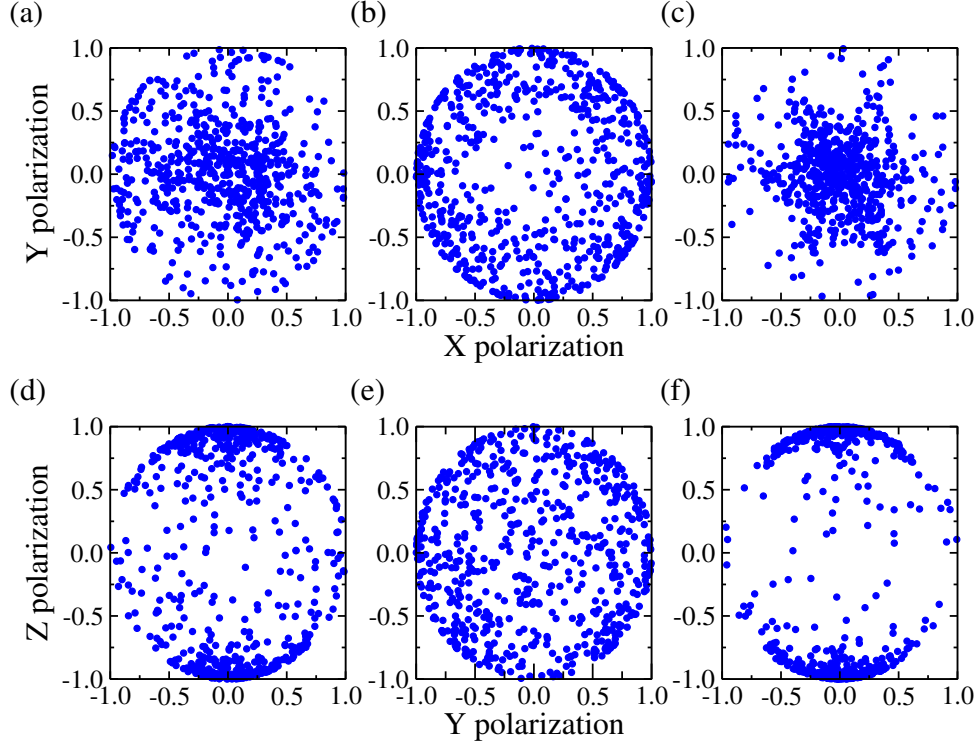


Figure 2.4: Projections of the polarization vectors onto Y-X and Z-Y planes for the T-shaped MoS₂ nanoribbon with $W_{LR} = 3.0$ after NEMD simulation in the forward direction ($T_0 = 300$ K and $\alpha = 0.1$) in the frequencies: (a,d) 50 cm^{-1} , (b,e) 350 cm^{-1} , and (c,f) 560 cm^{-1} .

here Mo atoms have a slightly larger spectral weight. For the backward heat flow direction a similar qualitative behavior was obtained (not shown).

Accordingly, the participation ratio (PR) has been calculated to characterize the degree of localization or delocalization of the vibrational modes (see Fig. 2.3(b)). Similar to the VDOS plot in Fig. 2.3(a), the PR for the relaxed T-shaped nanoribbon previous to starting the NEMD simulation is also shown. Moreover, partial PRs associated to Mo and S atoms are also shown [193]. The first point to notice is that the nonequilibrium vibrational spectrum is mostly modified in the higher frequency part with modes lying roughly above 400 cm^{-1} . While for the relaxed nanoribbon can be identified two clear groups of modes in this frequency range with $\text{PR} \sim 0.4$ and 0.25 . The nonequilibrium modes show a considerably larger degree of localization with PR below 0.1 . For lower frequencies the differences between these two cases are much weaker, though. The partial PRs show that modes with a higher degree of delocalization (larger PR) involve in general a larger contribution from S atoms. In short, apart from the very low frequency vibrations below 100 cm^{-1} and a narrow region between 150 cm^{-1} and 220 cm^{-1} , almost all modes in the nanoribbon display a stronger tendency to localization with PRs smaller than 0.4 , which is a signature of the strong impact of structural asymmetries, finite cross-section of the nanoribbons, and temperature.

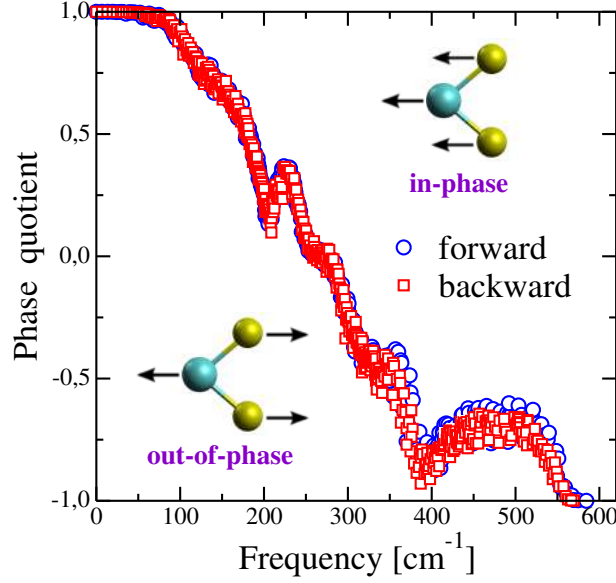


Figure 2.5: Frequency dependence of the phase quotient for the T-shaped MoS₂ nanoribbon with $W_{\text{LR}} = 3.0$ after a NEMD simulation in the forward (○-blue lines) and backward (□-red lines) directions ($T_0 = 300$ K and $\alpha = 0.1$).

Fig. 2.4 shows the projections of the polarization vectors onto the Y-X and the Z-Y planes for the T-shaped MoS₂ nanoribbon with $W_{\text{LR}} = 3.0$ after NEMD simulations with heat flowing in the forward direction. Only three representative frequencies have been selected for this analysis: 50 cm⁻¹ (Fig. 2.4(a,d)), 350 cm⁻¹ (Fig. 2.4(b,e)), and 560 cm⁻¹ (Fig. 2.4(c,f)). The results show that frequencies <90 cm⁻¹ behave like a propagon mode, while frequencies between 90 cm⁻¹ and 550 cm⁻¹ are diffusion modes with frequency dependence of their participation ratio [188, 189]. Highest frequencies, >550 cm⁻¹, tend to have a unit polarization vector component in the Z direction and are expected to be locon modes as discussed in the context of amorphous systems [189]. Therefore, the atoms are essentially vibrating in the plane during the NEMD simulation but this phenomena depends on the frequency of the vibrational mode. Similar behavior has been found for the other geometries studied in the present work.

Furthermore, in Fig. 2.5, the phase quotient Ψ_λ for the T-shaped MoS₂ nanoribbon with $W_{\text{LR}} = 3.0$ is showed. For low frequencies values, independently of the heat flux direction, Ψ_λ is near 1.0 indicating that nearest-neighbors atoms vibrate mostly in-phase like an acoustic mode, while, for high frequencies, Ψ_λ values are close to -1.0 which says that they are vibrating out-of-phase in a manner characteristic of an optical mode. Also, one can see that the frequency dependence of the phase quotient for forward or backward direction forms a band of monotonically decreasing values. However, there is an increase of phase quotient in the range 200-230 cm⁻¹. As was reported in Ref. [189], this increase coincides with the end of the transverse acoustic TA branch in MoS₂ bulk which is 210 cm⁻¹, which is related to the presence of a local minimum in the vibrational density of states. As the TA branch ends, the modes begin to acquire features akin to LA, leading to an increase in the phase quotient. These properties have been properly invoked for diffusion modes in amorphous silicon, but apparently similar

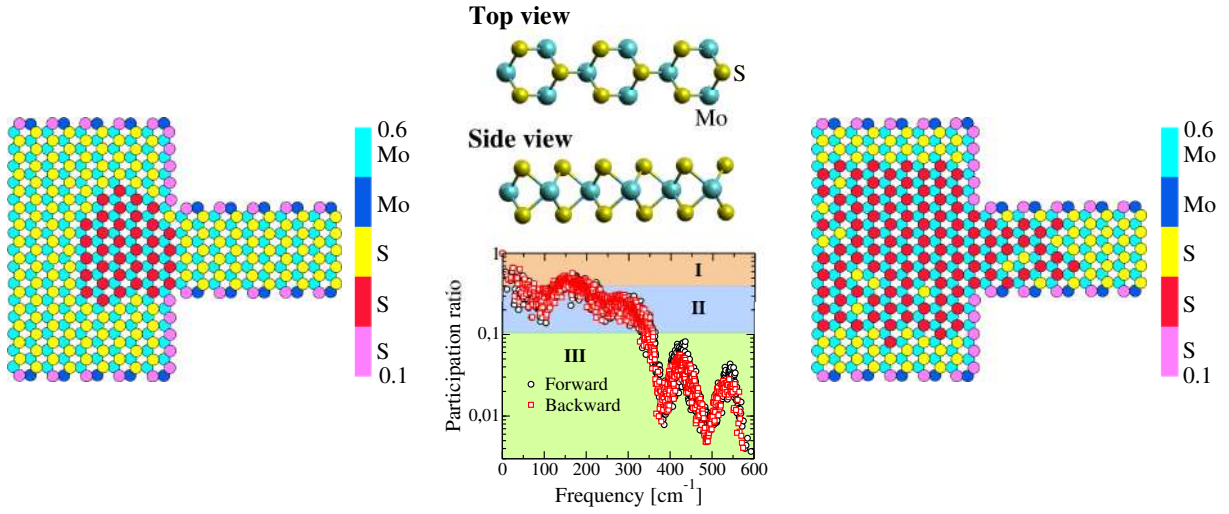


Figure 2.6: Spatial distributions, ϕ , of vibrational modes for T-shaped MoS₂ nanoribbons of $L = 5.9$ nm and $W_{LR} = 3.0$ (XY plane). Here, only vibrational modes with $P < 0.1$ have been considered for the system obtained after NEMD simulation in the (left panel) forward and (right panel) backward direction of the heat flux ($\alpha = 0.1$). The color scale has the same meaning for all the cases, i.e., cyan balls mean highest contribution while pink balls lowest contribution for the vibrational modes. In these pictures, only contributions arising from the top S-layer as well as the Mo-layer are shown.

physics is taking place in asymmetric MoS₂ nanoribbons because of the finite size effects and the non-equilibrium conditions.

To complement the previous analysis, the spatial distribution of the vibrational modes located within a specific spectral range (Λ) is analyzed by defining the quantity $\phi_{i\alpha,\Lambda}$ (see Sec. 2.1.4). To define the set Λ , three possible PR regions are selected as shown in the central panel of Fig. 2.6: I) $P > 0.4$, II) $0.1 < P < 0.4$, and III) $P < 0.1$. $\phi_{i\alpha,\Lambda}$ for the domains I and II turns out to have almost the same behavior for forward and backward heat flows (see Appendix A). Thus, modes in those spectral ranges do not seem to strongly determine the rectification of the heat current. Major differences were however found for region III as displayed in the left and right panels of Fig. 2.6. Here, in contrast to other 2D materials, which consist of a single atomic layer like graphene or BN, MoS₂ nanoribbons are built up of three atomic layers. This makes the visualization of the quantity $\phi_{i\alpha,\Lambda}$ more involved. However, by analyzing the contribution of each atomic layer separately, it was found that the two sulfur planes contribute in similar ways to the spatial distribution of the modes, something to be expected for symmetry reasons. Therefore, contributions arising from the top S-layer as well as from the Mo-layer are only shown in Fig. 2.6. The left and right panels of Fig. 2.6 illustrate the spatial distribution for modes in region III for the forward (left panel) and backward (right panel) directions. The main observed feature is the strong increase, in the backward flow direction, of the number of atoms giving a low contribution (0.2-0.3) to modes in spectral region III, i.e. for frequencies above 350 cm^{-1} . This mainly affects a set of atoms in the bulk of the nanoribbon, while atoms along the edges do not appreciably

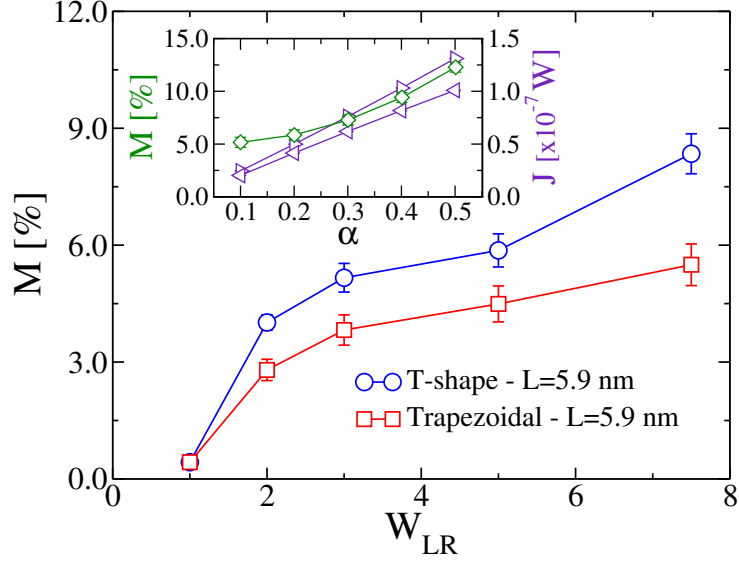


Figure 2.7: Dependence of M parameter with the asymmetry degree, W_{LR} , for the T-shaped and trapezoidal MoS₂ nanoribbons. Values obtained by considering frequencies with $P < 0.1$ have been only considered. Inset: variation of M parameter (\diamond) and heat flux (\triangleright –forward and \triangleleft –backward direction) after increasing the temperature bias for the T-shaped nanoribbon with $W_{LR} = 3.0$.

change the degree of their contribution to the selected spectral range. Moreover, it was found that S atoms are mostly influenced upon reversal of the heat flow, while the contribution from Mo atoms is considerably less modified and remains relatively high ($\phi_{i\alpha,\Lambda} > 0.5$). A simple mathematical relationship between the degree of spatial localization of the vibrational modes and the heat current as computed in a NEMD run is difficult to establish. In this sense, these results only hint at the fact that the strong modification in the spatial distribution of certain groups of modes upon reversal of the direction of heat current flow in asymmetric nanostructures is a major factor determining the size of the thermal rectification effect found in the structurally asymmetric MoS₂ nanoribbons. Trapezoidal shaped nanoribbons also show a very similar behavior (see Appendix A). To this effect, which has been highlighted in earlier works on graphene nanoribbons [37, 72], one also needs to add, as mentioned previously, the finite transversal size of the ribbons, which modifies the boundary conditions for the vibrational spectrum as well as its localization properties, and thus also strongly determines the heat transport features of the system. Clearly, these factors – asymmetry, finite size, modes localization – are not independent from each other and their interplay induces the observed rectification features in the MoS₂ nanoribbons.

Finally, to round off our discussion and to provide a better illustration of the influence of the lateral confinement on the thermal rectification, the parameter M is introduced as:

$$M[\%] = \left(\frac{|\Pi_f - \Pi_b|}{\Pi_b} \right) \times 100, \quad (2.38)$$

with $\Pi = \langle P \rangle_\lambda$ as the frequency averaged participation ratio. λ modes belong to a specified spectral range Λ . It was found that, as expected from the previous discussion, the average

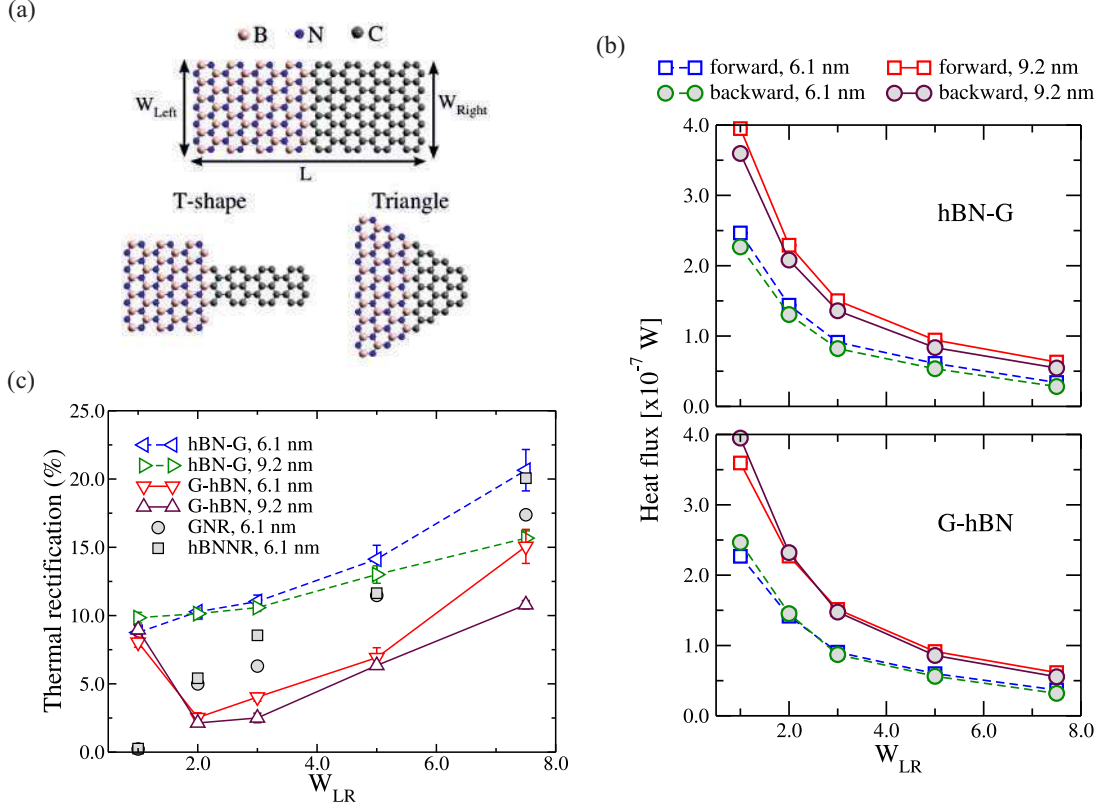


Figure 2.8: (a) Schematic representation of hBN-G heterojunctions with zigzag interface (B-C bridge bonding). The degree of asymmetry is measured by $W_{LR} = W_{Left}/W_{Right}$. (b) Variation of heat flux after increasing the asymmetry degree for hBN-G and G-hBN nanoribbons. Results for two different system size ($L= 6.1$ nm and 9.2 nm) are compared. (c) Thermal rectification as a function of W_{LR} for both type of nanoribbons. η values for pure graphene and hBN nanoribbons are also shown.

participation ratios in forward and backward direction for the spectral ranges I and II defined above are almost identical, implying $M \sim 0$. Hence, Fig. 2.7 only shows the dependence of M with the W_{LR} parameter corresponding to the case III with $P < 0.1$ for T-shaped and trapezoidal MoS₂ nanoribbons. Alike the behavior of the thermal rectification factor η , M increases when the nanoribbon becomes more asymmetric and consistently, the effect is stronger for the T-shaped ribbon. Moreover, the inset of Fig. 2.7 suggests that another alternative to increase the rectification ratio is to enhance the applied temperature bias, as has been reported for other systems [37, 71, 73].

hBN/C-based thermal rectifier

In the search of novel thermal rectifiers, it has been found that the presence of interfaces can considerably improve the thermal rectification in the device. As mentioned in Chapter 1, heterojunctions composed by graphene and hexagonal boron-nitride (hBN) domains have attracted considerable attention [125–128] and, specially, the synthesis of coplanar hybrid graphene/hBN

monolayers has been successfully reported [125, 126]. Moreover, their thermal transport properties have been extensively studied in several experimental and theoretical works [127, 134, 136–143]. However, up to now, the influence of the geometry on these properties is still an open issue. Hence, coplanar symmetric and asymmetric graphene/hBN nanoribbon heterojunctions with zigzag interface (B-C bridge bonding) have been studied in this section (see Fig. 2.8(a)). Interactions among C, B, and N atoms are simulated by using an optimized Tersoff potential parametrized by Kinaci et al. [139], which has been successfully used to study thermal transport properties of many BNC nanomaterials [139, 143]. Temperature equilibration runs at $T_0 = 300$ K are carried out for 5 ns by considering an NVT ensemble with a Nosé-Hoover thermostat (relaxation time equal to 0.1 ps). Once the temperature reached the required value, the thermostat is removed, and the NEMD simulations are carried out for 40 ns. Each heat bath extended over six atomic layers corresponding to a length of roughly ~ 2.6 nm. Time averages of the temperature and the heat current are carried out over the last 15 ns of the simulation.

Firstly, the thermal transport properties of both types of free-standing nanoribbon heterojunctions, hBN-G and G-hBN, are studied. For the sake of clarity, only the results for T-shaped nanoribbon with $L = 6.1$ nm and $W_{LR} = 3.0$ will be shown, since the results for the triangular shape are qualitatively similar [195]. Fig. 2.8(b) shows that independently of the system size and transport direction the heat flux decreases after increasing degree of asymmetry, as given by the parameter W_{LR} . This is a result of edge effects getting stronger once the number of atoms involved in the heat transfer is reduced [37, 194]. The heat flux for forward direction (from hBN towards graphene nanoribbons) is always greater than the backward direction for all hBN-G structures, which is in agreement with the results of Chen et al. [137]. For the fully symmetric case ($W_{LR} = 1.0$), it has been proven that this effect vanishes when periodic boundary conditions on the axis perpendicular to the transport direction are considered. In fact, the heat flux is independent of the transport direction and $J_{hBN \rightarrow G} = J_{G \rightarrow hBN}$ [136]. In this study, the thermal rectification in hBN-G structures roughly displays a linear dependence on the asymmetry parameter W_{LR} , reaching values $\sim 21\%$ for $L = 6.1$ nm. However, the forward and backward heat fluxes for G-hBN nanoribbon crosses in the range $W_{LR} \in [2.0, 3.0]$. As a result, $J_{G \rightarrow hBN} > J_{hBN \rightarrow G}$ for $W_{LR} > W_C$, and therefore, the corresponding thermal rectification displays a non-monotonous dependence with respect to W_{LR} with a minimum at the crossing point of the forward and backward heat fluxes, see Fig. 2.8(c). Notice that unlike single-material (hBN or Graphene) based nanoribbons, symmetric heterojunctions display rectification effects owing to interface effects which induce an asymmetric temperature profile and, hence, alter the heat flux intensity. A similar phenomenon was reported for heterojunctions made of carbon isotopes [77] and graphene/silicene monolayers [203].

Similar to MoS₂ nanoribbons case, to gain insight into the influence of the degree of asymmetry on the thermal transport of the heterojunctions, a real-space mode analysis in the device region has been performed [37, 194]. Figs. 2.9(a, b) show $S(\omega)$ of T-shaped hBN-G and G-hBN nanoribbons with $L = 6.1$ nm and different W_{LR} . The vibrational density of states for G-hBN

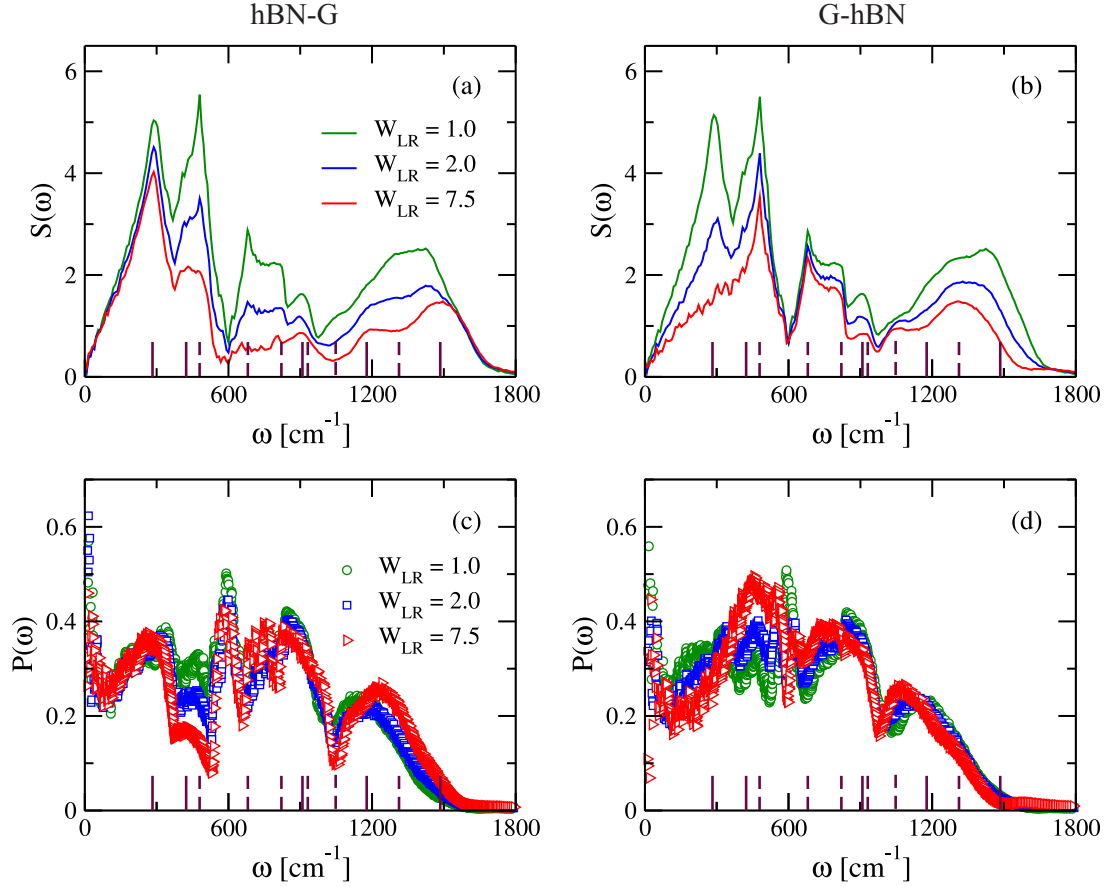


Figure 2.9: Real-space mode analysis of asymmetric heterojunctions. Vibrational density of states and participation ratio at different asymmetry degree W_{LR} for (a,c) hBN-G and (b,d) G-hBN nanoribbons, respectively. The results are for the forward direction of the heat flux. The frequencies corresponding to the vibrational modes of BN atom pairs (solid bar line) and C atoms (dashed bar line) are highlighted.

nanoribbons reduces with increasing W_{LR} . Whereas, $S(\omega)$ of hBN-G nanoribbons is stronger modified in the frequency region $\omega \in [430, 1350] \text{ cm}^{-1}$, which is related to the fact that most of the vibrational modes involving carbon atoms are located within this spectral region. On the contrary, in G-hBN nanoribbons, vibrational modes at lower ($\omega \in [0, 430] \text{ cm}^{-1}$) and higher ($\omega \in [1100, 1700] \text{ cm}^{-1}$) frequencies are suppressed due to the reduction of B and N atoms after increasing W_{LR} . Besides, in order to gain information on the degree of localization of the vibrational modes in different spectral ranges – which has been proven to be one of the mechanisms for thermal rectification – the participation ratio P_λ of each mode λ has been calculated. In Fig. 2.9(c) and (d), one can see that the localization behavior of the vibrational modes in asymmetric nanoribbons is complex and strongly depends on two factors: the planar stacking order and the frequency range. Thus, low frequency modes (up to 350 cm^{-1}) in hBN-G nanoribbons are not much affected with increasing ribbon asymmetry, while the participation ratio is reduced for G-hBN nanoribbons. This effect gets stronger for hBN-G nanoribbons in the range $\omega \in [350, 540] \text{ cm}^{-1}$, where the reduction in the number of C atoms localizes these vibrational modes. For G-hBN, the mode delocalization can increase, $P \sim 0.45$ for $\omega \in [390, 560] \text{ cm}^{-1}$, by making the

Table 2.1: Lennard-Jones parameters for the interaction between the nanoribbon heterojunctions and the different substrates used in the present study. LJ potential, $V(r) = 4\epsilon [(\sigma/r)^{12} - (\sigma/r)^6]$. A cut-off= 6\AA has been considered.

Substrate		ϵ [meV]	σ [\AA]	Substrate		ϵ [meV]	σ [\AA]
Graphite	B-C	3.108	3.411	Si(100)	B-Si	10.268	3.421
	N-C	4.068	3.367		N-Si	12.616	3.595
	C-C	2.635	3.369		C-Si	8.172	3.597
SiC(0001)	B-Si	10.268	3.421	SiO ₂	B-Si	7.357	3.639
	N-Si	12.616	3.595		N-Si	9.039	3.595
	C-Si	8.172	3.597		C-Si	5.855	3.597
	B-C	3.610	3.357		B-O	5.236	3.303
	N-C	4.435	3.313		N-O	6.434	3.259
	C-C	2.873	3.315		C-O	4.168	3.261

nanoribbons more asymmetric. Higher frequency modes ($\omega > 1500 \text{ cm}^{-1}$) are strongly localized for both types of heterojunctions. In short, heat transfer will be dominated by different spectral ranges depending on the junction type.

2.2.2 Substrate deposition

During the last decades, most of studies about thermal transport properties of two-dimensional materials (e.g., Graphene/hBN heterojunctions) have been carried out on free-standing structures, thus neglecting substrate effects. However, very recently, the impact of the substrate on the thermal conductance has been shown for graphene [45, 176, 204], silicene [205–207], molybdenum disulfide MoS₂ [208], and phosphorene monolayers [209]. For instance, both experimental and theoretical investigations have shown that the substrate has always a negative effect on phonon transport in graphene [45, 176, 204]. Whereas, the thermal conductivity of silicene can be either enhanced or suppressed by changing the surface crystal plane of a SiC substrate [205, 206]. Moreover, the thermal conductivity of silicene displays a large reduction of almost 80% at 300 K by considering an amorphous SiO₂ substrate [207]. It has been also found that the interaction between MoS₂ monolayers and an amorphous SiO₂ substrate causes a lifting of the long-wavelength flexural modes leading to a reduction of the in-plane thermal conductivity [208]. This strong dependence of the thermal transport properties on the substrate features highlights the importance of studying coplanar graphene/hBN heterojunctions deposited on several substrates, which is the main goal in this section. Thus, the atomic interactions in graphite, Si(100), SiC(0001), and SiO₂ substrates have been modelled by a Tersoff potential [210–212]. The coupling between the heterojunctions and substrates are described by a LJ potential, see Eq. (2.11). The parameters of the LJ potential for each element were taken from Refs. [213, 214] and are listed on Table 2.1. The distance between graphene/hBN heterojunctions and substrate is taken as $\sim 3.4 \text{ \AA}$ (after geometry optimization). Periodic boundary conditions on the XY plane have been considered and the substrate is large enough to avoid any interaction between the nanoribbon and its replica.

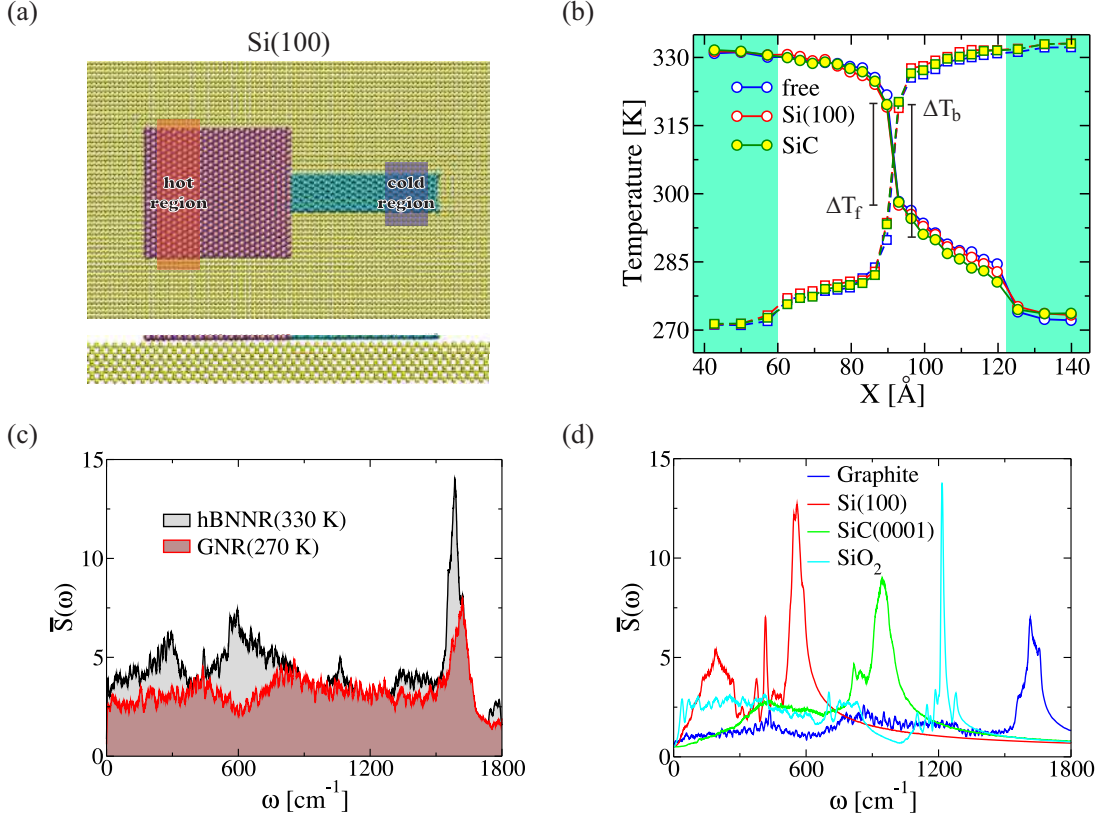


Figure 2.10: (a) Scheme of the setup used to perform NEMD simulations of deposited heterojunctions. (b) Temperature profiles for forward (\circ) and backward (\square) direction of the heat flux for a hBN-G nanoribbon with $W_{LR} = 2.0$ deposited on Si(100) and SiC substrates. The profiles for the free-standing case are also shown. Vibrational density of states, computed by using Eq. (2.30), of (c) the heat baths in a hBN-G nanoribbon with $W_{LR} = 1.0$ for a heat flux in forward direction and (d) the studied substrates at 300 K.

Fig. 2.10(a) shows the transport setup for all MD calculations. Here, the heat baths are only located in the nanoribbons and the temperature bias is fixed to $\Delta T = 60$ K. The following results have been obtained by equilibrating the substrates at $T_{subst} = 300$ K which is the mean temperature in the nanoribbons. In Fig. 2.10(b), one can see that the temperature profile for forward and backward directions of free-standing hBN-G nanoribbons for $W_{LR} = 2.0$ is slightly affected by the substrate. The main changes are at the central region and at the heat bath-device interface. Moreover, the temperature drop at the interface for the heat flux in backward direction, $\bar{\Delta T}_b$, is larger than the corresponding for forward direction, $\bar{\Delta T}_f$. Actually, independently of the substrate, $\bar{\Delta T}_f$ and $\bar{\Delta T}_b$ decreases and increases after increasing W_{LR} , respectively, i.e., heat flows preferentially in forward direction (direction of decreasing width). This happens for both heterojunctions and it is correlated with the previous discussion of heat flux in free-standing graphene/hBN nanoribbons. Similar observations were reported for pristine-hydrogenated carbon nanotube junction by increasing the H coverage [215].

Next, the vibrational density of states $\bar{S}_\alpha(\omega)$ is calculated by performing the Fourier transform

of the normalized autocorrelation function of atomic velocities in each polarization direction ($\alpha = x, y, z$) [71, 75]. $\bar{S}(\omega)$ is different to the one computed by the real-space mode analysis ($S(\omega)$, see Eq. (2.29)), because here scattering of vibrational modes coming from the anharmonic terms included in the force fields is also considered, while $S(\omega)$ is computed within the harmonic approximation. Fig. 2.10(c) shows $\bar{S}(\omega)$ for the left (hBN) and right (G) heat baths in the forward direction of the heat flux for a free-standing hBN-G nanoribbon. Clearly, $\bar{S}(\omega)$ values for G ribbons at 270 K are lesser than those one for hBN ribbons at 330 K in almost all the frequency range, but the overlap between both $\bar{S}(\omega)$ is very large, which is favorable for heat transport. Also, each substrate presents their main peaks of $\bar{S}(\omega)$ at different frequencies, as it can be seen in Fig. 2.10(d). Graphite covers the same frequencies as the heterojunctions, whereas the power spectrum at 300 K for Si(100), SiC(0001), and SiO₂ substrates goes up to $\sim 800 \text{ cm}^{-1}$, $\sim 1100 \text{ cm}^{-1}$, and $\sim 1350 \text{ cm}^{-1}$, respectively. In Fig. 2.11, one can see that the substrates strongly alter vibrational modes at low frequencies, almost fully suppressing them until a certain material-dependent critical frequency value $\omega = \omega_C$. This effect is mainly due to the coupling of the long-wavelength flexural modes with the substrate. The SiC(0001) substrate has the largest ω_C because it presents the strongest Van der Waals interaction with the heterojunction, which is measured by the ϵ parameter in the Lennard-Jones potential (see Table 2.1). Graphite and SiO₂ substrates suppress less vibrational modes because of their smaller coupling parameter (see insets of Fig. 2.11). It was also found that the mode suppression only affects the out-of-plane power spectrum (\bar{S}_z) rather than in-plane one (\bar{S}_{xy}). Indeed, \bar{S}_z at low frequencies is reduced and its magnitude varies with the substrate (see insets in Fig. 2.11). This phenomenon has also been theoretically reported in graphene and MoS₂ monolayers deposited on SiO₂ substrates [208].

As a consequence of these changes in $\bar{S}(\omega)$, it is expected that the overlap Λ between the power spectrum of heat baths could change. Then, the overlap of $\bar{S}(\omega)$ for the forward direction of the heat flux is analyzed. To compute Λ , the same expression as described in Ref. [75] has been used. Here, it was found that independently of the planar stacking order of materials, the power spectrum overlap increases by effect of the substrate, i.e., the heat flux is enhanced. Notice that Λ for the heat flux flowing from hBN \rightarrow G is larger than that one for the flux from G \rightarrow hBN for symmetric free-standing and deposited nanoribbons, which is in agreement with the previous heat flux values shown in Fig. 2.8(b). The maximum increment in hBN-G nanoribbons with $W_{LR} = 1.0$ occurs when it is deposited on a Si(100) substrate and amounts to 5.7% of the corresponding value for the free-standing case ($\Lambda_f^{hBN-G}(free) = 1.516$). Despite showing the strongest suppression of out-of-plane modes at low frequencies, the overlap slightly increases for deposition on SiC(0001) substrate (3.8%). For a G-hBN nanoribbon deposited on Si(100), the overlap is also maximal and equal to $\Lambda_f^{G-hBN}(Si(100)) = 1.584$, which corresponds to an increment of 6.4% of $\Lambda_f^{G-hBN}(free)$. The SiO₂ substrate improves the power spectrum overlap for both nanoribbons: $\Lambda_f^{hBN-G}(SiO_2) = 1.589$ and $\Lambda_f^{G-hBN}(SiO_2) = 1.570$. Moreover, the

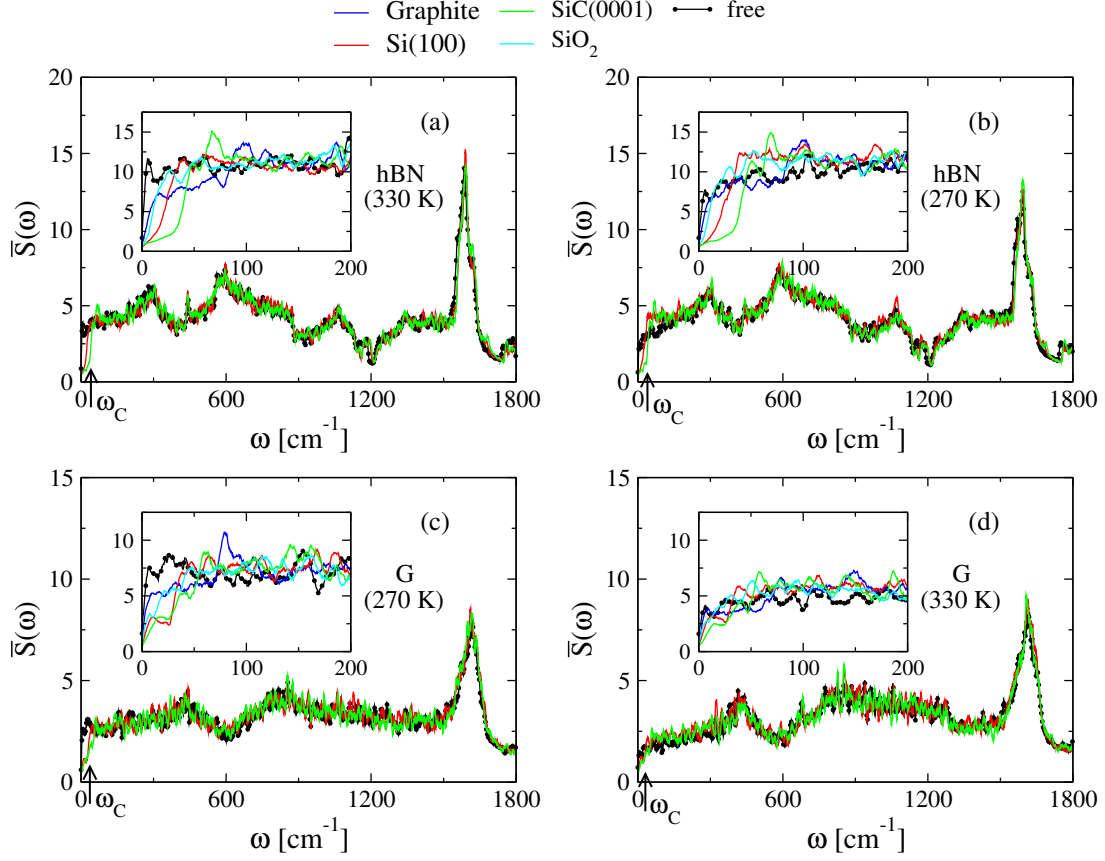


Figure 2.11: Total vibrational density of states of the heat baths in symmetric (a,c) hBN-G and (b,d) G-hBN nanoribbon heterojunctions ($W_{LR} = 1.0$) deposited on a given substrate ($T_{subst} = 300$ K). The results are for the forward direction of the heat flux. Inset: the out-of-plane mode contribution, \bar{S}_z . For comparison, the results for the free-standing case are also shown (solid lines with circles). ω_C represents the lift in frequency after substrate deposition.

overlap of $\bar{S}_{xy}(\omega)$ does not change at all after depositing the nanoribbons on substrates ($< 4\%$ of $\Lambda_f(free)_{xy}$, hBN-C=1.714 and C-hBN=1.701). On the contrary, for $\bar{S}_z(\omega)$, the overlap increases up to $\sim 11\%$ of $\Lambda_f(free)_z$ for hBN-G (1.889) and G-hBN (1.685) nanoribbons, becoming larger than the corresponding values to in-plane contributions. Accordingly, out-of-plane modes will have an important contribution for the thermal transport properties in these nanomaterials, as it has been previously reported for other 2D nanostructures [122, 134, 203, 208]. A similar phenomenon happens for the heat flux in the backward direction and varying asymmetry degrees. It is worth mentioning that the magnitude of the variations in spectral overlap can be controlled by the temperature bias ΔT between the heat baths. Hence, the increment of power spectrum overlap in the heterojunctions will enhance their heat flux and alter the performance of the material as a thermal rectifier.

In order to better capture the influence of the substrate on heat transport, the interface thermal conductance (ITR, or Kapitza resistance) is computed [75, 77], which is defined as

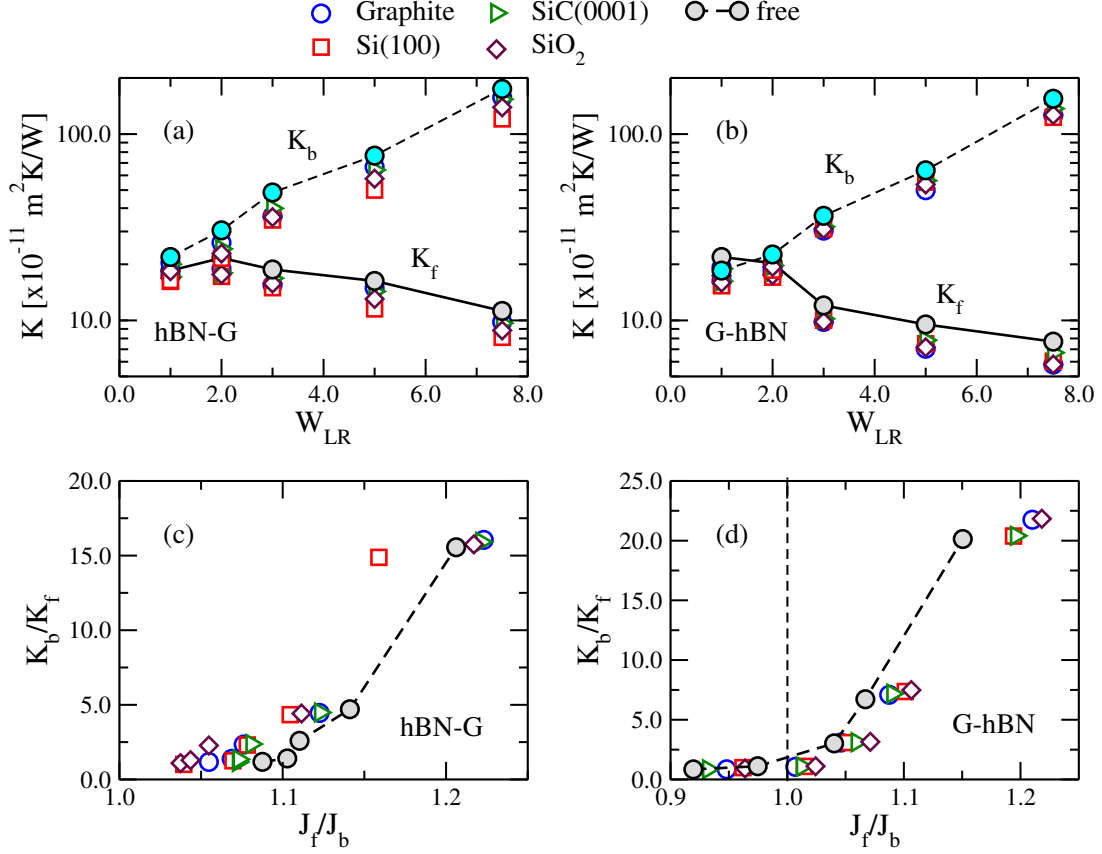


Figure 2.12: Interface thermal resistance of deposited (a) hBN-G and (b) G-hBN nanoribbon heterojunctions as a function of W_{LR} for the hat flux at forward (K_f) and backward (K_b) direction. Ratios of ITR K_b/K_f vs ratios of heat flux J_f/J_b for deposited (c) hBN-G and (d) G-hBN nanoribbon heterojunctions. The results for the free-standing case are also shown (filled circles).

$$K_{f,b} = \frac{A \bar{\Delta} T_{f,b}}{J_{f,b}}, \text{ with } \bar{\Delta} T \text{ as the temperature drop at the material interface and } J \text{ the heat flux.}$$

$A = W_A h$ is the transversal area of the nanoribbon, $W_A = (W_L + W_R)/2.0$ (effective width) and $h = 0.33 \text{ nm}$ (height of the ribbon). For hBN-G nanoribbons, ITR for backward direction of the heat flux is always greater than the forward direction (see Fig. 2.12(a)). Whereas, this only happens for G-hBN nanoribbons with $W_{LR} \geq 2.0$ (see Fig. 2.12(b)). The large difference between K_f and K_b for $W_{LR} \geq 3.0$ is mainly caused by the large ΠT_b produced by the strong structural asymmetry of nanoribbons. For example, for a hBN-G nanoribbon with $W_{LR} = 5.0$ deposited on Si(100) substrate: $\bar{\Delta} T_f \sim 8 \text{ K}$ and $\bar{\Delta} T_b \sim 32 \text{ K}$. Similar effect has been found for all the studied substrates. The interface thermal resistance, independently of the flux direction, is reduced after deposition, i.e., the thermal conductivity is enhanced in presence of a substrate, which confirms the preceding analysis. Interestingly, our results are in contrast to those found in supported graphene, where the substrate produces a negative effect in its thermal conductivity [45, 176, 204]. For hBN-G heterojunctions deposited on Si(100) substrate, $K_{f,b}$ shows the strongest reduction after increasing the asymmetry degree. On the other hand, Graphite and SiO₂ substrates lead to the largest increase of the thermal conduction in asymmetric G-hBN nanoribbons. Notice that

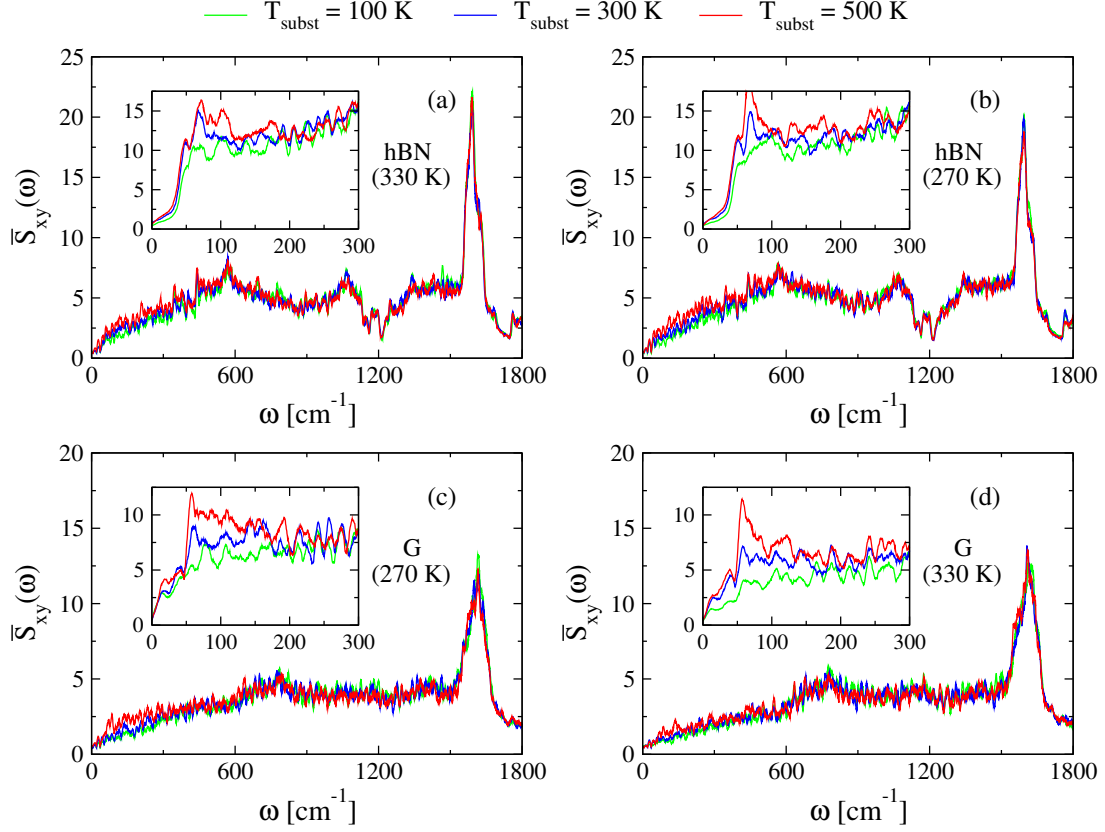


Figure 2.13: Substrate temperature dependence of the in-plane mode contribution $\bar{S}_{xy}(\omega)$ to the total vibrational density of states of the heat baths in symmetric hBN-G nanoribbon deposited on SiC(0001) substrate. The results are for the (a,c) forward and (b,d) backward direction of the heat flux. Inset: out-of-plane mode contributions, $\bar{S}_z(\omega)$.

ITR for G-hBN heterojunction also displays the same crossing point found in the analysis of the $J(W_{LR})$ -curve for forward and backward directions (see Fig. 2.8(b)).

Consequently, the variation of the ratios K_b/K_f and J_f/J_b at each W_{LR} value has been plotted for both heterojunctions deposited on all the substrates (see Figs. 2.12(c, d)). The behavior of J_f/J_b for free-standing and deposited nanoribbons is very similar. It was found that the thermal rectification (related to J_f/J_b , see Eq. (2.36)) for deposited hBN-G nanoribbons with $W_{LR} \leq 5.0$ is smaller than the corresponding values for free-standing ribbons. Whereas, at $W_{LR} = 7.5$, all the substrates, with the exception of Si(100), improve the thermal rectification of the heterojunction, which can reach values up to $\sim 24\%$, comparable to other asymmetric structures [37, 194], and heterojunctions [77]. The scenario is quite different for deposited G-hBN nanoribbons. Their $\eta(W_{LR})$ -curve also presents a minimum at $W_{LR} = 2.0$ as in the free-standing case, but its value has been increased for ribbons with $W_{LR} \geq 3.0$ up to $\sim 20\%$. Also, the rectification effect in G-hBN nanoribbons with $W_{LR} = 2.0$ can be strongly suppressed by depositing it on a graphite substrate, $\eta \sim 0.7\%$. These trends are verified by computing the interface thermal rectification defined using K_b/K_f instead of J_f/J_b , as it has been done in other related works [77]. Clearly, K_b/K_f only increases because of the considerable magnitude

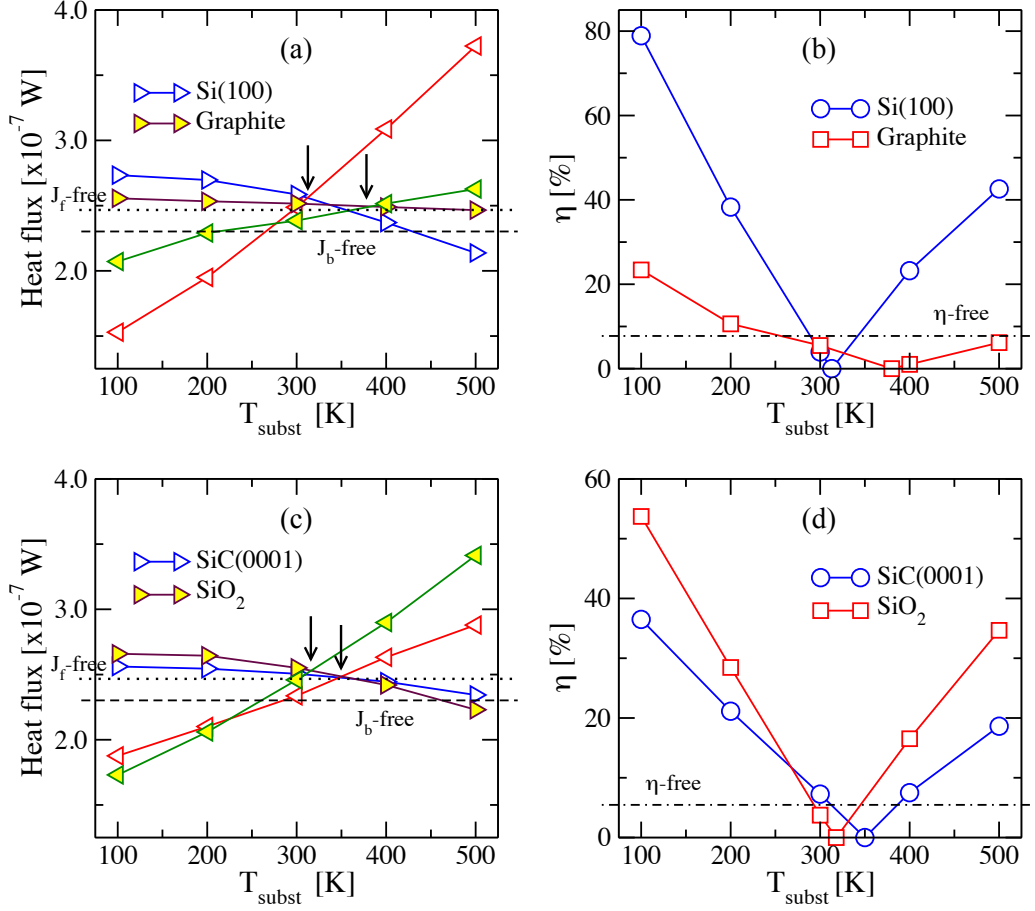


Figure 2.14: Variation of the heat flux in the forward (\triangleright) and backward (\triangleleft) directions for symmetric hBN-G nanoribbons deposited on (a) graphite and Si(100) substrates and (b) SiC(0001) and SiO₂ substrates as a function of the substrate temperature, T_{subst} . The arrows indicate the situation $J_f = J_b$ for each substrate. (b,d) Substrate temperature dependence of thermal rectification for hBN-G nanoribbons.

of K_b . Notice that a non-linear behavior for K_b/K_f vs J_f/J_b was obtained for asymmetric nanoribbons, which is different to the linear behavior expected by varying the temperature bias between the heat baths [75, 216].

Finally, the influence of the substrate temperature T_{subst} on the thermal transport properties of the heterojunctions is studied (see Fig. 2.14). For the sake of simplicity, this issue is only addressed in the case of a structurally symmetric hBN-G nanoribbon ($W_{LR} = 1.0$). It was found that, independently of the type of substrate, the heat flux for forward direction slightly decreases by increasing T_{subst} , while by reversing the temperature bias a considerable increment of the heat flux is obtained. Fig. 2.14(a) shows the results for graphite and Si(100) substrates which correspond to the weakest and strongest influence on the heat flux as a function of T_{subst} , respectively. The variation of T_{subst} yields an intersection between J_f - and J_b -curves at $T_{subst} \sim 380$ K for graphite and $T_{subst} \sim 313$ K for Si(100), which produces a full suppression of the rectification effect, i.e., $\eta = 0$. This occurs due to the fact that $\bar{S}(\omega)$ at low frequencies increases by heating up the substrate (see Fig. 2.13). Hence, the power spectrum overlap of the heat baths

is modified and, consequently, the heat flux. It has also been found that the high density peaks at low frequencies in the power spectrum of Si(100) (see Fig. 2.10(c)) make nanoribbons (deposited on this substrate) to have the largest increment of $\bar{S}(\omega)$, followed by SiO₂ and SiC(0001). In Fig. 2.14(b), one can see that the thermal rectification can reach values up to $\sim 79\%$ when the Si(100) substrate is equilibrated at 100 K, whose magnitude is of the same order as values reported for more complex structures such as graphene Y-junctions [78] and graphene/CNT heterostructures [124, 217]. On the contrary, nanoribbons deposited on graphite substrates display the lowest thermal rectification for almost the entire temperature range [100,500] K. Around $T_{subst} = 300$ K, which is the mean temperature of the nanoribbon (NEMD run), the influence of the type of substrate varies. Results for SiC(0001) and SiO₂ substrates are between those extreme cases, see Fig. 2.14(c,d). In brief, the thermal transport properties of the heterojunctions can be sensitively controlled by tuning the substrate temperature without the need of modifying the geometry of the heterojunctions.

2.3 SUMMARY

In the present chapter, thermal rectification effects have been studied in novel nanodevices made of two-dimensional materials such as MoS₂ monolayer, graphene, and hexagonal boron-nitride. To do this, NEMD simulations were carried out as implemented in LAMMPS software. Here, two main issues have been addressed: i) the influence of structural asymmetry and ii) the influence of substrate deposition on the thermal transport properties of these nanodevices.

Firstly, it was found that the performance as a thermal rectifier of both MoS₂ nanoribbons and coplanar graphene/hBN nanoribbons can be enhanced by increasing structural symmetry. Thus, they can achieve rather high thermal rectification values of roughly 30 % (for MoS₂) and 20 % (for graphene/hBN), values which are comparable with those found in more complex engineered nanostructures [37, 78]. One of the reasons to have this effect is the difference in the localization degree (at the edges) of vibrational modes for the forward and backward direction of the heat flux. This effect is however reduced after increasing the size of the nanostructures. Moreover, unlike MoS₂ nanoribbons, thermal rectification effects in coplanar graphene/hBN nanoribbons can be suppressed by effect of the structural asymmetry. For both two-dimensional thermal rectifiers, T-shaped nanoribbons display the largest thermal rectification comparing to other geometrical shapes.

In the second place, the calculations after substrate deposition showed that thermal conduction in coplanar graphene/hBN nanoribbons is improved by the effect of the interaction between the nanoribbons and the surface, which is described by Van der Waals forces. Moreover, it was found that substrates strongly affect vibrational modes at low frequencies (mostly out-of-plane modes), almost fully suppressing them until a certain material-dependent critical frequency value ω_C . Hence, the heat flux will be altered and, then, the thermal rectification. On the other hand, besides having a dependence on the type of substrate, thermal rectification effects can be tuned

by the substrate temperature. In fact, thermal rectification values up to $\sim 80\%$ and $\sim 40\%$ can be obtained when Si(100) substrate is heated up at 100 K and 500 K, respectively.

3 QUANTUM PHONON TRANSPORT

In this chapter, quantum phonon transport in nanomaterials will be treated by combining the nonequilibrium Green's functions (NEGF) formalism with the density functional tight-binding (DFTB) method. Unlike nonequilibrium molecular dynamics whose implementation was already efficiently working in LAMMPS software, here, NEGF-DFTB approach had to be numerically implemented. This implementation was inserted as a tool in the DFTB+ software (in-house version). The idea of combining NEGF formalism with DFTB method mainly raised because of the necessity of an atomistic method to deal with thermal transport, from a quantum point of view, in nanoscale systems up to ~ 2000 atoms, which goes beyond the current capabilities of density functional theory. Moreover, comparing to NEMD simulations, in which anharmonic interactions are included, in the present work, NEGF-DFTB method will deal only with harmonic interactions.

The NEGF-DFTB method relies on two main pillars: i) the first-principle computation of the relevant dynamical matrix encoding information on the vibrational spectrum of the system, and ii) Green's function technique to deal with the quantum thermal transport problem. Thus, the influence of several intrinsic and external factors (e.g., structural anisotropy [218], topological defects [219], molecular functionalization [220], uniaxial strain [221], doping) on the ballistic phonon transport of nanoscale systems can be addressed. The most important concepts of NEGF formalism and DFTB method will be introduced in the following sections.

3.1 THEORETICAL BACKGROUND

3.1.1 Ballistic phonon transport

The formulation of the phonon transport problem is dependent on the length scale of the material under study. For instance, in bulk materials, the heat carriers can be visualized as

behaving like little beads with Brownian-like trajectories, i.e., suffering frequent and random changes of directions. These movements are produced by continuous collisions between the carrier due to their high density (diffuse regime). However, when this density decreases, the distance traveled by a heat particle between two collisions can exceed the characteristic length scale of the material. The particle will then enter into more collisions with the walls of the system than with its counterparts inside it. Hence, this regime is no longer Brownian, but ballistic, because the particle will basically move in a straight line at constant speed between consecutive reflections from the system boundaries. The word 'particle' is used to cover the more detailed reality of a localized wave packet. This wave packet or phonon is made up of several waves in different resonant or normal modes, which contain the energy of the system [222].

One of the most effective approaches to study ballistic phonon transport in nanoscale systems is Green's functions formalism [35, 223]. The most general description for this method is based on nonequilibrium Green's functions. The NEGF method has its root in quantum field theory [224], and has been developed to study the many-particle quantum system under equilibrium and nonequilibrium conditions. In the early 1960s, various formulations have been derived by Martin and Schwinger [225], Kadanoff and Baym [226], and Keldysh [227]. Keldysh developed a diagram approach by using the Feynman diagrams; Kadanoff and Baym created an equation of motion approach. Both approaches are suitable for studying a dynamic system in nonequilibrium. Thus, one can obtain formal expressions of the current and other quantities such as electron density by using the Keldysh formalism of NEGF, which has also been generalized to cases of correlated initial states [228]. The NEGF method is an elegant and powerful method to calculate steady state properties of a finite system connected to leads, hence, it has been already successfully adapted to study electron transport properties [229, 230]. However, the application of NEGF method to thermal transport is relatively new. In recent years, the NEGF approach has been used on thermal transport not only in ballistic regime [180, 231, 232] but also including nonlinear interaction, and thus phonon-phonon scattering [233–236]. For more information regarding the application of NEGF method see Refs. [35, 223]. In the present work, NEGF formalism will be applied to study ballistic phonon transport in nanostructures¹.

The main difference between the NEGF formalism and ordinary equilibrium theory is that all time-dependent functions are defined for time-arguments on a contour, called the Keldysh contour. A general contour widely used with NEGF is the Schwinger/Keldysh-contour (see Fig. 3.1). However, a simplification occurs when $t_0 \rightarrow -\infty$ is set (Keldysh contour). If the interactions are coupled adiabatically, the contribution from the $[t_0, t_0 + \beta]$ piece vanishes. The information lost by this procedure is related to initial correlations. In many physical situations, for example, in steady state transport, it appears plausible that the initial correlations have been washed out by the interactions when one reaches the steady state. On the contrary, if one study transient response, the role of initial correlations can be important (see Chapter 4). Here, it has been considered the $t_0 \rightarrow -\infty$ limit. Then, the Keldysh contour thus consists of two branches running

¹For the thermal transport including nonlinear interactions, the procedure is similar, except for the self-energy which must be treated self-consistently and using Feynman diagrams [35, 223].

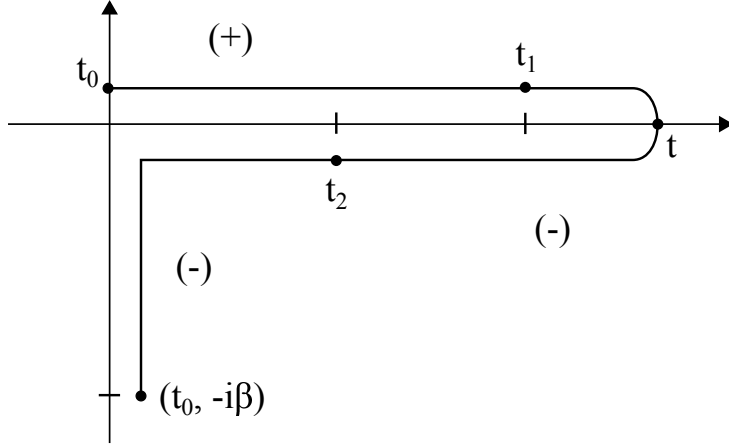


Figure 3.1: Schwinger/Keldysh-contour C in the imaginary time plane, $C = \{t \in \mathcal{C}, \Re t \in [t_0, \infty] \Im t \in [t_0, -\beta]\}$. For more clarity, the different contour branches are displayed slightly off the axes. Time-ordering: time t_2 is later on the contour than time t , and t is larger than t_1 .

from $-\infty$ to ∞ and from ∞ to $-\infty$. Therefore, based on the definition of the contour-ordered Green's function which read as

$$G(\tau, \tau') = -i \langle T_C A(\tau) B^T(\tau') \rangle \quad (3.1)$$

with T_C as the time-order operator, six real-time Green's functions can be defined as [237]:

- The lesser GF, $G^<(t, t') = -i \langle A(t') B^T(t) \rangle$.
- The greater GF, $G^>(t, t') = -i \langle A(t) B^T(t') \rangle$.
- The retarded GF, $G^r(t, t') = -i \theta(t - t') \langle [A(t), B^T(t')] \rangle$.
- The advanced GF, $G^a(t, t') = i \theta(t' - t) \langle [A(t), B^T(t')] \rangle$.
- The time-ordered GF, $G^t(t, t') = \theta(t - t') G^>(t, t') + \theta(t' - t) G^<(t, t')$.
- The anti-time-ordered GF, $G^{\bar{t}}(t, t') = \theta(t' - t) G^>(t, t') + \theta(t - t') G^<(t, t')$.

Where $A(t)$ and $B(t)$ are operators in the Heisenberg picture and $\theta(t)$ is the step function. The angular brackets denote trace with the canonical density matrix, i.e., $\langle \dots \rangle = \text{Tr}(\rho \dots)$, with $\rho = e^{-\beta H} / \text{Tr}(e^{-\beta H})$ and $\beta = 1/(k_B T)$. H represents the Hamiltonian of the system. The notation $\langle [A, B^T] \rangle$ represents a matrix and should be interpreted as $\langle AB^T \rangle - \langle BA^T \rangle^T$.

In equilibrium or non-equilibrium steady states, the Green's functions depend only on the difference in time, $t - t'$. The Fourier transform of $G^r(t - t') = G^r(t, t')$ is defined as $G^r[\omega] =$

$\int_{-\infty}^{+\infty} G^r(t)e^{i\omega t} dt$. The following linear relations hold in both frequency and time domains from the basic definitions [237]:

$$\begin{aligned} G^r - G^a &= G^> + G^<, \\ G^t + G^{\bar{t}} &= G^> + G^<, \\ G^t - G^{\bar{t}} &= G^r + G^a. \end{aligned} \tag{3.2}$$

Among the six Green's functions, only three of them are linearly independent. However, in systems with time translational invariance, the functions G^r and G^a are Hermitian conjugate of one other, i.e., $G^a[\omega] = (G^r[\omega])^\dagger$. Moreover, only two of them are independent in general nonequilibrium steady-state situations. One of the best choices is to consider G^r and $G^<$, but other combinations are possible. Extra relations in the frequency domain are also defined and, for bosons (phonons), they read as [171]:

$$\begin{aligned} G^<[\omega]^\dagger &= -G^<[\omega], \\ G^r[-\omega] &= G^r[\omega]^*, \\ G^<[-\omega] &= G^>[\omega]^T = -G^<[\omega]^* + G^r[\omega]^T - G^r[\omega]^*. \end{aligned} \tag{3.3}$$

Based on the last two equations, it is only needed to compute the positive frequency part of the functions. Eqs. (3.2) and (3.3) are generally valid for nonequilibrium steady states. Nevertheless, for systems in thermal equilibrium, since equilibrium systems satisfy the fluctuation-dissipation theorem [238], there is an additional equation relating G^r and $G^<$:

$$G^<[\omega] = f(\omega) (G^r[\omega] - G^a[\omega]), \tag{3.4}$$

where $f(\omega) = \left(e^{\frac{\hbar\omega}{k_B T}} - 1 \right)^{-1}$ is the Bose-Einstein distribution function at temperature T . k_B is the Boltzmann constant. In fact, the correlation function $G^<$ contains information of fluctuations, while $G^r - G^a$ describes dissipation of the system. The relation $G^>[\omega] = e^{\beta\omega} G^<[\omega]$ also applies for equilibrium systems. Thus, in equilibrium, there is only one independent Green's function.

In a typical phonon transport calculation, one connects a central region (also known as device region) to two or more thermal baths on the left (L) and right (R) (see Fig. 3.2). Similar setup was also used to performed NEMD simulations. However, by using NEGF formalism, the thermal baths are composed of semi-infinite ideal systems, in which phonon transport experiences no scattering. Therefore, it will be assumed that all the scattering processes only occur in the central part. Since we focus on thermal transport mediated by the vibrational system, the phonon Hamiltonian of the whole system will be given by

$$H = \sum_{\alpha=L,C,R} H_\alpha + (u^L)^T V^{LC} u^C + (u^C)^T V^{CR} u^R + V_n, \tag{3.5}$$

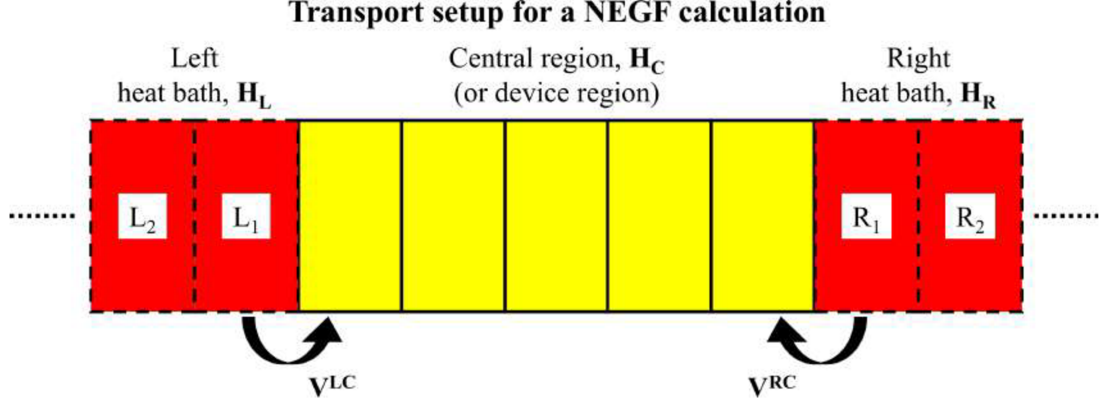


Figure 3.2: Schematic representation of the partition scheme for transport calculation using Green's function technique. The entire system is divided into three regions: central region and, left and right heat baths. Each of this region are characterized by their own Hamiltonian H_α with $\alpha = L, C, R$. The coupling matrices between heat baths and central region are V^{LC} and V^{RC} .

where $H_\alpha = \frac{1}{2}(\dot{u}^\alpha)^T \dot{u}^\alpha + \frac{1}{2}(u^\alpha)^T K^\alpha u^\alpha$ represents the Hamiltonian of the region α ; $\alpha = L, C, R$, for the left, center, and right regions, respectively. u^α is a column vector consisting of all the displacement variables in region α , and \dot{u}^α is the corresponding conjugate momentum. The following transformation of coordinates has been considered, $u_j = \sqrt{m_j} x_j$, where x_j is the relative displacement of j -th degree of freedom. K^α is the mass-reduced force constant matrix² and $V^{LC} = (V^{CL})^T$ is the coupling matrix between the left lead to the central region; similarly for V^{CR} . There is no interaction between the two leads. The last term V_n represents the nonlinear or the many-body interactions [237]. In this context, it denotes the anharmonic interactions in the central part³. It contains the high order (higher than 2) derivatives of energy respective to displacement at the equilibrium positions. However, in the present work, harmonic interactions will only be considered, i.e., the system will not have phonon-phonon interactions. Hence, $V_n = 0$ for ballistic transport.

As well known, the most important quantity to calculate in thermal transport is the heat flux J . The heat flux is defined as the energy transferred from the heat source to the junction in a unit time, which is equal to the energy transferred from the junction to the heat sink in a unit time, with the assumption that no energy is accumulated in the junction. According to this

²This matrix is the mass-weighted second derivative of energy with respect to displacement at the equilibrium positions

$$[K_{\gamma\beta}]_{ij} = K_{ij}^{\gamma\beta} = \frac{1}{\sqrt{m_i m_j}} \frac{\partial^2 E}{\partial u_i^\gamma \partial u_j^\beta}. \quad (3.6)$$

³Most theoretical treatments, if considering anharmonic interactions, will include V_n until the 4th term. This is because higher order terms usually have negligible effects on thermal transport and dealing with those terms is extremely troublesome. While it is important to include the 4th term that helps stabilizing the system. The inclusion of the 3rd anharmonic term only sometimes causes the system energetically unstable, i.e., absence of lower boundary for the energy [237].

definition, the heat flux out of the left lead is

$$J_L = -\langle \dot{H}_L(t) \rangle = i \langle [H_L(t), H] \rangle = i \langle [H_L(t), V^{LC}(t)] \rangle. \quad (3.7)$$

In the steady state, energy conservation means that $J_L + J_R = 0$. For simplicity, $\hbar = 1$ has been set in this section. Then, using the Heisenberg equation of motion, J_L can be written as

$$\begin{aligned} J_L &= \langle (\dot{u}^L)^T(t) V^{LC} u^C(t) \rangle \\ &= \sum_{j,k} \langle (\dot{u}_j^L)^T(t) V_{jk}^{LC} u_k^C(t) \rangle \\ &= \lim_{t' \rightarrow t} \sum_{j,k} V_{jk}^{LC} \langle (\dot{u}_j^L)^T(t') u_k^C(t) \rangle. \end{aligned} \quad (3.8)$$

Consequently, the heat flux depends on the expectation value of $(\dot{u}_j^L)^T(t') u_k^C(t)$, which can be expressed in terms of the lesser Green's function $G_{CL}^<(t, t') = -i \langle u^L(t') u^C(t)^T \rangle^T$. Since operators u and \dot{u} are related in Fourier space (frequency domain) as $\dot{u}[\omega] = -i\omega u[\omega]$, the derivative is eliminated and, as a result,

$$J_L = -\frac{1}{2\pi} \int_{-\infty}^{\infty} \text{Tr} (V^{LC} G_{CL}^<[\omega]) \omega d\omega. \quad (3.9)$$

Hence, the heat flux can be calculated by only knowing $G_{CL}^<[\omega]$, which mixes the degrees of freedom of the left lead and the central region. An efficient method to obtain the Green's functions of interacting systems is through their equation of motion (EOM) [223]. This topic will be expanded with more details in Chapter 4. In this section, equations of motion are used in a straightforward way in order to get the expressions for the retarded and lesser GF of the central region. Thus, by considering the system as a whole, the contour ordered Green's function $G(\tau, \tau') = -i \langle T_\tau u(\tau) u(\tau')^T \rangle$ satisfies the following equation

$$-\frac{\partial^2 G(\tau, \tau')}{\partial \tau^2} - KG(\tau, \tau') = I\delta(\tau, \tau') \quad (3.10)$$

Then, the equation per each region is obtained by partitioning the matrices G and K into submatrices $G^{\alpha, \alpha'}$ and $K^{\alpha, \alpha'}$, $\alpha, \alpha' = L, C, R$. Consequently, the free Green's function for the system decoupled g is easily achieved through the solution of

$$-\frac{\partial^2 g^\alpha(\tau, \tau')}{\partial \tau^2} - K^\alpha g^\alpha(\tau, \tau') = I\delta(\tau, \tau'). \quad (3.11)$$

Also, their corresponding free Green's functions in frequency domain can be written as

$$g_\alpha^r[\omega] = [(\omega + i\eta)^2 - K^\alpha]^{-1}, \quad (3.12)$$

where η is an infinitesimal positive quantity to single out the correct path around the poles when performing an inverse Fourier transform, such that $g^r = 0$ for $t < 0$. Other Green's functions can be obtained using the general relations among them (see Eqs. (3.2) and (3.3)).

Additionally, the contour-ordered non-equilibrium Green's function can be expressed as

$$G^{LC}(\tau, \tau') = \int d\tau'' g^L(\tau, \tau'') V^{LC} G^{CC}(\tau'', \tau), \quad (3.13)$$

$$G^{CC}(\tau, \tau') = g^C(\tau, \tau') + \int d\tau_1 \int d\tau_2 g^C(\tau, \tau_1) \Sigma(\tau_1, \tau_2) G^{CC}(\tau_2, \tau'), \quad (3.14)$$

with $\Sigma(\tau_1, \tau_2)$ as the total self-energy which includes all the effects with the baths and is given by

$$\Sigma(\tau_1, \tau_2) = \Sigma_L(\tau_1, \tau_2) + \Sigma_R(\tau_1, \tau_2) = V^{CL} g^L(\tau_1, \tau_2) V^{LC} + V^{CR} g^R(\tau_1, \tau_2) V^{RC} \quad (3.15)$$

Here, g^L and g^R are the GF of the isolated semi-infinite thermal lead (also known as the surface GF). The surface Green's function can be calculated by a simple iteration method [239] or by a more efficient decimation approach [240] (the latter method is used in the present work). Then, the above Dyson equation (see Eq. (3.14)) has the following solutions in the frequency domain:

$$G_{CC}^r[\omega] = ((\omega + i\eta)^2 I - K^C - \Sigma^r[\omega])^{-1}, \quad (3.16)$$

$$G_{CC}^<[\omega] = G_C^r[\omega] \Sigma^<[\omega] G_C^a[\omega]. \quad (3.17)$$

In short, up to now, all Green's functions have been successfully defined and it has been explained the procedure to compute them. Hence, physical quantities are calculated by using these relations. Let's start with the phonon density of states (PDOS). Assuming that the system has $3N$ degrees of freedom. The n^{th} phonon mode has a frequency of ω_n and an eigenvector of $|u^n\rangle$ whose i^{th} component is u_i^n . Thus, this system will follow the dynamical equation given by

$$K|u^n\rangle = \omega^2|u^n\rangle. \quad (3.18)$$

Therefore, its phonon DOS will be defined as

$$\eta(\omega) = \sum_n \delta(\omega - \omega_n) = \sum_i \eta_i(\omega) \quad (3.19)$$

Where $\eta_i(\omega)$ is the phonon local DOS (LDOS) of the i^{th} degree of freedom, which is expressed as

$$\eta_i(\omega) = \sum_n |u_i^n|^2 \delta(\omega - \omega_n). \quad (3.20)$$

Moreover, the phonon DOS satisfies the relation $\int_0^\infty d\omega \eta(\omega) = 3N$. However, it can be also given in terms of Green's functions:

$$\begin{aligned} G^r[\omega] &= \frac{1}{(\omega + i\delta)^2 - K} \\ &= \sum_n \frac{|u^n\rangle\langle u^n|}{2(\omega + i\delta)} \left(\frac{1}{\omega + i\delta - \omega_n} + \frac{1}{\omega + i\delta + \omega_n} \right). \end{aligned} \quad (3.21)$$

This can be further simplified,

$$-\frac{2\omega}{\pi} (\text{Im}G^r[\omega])_{ii} = \sum_n |u_i^n|^2 [\delta(\omega - \omega_n) + \delta(\omega + \omega_n)] . \quad (3.22)$$

When $\omega > 0$, $\delta(\omega + \omega_n) = 0$. As consequence, the phonon LDOS can be written as

$$\eta_i(\omega) = -\frac{2\omega}{\pi} (\text{Im}G^r[\omega])_{ii} , \quad (3.23)$$

and, then, the total phonon DOS is $\eta(\omega) = \sum_{i=1}^N \eta_i(\omega)$. Although Eq. (3.23) is obtained from a special case of no phonon-phonon interactions, the same formula work also for cases including phonon-phonon interactions providing that the quasi-particle picture does not break down. The phonon DOS and LDOS gives the distribution of phonons in frequency space and in real space [171]. This kind of information is very helpful to analyze quantum thermal transport processes, as it will be shown below.

To continue the description of relevant physical quantities, two useful functions in the NEGF formalism are defined. The first one is the spectral function,

$$A[\omega] = i(G^r[\omega] - G^a[\omega]) = i(G^>[\omega] - G^<[\omega]) . \quad (3.24)$$

and, the second one, is the Γ function, which describes the scattering rate of phonons, given by

$$\Gamma[\omega] = i(\Sigma^r[\omega] - \Sigma^a[\omega]) = \Gamma_L[\omega] + \Gamma_R[\omega] \quad (3.25)$$

Moreover, there is an important relation between them: $A[\omega] = G^r[\omega]\Gamma[\omega]G^a[\omega]$. Then, by applying the Langreth theorem⁴ to Eq. 3.13, the lesser GF $G_{CL}^<$ turns into

$$G_{CL}^<[\omega] = G_{CC}^r[\omega]V^{CL}g_L^<[\omega] + G_{CC}^<[\omega]V^{CL}g_L^a[\omega]. \quad (3.29)$$

Consequently, the heat flux coming from the left lead (see Eq. (3.9)) can be written as

$$J_L = -\frac{1}{2\pi} \int_{-\infty}^{+\infty} d\omega \omega \text{Tr} (G^r[\omega]\Sigma_L^<[\omega] + G^<[\omega]\Sigma_L^a[\omega]) , \quad (3.30)$$

⁴In dealing with the contour-ordered Green's functions, we often encounter convolution of the form

$$B(\tau, \tau') = \int d\tau_1 \int d\tau_2 \cdots A_1(\tau, \tau_1) A_2(\tau_1, \tau_2) \cdots A_n(\tau_{n-1}, \tau'). \quad (3.26)$$

This form of expression can be easily translated into the retarded and lesser Green's functions in frequency domain by the Langreth theorem as [223]

$$B^{r,a}[\omega] = A_1^{r,a}[\omega] A_2^{r,a}[\omega] \cdots A_n^{r,a}[\omega], \quad n = 2, 3, \cdots \quad (3.27)$$

$$\begin{aligned} B^{<, >}[\omega] &= A_1^>[\omega] \cdots A_{n-1}^>[\omega] A_n^{<, >}[\omega] + \\ &A_1^>[\omega] \cdots A_{n-2}^>[\omega] A_{n-1}^{<, >}[\omega] A_n^a[\omega] + \\ &\cdots + A_1^{<, >}[\omega] A_2^a[\omega] \cdots A_{n-1}^a[\omega] A_n^a[\omega]. \end{aligned} \quad (3.28)$$

For notational simplicity, the subscripts C on the Green's functions denoting the central region have been dropped. After symmetrization with respect to left and right lead, the heat flux expression becomes explicitly real and is given by [33]

$$J = \frac{1}{4} (J_L + J_L^* - J_R - J_R^*) \quad (3.31)$$

In the end, one can get the Landauer-like formula

$$J = \int_0^\infty \frac{d\omega}{2\pi} \hbar\omega \tau_{ph}[\omega] (f_L - f_R), \quad (3.32)$$

where $f_{L,R}$ are the Bose-Einstein distributions for the left and right leads. $\tau_{ph}[\omega]$ is known as the phonon transmission function and it is expressed as

$$\tau_{ph}[\omega] = \text{Tr} (G^r[\omega] \Gamma_L[\omega] G^a[\omega] \Gamma_R[\omega]). \quad (3.33)$$

Here, the retarded GF of the central region connected to two leads is defined as:

$$G^r[\omega] = [(\omega + i\eta)^2 I - K^C - \Sigma_L^r[\omega] - \Sigma_R^r[\omega]]^{-1} \quad (3.34)$$

Notice that the two thermal leads always give the same total current for steady states. However, their spectral functions can be different if asymmetry exists. A thorough investigation of thermal rectification requires such information. Hence, the thermal conductance is defined as

$$\kappa_{ph} = \lim_{\Delta T \rightarrow 0} \frac{J}{\Delta T}, \quad (3.35)$$

where ΔT is the difference of the temperatures between the two thermal leads, assuming that the temperature of the left and right leads are $T_L = T + \Delta T/2$ and $T_R = T - \Delta T/2$, respectively. Thus, by performing a linear expansion of the Bose-Einstein distribution in ΔT , the thermal conductance can be written as

$$\kappa_{ph} = \frac{1}{2\pi} \int_0^\infty d\omega \omega T[\omega] \frac{\partial f(\omega)}{\partial T}. \quad (3.36)$$

To gain insight of the phonon transport properties, the in-plane and out-of-plane mode contribution to the total transmission function and thermal conductance can be computed, i.e., $(\tau, \kappa)_{total} = (\tau, \kappa)_{in} + (\tau, \kappa)_{out}$.

3.1.2 Density functional tight-binding method

Based on the equations of NEGF formalism, the main inputs to describe the quantum phonon transport properties of nanomaterials are the mass-reduced force constant matrix per each region K^α ($\alpha = L, C, R$) and the coupling matrices of the left and right lead to the central region,

V^{LC} and V^{CR} , respectively. The accuracy of the results will depend on the reliability of these quantities to catch all the features of the whole system. Thus, the choice of the method to compute the total system energy is very important and, hence, K and V matrices. In fact, despite the tremendous success of the Schrodinger equation to describe the quantum mechanical effects in several nanoscale systems, full electronic description of even simple structures (say small molecules) is very complex and it is usually unfeasible to solve them analytically. In practice, one has to resort to approximate methods that can be solved in a numerical fashion [241]. In this sense, DFT has become very popular during the last decades and is now widely accepted as a tool for quantitative studies on molecular and atomic levels [168]. DFT implementations are widely used in chemistry and physics mainly due to its beneficial accuracy-to-computational-time ratio. The overwhelming progress in accuracy due to gradient corrected and hybrid functionals such as PBE and B3LYP curing deficiencies of older models contributed fundamentally to its popularity. On the other hand, the accuracy of DFT comes, however, at the trade-off to be computationally very demanding. DFT calculations using well-established implementations are currently limited to a maximum of a few hundred of atoms, depending on the chemical species. One solution to this problem is the use of parametrized force fields to simulate interatomic interactions. This is mainly used for molecular dynamics simulations, as discussed in Chapter 2. Computing force constant matrices with parametrized force fields allow us to deal systems with thousands of atoms. However, such classical force fields can be very accurate for the system they have been parametrized for, but may suffer from a limited transferability and, also, they do not provide any information about the electronic structure.

Consequently, another option is to turn to semiempirical methods, which lie conceptually between empirical force fields and first principle methods and allow for the treatment of thousands of atoms [242]. Semiempirical electronic structure methods can be understood as direct approximations to more accurate methods (usually DFT or Hartree-Fock), but additionally include empirical parameters that can be tuned to reproduce reference data. One particular example of a semiempirical method is the density functional tight-binding method [243–245]. Here, the parameters are consistently obtained from DFT calculations of few molecules per pair of atoms types. Whereas, the electronic structure equations are solved by means of the tight-binding approach (see Appendix B). During the last decades, a great amount of studies have been carried out by using DFTB method, e.g., proton-transfer barrier in biological systems [246], transport properties of two-dimensional materials [153, 247, 248], stability and mechanical properties [249], vibrational properties [250], absorption spectra of molecules [251], charge transfer excitation energy of a donor-acceptor pair [252], spectroscopic properties for large systems [253]. More information can be found in recent review papers [254–256].

To have a better understanding of DFTB method, a brief description of DFT is given. Density functional theory is based on the two theorems by Hohenberg and Kohn [257]. The first theorem states that the ground state properties of many-electron system are uniquely determined by an electron density $\rho(\mathbf{r})$; \mathbf{r} is a vector specifying the spatial coordinates. The second theorem

proves that the energy $E[\rho(\mathbf{r})]$ of this system takes its minimum value when the density is the ground-state density $\rho^{GS}(\mathbf{r})$. Moreover, the energy of a molecular system is calculated within the Born-Oppenheimer approximation [258], i.e., due to the great difference in mass the motion of the nuclei and the motion of the electrons are examined separately. It is common to describe the nuclei as classical particles and the electrons moving within their Coulomb potential. Hence, the DFT total energy can be written as a functional of the electron density,

$$E^{DFT}[\rho(\mathbf{r})] = T[\rho(\mathbf{r})] + E^{ne}[\rho(\mathbf{r})] + E^J[\rho(\mathbf{r})] + \tilde{E}^{xc}[\rho(\mathbf{r})] + E^{nn}, \quad (3.37)$$

where T is the kinetic energy of the electrons, E^{ne} the energy of the nucleus-electron interaction, E^J is the classical portion of the electron-electron energy, \tilde{E}^{xc} the exchange-correlation energy (the non-classical portion of the electron-electron interaction), and E^{nn} the nucleus-nucleus interaction. The energy contributions are defined as

$$\begin{aligned} E^{ne}[\rho(\mathbf{r})] &= \int V^{ne}(\mathbf{r})\rho(\mathbf{r})d\mathbf{r} = - \sum_a \int \frac{Z_a\rho(\mathbf{r})}{|\mathbf{R}_a - \mathbf{r}|}d\mathbf{r} \\ E^J[\rho(\mathbf{r})] &= \frac{1}{2} \int \int V^J[\rho(\mathbf{r}')] \rho(\mathbf{r})d\mathbf{r}'d\mathbf{r} = \frac{1}{2} \int \int \frac{\rho(\mathbf{r})\rho(\mathbf{r}')}{|\mathbf{r} - \mathbf{r}'|}d\mathbf{r}'d\mathbf{r} \\ E^{nn} &= \frac{1}{2} \sum_{a,b \neq a} \frac{Z_a Z_b}{|\mathbf{R}_a - \mathbf{R}_b|} \end{aligned} \quad (3.38)$$

where a and b are indices for atoms, Z is the nuclear charge, \mathbf{R} the coordinates of the nucleus, and V the potential of the respective energy. The exact functionals $T[\rho(\mathbf{r})]$ and $\tilde{E}^{xc}[\rho(\mathbf{r})]$ are not known such that several approximation were developed [168]. DFT methods become more practical only after Kohn and Sham published their famous idea of approximating the kinetic energy by introducing so called Kohn-Sham orbitals $\psi(\mathbf{r})$ [259]. Then, the Schrodinger equation is separated for an imaginary non-interacting system of one-electron equations of the form

$$\left[-\frac{1}{2}\nabla^2 + V(\mathbf{r}) \right] \psi_i(\mathbf{r}) = \epsilon_i \psi_i(\mathbf{r}) \quad \forall i \quad (3.39)$$

with the requirement that

$$\rho(\mathbf{r}) = \sum_i n_i \psi_i^*(\mathbf{r})\psi_i(\mathbf{r}) \quad \text{and} \quad \int \rho(\mathbf{r})d\mathbf{r} = \sum_i n_i = N \quad (3.40)$$

where $-\nabla^2/2$ is the kinetic energy operator of the Schrodinger equation, $V(\mathbf{r})$ is the one-electron potential and n_i is the electron occupation number of an orbital and N the total number of electrons in the system [259]. Eq. (3.39) can be interpreted as one electron moving within an effective potential $V(\mathbf{r})$. That electron, however, is not interacting directly with other electrons. Therefore, the kinetic energy of such a non-interacting system $T^s[\rho(\mathbf{r})]$ can be written as

$$T^s[\rho(\mathbf{r})] = \sum_i n_i \int \psi_i^* \left(-\frac{1}{2}\nabla^2 \right) \psi_i(\mathbf{r})d\mathbf{r} = \sum_i n_i \epsilon_i - \int V(\mathbf{r})\rho(\mathbf{r})d\mathbf{r}. \quad (3.41)$$

In order to have a formally exact theory the difference between T^s and the kinetic energy of a system of interacting electrons T is added to the exchange-correlation energy

$$E^{xc} = \tilde{E}^{xc} + (T - T^s). \quad (3.42)$$

Accordingly, the total energy is then given by

$$E^{DFT}[\rho(\mathbf{r})] = T^s[\rho(\mathbf{r})] + E^{ne}[\rho(\mathbf{r})] + E^J[\rho(\mathbf{r})] + E^{xc}[\rho(\mathbf{r})] + E^{nn}, \quad (3.43)$$

After that, to yield the ground state energy, the energy $E^{DFT}[\rho]$ is minimized in a variational search in the space of ρ with the constraint that [168]

$$\int \delta\rho(\mathbf{r})d\mathbf{r} = 0 \quad (3.44)$$

As a result,

$$\left. \frac{\delta E^{DFT}[\rho]}{\delta\rho} \right|_{\rho=\rho(\mathbf{r})} = -V(\mathbf{r}) + [V^{ne}(\mathbf{r}) + V^J[\rho] + V^{xc}[\rho]]_{\rho=\rho(\mathbf{r})} + const = 0, \quad (3.45)$$

where

$$V^{xc}[\rho(\mathbf{r})] = \frac{\delta E^{xc}[\rho(\mathbf{r})]}{\delta\rho(\mathbf{r})}. \quad (3.46)$$

Solving for $V(\mathbf{r})$ yields

$$V(\mathbf{r}) = [V^{ne}(\mathbf{r}) + V^J[\rho]V^{xc}[\rho]]_{\rho=\rho(\mathbf{r})} + const. \quad (3.47)$$

This forms a self-consistent condition which can be solved iteratively using a proper starting condition: The potential $V(\mathbf{r})$ can be evaluated by Eq. (3.47) for a given $\rho(\mathbf{r})$ which in turn is generated by solving Eqs. (3.39) and (3.40) where $V(\mathbf{r})$ enters. With the idea of Kohn and Sham, the dominant part of the kinetic energy, i.e., the kinetic energy of a non-interacting system T^s can be calculated indirectly but exactly. Inserting Eqs. (3.38) and (3.41) into Eq. (3.43), the DFT total energy can be written as

$$E^{DFT}[\rho(\mathbf{r})] = \sum_i n_i \epsilon_i - \frac{1}{2} \int V^J[\rho(\mathbf{r})]\rho(\mathbf{r})d\mathbf{r} - \int V^{xc}[\rho(\mathbf{r})]\rho(\mathbf{r})d\mathbf{r} + E^{xc}[\rho(\mathbf{r})] + E^{nn}. \quad (3.48)$$

This is the basic equation to start the derivation of the DFTB total energy. Here, a Taylor series expansion of the KS density functional total energy (see Eq. (3.48)) around a properly chosen reference density, $\rho(\mathbf{r}) = \sum_i n_i \psi_i^*(\mathbf{r})\psi_i(\mathbf{r}) = \rho^0(\mathbf{r}) + \Delta\rho(\mathbf{r})$, is performed. Then, the DFT total energy can be expressed as

$$\begin{aligned} E[\rho^0 + \Delta\rho] &= \sum_i n_i \int \int \psi_i^* \left(-\frac{\nabla^2}{2} + V^{ne} + \int' \frac{\rho^{0'}}{|\mathbf{r} - \mathbf{r}'|} + V^{xc}[\rho^0] \right) \psi_i \\ &\quad - \frac{1}{2} \int \int' \frac{\rho^{0'}\rho^0}{|\mathbf{r} - \mathbf{r}'|} + \frac{1}{2} \int \int' \frac{\Delta\rho'\Delta\rho}{|\mathbf{r} - \mathbf{r}'|} \\ &\quad - \int V^{xc}[\rho^0]\rho^0 - \int V^{xc}[\rho^0]\Delta\rho + E^{xc}[\rho^0 + \Delta\rho] + E^{nn}. \end{aligned} \quad (3.49)$$

With this rearrangement it is not clear anymore how to obtain the exact Kohn-Sham wave functions ψ_i . However, within the DFTB formalism one can obtain approximate ψ_i by a linear combination of atomic orbitals (LCAO) centered on the nuclei (see Appendix B). In a last step the exchange-correlation energy is expanded in a Taylor series expansion as

$$\begin{aligned}
E^{xc}[\rho^0 + \Delta\rho] &= E^{xc}[\rho^0] + \int \left[\frac{\delta E^{xc}[\rho]}{\delta \rho} \right]_{\rho^0} \Delta\rho + \frac{1}{2} \int \int' \left[\frac{\delta^2 E^{xc}[\rho]}{\delta \rho \delta \rho'} \right]_{\rho^0, \rho^{0'}} \Delta\rho \Delta\rho' \\
&+ \frac{1}{6} \int \int' \int'' \left[\frac{\delta^3 E^{xc}[\rho]}{\delta \rho \delta \rho' \delta \rho''} \right]_{\rho^0, \rho^{0'}, \rho^{0''}} \Delta\rho \Delta\rho' \Delta\rho'' + \dots
\end{aligned} \tag{3.50}$$

Applying Eq. (3.46), the DFT total energy can be written as

$$\begin{aligned}
E[\rho^0 + \Delta\rho] &= \sum_i n_i \int \int \psi_i^* \left(-\frac{\nabla^2}{2} + V^{ne} + \int' \frac{\rho^{0'}}{|\mathbf{r} - \mathbf{r}'|} + V^{xc}[\rho^0] \right) \psi_i \\
&- \frac{1}{2} \int \int' \frac{\rho^{0'} \rho^0}{|\mathbf{r} - \mathbf{r}'|} - \int V^{xc}[\rho^0] \rho^0 + E^{xc}[\rho^0] + E^{nn} \\
&+ \frac{1}{2} \int \int' \left(\frac{1}{|\mathbf{r} - \mathbf{r}'|} + \frac{\delta^2 E^{xc}[\rho]}{\delta \rho \delta \rho'} \Big|_{\rho^0, \rho^{0'}} \right) \Delta\rho \Delta\rho' \\
&+ \frac{1}{6} \int \int' \int'' \left[\frac{\delta^3 E^{xc}[\rho]}{\delta \rho \delta \rho' \delta \rho''} \right]_{\rho^0, \rho^{0'}, \rho^{0''}} \Delta\rho \Delta\rho' \Delta\rho'' + \dots
\end{aligned} \tag{3.51}$$

Approximations of different levels of sophistication can be introduced by truncation of the Taylor series [260]. For instance, standard tight-binding methods like non-self-consistent DFTB (non-scc DFTB) does not consider the second and higher order terms in the density fluctuations $\Delta\rho$ [244], i.e., the generalized eigenvalue problem has to be diagonalized only once. Therefore, the total energy will be only composed for the terms in the first two lines of Eq. (3.51) and can be expressed as

$$E^{nsc-DFTB} = \sum_i n_i \epsilon_i + E^{rep}, \tag{3.52}$$

with E^{rep} as the repulsive energy between the atoms. The procedure to calculate ϵ_i within the DFTB scheme is given with more details in Appendix B. However, to improve on the requirement of local charge neutrality, Elstner et al. [245] suggested to go beyond the first-order expansion of the Kohn-Sham energy functional and to include the second order corrections to the exchange-correlation energy. This new method is called self-consistent charge DFTB (scc-DFTB) and it is very important for systems with sizable charge reorganization. Hence, the scc-DFTB total energy finally reads [261]

$$E^{scc-DFTB} = \sum_i n_i \epsilon_i - \frac{1}{2} \sum_{ab} \Delta q_b (q_a \gamma_{ba} + q_a^0 \gamma_{ab}) + E^{rep}. \tag{3.53}$$

Here, $\Delta q_x = q_x - q_x^0$ is the Mulliken charge (charge fluctuation) for the atom $x = a$ or b , where q_x^0 is the charge of the valence electrons of a neutral atom x and q_x is the charge of that atom

within the molecule. γ represents the interaction between the charge density fluctuations (see Appendix B).

The choice of the DFTB method depends on the system under study. For instance, nsc-DFTB method is more suitable for system where the charge transfer between the atoms is small, typically homonuclear systems or systems with atoms of similar electronegativity, e.g., hydrocarbons [262]. Ionic systems like NaCl with large charge transfer between the atoms have been also treated successfully with this method [263]. On the other hand, for systems with delicate charge balance, a self-consistent charge treatment is usually required. This is often the case for biological and organic systems containing oxygen [260, 264]. Moreover, recently, it has been developed a new DFTB method which considers up to the third order term in the Taylor expansion of the exchange-correlation energy functional (see Eq. (3.51)). However, this issue is beyond the goal of this thesis, thus, for more details go to Refs. [256, 261]. Accordingly, based on the potential of DFTB method to deal with large systems (few thousand of atoms), force constant matrices (or Hessian matrices) of the studied nanosystems have been numerically obtained by applying finite difference method to compute the second derivatives of the total energy respect to the atomic displacements, as implemented in DFTB+ software.

3.2 THERMAL TRANSPORT IN LOW-DIMENSIONAL SYSTEMS

After implementing NEGF-DFTB method to study quantum phonon transport as a tool in the DFTB+ code (in-house version), several studies were carried out in novel low-dimensional systems.⁵ From electron transport studies, it is well-known that transport properties of nanoscale systems can be tailored by varying various control parameters. This can include covalent or non-covalent chemistry [265, 266], atomic doping [237, 267], topological defects [268, 269], quantum confinement [119], and mechanical strain [154, 155], among others. However, this is still an open issue when dealing with thermal transport properties. Thus, in the present section, the influence of intrinsic and external factors on the quantum phonon transport of low-dimensional materials will be studied. This is done with the aim of understanding the possible features that could make a nanomaterial becoming a potential candidate for the design of phononic devices.

3.2.1 Structural anisotropy

Firstly, the effect of anisotropic atomic structure on the phonon transport of two-dimensional puckered materials is presented [218]. From this new family of 2D materials [85, 95, 97, 100], three representative members have been selected: phosphorene, arsenene, and SnS monolayer; which display the main features of this family. The unit cell of these materials is composed by four atoms, as it is depicted in Fig. 3.3. Each atom is pyramidally bonded to three neighboring

⁵See details of the PHONON tool in the Appendix B.

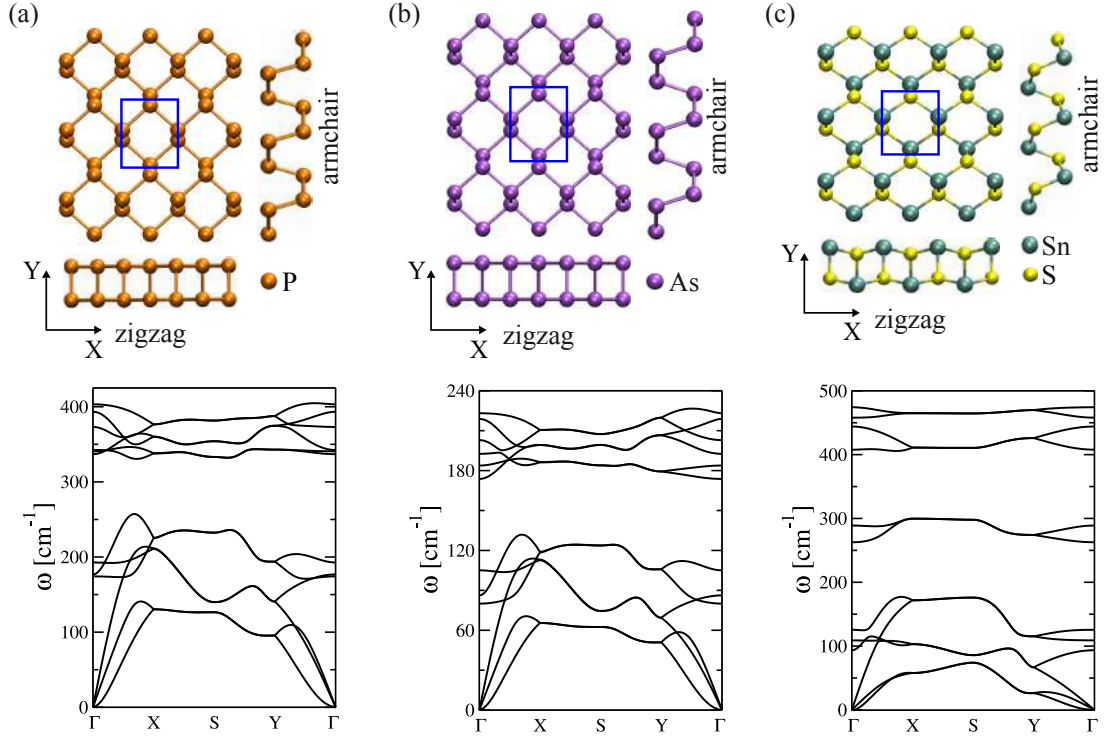


Figure 3.3: Phonon band structures for homo- and heteroatomic puckered materials. (a) phosphorene, (b) arsenene, and (c) tin sulphide (SnS) monolayer. It is also shown the atomistic view of the 2D nanostructures, highlighting the zigzag (ZZ) and armchair (AC) transport direction.

atoms of the same (phosphorene and arsenene, for homoatomic) or different (tin sulfide (SnS), for heteroatomic) species forming a puckered-like honeycomb lattice. As shown in Table 3.1, the lattice constants computed with the DFTB approach quantitatively agree (error $\leq 5\%$) with those obtained at the full DFT level by other authors for all three materials.

Before computing transport properties, a phonon dispersion analysis of these materials is performed. Phonon dispersion is constructed by diagonalizing the dynamical matrix at arbitrary k -point vectors. Dynamical matrices are obtained by Fourier transforming the real-space force constants. This methodology is also included in the tool implemented in the DFTB+ software. Based on this analysis, all studied systems are mechanically stable and do not show imaginary modes (see the three lower panels of Fig. 3.3). As it can be seen in the phonon spectrums, the acoustic branches display the typical dispersion of 2D materials: the longitudinal (LA) and transversal (TA) acoustic branches have linear dispersion as the wave vector approaches the Γ point, while out-of-plane ZA branches exhibit quadratic dispersion due to the rapid decay of transversal forces. Moreover, the distribution and dispersion of the phonon branches for homoatomic puckered materials are almost identical, except for their maximum frequency value, which is a consequence of the mass difference between As (~ 75 uma) and P (~ 31 uma). Thus, the DFTB phonon band structures for P and As agree quite well with those computed with DFT [218]. Only for SnS the high frequency optical modes are shifted upwards.

Table 3.1: Calculated lattice constants of 2D puckered materials along zigzag (ZZ) and armchair (AC) directions. For comparison, the lattice constants from other published theoretical studies are given. In general, the difference between the DFTB lattice parameters agree quite well (error $\leq 5\%$) with those at the full DFT level.

Systems	Transport direction		Other works (ZZ, AC) [\AA]
	ZZ [\AA]	AC [\AA]	
Phosphorene	3.49	4.34	(3.28, 4.43)[89] (3.32, 4.58)[270]
Arsenene	3.81	4.75	(3.68, 4.77)[96] (3.69, 4.77)[98]
SnS monolayer	3.93	4.51	(4.03, 4.26)[100] (4.01, 4.35)[271]

Furthermore, comparing the group velocities (i.e., the slope of the acoustic branches) for ZZ ($\Gamma \rightarrow X$) and AC ($\Gamma \rightarrow Y$) transport directions, it is expected that these materials will display strong thermal anisotropy. In fact, the group velocities for the longitudinal acoustic (LA) branch in phosphorene are 8.35 Km/s and 4.74 Km/s along the Γ -X (ZZ) and Γ -Y (AC) directions, respectively, which are very close to previous DFT results [90, 94, 270]. The values for arsenene, ZZ-5.01 Km/s and AC-2.71 Km/s, are also in agreement with those reported by Zeraati et al. [98]. While, SnS monolayer gives group velocities of ZZ-6.48 Km/s and AC-2.14 Km/s. Notice that, up to now, thermal anisotropy has only been reported for phosphorene [89, 94] and arsenene [96, 98], but not for SnS monolayers. Hence, it is expected that SnS monolayers will display the largest anisotropy in the thermal conductance due to the predominance of acoustic modes in the thermal transport.

Consequently, phonon transport calculations are carried out using periodic boundary conditions in the perpendicular direction to transport and with the same number of unit cells for all materials. Also, to avoid additional effects arising from different material compositions of the phonon reservoirs and of the scattering region, the reservoirs consist of the same material as the scattering region. With this, intrinsic transport features of the different systems will be revealed. The transmission function is calculated for each material along the zigzag (ZZ) and armchair (AC) direction at equilibrium conditions. As it is expected from the phonon dispersion analysis presented before, phosphorene and arsenene display relatively similar phonon transmission functions (Figs. 3.4(a) and 3.4(c)). The only differences are the phonon bandgaps ($\sim 67\text{cm}^{-1}$ and $\sim 45\text{cm}^{-1}$, respectively) and the maximum frequency value in the phonon dispersion. Likewise, it was found that transmission function values in the ZZ direction are larger than in the AC direction for almost the whole frequency range. Specially, SnS monolayer turns out to display the strongest thermal anisotropy.

This effect is also reflected on their thermal conductance, see Figs. 3.4(b,d,f). In fact, κ_{ph} for ZZ direction is larger than the corresponding for AC direction for the three puckered materials. The anisotropic effect rapidly enhances at low temperatures. Moreover, it is found that κ_{ph} remains constant above 200 K, independently of the transport direction, since the whole phonon spectrum has been already covered by the frequency integration in Eq. (3.36). To measure the anisotropic influence on the thermal conductance, $P_{AZ} = \kappa_{ph-ZZ}/\kappa_{ph-AC}$ is defined. Thus,

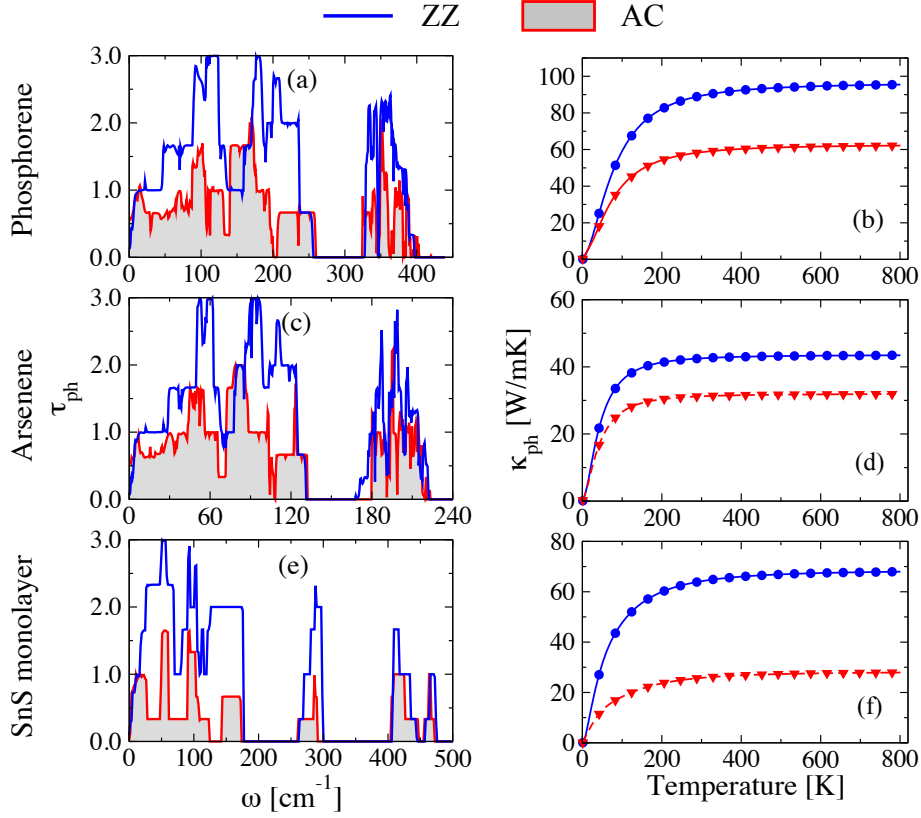


Figure 3.4: Phonon transmission function and thermal conductance along the ZZ (blue line) and AC (red line with shadow) transport direction: (a,b) phosphorene, (c,d) arsenene, and (e,f) SnS monolayer, respectively.

As it is expected due to the strong anisotropy in its phonon transmission function and group velocities, SnS monolayer displays the highest thermal anisotropy at 300 K, $P_{AZ} \sim 2.5$, followed by phosphorene ($P_{AZ} \sim 1.6$), which is slightly more thermal anisotropic than arsenene ($P_{AZ} \sim 1.35$). The P_{AZ} value for phosphorene is slightly different from that obtained by employing DFT calculations,[91, 270] while for arsenene there is more discrepancy from that reported by Zeraati et al. [98], which is mainly due to the methodology used. In the latter work they employed self-consistent calculations to solve the Boltzmann transport equation.

3.2.2 Nanoscale grain boundaries

Secondly, the influence of one-dimensional topological defects, also known as grain boundaries (GBs), is studied. Because of the relevance for the development of the next generation of nanoelectronic devices, gran boundaries in polycrystalline graphene has attracted considerable attention during the last decades and it is the chosen material to analyze in this section. These GBs have been experimentally shown to be formed by non-hexagonal rings (pentagons, heptagons, nonagons etc) among misoriented, but crystallographically perfect, graphene lattices. Hence, effects of integrity (structure and dynamics) and the geometry (linear and curved [272]),

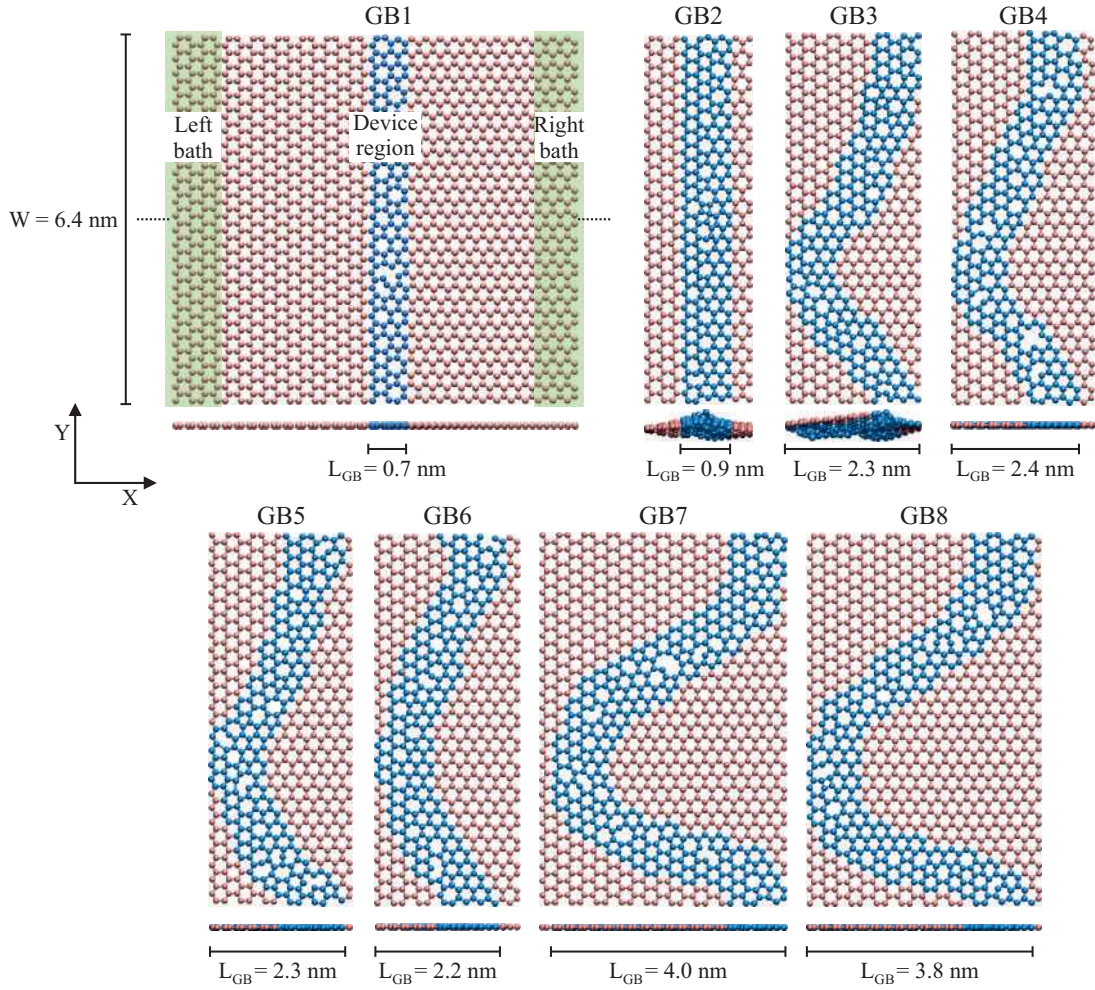


Figure 3.5: Top and side views of the structures of linear (GB1 and GB2) and curved (GB3-GB8) graphene grain boundaries. L_{GB} is the length of the grain boundary. The same width (W) has been used for all the systems. For similar L_{GB} , different defects were considered. For GB1, it is also shown a schematic representation of the partition scheme for transport calculation using the Green's function technique. The carbon atoms in blue color are the atoms mainly forming the grain boundary while the carbon atoms in pink color are the atoms far from the boundary region.

see Fig. 3.5) of the GB on phonon transport properties will be addressed [219]. Here, the crystallographic orientations of the grains are armchair and zigzag at opposite sides. The two initial seeds are located approximately 10 to 25 Å apart, depending on the target GB geometry. For the generation of a linear boundary (GB1 and GB2), the initial seeds have clean linear edges and, then, carbon atoms are added one by one to cover the available sites. The positions of the added atoms are determined by taking into account the positions of the nearest neighbor atoms. Addition of carbon atoms to random sites continues until the grains converge together. Afterwards, excess atoms, which give rise to coordination numbers larger than three are removed. To generate curved boundaries, edges that have asperities towards each other were initially used. The asperities are thin ribbons of graphene. GBs with larger curvatures (GB7 and GB8) were obtained by increasing the length of the asperity. The growth process is carried out so as to

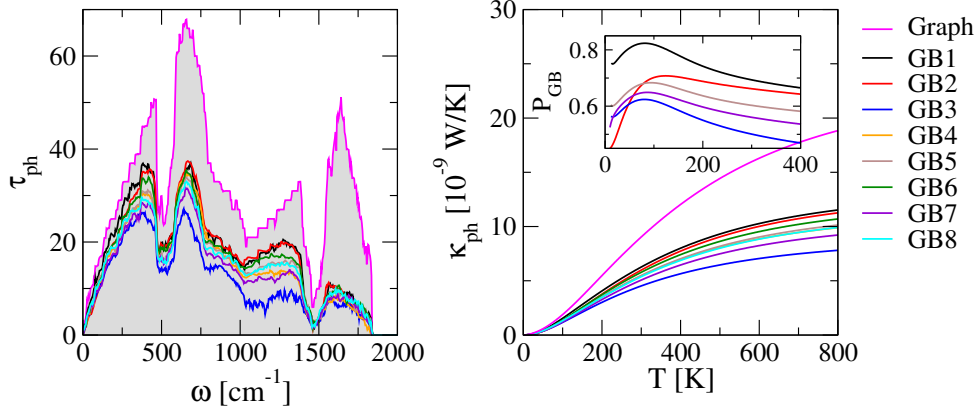


Figure 3.6: Phonon transmission (left panel) and thermal conductance (right panel) for graphene grain boundaries. The results are compared with the corresponding functions for pristine graphene (labeled as graph). Inset of right panel shows the temperature dependence of $P_{GB} = \kappa_{GB}/\kappa_{graph}$.

fulfill periodic boundary conditions in the transverse direction (y-direction) and spurious effects due to edges are avoided.

Structural optimizations of GBs were performed by using DFTB method until the absolute value of the inter-atomic forces is below 10^{-5} atomic units, with a k-point mesh of $1 \times 12 \times 1$. A width of ~ 6.4 nm for all the grain boundaries and periodic boundary conditions along y-direction have been considered. The GB length and curvature are measured by L_{GB} . Structures with similar L_{GB} present different type of non-hexagonal rings. In this study, the device region includes the periodic linear/curved defect (grain boundary), whereas the left and right leads are taken as a unit cell of the 2D graphene grains in each side, i.e., armchair and zigzag, respectively (see Fig. 3.5 for the case of GB1). These grains are considered semi-infinite along x-direction based on the Green's function formalism [33].

Fig. 3.6 shows the transmission spectra of different GB structures. For comparison, $\tau_{ph}[\omega]$ of pristine graphene is included (pink solid line). One can see that the transmission over the entire spectrum is lowered as expected due to local structural defects [220, 273]. Moreover, transport channels in linear GBs present higher transmission than those in curved GBs, mainly in the high frequency region which corresponds to in-plane mode contributions. GB3 displays the lowest transmission probability because of its curved structure and the out-of-plane distortions (see Fig. 3.6), which strongly reduces τ_{in} . In graphene, out-of-plane distortions locally couple in-plane and out-of-plane degrees of freedom, which are decoupled otherwise, and this coupling is the main scattering mechanism for phonons in deformed graphene structures [274]. Accordingly, linear GBs show higher values of thermal conductance. However, slight differences in κ for GB1 and GB2 are also found, being more pronounced for $T < 200$ K, see the inset in the right panel of Fig. 3.6. Here, $P_{GB} = \kappa_{GB}/\kappa_{graph}$ as a function of the temperature is showed, being κ_{GB} and κ_{graph} the thermal conductance for a given grain boundary and graphene pristine, respectively [275]. This behavior is related to the reduction of the transmission probability for low frequency

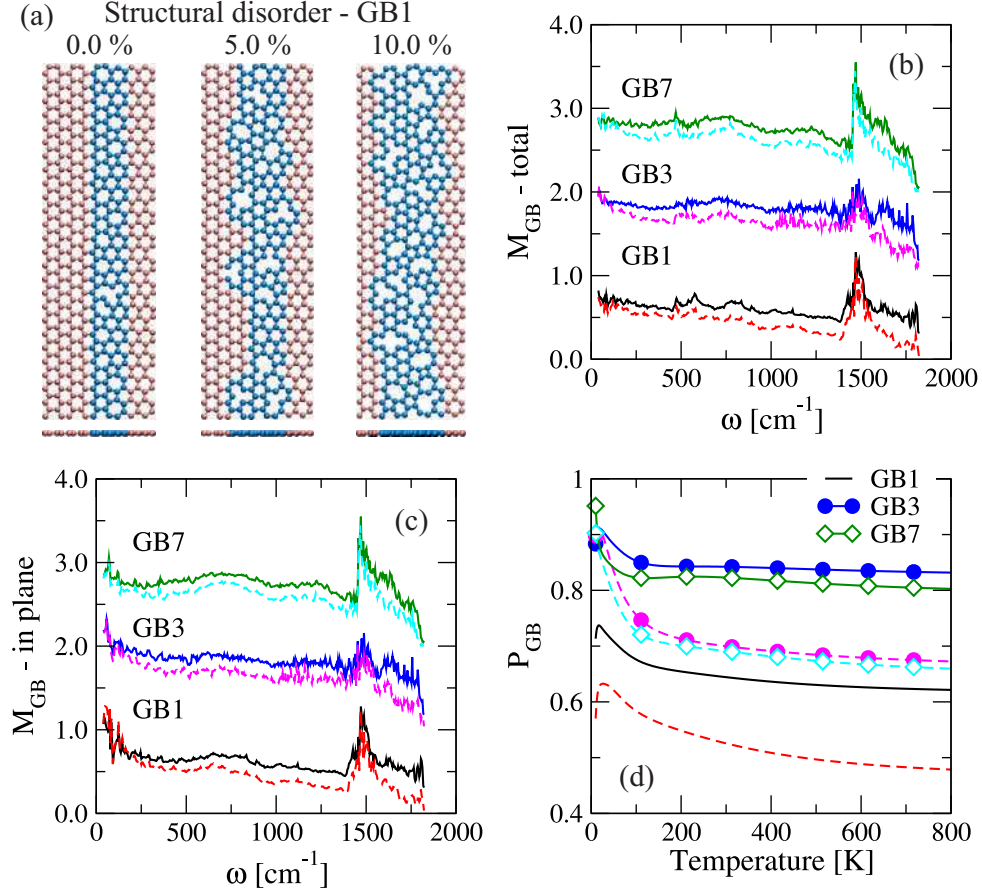


Figure 3.7: (a) Schematic representation of the mechanism for introducing atomic defects (structural disorder) into the boundaries. M_{GB} parameter as a function of mode frequency for (b) total and (c) in-plane phonon transmission of graphene GBs at different level of atomic defects. (d) Temperature dependence of P_{GB} parameter. For all the graphs, solid and dashed lines correspond to 5% and 10% of atomic defects, respectively. The high peak around $\omega \sim 1500 \text{ cm}^{-1}$ on panels (b) and (c) is coming from the small values on the phonon transmission.

modes induced by the out-of-plane distortions at the boundary. This effect also takes place for GB4, GB5, and GB6, which have similar L_{GB} but different thermal conductances. GB6 presents the highest thermal conductance among the three due to the smaller number of structural defects at the boundary. In addition, it was found that from all the curved GBs, independently of L_{GB} , GB3 displays the lowest κ as result of the large suppression of transmission over the whole frequency range, while GB7 shows the second lowest thermal conductance indicating that the influence of curvature (L_{GB}) is weaker than the out-of-plane structural distortions [219].

Then, the influence of structural modifications of the boundaries, which are produced by randomly removing atoms (see Fig. 3.7(a) for GB1), is studied. All the results are averaged over three random configurations. To gain a better quantitative understanding, the parameter $M_{GB} = \tau_{GB}(\%)/\tau_{GB}(0)$ is defined, where $\tau_{GB}(\%)$ is the phonon transmission for a given percentage of atomic defects and $\tau_{GB}(0)$ is the initial transmission (i.e., without extra defects). The phonon transmission for both types of GBs is reduced after increasing the percentage of atomic defects

[276], the effect being more dramatic for linear GBs because of its higher degree of structural order compared to curved GBs (see Fig. 3.7(b)). This is a consequence of τ_{in} and τ_{out} being influenced by the atomic defects in different frequency ranges. As it is shown in Fig. 3.7(c), τ_{out} is the most affected for $\omega < 200 \text{ cm}^{-1}$ while the reduction of transmission probability for in-plane modes becomes larger at high frequencies $\omega > 1000 \text{ cm}^{-1}$. In addition, $P_{GB} = \kappa_{GB}(\%) / \kappa_{GB}(0)$ is computed to study the variation of the thermal conductance with the level of atomic defects for the GBs (see Fig. 3.7(d)). Here, GB1 shows the highest reduction of thermal conductance at any percentage of atomic defects. Whereas curved GBs, independent of the L_{GB} value, display similar reduction of their corresponding thermal conductance, which is slightly reduced at very low temperatures $T < 50 \text{ K}$. The later effect is a consequence of the small variation on τ_{ph} for $\omega < 200 \text{ cm}^{-1}$ where out-of-plane modes are dominant. It has been observed that κ for linear and curved GBs with 5% of atomic defects is reduced by the same factor at $T > 200 \text{ K}$, i.e., P_{GB} remains constant. On the contrary, P_{GB} decreases as a function of the temperature at 10%. Moreover, regardless the type of GBs, all of them have very similar thermal conductance at 10% of atomic defects. These findings are in agreement with the recent thermal conductance measurements in single graphene grains done by Yasaei et al. [277].

As a final point, the influence of dynamical disorder produced by coupling a Nose-Hoover thermostat only to the device region of the transport setup is addressed, (see Fig. 3.8(a)). Thus, the magnitude of atomic displacements around the equilibrium position (i.e., at 0 K) will be controlled by the device temperature T_D . Quantum molecular dynamics simulations QM/MD are carried out using the DFTB+ code [278], i.e., the corresponding total energy is calculated every MD step and the Verlet algorithm is used for the time integration of the Newton's equation of atomic motion with a time step of 0.5 fs. The results are then averaged over 10 configurations which were taking every 0.05 ps after the device region reached the temperature equilibration ($\sim 2.5 \text{ ps}$). Phonon transmission functions obtained at different temperatures, $\tau_{GB}(T)$, has been compared with the corresponding to zero temperature, $\tau_{GB}(0)$, by redefining $M_{GB} = \tau_{GB}(T) / \tau_{GB}(0)$.

In Fig. 3.8(b), one can see that the phonon transmission of GBs is reduced when the device temperature T_D increases. Similar effect was found in the case of the structural disorder. However, transmission probability for $\omega < 1300 \text{ cm}^{-1}$ remains almost the same at $T_D = 100 \text{ K}$, i.e., $M_{GB} \sim 1.0$. At $T_D = 500 \text{ K}$, the transmission function has been completely altered for low ($\omega < 500 \text{ cm}^{-1}$) and high ($\omega > 1000 \text{ cm}^{-1}$) frequency modes. Unlike the effect observed with atomic defects, in which both τ_{in} and τ_{out} are strongly affected, the reduction at low frequencies modes is mainly due to the strong suppression of transfer channels belonging to out-of-plane modes since τ_{in} is slightly reduced after increasing T_D (see Fig. A.3(c)). It was also found that the influence of the dynamics is stronger for linear GBs. The parameter $P_{GB} = \kappa_{GB}(T) / \kappa_{GB}(0)$ is now used to find out the impact of dynamical disorder on κ_{ph} of graphene GBs (see Fig. A.3(d)). Hence, the thermal conductance for linear GBs is the most altered, specially, at low temperature of the leads ($T < 100 \text{ K}$), $P_{GB} \rightarrow 0$, showing an opposite behavior to this with

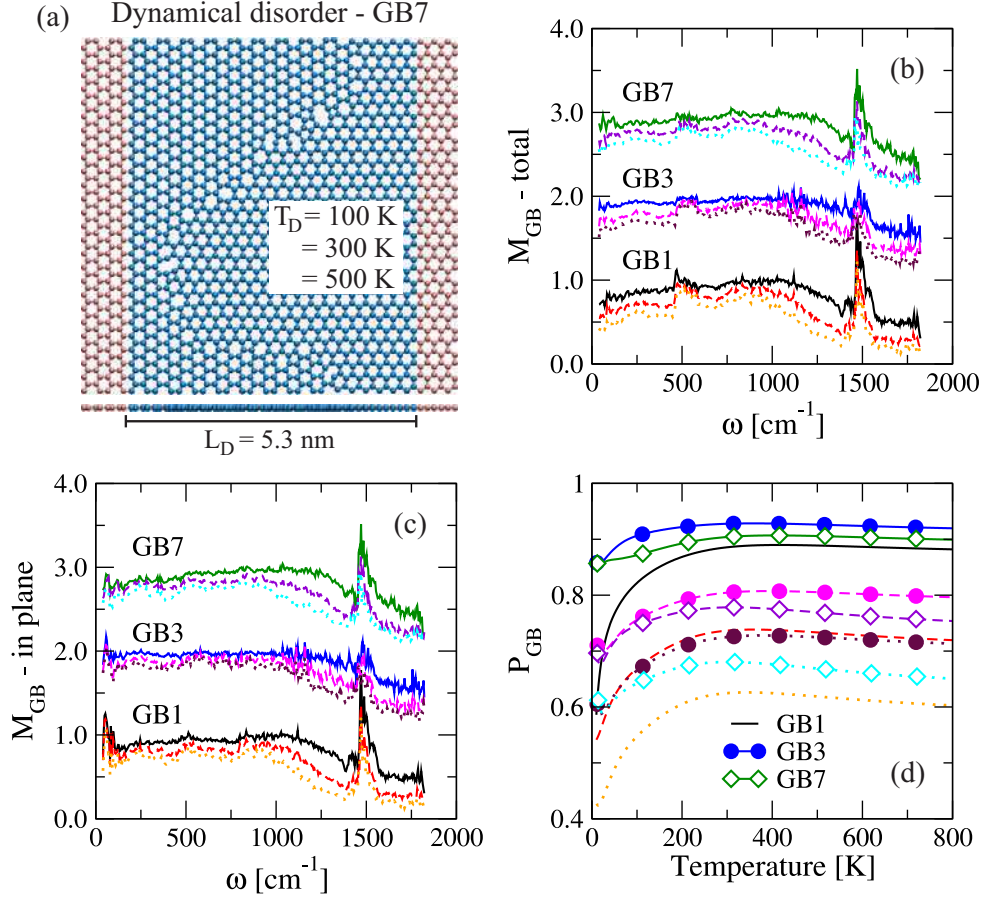


Figure 3.8: (a) Schematic representation of the transport setup to perform the MD simulations. The thermostat is only imposed to the atoms on the device region (blue balls). M_{GB} parameter as a function of mode frequency for (b) total and (c) in-plane phonon transmission of graphene GBs at different T_D . (d) Temperature dependence of P_{GB} parameter. For all the graphs, solid, dashed, and dotted lines correspond to $T_D = 100$ K, 300 K, and 500 K, respectively. The high peak around $\omega \sim 1500 \text{ cm}^{-1}$ on panels (b) and (c) is coming from the small values on the phonon transmission.

atomic defects where κ_{ph} is slightly reduced at this temperature range ($P_{GB} \sim 1$). This effect is related to small modifications on the in-plane phonon transmission. GBs with large curvature are more influenced by T_D . Besides, the reduction factor of κ_{ph} for all the GBs at a given T_D is the same when $T > 200$ K, i.e., P_{GB} is invariant. Notice that despite considering very high T_D , the thermal conductance is still larger to those obtained at 10% of structural disorder.

3.2.3 Molecular functionalization

Thermal transport properties can be also controlled by ad-atoms and molecular functionalization. Thus, one possible strategy to influence the properties of graphene GBs can be their functionalization with molecules or ad-atoms [265, 279], which can act as electronically active dopants controlling their electronic and phonon transport properties and, hence, its thermoelectric behavior. Therefore, the influence of ad-atoms (Hydrogen and Oxygen) and chemisorbed

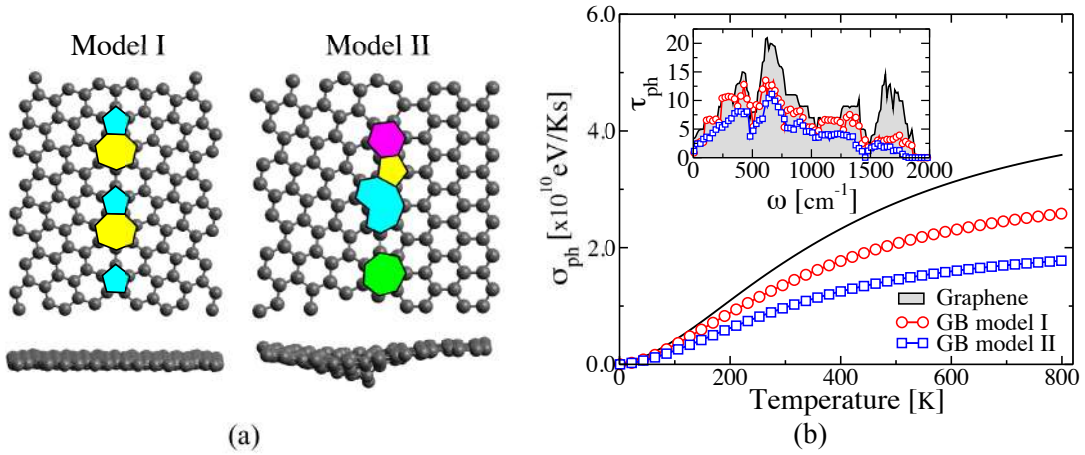


Figure 3.9: (a) Atomistic representation of the two graphene grain boundary models investigated in this study: symmetric (model I) and asymmetric (model II). (b) Phonon thermal conductance for pristine graphene and the two models of grain boundaries. Inset: their corresponding phonon transmission functions.

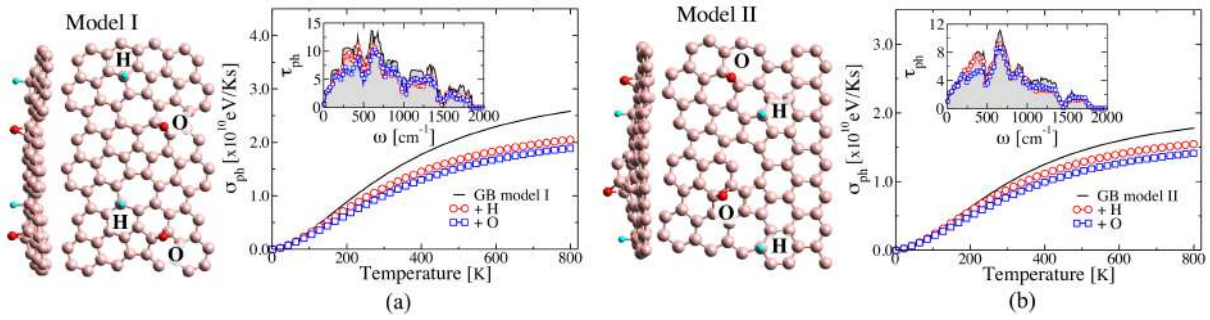


Figure 3.10: Temperature dependence of the phonon thermal conductance in the (a) GB model I and (b) GB model II upon functionalization with H- and O-atoms. The insets show the corresponding phonon transmission functions. In all figures, the lines correspond to pristine grain boundaries (solid lines), hydrogen ad-atoms (\circ), and oxygen ad-atoms (\square).

molecules (Hydroxyl-OH, Methyl-CH₃, and nitrophenyl-NO₂C₆H₄ (NPD)) on the thermal transport properties of two possible graphene GBs, symmetric (model I) and asymmetric (model II), is explored [220]. The model I consists of two graphene sheets with the same orientation (8°) but in opposite directions, clockwise and counterclockwise, whereas model II has been built with a graphene sheet oriented in the armchair direction and another in the zigzag (10° in the clockwise) direction (see Fig. 3.9(a)). Both GBs are composed by pentagons and heptagons, and model II also presents a nonagon.

As shown in Fig. 3.9(b), the phonon thermal conductance, κ_{ph} , for both graphene GBs is lower than the corresponding one to pristine graphene for the whole range of temperature because of local structural defects which induce additional phonon scattering. Moreover, when comparing κ_{ph} for the two GBs, one can see that model II has the smallest phonon thermal conductance. This is related to the more disordered structure of the GB region in model II. After geometry

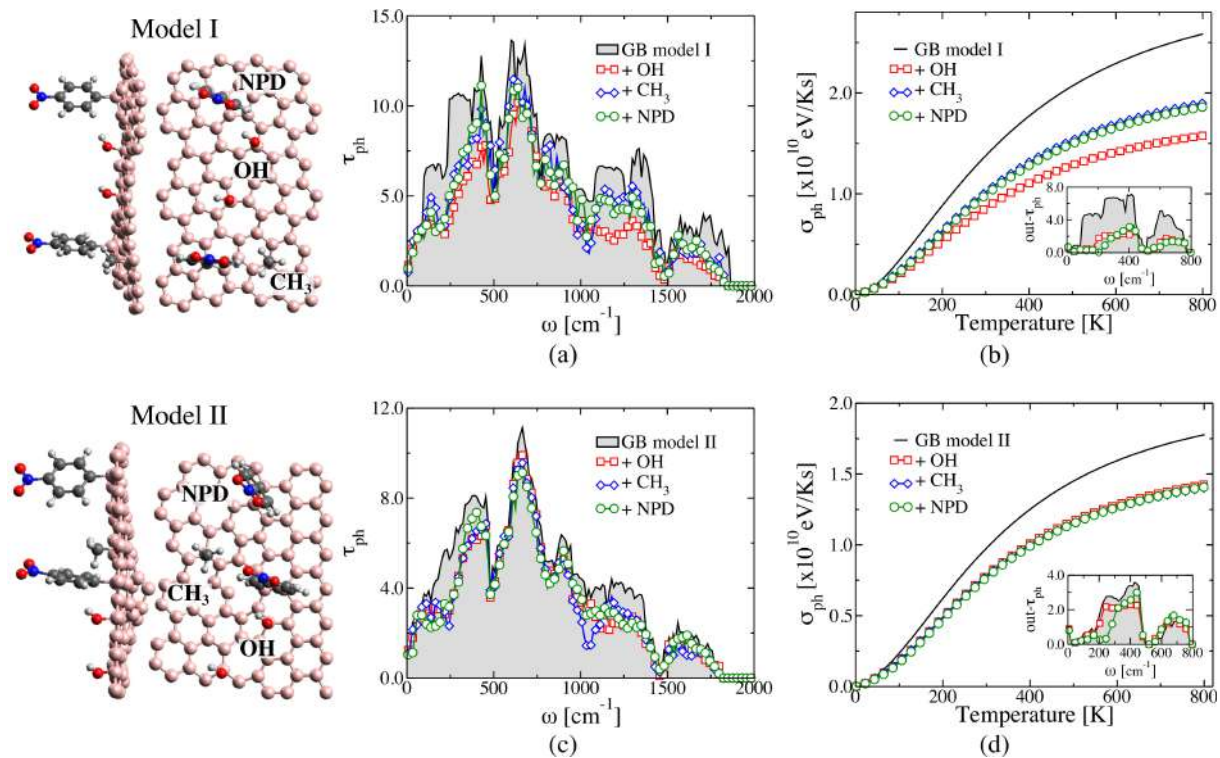


Figure 3.11: Phonon transmission and phonon thermal conductance for functionalized grain boundaries: (a,b) GB model I and (c,d) GB model II. In all plots, the transport coefficients for the pristine grain boundaries are shown with solid lines, Hydroxyl-OH (\square), Methyl-CH₃ (\diamond), and Nitrophenyl-NPD (\circ). The insets in panels (b) and (d) show the component of the phonon transmission function corresponding to the out of plane modes to highlight the impact of the functionalization on these vibrational modes. Notice that the strongest modification of the transmission in this case takes place at low frequencies, below 200 cm^{-1} .

optimization of ad-atoms, it was found that H atoms prefer to be located on top of carbon sites (C-H bond length is 1.14 Å), while O atoms are attached to bridge (B) sites (the C-O bond length is 1.49 Å) for both GBs, in good agreement with results reported by Mu et al. [280]. The phonon transmission of both grain boundaries is reduced over the whole spectrum of frequencies by the inclusion of ad-atoms (see Fig. 3.10). H and O ad-atoms strongly affect out-of-plane modes which correspond to $\omega < 750$ cm^{-1} . The analysis of the projected vibrational density of states reveals that the lighter H atoms have a stronger influence at high frequencies ($\omega \in [1000 - 1500]$ cm^{-1}) and O atoms at lower frequencies ($\omega < 900$ cm^{-1}). The major contribution to the transmission spectrum comes from a spectral region between 250 cm^{-1} and 750 cm^{-1} , which coincides with the range where oxygen functionalization shows up in phonon transport, i.e., attaching oxygen atoms has a stronger influence on the thermal conductance of both GBs (see Fig. 3.10).

Additionally, OH, CH₃, and NPD molecules are covalently bonded to carbon atoms to the grain boundaries on T sites. For both GB models, the largest influence of the functionalization is seen in the low frequency domain ($\omega \leq 400$ cm^{-1}) as well as at higher frequencies $\omega > 1100$ cm^{-1} (see Fig. 3.11). Besides of this reduction on the phonon transmission, thermal conductance of GB

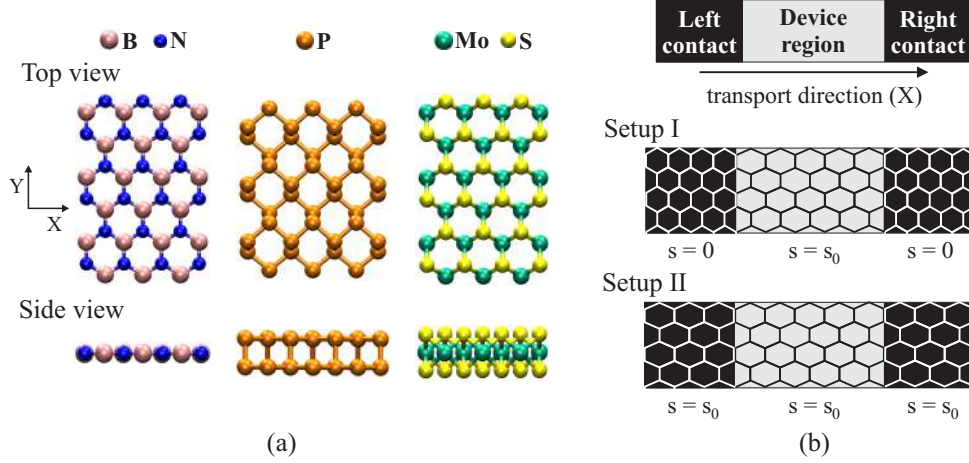


Figure 3.12: (a) Atomistic view of the studied two-dimensional materials: hexagonal boron-nitride, phosphorene, and molybdenum disulfide (MoS₂) monolayer. (b) Schematic representation of the partition scheme for transport calculation using Green's function technique. The transport setups under consideration are also shown. For all the 2D materials, phonon transport is along the zigzag direction (X-axis).

model II turns out to be less sensitive to changes in the type of molecule for $T > 200$ K (see Fig. 3.11(b,d)). The variations at low temperatures come from the strong suppression of out-of-planes modes produced by the functionalization group, as shown in the inset of Fig. 3.11(b,d). For GB model I, CH₃ and NPD molecules affect in a very similar magnitude its phonon transmission which is reflected in the thermal conductance values (see Fig. 3.11(a,b)). Whereas for OH groups, κ_{ph} shows a higher decrement due to the fact that high frequency in-plane modes were suppressed after bonding. Deviations from the conductance of non-functionalized GB clearly increase with temperature as molecular higher frequency modes become thermally activated.

3.2.4 Uniaxial strain

Strain engineering is a powerful route to tailor the physical properties of novel nanomaterials, and it opens up the possibility of new potential device applications in nanophononics. Thus, NEGF-DFTB method is applied to address the influence of strain engineering of the transport setup on the phonon transport properties of two-dimensional materials, focusing on hexagonal boron-nitride (hBN), phosphorene, and MoS₂ monolayer (see Fig. 3.12(a)) [221]. Based on the partitioning scheme shown in Fig. 3.12(b), two possible theoretical setups are considered, which may mimic different experimental ones: I) the device region is uniaxially strained (along ZZ direction) while the contact regions are not and II) both the device and contact regions have the same strain level (i.e., homogeneously strained system). Here, it has been considered the same box length along the y-direction for all strain levels in x-direction (ZZ), which produces an extra force in the periodic direction after increasing the strain. To gain additional insight into the influence of strain on the thermal transport properties, the parameter D is defined as:

$$D_{i-j} = \text{Trace} [K_{i-j}(K^T)_{i-j}] . \quad (3.54)$$

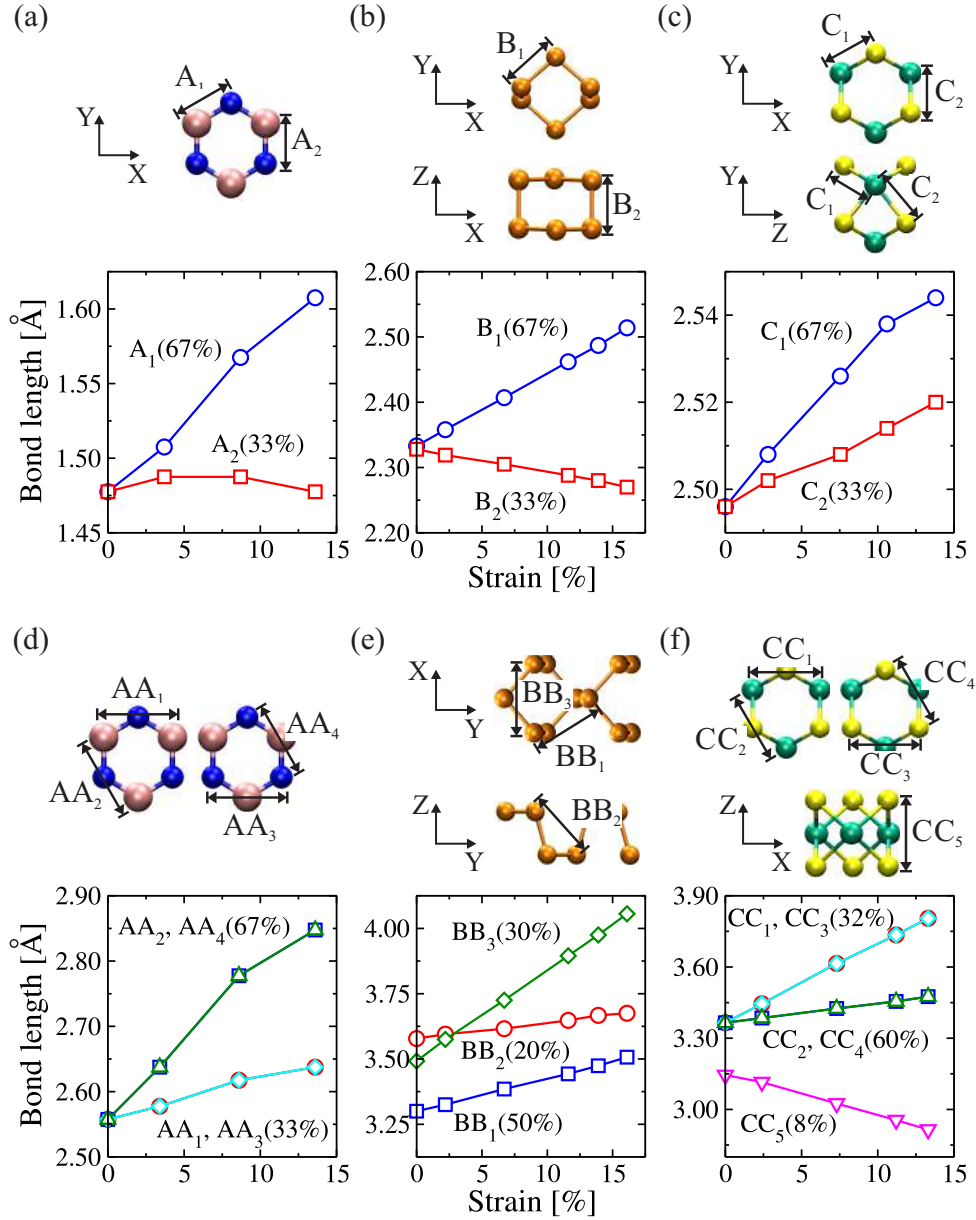


Figure 3.13: Bond lengths at first and second neighbors as a function of the applied strain for (a, d) hexagonal boron-nitride, (b, e) phosphorene, and (c, f) MoS₂ monolayer, respectively. Here, the population of each bond has been analyzed by separating first and second neighbors and it is shown in all the graphs. These results correspond to homogeneously strained materials, setup II.

Here, the indices i, j denote neighboring atoms in the corresponding structure. The real number D_{i-j} is obtained by using the 3×3 sub-matrix K_{i-j} associated with the force constants of atoms i and j . D_{i-j} thus gives information on the bond strength for each atomic pair ($i - j$). Moreover, to have a better understanding of the transport setups defined in this work, the results are compared to those corresponding to the standard model of uniaxial strain, i.e., not fixing the box length along the periodic direction (y-axis), which removes the imposed extra force.

The strain dependence of the nearest-neighbor (first and second) bonds is shown in Fig. 3.13.

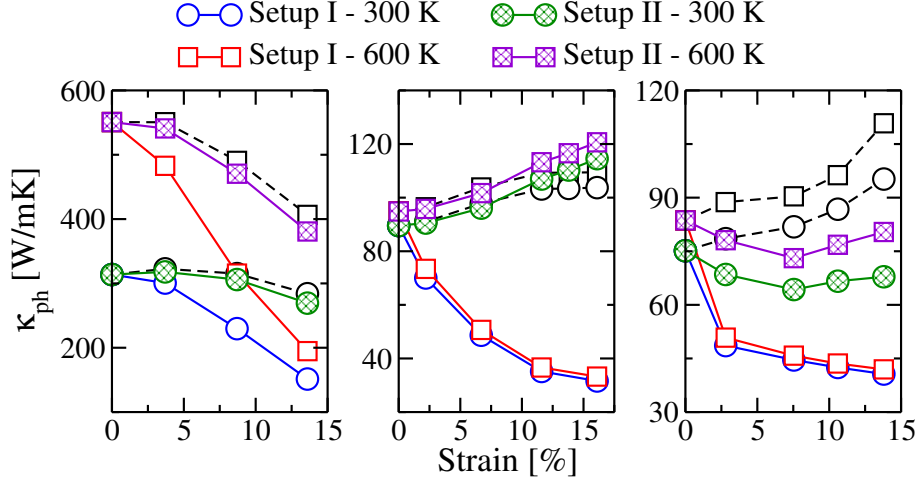


Figure 3.14: The change of the thermal conductance as a function of the applied strain for hexagonal boron-nitride (left panel), phosphorene (center panel), and MoS₂ monolayer (right panel). For comparison, the results for the standard uniaxial strain are also plotted (dashed lines).

The initial bond lengths f (unstrained systems) found after geometry optimization are: hBN: $A_1 = A_2 = 1.48 \text{ \AA}$, P: $B_1 = 2.334 \text{ \AA}$, $B_2 = 2.328 \text{ \AA}$, and MoS₂: $C_1 = C_2 = 2.50 \text{ \AA}$. These values are comparable to those obtained by performing full DFT calculations [94, 281]. Fig. 3.13 shows that bonds along the transport direction are strongly influenced by the applied strain with exception of C_1 due to the more compact structure of the MoS₂ monolayer. Whereas, the strain dependence of A_2 , B_2 , and C_2 bonds depends on the number of atomic layers. In fact, the A_2 bond slightly increases in magnitude, but after 6% of strain it starts to decrease again. On the contrary, for the other 2D materials composed of more than one atomic layer, the influence of strain on the bonds is quite different: the B_2 and C_2 bonds monotonically decrease and increase, respectively. This effect mainly occurs due to the periodic boundary conditions (extra force) and the corresponding reduction of the interlayer distance after stretching the material. It disappears, though, by applying standard uniaxial strain [221]. Besides, when the bond analysis goes to second neighbors (see Fig.3.13(d)-(f)), the B-B ($AA_{1,2}$), N-N ($AA_{3,4}$), and Mo-Mo ($CC_{1,2}$) bonds generate planar isosceles triangles whose size uniformly increase with the strain. However, because of the number of atomic layers, P-P and S-S bonds also display an extra bond between atoms located at different layers, which slightly increases for P-P (BB_2) bonds and decreases for S-S (CC_5) bonds upon increasing the strain. In short, bond lengths in phosphorene and MoS₂ monolayers display a non-monotonous strain dependence, while those for hBN are uniformly stretched.

As it can be seen in Fig. 3.14, the thermal conductance depends on the transport setup. Here, to have a better comparison to other works, a length of 100 nm has been considered in order to convert thermal conductance units [in units of W/K] into thermal conductivity [in units of W/mK]. Among the three studied two-dimensional materials, hBN monolayer displays the highest thermal conductance κ_{ph} at 300 K ($\sim 310 \text{ W/mK}$), followed by phosphorene (~ 90

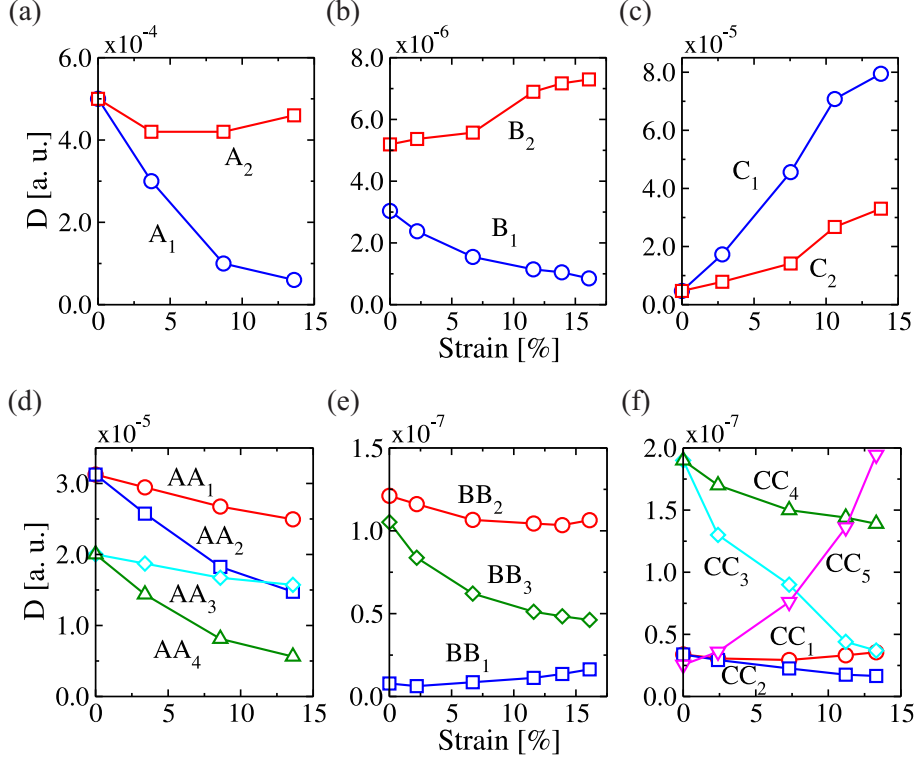


Figure 3.15: D parameter as a function of the applied strain for (a, d) hexagonal boron-nitride, (b, e) phosphorene, and (c, f) MoS₂ monolayer, respectively. The population of the each bond is the same as presented in Fig. A.2. In the graph (f), D values for CC₅ has been reduced by a factor of 20. These results correspond to homogeneously strained materials, setup II.

W/mK). However, by analyzing the D_{ij} parameter (bond strenght) introduced in Eq. (3.54), phosphorene shows the weakest bonds and hBN the strongest ones (see Fig. 3.15), a result related to their difference in Young's modulus [282]. Based on the strain dependence of bond lengths in the hBN monolayer (see Fig. 3.13(a) and (d)), it is expected that with the exception of the A_2 bond, the strength of the first and second neighbor bonds will decrease after increasing the strain (see Fig. 3.15(a) and (d)). Consequently, the components of the dynamical matrix associated to these bonds (the strongest ones) become smaller and, then, the thermal conductance continuously decreases with increased applied strain, see Fig. 3.13(a). This reduction of κ_{ph} is higher for setup I because of the presence of an additional interface resistance between contact and device regions, which strongly blocks phonon transfer at higher frequencies, $> 800cm^{-1}$ [221]. Notice that κ_{ph} at room temperature (300 K) shows a slightly increment by considering setup II. Similar results were reported by Zhu and Ertekin [134] using non-equilibrium molecular dynamics and Boltzmann transport equation methods. Other one-atom thick layer materials have been found to show similar effect by performing a self-consistent study of the linearized Boltzmann-Peierls equation for phonon transport [152].

The influence of the strain in phosphorene and MoS₂ monolayer is qualitatively different because of the presence of additional transport channels related to high frequency out-of-plane

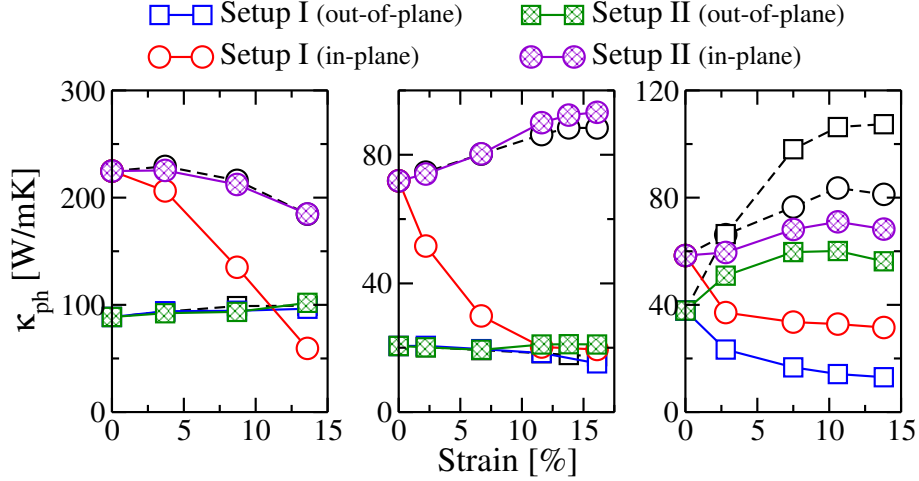


Figure 3.16: The change of in-plane and out-of-plane mode contributions to the the thermal conductance at 300 K as a function of the applied strain for hexagonal boron-nitride (left panel), phosphorene (center panel), and MoS₂ monolayer (right panel). For comparison, the results for the standard uniaxial strain are also plotted (dashed lines).

modes, which have their origin in the additional atomic layers [221]. The thermal conductance in phosphorene monotonously decreases (setup I) and increases (setup II) with the strain, see Fig. 3.14. The interlayer distance is reduced by the increment in strain and, hence, the strength of the B_2 bonds increases, becoming higher than the B_1 bond (see Fig. 3.15(b)). Accordingly, the transmission probability increases at low frequencies (in-plane modes) and so does the thermal transport, as it was also observed by Z.-Y. Ong et al. [91]. For MoS₂ monolayer, despite the relatively small change of first neighbor bonds ($\sim 10^{-2}$ Å), its D parameter considerably increases with the strain (see Fig. 3.15(c)). This sensitivity to the strain level is more pronounced for out-of-plane bonds (C_1 and CC_5 bonds) which increase 8 times their initial strength at 13.8% of strain, see Figs. 3.15(c, f). Hence, the range of transmitting frequencies and the vibrational band gap increase and, after $\sim 7.3\%$ of strain, new transmission peaks emerge at the edge of the acoustic branch. As a result, κ_{ph} decreases for low strain levels and then it increases reaching values close to the initial ones at zero strain independently of the temperature (see Fig. 3.14). In the case of unstrained contact regions, κ_{ph} only decreases with increasing strain level due to the continuous suppression of high frequency in-and out-of-plane modes.

To gain further insight into the phonon transport properties, in-plane and out-of-plane mode contributions to the thermal conductance have also been analyzed (see Fig. 3.16). The approach to compute these contributions is quite different to that one explained in previous section, for more information see supplementary information of Ref. [221]. It was found that mostly in-plane modes are responsible for thermal transport in homogeneously strained hBN and phosphorene monolayers (setup II). Whereas, for setup I, in-plane mode contribution to κ_{ph} is, as expected, strongly affected by imposing an extra device-contact interface. Consequently, the total thermal conductance will be reduced as it was shown in Fig. 3.14. For MoS₂ monolayer (see right panel in

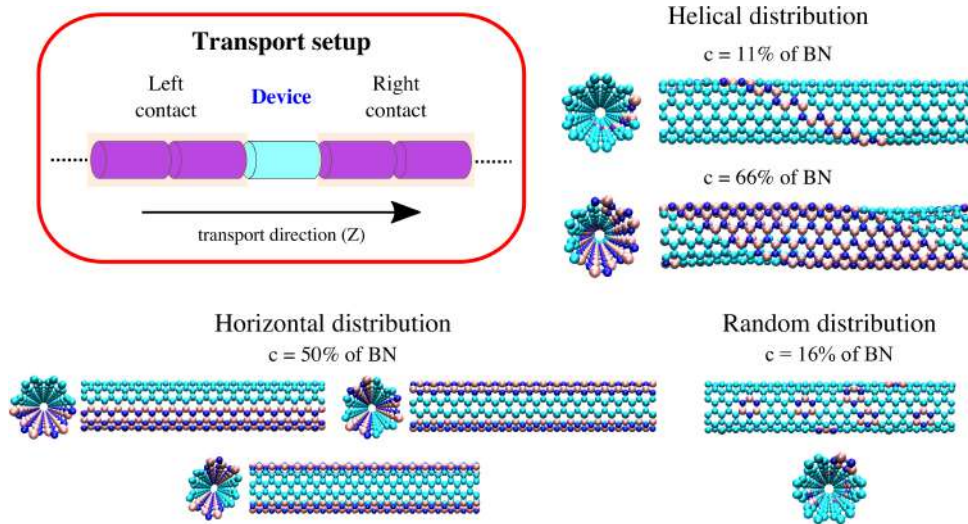


Figure 3.17: Atomistic view of BNC heteronanotubes with helical, horizontal, and random distribution of BN domains. We also show a schematic representation of the partition scheme for transport calculation in helical BNC heteronanotubes by using the Green's function technique. For all nanotubes, electron and phonon transport is along the Z direction. Carbon atoms (cyan), Boron atoms (pink), and Nitrogen atoms (blue).

Fig. 3.16), the situation is different, the contributions of in-plane and out-of-plane modes to κ_{ph} are quite similar due to the large overlap in their associated frequencies. In fact, in homogeneous strained MoS₂ systems, both contributions monotonically increases up to strain level of $\sim 9.0\%$, then it starts to decrease. Therefore, the total κ_{ph} changes its trend and slightly increases. This effect is strong at high temperatures. Also, by considering setup II, the strain dependence of the thermal conductance for hexagonal boron-nitride and phosphorene is similar to that obtained by employing the standard model for uniaxial strain (see dashed lines in Fig. 3.14 and Fig. 3.16). On the contrary, for MoS₂ monolayer, unlike the effect on the transmission function observed with the setup II, the transmission probability increases at low frequencies by applying uniaxial strains and, hence, κ_{ph} will only increase. Hence, by imposing the extra force in the periodic direction (y-direction), transport channels corresponding to low frequencies which strongly influences the conduction through out-of-plane modes are blocked, as one can see in Fig. 3.16.

3.2.5 Doping distribution

The last parameter treated for controlling the thermal transport properties of nanomaterials is doping concentration. In particular, BNC heteronanotubes are expected to play an important role as new generation of thermoelectric materials, and are also of great interest in environmentally relevant issues such as waste heat recovery and solid-state cooling [9]. Thus, in this study three different BN doping distribution patterns of a carbon nanotube are considered: helical, horizontal, and random. For this, a (6,6)-CNT of length 43.3 Å will be the reference structure (supercell composed by 432 C atoms). Helical BN strips, BN chains (parallel to the transport

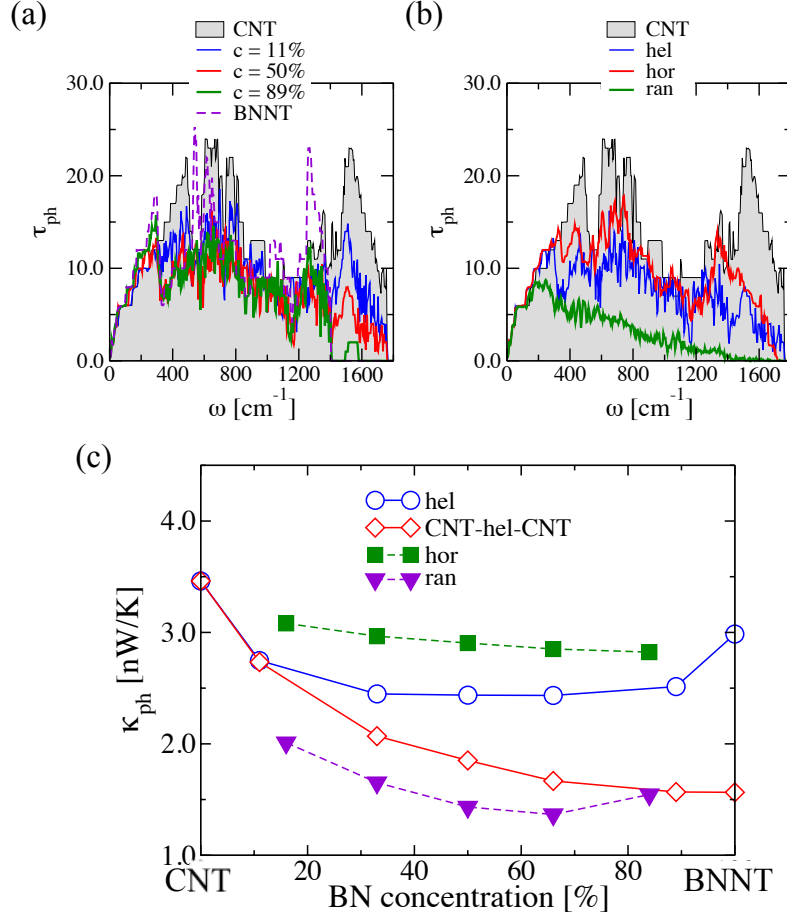


Figure 3.18: Phonon transport properties of BNC heteronanotubes. (a) Phonon transmission function, τ_{ph} , of helical BNC heteronanotubes for different BN concentrations, c . (b) Comparison of τ_{ph} for several doping distribution patterns with 50% of BN concentration. (c) Phonon thermal conductance as a function of the BN concentration for the studied doping distributions.

direction, which corresponds to the Z-axis), and BN rings (one ring containing 3B and 3N atoms) have then been introduced in an otherwise perfect (6,6)-CNT to represent helical, horizontal, and random impurity distributions, see Fig. 3.17. For the helical distribution, the BN concentration is varied from $c = 11\%$ to $c = 89\%$. While for the other cases, concentrations ranging from $c = 16\%$ to $c = 84\%$ are considered. The limits of 0% and 100% correspond to carbon and hexagonal boron-nitride nanotubes, respectively.

All BNC heteronanotube geometries are optimized by using DFTB method [283, 284] until the absolute value of the inter-atomic forces was below 10^{-6} atomic units, with a k-point mesh of 1x1x8. Periodic boundary conditions were imposed along the Z-axis. The values of C-C and B-N bond lengths are 1.43 Å and 1.48 Å, respectively. After geometry optimization, the helical BNC heteronanotubes display a smooth wave-like profile along the axial direction (mainly around the C stripes). This is related to the difference between bond lengths at the interfaces: C-B~1.49 Å and C-N~1.36 Å see e.g. Refs. [133, 285]. The horizontally doped nanotubes have

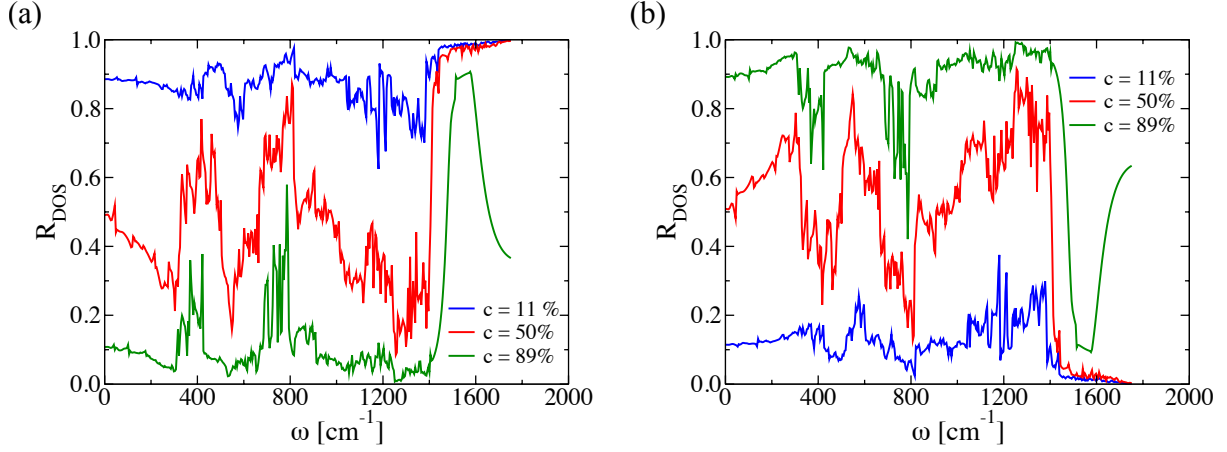


Figure 3.19: Variation of R_{DOS} for (a) carbon and (b) boron-nitride domains as a function of the vibrational frequency for helical BNC heteronanotubes. Results for three different concentrations are shown.

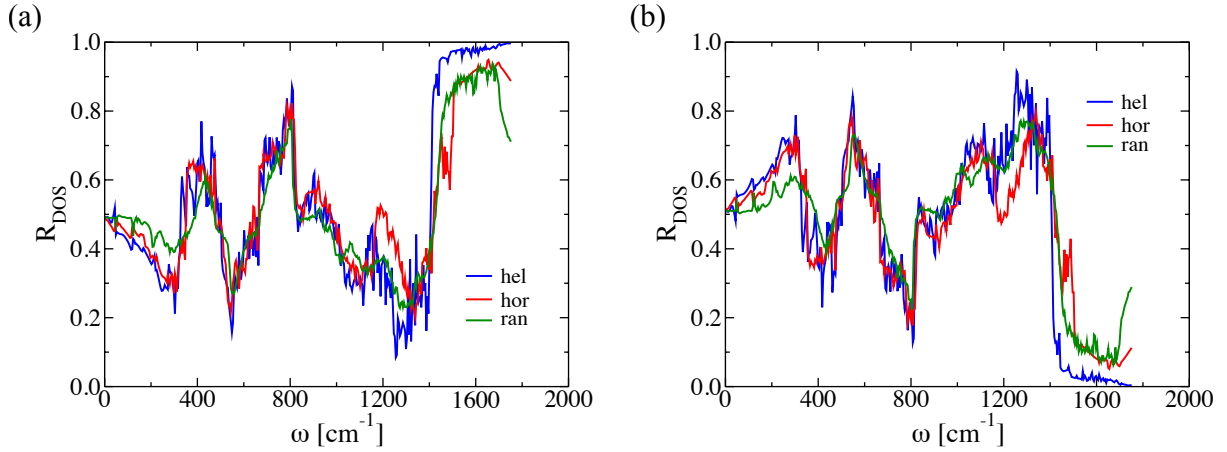


Figure 3.20: Variation of R_{DOS} for (a) carbon and (b) boron-nitride domains as a function of the vibrational frequency for helical, horizontal, and random BNC heteronanotubes. These results are for a fixed BN concentration equal to 50%.

weakly elongated cross sections with a BN concentration dependent eccentricity (see Fig. 3.17), confirming the results reported by Guedes et al. [286]. Moreover, to account for the variations in the possible doping patterns, the transmission functions for random and horizontal distributions are configurationally averaged over five and three different atomic configurations, respectively. For the horizontal stripes, these configurations are shown in Fig. 3.17 for $c = 50\%$.

For the phonon transport calculations, a common partitioning scheme has been also used, i.e., the whole system is divided into three regions, namely left lead, right lead, and a central region, as it is displayed in Fig. 3.17. For all doping distributions the leads are composed by twice the optimized supercell and the central (or device) region includes only one supercell. Thus, there are no effects related to interface scattering between the leads and the central region. For the helical distribution, an extra case has been studied by considering leads purely made of (6,6)-CNTs and the central scattering region including a finite helical BNC heteronanotube. To have

a better understanding of the doping influence on the transport properties, the R_{DOS} parameter is defined as

$$R_{DOS} = \frac{\eta_X(\omega)}{\eta_{Total}(\omega)} \quad (3.55)$$

where $\eta_{Total}(\omega)$ is the total phonon DOS as computed by using Eq. 3.23, and $\eta_X(\omega)$ can be either the local phonon DOS of C or BN domains.

In Fig. 3.18(a), the influence of helical BN stripes on the phonon transmission function of a (6,6)-CNT is shown. The width of the B-N stripes is given by W_{BN} ; the corresponding widths for a concentration of $c = 11\%$ and $c = 89\%$ are $W_{BN} = 2.46 \text{ \AA}$ and $W_{BN} = 27.06 \text{ \AA}$, respectively. The effect of increasing concentration for a given BN helical distribution is mostly seen in a dramatic suppression of high frequency vibrational modes ($\omega > 1400 \text{ cm}^{-1}$), which correspond to relatively local vibrations involving carbon atoms. This is clearly seen from the behavior of R_{DOS} after increasing the doping concentration (see Fig. 3.19). The transmission of low-frequency (long wavelength) vibrations below 200 cm^{-1} is, on the contrary, barely changed when varying the disorder concentration (width of the helical stripes). Then, the phonon transmission functions of BNC heteronanotubes with fixed concentration $c = 50\%$ and different BN spatial arrangements is plotted in Fig. 3.18(b). Overall, the phonon transmission is strongly suppressed for all BN spatial distributions when compared with the pristine CNT reference system, with the exception of the long wavelength modes. As expected, a purely random distribution of B and N atoms largely blocks the transmission over almost the whole frequency spectrum; only the low-frequency modes experience less scattering at the localized impurities and therefore their transmission is much less affected. Regarding the more structurally ordered helical and horizontal arrangements, one can see that the former leads to a stronger reduction of the transmission in the high-frequency domain ($\omega > 1400 \text{ cm}^{-1}$) of the spectrum due to the absence of B-N-C local vibrations. Most of high-frequency vibrations in helical BNC heteronanotubes only correspond to carbon atoms, as it can be seen in Fig. 3.20.

The corresponding phonon thermal conductances, κ_{ph} , as a function of the BN concentration for each doping distribution pattern at $T = 300 \text{ K}$ are displayed in Fig. 3.18(c). Here, the thermal conductance of semi-infinite helical BNC heteronanotubes remains nearly constant ($\sim 2.5 \text{ nW/K}$) for concentrations between 30% and 80%, and then increases until it reaches the value corresponding to a pristine BNNT, $\kappa_{ph} \sim 3.0 \text{ nW/K}$. Moreover, as it is expected from the behavior of the phonon transmission function, horizontal BNC heteronanotubes show the highest thermal conductance while the lowest κ_{ph} values were obtained for (6,6)-CNT with BN domains randomly distributed. Connecting the helical BNC heteronanotube to purely CNT leads to a continuous suppression of the thermal conductance with increasing concentration. Notice that for the temperature used in this calculation ($T = 300 \text{ K}$), the dominant contribution to the thermal conductance mostly originates from long wavelength modes with frequencies $\leq 200 \text{ cm}^{-1}$.

3.3 SUMMARY

In the present chapter, quantum phonon transport has been studied in novel two-dimensional materials and BNC heteronanotubes. To do this, a new atomistic approach was implemented, which combines nonequilibrium Green's function formalism with density functional tight-binding method. This implementation is a new tool in the DFTB+ software (in-house version). Hence, the influence of several intrinsic and external factors on the quantum thermal transport properties of novel nanomaterials can be explored.

First of all, the structural anisotropy in two-dimensional puckered materials produced two different behaviors for their thermal transport. Thus, in the three different materials studied here (phosphorene, arsenene, and SnS monolayer), thermal conductance across the zigzag direction is larger than this corresponding to armchair direction. This is due to the higher phonon group velocities along the zigzag direction. Another characteristic factor that always alters the transport properties of nanomaterials are 1D topological defects or grain boundaries. In fact, transmission probability of high frequency vibrational modes in graphene is strongly reduced by the effect of any grain boundary. Consequently, the thermal conductance values are also dependent on the type of grain boundary. Moreover, their thermal transport properties can be controlled by distorting or heating up the grain boundaries, having a stronger negative effect when boundaries are structurally damaged. It was also found that the thermal conductance of graphene grain boundaries is reduced after functionalization with small molecules or ad-atoms. However, the magnitude of the effect depends on the symmetry of the boundary.

Strain engineering was used to tune the thermal transport properties of hexagonal boron-nitride, phosphorene, and MoS₂ monolayer. Here, the strain dependence of the thermal conductance at 300 K is different for each material when the whole system is homogeneously stretched. However, the thermal conductance only reduces after increasing the strain level in the central region (device). This is because of the extra contact-device interface, which blocks many transport channels. Moreover, as a consequence of strain dependence of several bond lengths, in-plane modes are strongly affected comparing to out-of-plane ones. However, for strain levels < 10%, they are predominant in the heat transport of these two-dimensional materials.

Finally, the influence of BN doping concentration on the thermal transport properties of a (6,6)-CNT was also treated. Thus, the phonon transmission is mainly reduced at high frequencies after increasing the BN concentration, which correspond to local vibrations involving C atoms. Although, this effect is different for each doping distribution pattern. Indeed, among all them, horizontal and random BNC heteronanotubes present the highest and lowest thermal conductance values at 300 K, respectively. For helical BNC heteronanotubes, the thermal conductance is between these two extreme cases and it remains constant for the concentration range [30, 80]%

4 TIME-DEPENDENT QUANTUM PHONON TRANSPORT

In this chapter, a novel atomistic method capable of studying the transient and steady-state phonon transport properties of nanoscale systems by combining time-dependent NEGF approach and DFT-based modelling is developed. This numerical method is based on the solution of the equation of motion of the phonon density matrix $\sigma(t)$ by developing an auxiliary-mode approach. This very efficient approach has already been successfully used for various investigations of time-resolved electron transport [55–57]. Unlike recent related approaches whose application is limited to simple model systems [61–63], the main goal for developing our method is to combine a time-dependent approach with an atomistic material description, which is still an open and very challenging issue. As a proof-of-principle, it is first applied to study the non-equilibrium dynamics of quantum heat transport in an 1D atomic chain and, in a second step, in molecular junctions made of poly-acetylene and poly-ethylene dimers. In the latter case the vibrational structure of the junction is described at the density-functional theory level. Some basic concepts of the NEGF approach have been already explained in Sec. 3.1.1, therefore, the next section will only focus on the detailed derivation of the equation of motion for $\sigma(t)$, which can be expressed in terms of real-time Green’s functions.

4.1 NONEQUILIBRIUM GREEN’S FUNCTIONS

4.1.1 Theoretical model

The basic setup of this approach is shown in Fig. 4.1. Two thermal baths consisting of non-interacting harmonic oscillators which are in thermal equilibrium are connected to a generic scattering region, whose vibrational properties are assumed to be well represented by a purely

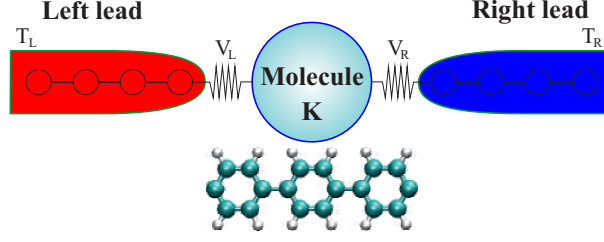


Figure 4.1: Schematic representation of the target molecular junctions in the present study. A molecular system is connected to two harmonic thermal baths, which are the source for the heat flow in the molecule.

harmonic Hamilton operator. The total system is then described by the following Hamiltonian

$$H = H_C + \sum_{\alpha k} \left(\frac{1}{2} p_{\alpha k}^2 + \frac{1}{2} \omega_{\alpha k}^2 u_{\alpha k}^2 \right) + \sum_{\alpha, k} \frac{1}{2} (\mathbf{u}^T \cdot \mathbf{V}_{\alpha k} u_{\alpha k} + u_{\alpha k} \mathbf{V}_{\alpha k}^T \cdot \mathbf{u}) . \quad (4.1)$$

The first term $H_C = (1/2)\mathbf{p}^T \cdot \mathbf{p} + (1/2)\mathbf{u}^T \cdot \mathbf{K}_{\text{eff}} \cdot \mathbf{u}$ is the Hamiltonian of the central region, \mathbf{u} is a column vector consisting of all the atomic displacement variables in the region, and \mathbf{p} contains the corresponding momenta. Both vectors have length N , where N is the number of vibrational degrees of freedom in the central region. We have chosen renormalized displacements $u_i = \sqrt{m_i} x_i$, where m_i is the mass associated with the i th vibrational degree of freedom and x_i is the actual displacement having the dimension of length. The effective force-constant matrix $\mathbf{K}_{\text{eff}} = \mathbf{K} + \mathbf{K}_{\text{ct}}$ has dimension $N \times N$ and includes the force constant matrix of the central region, \mathbf{K} , as well as a counter-term \mathbf{K}_{ct} , whose meaning is explained below. The index $\alpha \in \{L, R\}$ labels the left (L) and right (R) heat baths, while k denotes their corresponding vibrational mode with frequency $\omega_{\alpha k}$. The second term of Eq. (4.1) is the Hamiltonian of the heat bath. The last term represents the interaction between the central region and the baths, which is given by coupling vectors $\mathbf{V}_{\alpha k}$ that are assumed to vanish before time $t_0 \rightarrow -\infty$. Written in this form, the coupling leads to a renormalization of the bare force-constant matrix, which can be canceled by the previously mentioned counter term $\mathbf{K}_{\text{ct}} = \sum_{\alpha, k} (\mathbf{V}_{\alpha k} \cdot \mathbf{V}_{\alpha k}^T) / \omega_{\alpha k}^2$. Consequently, the coupling to the thermal baths will solely introduce dissipation rather than a shift in the vibrational spectrum of the system [287]. Then, the equations of motion for central region (\mathbf{u} and \mathbf{p}) and normal modes of (one) lead (u_k) are given by

$$\begin{aligned} \dot{\mathbf{u}} &= \mathbf{p} , \\ \dot{\mathbf{p}} &= \ddot{\mathbf{u}} = -\mathbf{K}_{\text{eff}} \cdot \mathbf{u} - \sum_k \mathbf{V}_k u_k , \\ \ddot{u}_k &= -\omega_k^2 u_k - \mathbf{V}_k^T \cdot \mathbf{u} . \end{aligned}$$

These equations can be also expressed as

$$\frac{\partial}{\partial t} \begin{pmatrix} \mathbf{u} \\ \mathbf{p} \end{pmatrix} = \begin{pmatrix} \mathbf{0} & \mathbf{I} \\ -\mathbf{K}_{\text{eff}} & \mathbf{0} \end{pmatrix} \cdot \begin{pmatrix} \mathbf{u} \\ \mathbf{p} \end{pmatrix} - \sum_k u_k \begin{pmatrix} \mathbf{0} \\ \mathbf{V}_k \end{pmatrix} . \quad (4.2)$$

Here, $2N \times 2N$ dimensional auxiliary matrices are defined as

$$\mathcal{I} \equiv \begin{pmatrix} \mathbf{I} & \mathbf{0} \\ \mathbf{0} & \mathbf{I} \end{pmatrix}, \quad \mathcal{Q} \equiv \begin{pmatrix} \mathbf{0} & \mathbf{I} \\ -\mathbf{I} & \mathbf{0} \end{pmatrix}, \quad \mathcal{K}_{\text{eff}} \equiv \begin{pmatrix} \mathbf{0} & \mathbf{I} \\ -\mathbf{K}_{\text{eff}} & \mathbf{0} \end{pmatrix} \equiv \begin{pmatrix} \mathbf{0} & \mathbf{I} \\ -\mathbf{K} & \mathbf{0} \end{pmatrix} + \begin{pmatrix} \mathbf{0} & \mathbf{0} \\ -\mathbf{K}_{\text{ct}} & \mathbf{0} \end{pmatrix}.$$

Caligraphic symbols are used to denote matrices with dimension $2N \times 2N$ throughout this chapter. Hence, the mechanical energy of the central region can be expressed in terms of the phonon density matrix $\sigma(t) = i\mathcal{G}^<(t, t)$, where $\mathcal{G}^<(t, t)$ is the lesser Green's function (GF), as

$$E_C(t) = \frac{\hbar}{2} \text{Tr} \{ \mathcal{K}_{\text{eff}}^T \cdot \mathcal{Q} \cdot \sigma(t) \}. \quad (4.3)$$

Thus, the total energy of a system connected to heat baths is,

$$E_{\text{Tot}}(t) = E_C(t) + E_{\text{bath}}(t).$$

If no external force (driver) is acting on the system, the total energy must be conserved, i.e.,

$$\frac{\partial}{\partial t} E_{\text{Tot}}(t) = \frac{\partial}{\partial t} E_C(t) + \frac{\partial}{\partial t} E_{\text{bath}}(t) = 0.$$

Then, the heat current coming from the heat baths can be defined as $J(t) = -\frac{\partial}{\partial t} E_C(t)$. Therefore, the time evolution of the heat flux is related to the lesser GF, which can be written as a $2N \times 2N$ block matrix [62, 63],

$$\mathcal{G}^<(t, t') = -i \begin{pmatrix} \langle \mathbf{u}(t') \mathbf{u}^T(t) \rangle & \langle \mathbf{u}(t') \mathbf{p}^T(t) \rangle \\ \langle \mathbf{p}(t') \mathbf{u}^T(t) \rangle & \langle \mathbf{p}(t') \mathbf{p}^T(t) \rangle \end{pmatrix}. \quad (4.4)$$

Notice that the GF includes displacement \mathbf{u} and momentum \mathbf{p} vectors on the same footing.

4.1.2 Equation of motion for the Green's functions

To obtain the time dependence of the lesser GF, firstly, the Dyson's equation for this physical problem must be derived. To do this, by considering $\hbar = 1$, the contour ordered Green's function of the central region is defined as

$$\mathcal{G}(\tau, \tau') = -i \mathcal{T}_C \begin{pmatrix} \langle \mathbf{u}(\tau) \mathbf{u}^T(\tau') \rangle & \langle \mathbf{u}(\tau) \mathbf{p}^T(\tau') \rangle \\ \langle \mathbf{p}(\tau) \mathbf{u}^T(\tau') \rangle & \langle \mathbf{p}(\tau) \mathbf{p}^T(\tau') \rangle \end{pmatrix}. \quad (4.5)$$

Then, the partial derivative respect to the argument τ is taken in order to get the equation of motion (EOM) of the contour GF,

$$\frac{\partial}{\partial \tau} \mathcal{G}(\tau, \tau') = \delta(\tau - \tau') \mathcal{Q} + \mathcal{K}_{\text{eff}} \cdot \mathcal{G} - \sum_k (-i) \mathcal{T}_C \begin{pmatrix} \mathbf{0} & \mathbf{0} \\ \langle u_k(\tau) \mathbf{V}_k \mathbf{u}^T(\tau') \rangle & \langle u_k(\tau) \mathbf{V}_k \mathbf{p}^T(\tau') \rangle \end{pmatrix}. \quad (4.6)$$

Next, a new GF is defined as

$$\mathcal{G}_k(\tau, \tau') = -i\mathcal{T}_C \left(\begin{array}{cc} \mathbf{0} & \mathbf{0} \\ \langle u_k(\tau) \mathbf{u}^T(\tau') \rangle & \langle u_k(\tau) \mathbf{p}^T(\tau') \rangle \end{array} \right),$$

which obeys

$$\begin{aligned} [\partial_\tau^2 + \omega_k^2] \mathcal{G}_k(\tau, \tau') &= -i\mathcal{T}_C \left(\begin{array}{cc} \mathbf{0} & \mathbf{0} \\ -\mathbf{V}_k^T \langle \mathbf{u}(\tau) \mathbf{u}^T(\tau') \rangle & -\mathbf{V}_k^T \langle \mathbf{u}(\tau) \mathbf{p}^T(\tau') \rangle \end{array} \right) \\ &= \mathbf{V}_k^T \left(\begin{array}{cc} \mathbf{0} & \mathbf{0} \\ -\mathbf{I} & \mathbf{0} \end{array} \right) \cdot \mathcal{G}(\tau, \tau'). \end{aligned}$$

The solution of this equation reads

$$\mathcal{G}_k(\tau, \tau') = - \int d\tau'' \mathcal{G}_k^0(\tau, \tau'') \mathbf{V}_k^T \left(\begin{array}{cc} \mathbf{0} & \mathbf{0} \\ -\mathbf{I} & \mathbf{0} \end{array} \right) \cdot \mathcal{G}(\tau'', \tau') \quad (4.7)$$

with $[\partial_\tau^2 + \omega_k^2] \mathcal{G}_k^0(\tau, \tau') = -\delta(\tau - \tau')$. By inserting Eq. (4.7) into Eq. (4.6), the equation of motion of the contour ordered GF becomes

$$\frac{\partial}{\partial \tau} \mathcal{G}(\tau, \tau') = \delta(\tau, \tau') \mathcal{Q} + \mathcal{K}_{\text{eff}} \cdot \mathcal{G} + \int d\tau'' \mathcal{Q} \cdot \sum_k \left(\begin{array}{cc} \mathbf{V}_k \mathcal{G}_k^0(\tau, \tau'') \mathbf{V}_k^T & \mathbf{0} \\ \mathbf{0} & \mathbf{0} \end{array} \right) \cdot \mathcal{G}(\tau'', \tau').$$

Here, $\Sigma(\tau, \tau') = \sum_k \mathbf{V}_k \mathcal{G}_k^0(\tau, \tau'') \mathbf{V}_k^T$ is the self-energy of the system. To continue the $2N \times 2N$ notation, the general self-energy is expressed as

$$\mathcal{S}(\tau, \tau') \equiv \left(\begin{array}{cc} \Sigma(\tau, \tau') & \mathbf{0} \\ \mathbf{0} & \mathbf{0} \end{array} \right).$$

Moreover, the decoupled Green's function \mathcal{G}^0 is the solution to the following equation of motion,

$$\frac{\partial}{\partial \tau} \mathcal{G}^0(\tau, \tau') \cdot \mathcal{Q}^T = \delta(\tau, \tau') \mathcal{I} + \mathcal{K} \cdot \mathcal{G}^0 \cdot \mathcal{Q}^T.$$

Hence, the Dyson's equation for the central region Green's function is given by

$$\mathcal{G}(\tau, \tau') = \mathcal{G}^0(\tau, \tau') + \int d\tau_2 \int d\tau_3 \mathcal{G}^0(\tau, \tau_2) \cdot \mathcal{S}(\tau_2, \tau_3) \cdot \mathcal{G}(\tau_3, \tau'). \quad (4.8)$$

Thus, by using the Langreth's rules, the equations for the real-time retarded (R) and lesser (<) Green's functions are written as

$$\mathcal{G}^R(t, t') = \mathcal{G}^{0,R}(t, t') + \int d\tau_2 \int d\tau_3 \mathcal{G}^{0,R}(t, \tau_2) \cdot \mathcal{S}^R(\tau_2, \tau_3) \cdot \mathcal{G}^R(\tau_3, t'), \quad (4.9)$$

$$\mathcal{G}^<(t, t') = \int d\tau_2 \int d\tau_3 \mathcal{G}^R(t, \tau_2) \cdot \mathcal{S}^<(\tau_2, \tau_3) \cdot \mathcal{G}^A(\tau_3, t'). \quad (4.10)$$

The expression for the advanced GF, $\mathcal{G}^A(t, t')$, is also derived in a similar manner. This is obtained by taking the derivative of the Eq. (4.5) respect to the second argument τ' (see derivation in Appendix C) and, hence,

$$\mathcal{G}^A(t, t') = \mathcal{G}^{0,A}(t, t') + \int d\tau_2 \int d\tau_3 \mathcal{G}^A(t, \tau_2) \cdot \mathcal{S}^A(\tau_2, \tau_3) \cdot \mathcal{G}^{0,A}(\tau_3, t'). \quad (4.11)$$

The EOM for the retarded and advanced GFs can be obtained by taking the time derivative of Eqs. (4.9) and (C.3), respectively. Thus,

$$\frac{\partial}{\partial t} \mathcal{G}^R(t, t') = \delta(t, t') \mathcal{Q} + \mathcal{K}_{\text{eff}} \cdot \mathcal{G}^R(t, t') + \mathcal{Q} \cdot \int dt_2 \mathcal{S}^R(t, t_2) \cdot \mathcal{G}^R(t_2, t'). \quad (4.12)$$

$$\frac{\partial}{\partial t'} \mathcal{G}^A(t, t') = \delta(t, t') \mathcal{Q}^T + \mathcal{G}^A(t, t') \cdot \mathcal{K}_{\text{eff}}^T + \int dt_2 \mathcal{G}^A(t, t_2) \cdot \mathcal{S}^A(t_2, t') \cdot \mathcal{Q}^T. \quad (4.13)$$

Now, the equation of motion for the lesser GF (see Eq. (4.10)) is given in terms of the EOM of $\mathcal{G}^R(t, t')$ and $\mathcal{G}^A(t, t')$ as

$$\begin{aligned} \frac{\partial}{\partial t} \mathcal{G}^<(t, t) &= \int d\tau_2 \int d\tau_3 \left[\frac{\partial}{\partial t} \mathcal{G}^R(t, \tau_2) \cdot \mathcal{S}^<(\tau_2, \tau_3) \cdot \mathcal{G}^A(\tau_3, t) \right. \\ &\quad \left. + \mathcal{G}^R(t, \tau_2) \cdot \mathcal{S}^<(\tau_2, \tau_3) \cdot \frac{\partial}{\partial t} \mathcal{G}^A(\tau_3, t) \right]. \end{aligned} \quad (4.14)$$

Replacing Eqs. (4.12) and (4.13) into Eq. (4.14),

$$\begin{aligned} \frac{\partial}{\partial t} \mathcal{G}^<(t, t) &= \mathcal{K}_{\text{eff}} \cdot \mathcal{G}^<(t, t) + \mathcal{G}^<(t, t) \cdot \mathcal{K}_{\text{eff}}^T \\ &\quad + \mathcal{Q} \cdot \left[\int d\tau_2 \mathcal{S}^<(t, \tau_2) \mathcal{G}^A(\tau_2, t) + \int d\tau_4 \mathcal{S}^R(t, \tau_4) \mathcal{G}^<(\tau_4, t) \right] \\ &\quad + \left[\int d\tau_2 \mathcal{G}^R(t, \tau_2) \mathcal{S}^<(\tau_2, t) + \int d\tau_4 \mathcal{G}^<(t, \tau_4) \mathcal{S}^A(\tau_4, t) \right] \cdot \mathcal{Q}^T \end{aligned} \quad (4.15)$$

Notice that the relations among Green's functions described in the previous chapter are also valid for those one with dimension $2N \times 2N$, i.e.,

$$\begin{aligned} \mathcal{G}^R - \mathcal{G}^A &= \mathcal{G}^> - \mathcal{G}^<, \quad \mathcal{S}^R - \mathcal{S}^A = \mathcal{S}^> - \mathcal{S}^<, \\ \mathcal{G}^R(t, t') &= \Theta(t - t') [\mathcal{G}^> - \mathcal{G}^<] \quad , \quad \mathcal{G}^A(t, t') = \Theta(t' - t) [\mathcal{G}^< - \mathcal{G}^>] \quad , \\ \mathcal{S}^R(t, t') &= \Theta(t - t') [\mathcal{S}^> - \mathcal{S}^<] \quad , \quad \mathcal{S}^A(t, t') = \Theta(t' - t) [\mathcal{S}^< - \mathcal{S}^>] \quad , \end{aligned}$$

Therefore, the EOM for lesser GF becomes

$$\begin{aligned} \frac{\partial}{\partial t} \mathcal{G}^<(t, t) &= \mathcal{K}_{\text{eff}} \cdot \mathcal{G}^<(t, t) + \mathcal{G}^<(t, t) \cdot \mathcal{K}_{\text{eff}}^T \\ &\quad + \mathcal{Q} \cdot \left[\int_{\tau_2}^t d\tau_2 (\mathcal{S}^>(t, \tau_2) \mathcal{G}^<(\tau_2, t) - \mathcal{S}^<(t, \tau_2) \mathcal{G}^>(\tau_2, t)) \right] \\ &\quad + \left[\int_{\tau_2}^t d\tau_2 (\mathcal{G}^>(t, \tau_2) \mathcal{S}^<(\tau_2, t) - \mathcal{G}^<(t, \tau_2) \mathcal{S}^>(\tau_2, t)) \right] \cdot \mathcal{Q}^T \end{aligned} \quad (4.16)$$

Here, the phonon current matrices, $\Pi_\alpha(t)$, are defined in terms of \mathcal{G} and \mathcal{S} ,

$$\Pi_\alpha(t) = \int_{\tau_2}^t d\tau_2 \left(\mathcal{G}^>(t, \tau_2) \mathcal{S}_\alpha^<(\tau_2, t) - \mathcal{G}^<(t, \tau_2) \mathcal{S}_\alpha^>(\tau_2, t) \right) \quad (4.17)$$

where the lesser and greater self-energies of the heat bath α are expressed as (see derivation in Appendix C),

$$\mathcal{S}_\alpha^<(t, t') = -i \int_0^\infty \frac{d\omega}{\pi} \left[\coth \frac{\omega}{2k_B T} \cos \omega(t - t') + i \sin \omega(t - t') \right] \mathcal{L}_\alpha(\omega) \quad (4.18)$$

$$\mathcal{S}_\alpha^>(t, t') = -i \int_0^\infty \frac{d\omega}{\pi} \left[\coth \frac{\omega}{2k_B T} \cos \omega(t - t') - i \sin \omega(t - t') \right] \mathcal{L}_\alpha(\omega) \quad (4.19)$$

with $\mathcal{L}_\alpha \equiv \begin{pmatrix} \Lambda_\alpha(\omega) & \mathbf{0} \\ \mathbf{0} & \mathbf{0} \end{pmatrix}$ as the bath spectral density, which characterizes the action of the environment on the open system [287]. Finally, the EOM for the phonon density matrix is given by

$$\frac{\partial}{\partial t} \sigma(t) = \mathcal{K}_{\text{eff}} \cdot \sigma(t) + \sigma(t) \cdot \mathcal{K}_{\text{eff}}^T + i \sum_{\alpha \in \{L, R\}} \left(\Pi_\alpha(t) \cdot \mathcal{Q}^T - h.c. \right) . \quad (4.20)$$

4.1.3 Auxiliary-mode approach

Now, the next step is to get an expression for calculating the time evolution of the phonon current matrices per each heat bath $\Pi_\alpha(t)$. To do this, an auxiliary-mode approach is used to expand the self-energies $\mathcal{S}_\alpha^{<,>}(t, t')$ in terms of exponential functions, which has been previously developed for electrons [55–57] and for vibrations [288, 289]. Since the cos and sin functions in Eqs. (4.18) and (4.19) are easily to express in exponential form, the only term to be worried is the hyperbolic cotangent. Several schemes have been proposed to obtain a suitable pole decomposition of this term [288]. The most common one is the so-called Matsubara decomposition which is straightforward to apply but, converges very slowly towards the exact result. To overcome this problem more advanced pole decomposition has been suggested. For example, Croy and Saalman [55] suggested a partial fraction decomposition method which converges faster than the Matsubara decomposition. However, to apply this method, one needs a high-precision arithmetic to calculate the poles of the approximation correctly, otherwise, it can lead to severe deviation for the approximation of the self-energies. To handle all these problems, it is therefore beneficial to have a pole decomposition of the coth function with only purely imaginary poles (except from the pole at zero). Thus, recently, the Pade decomposition method has been proposed by Hu et al. [290] which shows very rapid convergence. By using this method, the hyperbolic cotangent is expressed into simple poles as [288]

$$\coth(x) \approx \frac{1}{x} + \sum_{p=1}^{N_P} \eta_p \left(\frac{1}{x - \xi_p} + \frac{1}{x - \xi_p^*} \right) , \quad (4.21)$$

where η_p are the residues and ξ_p (with $\text{Im } \xi_p > 0$) are the poles. Both quantities can be calculated by diagonalizing a matrix. Here, N_P denotes the number of expansion terms (or number of poles). Hence, the only missing and very relevant term in the self-energies is the spectral density. In the present work, two cases of this quantity have been considered: I) the wide-band limit and II) the Drude regularization.

Case I: Wide-band limit (WBL)

In the wide-band limit case, the spectral density linearly depends on the frequency. Thus,

$$\mathcal{L}_\alpha(\omega) = \omega \mathcal{L}_\alpha^{(0)}, \quad (4.22)$$

with $\mathcal{L}_\alpha^{(0)} \equiv \begin{pmatrix} \Lambda_\alpha^{(0)} & \mathbf{0} \\ \mathbf{0} & \mathbf{0} \end{pmatrix} \equiv \text{diag}(\Lambda_\alpha^{(0)}, \mathbf{0})$ as the measure of the coupling strength of the central region to the baths. Then, the spectral density is inserted into the expression for the lesser self-energy (see Eq. (4.18)),

$$\begin{aligned} \mathcal{S}_\alpha^<(t, t') &= -i \int_0^\infty \frac{d\omega}{\pi} \mathcal{L}_\alpha^{(0)} \left[\omega \coth \frac{\omega}{2k_B T_\alpha} \cos \omega(t-t') + i\omega \sin \omega(t-t') \right] \\ &= -i \int_0^\infty \frac{d\omega}{\pi} \mathcal{L}_\alpha^{(0)} \left[\omega \coth \frac{\omega}{2k_B T} \cos \omega(t-t') \right] - \frac{1}{\hbar} \mathcal{L}_\alpha^{(0)} \partial_t \delta(t-t'). \end{aligned} \quad (4.23)$$

In the following, the imaginary part will be denoted by

$$\begin{aligned} C_\alpha(t-t') &= -i \int_0^\infty \frac{d\omega}{\pi} \omega \coth \frac{\omega}{2k_B T_\alpha} \cos \omega(t-t') \\ &= -i \int_{-\infty}^\infty \frac{d\omega}{2\pi} \omega \coth \frac{\omega}{2k_B T_\alpha} e^{i\omega(t-t')}. \end{aligned} \quad (4.24)$$

Thus, the self-energies can be written as

$$\begin{aligned} \mathcal{S}_\alpha^<(t, t') &= \mathcal{L}_\alpha^{(0)} [C_\alpha(t-t') - \partial_t \delta(t-t')] , \\ \mathcal{S}_\alpha^>(t, t') &= \mathcal{L}_\alpha^{(0)} [C_\alpha(t-t') + \partial_t \delta(t-t')] . \end{aligned}$$

Using the relation between lesser/greater and retarded/advanced functions, one finds for the latter:

$$\begin{aligned} \mathcal{S}_\alpha^R(t, t') &= \Theta(t-t') \mathcal{L}_\alpha^{(0)} 2 [\partial_t \delta(t-t')] , \\ \mathcal{S}_\alpha^A(t, t') &= \Theta(t'-t) \mathcal{L}_\alpha^{(0)} 2 [-\partial_t \delta(t-t')] . \end{aligned}$$

Now, by using the Pade decomposition for the hyperbolic cotangent (see Eq. (4.21)), Eq. (4.24) becomes

$$\begin{aligned}
C_\alpha(\tau) &= -i \int_{-\infty}^{\infty} \frac{d\omega}{2\pi} \omega \coth \frac{\omega}{2k_B T_\alpha} e^{i\omega\tau} \\
&= -i \int_{-\infty}^{\infty} \frac{d\omega}{2\pi} \omega \frac{2k_B T_\alpha}{\omega} e^{i\omega\tau} - i \sum_{p=1}^{N_P} \eta_p \int_{-\infty}^{\infty} \frac{d\omega}{2\pi} \omega \left(\frac{1}{\omega/2k_B T_\alpha - \xi_p} + \frac{1}{\omega/2k_B T_\alpha - \xi_p^*} \right) e^{i\omega\tau} \\
&= -i 2k_B T_\alpha \delta(t) + \sum_{p=1}^{N_P} C_{\alpha,p}(\tau). \tag{4.25}
\end{aligned}$$

where $C_{\alpha,p}(\tau) = R_{\alpha,p} \exp(i\chi_{\alpha,p}\tau)$ with $\chi_{\alpha,p} = 2k_B T_\alpha \xi_p$ and $R_{\alpha,p} = \eta_p \xi_p (2k_B T_\alpha)^2$. The first term is essentially the high-temperature limit case. Whereas, the second term holds for $\tau > 0$ otherwise the poles in the lower half-plane have to be taken.

Consequently, the convolution of a lesser/greater Green's function and an advanced/retarded self-energy (see Eq. (4.15)) can now be evaluated. The derivations of the four terms of this convolution are reported in Appendix C. Hence, from Eq. (C.12) and, considering $\mathcal{Q}^T = -\mathcal{Q}$ and $\mathcal{L}^{(0)} = \sum_{\alpha} \mathcal{L}_{\alpha}^{(0)}$, the EOM for $\mathcal{G}^<(t, t)$ can be expressed as

$$\begin{aligned}
\frac{\partial}{\partial t} \mathcal{G}^<(t, t) &= \mathcal{K}' \cdot \mathcal{G}^<(t, t) + \mathcal{G}^<(t, t) \cdot \mathcal{K}'^T \\
&+ \mathcal{Q} \cdot \left[\sum_{\alpha} \int_{t_0}^t d\tau C_{\alpha}(t - \tau) \mathcal{L}_{\alpha}^{(0)} \cdot \mathcal{G}^A(\tau, t) \right] - \frac{1}{4} \mathcal{Q} \cdot \mathcal{L}^{(0)} \cdot \mathcal{K} \cdot \mathcal{Q}^T \\
&+ \left[\sum_{\alpha} \int_{t_0}^t d\tau \mathcal{G}^R(t, \tau) \cdot \mathcal{L}_{\alpha}^{(0)} C_{\alpha}(\tau - t) \right] \cdot \mathcal{Q}^T + \frac{1}{4} \mathcal{Q} \cdot \mathcal{K}^T \cdot \mathcal{L}^{(0)} \cdot \mathcal{Q}^T,
\end{aligned}$$

where $\mathcal{K}' = [1 + \mathcal{Q} \cdot \mathcal{L}^{(0)}] \cdot \mathcal{K}$. Finally, the phonon current matrices for the wide-band limit approach, $\Pi_{\alpha}^{WBL}(t)$, are defined as

$$\Pi_{\alpha}^{WBL}(t) = \Phi_{\alpha}(t) + \frac{1}{4} \mathcal{Q} \cdot \mathcal{K}^T \cdot \mathcal{L}_{\alpha}^{(0)}, \tag{4.26}$$

with $\Phi_{\alpha}(t) = \int_{t_0}^t d\tau \mathcal{G}^R(t, \tau) \cdot \mathcal{L}_{\alpha}^{(0)} C_{\alpha}(\tau - t)$. Here, $\Pi^{WBL}(t) = \sum_{\alpha} \Pi_{\alpha}^{WBL}(t)$. Thus, the new

EOM for the phonon density matrix $\sigma(t)$ is,¹

$$\frac{\partial}{\partial t}\sigma(t) = \mathcal{K}' \cdot \sigma(t) + \sigma(t) \cdot \mathcal{K}'^T + i \sum_{\alpha} [\Pi_{\alpha}^{WBL}(t) \cdot \mathcal{Q}^T - h.c.] \quad (4.27)$$

Here, the auxiliary-mode approach (see Eq. (4.25)) is used to calculate $\Phi_{\alpha}(t) = \sum_{p=0}^{N_P} \Phi_{\alpha}^p(t)$. The high temperature contribution is related to the pole $p = 0$ and is thus given by

$$\Phi_{\alpha}^0(t) = -i2k_B T_{\alpha} \mathcal{G}^R(t, t) \cdot \mathcal{L}_{\alpha}^{(0)} = -ik_B T_{\alpha} \mathcal{Q} \cdot \mathcal{L}_{\alpha}^{(0)}. \quad (4.28)$$

Further, the following expression is valid only for $p > 0$

$$\Phi_{\alpha}^p(t) = \int_{t_0}^t d\tau \mathcal{G}^R(t, \tau) \cdot \mathcal{L}_{\alpha}^{(0)} C_{\alpha, p}(\tau - t) \quad (4.29)$$

Then, to complete the set of ODEs in order to get the time dependence of the heat flux, the equation of motion for $\Phi_{\alpha}^p(t)$ is derived,

$$\begin{aligned} \frac{\partial}{\partial t} \Phi_{\alpha}^p(t) &= \mathcal{G}^R(t, t) \cdot \mathcal{L}_{\alpha}^{(0)} C_{\alpha, p}(0) \\ &+ \int_{t_0}^t d\tau \left[\delta(t, \tau) \mathcal{Q} + \mathcal{K}_{\text{eff}} \cdot \mathcal{G}^R(t, \tau) + \mathcal{Q} \cdot \int d\tau_2 \mathcal{S}^R(t, \tau_2) \cdot \mathcal{G}^R(\tau_2, \tau) \right] \cdot \mathcal{L}_{\alpha}^{(0)} C_{\alpha, p}(\tau - t) \\ &- i\chi_{\alpha, p} \int_{t_0}^t d\tau \mathcal{G}^R(t, \tau) \cdot \mathcal{L}_{\alpha}^{(0)} R_{\alpha, p} e^{i\chi_{\alpha, p}(\tau - t)} \\ &= \mathcal{Q} \cdot \mathcal{L}_{\alpha}^{(0)} C_{\alpha, p}(0) + \mathcal{K} \cdot \Phi_{\alpha}^p(t) - i\chi_{\alpha, p} \Phi_{\alpha}^p(t) - 2\delta(0) \mathcal{Q} \cdot \mathcal{L}^{(0)} \cdot \Phi_{\alpha}^p(t) \\ &+ \mathcal{Q} \cdot \mathcal{L}^{(0)} \cdot \int_{t_0}^t d\tau \partial_{\tau_2} \mathcal{G}^R(\tau_2, \tau)|_{\tau_2=t} \cdot \mathcal{L}_{\alpha}^{(0)} C_{\alpha, p}(\tau - t) \end{aligned} \quad (4.30)$$

Hence, by replacing the equation of motion for \mathcal{G}^R , finally²,

$$\frac{\partial}{\partial t} \Phi_{\alpha}^p(t) = \mathcal{Q} \cdot \mathcal{L}_{\alpha}^{(0)} C_{\alpha, p}(0) + \left\{ [\mathcal{I} + \mathcal{Q} \cdot \mathcal{L}^{(0)}] \cdot \mathcal{K} - i\chi_{\alpha, p} \mathcal{I} \right\} \cdot \Phi_{\alpha}^p(t). \quad (4.31)$$

This equation of motion together with the corresponding to the phonon density matrix $\sigma(t)$ (see Eq. (4.27)) are enough to compute the time dependence of the heat flux into the heat baths.

¹Defining, $\mathcal{B}^R = \int_{t_0}^t d\tau \mathcal{G}^R(t, \tau) \cdot \mathcal{L}_{\alpha}^{(0)} C_{\alpha}(\tau - t)$ and $\mathcal{B}^A = \int_{t_0}^t d\tau C_{\alpha}(t - \tau) \mathcal{L}_{\alpha}^{(0)} \cdot \mathcal{G}^A(\tau, t)$. Then:

$$\begin{aligned} (\mathcal{B}^R)^{\dagger} &= \left[\int_{t_0}^t d\tau C_{\alpha}(\tau - t) \mathcal{L}_{\alpha}^{(0)} \cdot (\mathcal{G}^R(t, \tau))^T \right]^* \\ &= \int_{t_0}^t d\tau C_{\alpha}^*(\tau - t) \mathcal{L}_{\alpha}^{(0)} \cdot [(\mathcal{G}^R(t, \tau))^T]^* \\ &= - \int_{t_0}^t d\tau C_{\alpha}(\tau - t) \mathcal{L}_{\alpha}^{(0)} \cdot \mathcal{G}^A(t, \tau) \\ &= - \mathcal{B}^A \end{aligned}$$

Therefore, $[\mathcal{B}^R \cdot \mathcal{Q}^T]^{\dagger} = -\mathcal{Q} \cdot \mathcal{B}^A$.

² Notice that the term $\propto \delta(0)$ will be canceled by the counter term.

Thus, the total heat flux can be expressed as

$$\begin{aligned} J(t) &= -\frac{1}{2} \text{Tr} \left\{ \mathcal{K}_{\text{eff}}^T \cdot \mathcal{Q} \cdot [\partial_t \sigma(t)] \right\} \\ &= -\frac{1}{2} \text{Tr} \left\{ \mathcal{K}_{\text{eff}}^T \cdot \mathcal{Q} \cdot \left[\mathcal{K}' \cdot \sigma(t) + \sigma(t) \cdot \mathcal{K}'^T + i [\Pi^{WBL}(t) \cdot \mathcal{Q}^T - h.c.] \right] \right\} . \end{aligned}$$

Then, by using the properties of the trace³, it becomes

$$\begin{aligned} J(t) &= \text{Tr} \left\{ \mathcal{K}_{\text{eff}}^T \cdot \mathcal{L}^{(0)} \cdot \mathcal{K} \cdot \sigma(t) \right\} \\ &\quad - \text{Tr} \left\{ \sum_{\alpha} \left(k_B T_{\alpha} \mathcal{L}_{\alpha}^{(0)} + \frac{i}{2} \sum_{p>1} \mathcal{K}_{\text{eff}}^T \cdot \mathcal{Q} \cdot [\Phi_{\alpha}^p \cdot \mathcal{Q}^T - h.c.] \right) \right\} . \end{aligned} \quad (4.32)$$

Case II: Drude regularization (DR)

The linear frequency dependence of the spectral density in the wide-band limit case is, of course, an idealize situation. In reality, any particular real spectral density $\mathcal{L}(\omega)$ falls off in the limit $\omega \rightarrow \infty$. Otherwise, certain physical quantities, e.g., momentum dispersion, would diverge [287]. Hence, in the simplest form, the spectral density is regularized by a frequency cut-off ω_c ,

$$\mathcal{L}(\omega) = \frac{\omega_c^2 \omega}{\omega^2 + \omega_c^2} \mathcal{L}^{(0)} , \quad (4.33)$$

which is known as the Drude regularization. Then, this is inserted into the expression for the self-energies (4.18):

$$\mathcal{S}_{\alpha}^{<}(t, t') = -i \int_0^{\infty} \frac{d\omega}{\pi} \left(\frac{\omega_c^2 \omega}{\omega^2 + \omega_c^2} \right) \mathcal{L}_{\alpha}^{(0)} \left[\coth \frac{\omega}{2k_B T_{\alpha}} \cos \omega(t-t') + i \sin \omega(t-t') \right] .$$

By using the definition of Fourier transform and $\tau = t - t'$, this equation turns into

- For $\tau > 0$,

$$\mathcal{S}_{\alpha}^{<}(t, t') = -i \int_0^{\infty} \frac{d\omega}{\pi} \left(\frac{\omega_c^2 \omega}{\omega^2 + \omega_c^2} \right) \mathcal{L}_{\alpha}^{(0)} \left[\coth \frac{\omega}{2k_B T_{\alpha}} \cos \omega\tau \right] + \frac{\omega_c^2}{2} \mathcal{L}_{\alpha}^{(0)} e^{-\omega_c \tau} .$$

- For $\tau < 0$,

$$\mathcal{S}_{\alpha}^{<}(t, t') = -i \int_0^{\infty} \frac{d\omega}{\pi} \left(\frac{\omega_c^2 \omega}{\omega^2 + \omega_c^2} \right) \mathcal{L}_{\alpha}^{(0)} \left[\coth \frac{\omega}{2k_B T_{\alpha}} \cos \omega\tau \right] - \frac{\omega_c^2}{2} \mathcal{L}_{\alpha}^{(0)} e^{\omega_c \tau} .$$

³ Considering that $\text{Tr} \left\{ \mathcal{K}_{\text{eff}}^T \cdot \mathcal{Q} \cdot [\mathcal{K} + \mathcal{K}^T] \cdot \sigma \right\} = 0$, we only have the terms of \mathcal{K}' related to $\mathcal{Q} \cdot \mathcal{L}^{(0)} \cdot \mathcal{K}$. Moreover, the trace of the second term of $\Pi^{WBL}(t)$ and its h.c. are also zero.

Thus, the imaginary part will be denoted by

$$\begin{aligned} C_\alpha(\tau) &= -i \int_0^\infty \frac{d\omega}{\pi} \left(\frac{\omega_c^2 \omega}{\omega^2 + \omega_c^2} \right) \coth \frac{\omega}{2k_B T_\alpha} \cos \omega \tau \\ &= -i \int_{-\infty}^\infty \frac{d\omega}{2\pi} \left(\frac{\omega_c^2 \omega}{\omega^2 + \omega_c^2} \right) \coth \frac{\omega}{2k_B T_\alpha} e^{i\omega \tau}. \end{aligned} \quad (4.34)$$

Consequently, the lesser and greater self-energies for $\tau > 0$ become

$$\mathcal{S}_\alpha^<(t, t') = \mathcal{L}_\alpha^{(0)} \left[C_\alpha(\tau) + \frac{\omega_c^2}{2} e^{-\omega_c |\tau|} \right], \quad (4.35)$$

$$\mathcal{S}_\alpha^>(t, t') = \mathcal{L}_\alpha^{(0)} \left[C_\alpha(\tau) - \frac{\omega_c^2}{2} e^{-\omega_c |\tau|} \right]. \quad (4.36)$$

For $\tau < 0$, the corresponding self-energies also display similar expressions (take in account the difference of signs shown above). As it was mentioned before, the goal of the auxiliary-mode approach is to expand the self-energies and, hence, $C_\alpha(\tau)$ in terms of exponentials. To this end, the Pade decomposition of the hyperbolic cotangent into simple poles is used one more time (see Eq. (4.21)). This expansion can now be used in Eq. (4.34) as follows

$$\begin{aligned} C_\alpha(\tau) &= -i \int_{-\infty}^\infty \frac{d\omega}{2\pi} \left(\frac{\omega_c^2 \omega}{\omega^2 + \omega_c^2} \right) \coth \frac{\omega}{2k_B T_\alpha} e^{i\omega \tau} \\ &= -i \int_{-\infty}^\infty \frac{d\omega}{2\pi} \left(\frac{\omega_c^2 \omega}{\omega^2 + \omega_c^2} \right) \frac{2k_B T_\alpha}{\omega} e^{i\omega \tau} \\ &\quad - i \sum_{p=1}^L \eta_p \int_{-\infty}^\infty \frac{d\omega}{2\pi} \left(\frac{\omega_c^2 \omega}{\omega^2 + \omega_c^2} \right) \left(\frac{1}{\omega/2k_B T_\alpha - \xi_p} + \frac{1}{\omega/2k_B T_\alpha - \xi_p^*} \right) e^{i\omega \tau}. \end{aligned}$$

Here, by performing Fourier transforms of the individual terms, the following expression is obtained for $\tau > 0$,

$$C_\alpha(\tau) = -ik_B T_\alpha \omega_c e^{-\omega_c \tau} - i \sum_{p=1}^{N_P} R_{\alpha,p} (\omega_c e^{-\omega_c \tau} - \chi_{\alpha,p} e^{-\chi_{\alpha,p} \tau}),$$

with $R_{\alpha,p} = \frac{2k_B T_\alpha \omega_c^2}{\omega_c^2 - \chi_{\alpha,p}^2} \eta_p$ and $\chi_{\alpha,p} = -i2k_B T_\alpha \xi_p$. In the next step, $\mathcal{S}^{<,>}(t, t') = \frac{\partial}{\partial t} \mathcal{N}^{<,>}(t, t')$

has been set, where $\mathcal{N}^{<,>}(t, t')$ matrices are defined as

$$\mathcal{N}_\alpha^{<,>}(t, t') = \sum_{p=0}^{N_P} a_{\alpha,p}^{<,>} e^{-b_{\alpha,p}(t-t')} \mathcal{L}_\alpha^{(0)} = \sum_{p=0}^{N_P} \mathcal{N}_{\alpha,p}(t, t'), \quad (4.37)$$

with

$$\begin{aligned} a_{\alpha,0}^{<,>} &= \mp \frac{\omega_c}{2} + i \left(k_B T_\alpha + \sum_{p=1}^{N_P} R_{\alpha,p} \right), & b_{\alpha,0} &= \omega_c, \\ a_{\alpha,p \geq 1}^{<,>} &= -i R_{\alpha,p}, & b_{\alpha,p \geq 1} &= \chi_{\alpha,p}. \end{aligned}$$

For $\tau = t - t' < 0$, the coefficients are expressed as $a_{\alpha,p}^{*,<,>}$ and $b_{\alpha,p \geq 1}^*$ (see Appendix C). Therefore, unlike the wide-band limit case, the convolution of a lesser/greater Green's function and a lesser/greater self-energy (see Eq. (4.16)) can be evaluated with these findings. Thus, the first term of the convolution to analyze is

$$\begin{aligned} \int_{t_0}^t dt' (\mathcal{G}^>(t, t') \mathcal{S}^<(t', t) - \mathcal{G}^<(t, t') \mathcal{S}^>(t', t)) = \\ [\mathcal{G}^>(t, t') \cdot \mathcal{N}^<(t', t)]_{t'=t_0}^{t'=t} - [\mathcal{G}^<(t, t') \cdot \mathcal{N}^>(t', t)]_{t'=t_0}^{t'=t} \\ + \int_{t_0}^t dt' (\mathcal{G}^<(t, t') \cdot \mathcal{K}_{\text{eff}}^T \cdot \mathcal{N}^>(t', t) - \mathcal{G}^>(t, t') \cdot \mathcal{K}_{\text{eff}}^T \cdot \mathcal{N}^<(t', t)) . \end{aligned} \quad (4.38)$$

By considering $\mathcal{G}^>(t, t) - \mathcal{G}^<(t, t) = \mathcal{Q}$ and defining the phonon current matrices $\Pi_{\alpha}^{DR}(t)$ as

$$\Pi_{\alpha}^{DR}(t) = \sum_{p=0}^{N_P} \left[\Phi_{\alpha}^p(t) + a_{\alpha,p}^{*,<} \mathcal{Q} \cdot \mathcal{L}_{\alpha}^{(0)} \right] , \quad (4.39)$$

with

$$\Phi_{\alpha}^p(t) = \int_{t_0}^t dt' (\mathcal{G}^<(t, t') \cdot \mathcal{K}_{\text{eff}}^T \cdot \mathcal{N}_{\alpha,p}^>(t', t) - \mathcal{G}^>(t, t') \cdot \mathcal{K}_{\text{eff}}^T \cdot \mathcal{N}_{\alpha,p}^<(t', t)) ,$$

the two boundary terms in Eq. (4.38) are canceled with the counter-term \mathbf{K}_{ct} from Eq. (4.20).

Here, $\Pi^{DR}(t) = \sum_{\alpha} \Pi_{\alpha}^{DR}(t)$. Then, the equation of motion for $\Phi_{\alpha}^p(t)$ is

$$\frac{\partial}{\partial t} \Phi_{\alpha}^p(t) = \mathcal{A}_{\alpha}^p \cdot \Phi_{\alpha}^p(t, t) - \mathcal{B}_{\alpha}^p \cdot \mathcal{K}_{\text{eff}}^T \cdot \mathcal{L}_{\alpha}^{(0)} + \mathcal{Q} \cdot \Omega_{\alpha}^p(t) , \quad (4.40)$$

with $\mathcal{A}_{\alpha}^p = \mathcal{K} - b_{\alpha,p}^* \mathcal{I}$, $\mathcal{B}_{\alpha}^p = i\omega_c \delta_{p,0} \sigma(t) + a_{\alpha,p}^{*,<} \mathcal{Q}$. The functions $\Omega_{\alpha}^p(t) = \sum_{\alpha'} \sum_{p'=0}^{N_P} \Omega_{\alpha'\alpha}^{p'p}(t)$ correlate the main features of both heat baths and their values are obtained by performing the time derivative of $\Omega_{\alpha'\alpha}^{p'p}(t)$,

$$\begin{aligned} \Omega_{\alpha'\alpha}^{p'p}(t) = & + \int_{t_0}^t dt' \int_{t_0}^{t'} dt'' \mathcal{N}_{\alpha',p'}^>(t, t'') \cdot \mathcal{K}_{\text{eff}} \cdot [\mathcal{G}^<(t'', t') - \mathcal{G}^>(t'', t')] \cdot \mathcal{K}_{\text{eff}}^T \cdot \mathcal{N}_{\alpha,p}^<(t', t) \\ & + \int_{t_0}^t dt' \int_{t_0}^{t'} dt'' [\mathcal{N}_{\alpha',p'}^>(t, t'') - \mathcal{N}_{\alpha',p'}^<(t, t'')] \cdot \mathcal{K}_{\text{eff}} \cdot \mathcal{G}^>(t'', t') \cdot \mathcal{K}_{\text{eff}}^T \cdot \mathcal{N}_{\alpha,p}^<(t', t) \\ & - \int_{t_0}^t dt' \int_{t_0}^{t'} dt'' \mathcal{N}_{\alpha',p'}^<(t, t'') \cdot \mathcal{K}_{\text{eff}} \cdot [\mathcal{G}^<(t'', t') - \mathcal{G}^>(t'', t')] \cdot \mathcal{K}_{\text{eff}}^T \cdot \mathcal{N}_{\alpha,p}^>(t', t) \\ & - \int_{t_0}^t dt' \int_{t_0}^{t'} dt'' [\mathcal{N}_{\alpha',p'}^>(t, t'') - \mathcal{N}_{\alpha',p'}^<(t, t'')] \cdot \mathcal{K}_{\text{eff}} \cdot \mathcal{G}^<(t'', t') \cdot \mathcal{K}_{\text{eff}}^T \cdot \mathcal{N}_{\alpha,p}^>(t', t) \\ & - \int_{t_0}^t dt' \mathcal{N}_{\alpha',p'}^>(t, t') \cdot \mathcal{Q} \cdot \mathcal{K}_{\text{eff}}^T \cdot \mathcal{N}_{\alpha,p}^<(t', t) + \int_{t_0}^t dt' \mathcal{N}_{\alpha',p'}^<(t, t') \cdot \mathcal{Q} \cdot \mathcal{K}_{\text{eff}}^T \cdot \mathcal{N}_{\alpha,p}^>(t', t) . \end{aligned}$$

Then, calculating the time derivative of $\Omega_{\alpha'\alpha}^{p'p}(t)$,

$$\begin{aligned} \frac{\partial}{\partial t} \Omega_{\alpha'\alpha}^{p'p}(t) &= C_{\alpha'\alpha}^{p'p} \mathcal{L}_{\alpha'}^{(0)} \cdot \mathcal{Q} \cdot \mathcal{K}_{\text{eff}}^T \cdot \mathcal{L}_{\alpha}^{(0)} - D_{\alpha'\alpha}^{p'p} \Omega_{\alpha'\alpha}^{p'p}(t) \\ &\quad - \omega_c \left(\delta_{p',0} \mathcal{L}_{\alpha'}^{(0)} \cdot \mathcal{K}_{\text{eff}} \cdot \Phi_{\alpha}^p(t) - \delta_{p,0} \Phi_{\alpha'}^{p';\dagger}(t) \cdot \mathcal{K}_{\text{eff}}^T \cdot \mathcal{L}_{\alpha}^{(0)} \right), \end{aligned} \quad (4.41)$$

where $C_{\alpha'\alpha}^{p'p} = a_{\alpha',p'}^{<} a_{\alpha,p}^{*;>} - a_{\alpha',p'}^{>} a_{\alpha,p}^{*;<}$ and $D_{\alpha'\alpha}^{p'p} = b_{\alpha',p'} + b_{\alpha,p}^*$ are real numbers. In short, the original integro-differential equation for the reduced density matrix is mapped onto a closed set of ordinary differential equations (Eqs. (4.20), (4.40), and (4.41)), which are solved in this study by a fourth-order Runge-Kutta method with a timestep of 0.1 fs.

Finally, the thermal current into the heat baths is given by

$$\begin{aligned} J(t) &= -\frac{1}{2} \text{Tr} \{ \mathcal{K}_{\text{eff}}^T \cdot \mathcal{Q} \cdot [\partial_t \sigma(t)] \} \\ &= -\frac{1}{2} \text{Tr} \{ \mathcal{K}_{\text{eff}}^T \cdot \mathcal{Q} \cdot [\mathcal{K} \cdot \sigma(t) + \sigma(t) \cdot \mathcal{K}^T + i [\Pi^{DR}(t) \cdot \mathcal{Q}^T - h.c.]] \}. \end{aligned}$$

Then,⁴

$$J(t) = -\frac{i}{2} \text{Tr} \left\{ \mathcal{K}_{\text{eff}}^T \cdot \mathcal{Q} \cdot \sum_{\alpha} [\Pi_{\alpha}^{DR}(t) \cdot \mathcal{Q}^T - h.c.] \right\}. \quad (4.42)$$

4.2 TIME-DEPENDENT THERMAL CURRENT IN NANOSYSTEMS

4.2.1 One-dimensional atomic chain

To illustrate the novel method presented in this chapter, an one-dimensional (1D) linear chain consisting of N atoms coupled by force constants with magnitude $\lambda = 1.0 \text{ eV}/\mu\text{\AA}$ is considered (see Fig. 4.2(a) for the case of $N = 4$ atoms). The mass of the atoms is set to be 1.0μ and only interactions among first neighbors are considered. Hence, the force constant and the coupling matrices will be given by

$$\mathbf{K} \equiv \begin{pmatrix} 2\lambda & -\lambda & \cdots & 0 \\ -\lambda & 2\lambda & \cdots & \vdots \\ \vdots & \vdots & \ddots & -\lambda \\ 0 & \cdots & -\lambda & 2\lambda \end{pmatrix}, \quad \mathbf{\Lambda}_{\mathbf{L}}^{(0)} \equiv \begin{pmatrix} 0 & 0 & \cdots & 0 \\ 0 & 0 & \cdots & \vdots \\ \vdots & \vdots & \ddots & 0 \\ 0 & \cdots & 0 & \eta \end{pmatrix}, \quad \mathbf{\Lambda}_{\mathbf{R}}^{(0)} \equiv \begin{pmatrix} \eta & 0 & \cdots & 0 \\ 0 & 0 & \cdots & \vdots \\ \vdots & \vdots & \ddots & 0 \\ 0 & \cdots & 0 & 0 \end{pmatrix},$$

Before starting the analysis of the thermal transport properties at the transient state, a benchmark of the influence of the spectral density parameters on the steady states properties is performed.

⁴ Considering that $\text{Tr} \{ \mathcal{K}_{\text{eff}}^T \cdot \mathcal{Q} \cdot [\mathcal{K} + \mathcal{K}^T] \cdot \sigma(t) \} = 0$, the only remaining terms are these one related to the phonon current matrices $\Pi_{\alpha}^{DR}(t)$.

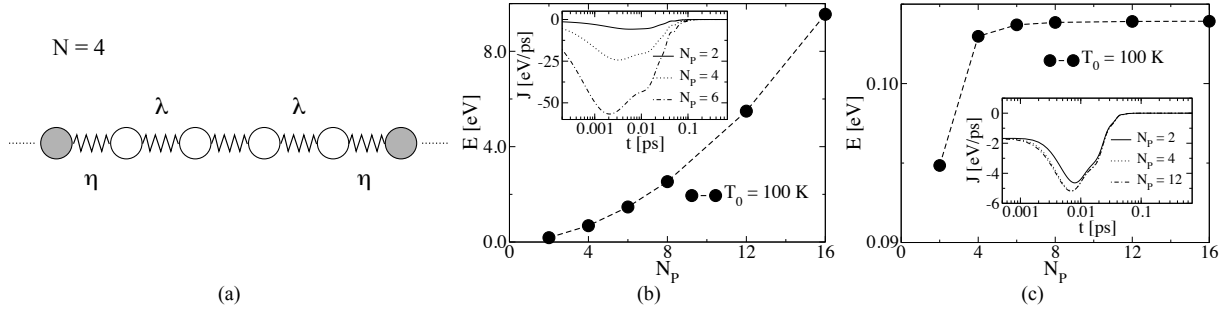


Figure 4.2: (a) Scheme of the one-dimensional atomic chain with $N = 4$ atoms. The filled atoms represent the beginning of the heat baths. λ and η are the spring force constant between the atoms and the coupling of the central region to the baths. Variation of the total energy of a dimer at $T_0 = 100$ K with the number of poles N_P in the auxiliary-mode approach by using the spectral density in the (b) wide-band limit and (c) Drude regularization case. Insets: Time dependence of the heat flux.

Benchmarking of spectral density parameters

In the first place, the results obtained by using the spectral density $\mathcal{L}^{(0)}$ for the wide-band limit and Drude regularization cases are discussed. Following the nonequilibrium molecular dynamics (NEMD) method described in Fig. 2.1, thermal equilibration of the 1D atomic chain is first carried out. Figs. 4.2(b,c) show the system energy values at the steady state of a diatomic chain ($N = 2$) at $T_0 = 100$ K as a function of the number of poles N_P employed in the auxiliary-mode expansion. One can clearly see that, despite the total heat flux goes to zero after equilibration (see inset of Fig. 4.2(b)), the system energy has a problem of convergence after increasing N_P for the wide-band limit case. This is due to that more frequencies are considered in the integral of the self-energies by considering a larger N_P and, hence, $S(\omega)$ will continuously increase without any limit. Similar effect has been also reported in other related works [61, 63]. In this sense, it is very relevant the inclusion of a high-frequency cut-off ω_c like given by the Drude regularization. ω_c is determined by the features of the system and by considering that $S(\omega)$ will drop to zero after this value. As a result, the heat flux and the system energy of the dimer converge for a finite number of poles, as it is shown in Fig. 4.2(c). Therefore, from now on, all the results will be calculated by only using the Drude spectral density.

In Figs. 4.3(b,c), it is displayed the dependence of the system energy at 300 K on the number of atoms in the chain. This is done for different cut-off frequency ω_c and η parameter. These energy values are compared to those obtained for an ideal harmonic oscillator in thermal equilibrium, $E_C = \sum_{i=1}^N \hbar\omega_i (n(\omega_i) + 1/2)$, where $n(\omega)$ is the Bose-Einstein distribution function and ω_i are the frequencies of the isolated central system. Thus, it was found, for $\eta = \lambda$ fixed, that by increasing ω_c the system energy also increase due to that the spectral density consider more vibrational states in the calculations. On the contrary, the energy values get closer to those corresponding to the ideal harmonic oscillator after reducing the coupling strength measured by η parameter for a given $\omega_c = 400$ THz. This is quite expected because of in the weak coupling

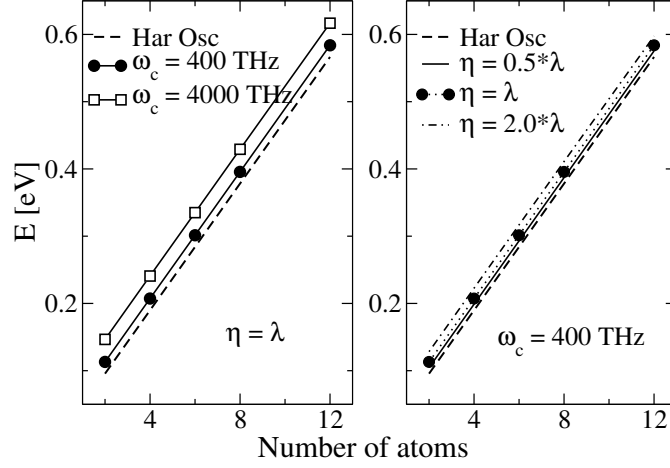


Figure 4.3: Variation of the total energy of a dimer at $T_0 = 300$ K as a function of the number of atoms in the 1D atomic chain for different cut-off frequency (left panel) and η parameter (right panel). For comparison, the corresponding values to the ideal harmonic oscillator case are also shown (dashed lines).

limit, $\eta \rightarrow 0$, the atomic chain can be considered as an isolated harmonic system with not thermal bath injecting heat, hence, $E_{1D\text{chain}} = E_C$.

This effect of the spectral density parameters on the system energy is also observed in the phonon transmission function $\tau_{ph}(\omega)$. This is calculated by using the method explained in Chapter 3. Here, the matrix notation has to return to the $N \times N$ dimension because only the GF terms related to the atomic displacements are considered (momentum operator terms are not involved). Thus, the spectral density $\Lambda(\omega) = (\omega_c^2 \omega) / (\omega^2 + \omega_c^2) \Lambda^{(0)}$ is inserted into the expression for the self-energies producing

$$\begin{aligned} \Sigma_{\alpha}^{\lessgtr}(t, t') &= -i \int_0^{\infty} \frac{d\omega}{\pi} \left(\frac{\omega_c^2 \omega}{\omega^2 + \omega_c^2} \right) \Lambda_{\alpha}^{(0)} \left[\coth \frac{\omega}{2k_B T_{\alpha}} \cos \omega(t - t') \pm i \sin \omega(t - t') \right] \\ &= -i \int_{-\infty}^{\infty} \frac{d\omega}{2\pi} \left(\frac{\omega_c^2 \omega}{\omega^2 + \omega_c^2} \right) \Lambda_{\alpha}^{(0)} \left[\coth \frac{\omega}{2k_B T_{\alpha}} \pm 1 \right] e^{i\omega(t-t')}. \end{aligned} \quad (4.43)$$

Consequently, the retarded self-energy in time domain can be expressed as

$$\Sigma_{\alpha}^r(t, t') = \Theta(t - t') 2i \Lambda_{\alpha}^{(0)} \int_{-\infty}^{\infty} \frac{d\omega}{2\pi} \left(\frac{\omega_c^2 \omega}{\omega^2 + \omega_c^2} \right) e^{i\omega(t-t')}. \quad (4.44)$$

Next, by using the definition of the Fourier transform, the retarded and advanced self-energies become

$$\begin{aligned} \Sigma_{\alpha}^r(\omega) &= \left[-\frac{\omega_c^3}{\omega^2 + \omega_c^2} + i \frac{\omega_c^2 \omega}{\omega^2 + \omega_c^2} \right] \Lambda_{\alpha}^{(0)}, \\ \Sigma_{\alpha}^a(\omega) &= \left[-\frac{\omega_c^3}{\omega^2 + \omega_c^2} - i \frac{\omega_c^2 \omega}{\omega^2 + \omega_c^2} \right] \Lambda_{\alpha}^{(0)}. \end{aligned}$$

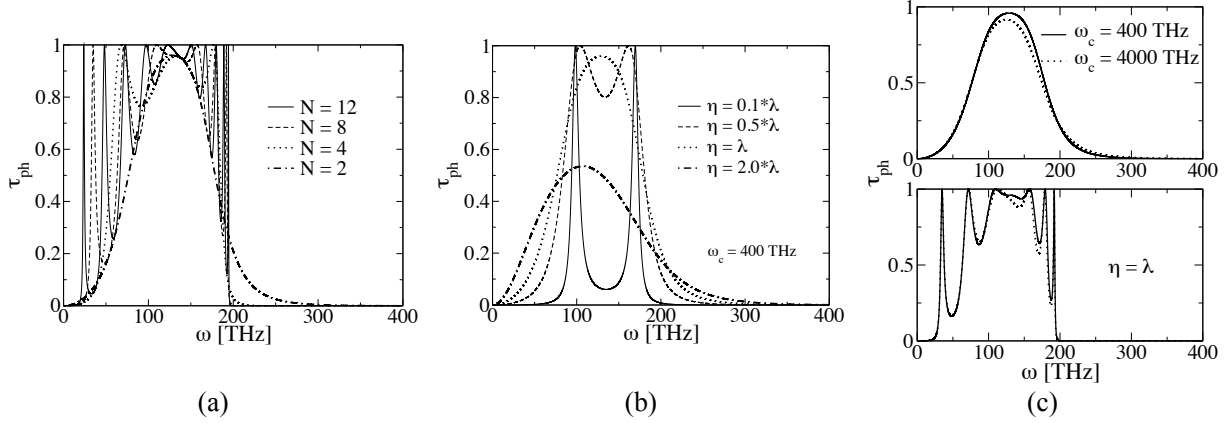


Figure 4.4: (a) Phonon transmission function τ_{ph} for an 1D atomic chain with different number of atoms. (b,c) Influence of the Drude spectral density parameters on the phonon transmission function of a dimer.

The real part for both expressions will be canceled by the counter-term and, hence,

$$\Sigma_{\alpha}^r(\omega) = \left[i \frac{\omega_c^2 \omega}{\omega^2 + \omega_c^2} \right] \Lambda_{\alpha}^{(0)} = [\Sigma_{\alpha}^a(\omega)]^{\dagger}. \quad (4.45)$$

Finally, the retarded Green-function reads

$$G^r(\omega) = [\omega^2 \mathbf{I} - \mathbf{K} - \Sigma_L^r(\omega) - \Sigma_R^r(\omega)]^{-1} \quad (4.46)$$

with \mathbf{K} as the force constant matrix of the 1D atomic chain. Then, the transmission function $\tau_{ph}(\omega)$ is calculated employing Eq. (3.33). Moreover, the heat flux value at the steady state is computed through the Landauer approach (see Eq. (3.32)).

Fig. 4.4(a) shows the phonon transmission function for different number of atoms in the 1D atomic chain at a cut-off frequency of 400 THz. Here, one can see the presence of new transmission peaks after increasing N , which is due to the rise of new vibrational modes. Also, the maximum frequency ω_{max} of the transmission function depends on N . Thus, for $N > 8$, ω_{max} is invariant and equal to ~ 195 THz. In the limit $N \rightarrow \infty$, τ_{ph} is a continuous constant function and drops to zero after ω_{max} , i.e., all vibrational modes present the same transmission probability, $\tau_{ph} = 1.0$, which is in agreement to this reported by Zhang et al. [33]. In Fig. 4.4(b), the influence of the coupling strength η for a dimer is shown, $\omega_c = 400$ THz is fixed. This parameter has been related to the magnitude of the force constant between two atoms λ . In fact, the magnitude of η has a strong influence on the phonon transmission function, affecting the resolution of the transmission probability per each vibrational modes. Thus, for $\eta \geq \lambda$, τ_{ph} looks like a Gaussian-type function and loses the description of the main system features. Whereas, for $\eta \leq 0.8\lambda$, the two main transmission peaks corresponding to the two vibrational modes of the dimer can finally be distinguished. For weaker couplings, τ_{ph} will result in two well-defined delta functions located at these frequencies, correctly describing the vibrations of the dimer. In short, this effect verifies the previous analysis done respect to the system energy (see Fig. 4.3). The

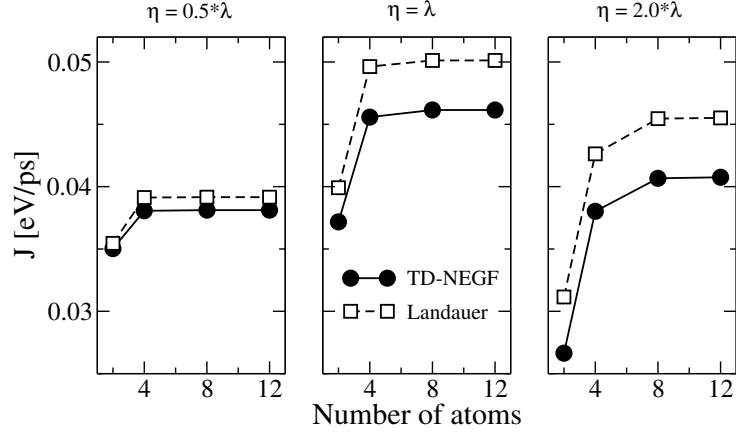


Figure 4.5: Variation of the heat flux in the steady state as a function of the number of atoms in the 1D atomic chain for different η values. For comparison, the values obtained by using Landauer approach are also shown. To perform these calculations, 8 poles in the self-energy expansion and a cut-off frequency of 400 THz have been considered.

influence of the cut-off frequency on τ_{ph} is weak comparing to this one of η parameter. Thus, by increasing ten times ω_c the phonon transmission is slightly reduced at high frequencies and the frequency spectrum gets wider (see fig. 4.4(c)).

Now, the steady-state heat flux values are calculated by using both the TD-NEGF method developed in the present work and the Landauer approach. Based on the latter, the temperature of the heat baths is only considered on their corresponding Bose-Einstein distribution function (see Eq. (3.32)). On the other side, in the case of the TD-NEGF, both temperatures are inserted in the expansion of the self-energies and, hence, in the ordinary differential equations. Thus, once the system has reached the thermal equilibrium, a symmetric temperature bias $\Delta T = T_L - T_R = 2\xi T_0$ ($\xi > 0$) is applied, with T_0 corresponding to the mean temperature at which the system was previously equilibrated. The temperatures for the left and right baths can be written as $T_L = (1 + \xi)T_0$ and $T_R = (1 - \xi)T_0$, respectively. Consequently, the thermal transport properties of the system evolves on time until this reaches the steady state for a nonequilibrium situation. Fig. 4.5 shows the heat flux values at the steady state as a function of the number of atoms for different η parameter ($\omega_c = 400$ THz is fixed). These values are calculated by considering a mean temperature of $T_0 = 300$ K and $\xi = 0.1$. Here, it can be seen that the values corresponding to both methods get closer after reducing the coupling strength, which is in agreement with the effects found for the system energy and τ_{ph} (see Figs. 4.3 and 4.4(b), respectively). Moreover, the heat flux converges at a given N for all η values. It is worth mentioning that the convergence time of the heat flux and total energy increases with the reduction of the coupling strength.

Additionally, the influence of the cut-off frequency ω_c on the steady state heat flux values of the dimer is examined for a given $\eta = \lambda$ parameter. In Fig. 4.6, one can see that heat flux increases and decrease after increasing ω_c for the TD-NEGF method and the Landauer approach, respectively. Also, the intensity of this effect can be controlled by the magnitude of the temperature bias ΔT . However, independently of ΔT , the heat flux values for both methods

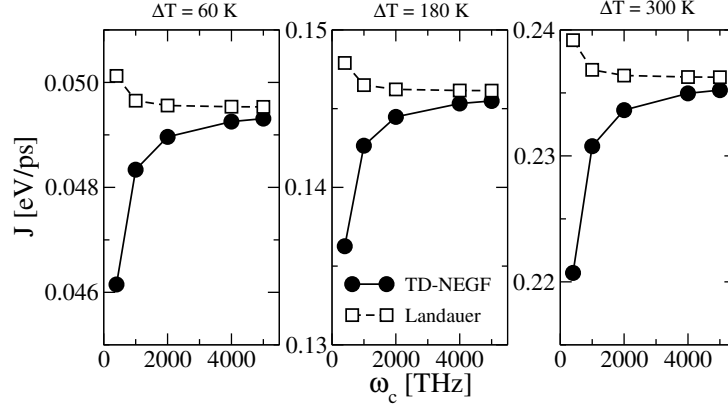


Figure 4.6: Cut-off frequency dependence of the steady state heat flux for the dimer at different temperatures bias. For comparison, the values obtained by using Landauer approach are also shown. To perform these calculations, 8 poles in the self-energy expansion and $\eta = \lambda$ have been considered.

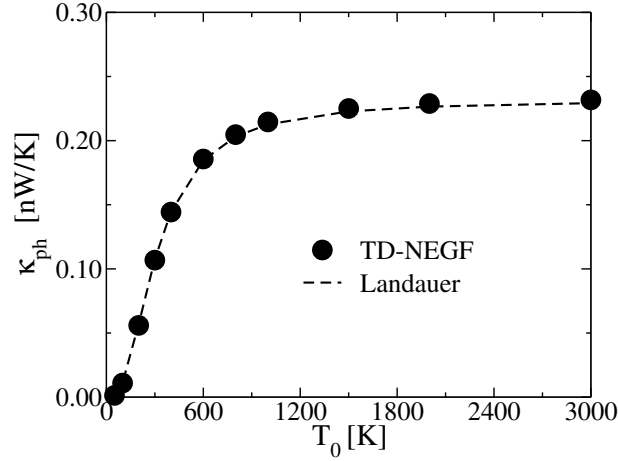


Figure 4.7: Thermal conductance as a function of the mean temperature for an 1D atomic chain with 8 atoms. The results obtained by using the time-dependent NEGF method (developed in the present work) and the Landauer approach are compared. To perform these calculations, $\xi = 0.1$, $\eta = 0.5 * \lambda$, and $\omega_c = 1000$ THz have been considered. The number of poles vary depending on the mean temperature value.

get closer after increasing ω_c . Hence, after analyzing the effects caused by the parameters of the Drude spectral density, $\eta = 0.5\lambda$ and $\omega_c = 1000$ THz are selected for both heat baths to perform a deeper study of the time dependence of the phonon transport properties. To verify the accuracy of these values to describe the transport properties, the thermal conductance $\kappa_{ph} = J/\Delta T$ at the steady state of an atomic chain with $N = 8$ is computed by using both methods. This is computed by remaining close to the linear response regime, i.e., small ΔT ($\xi = 0.1$) [291]. Fig. 4.7 shows the good agreement of the results calculated by employing the Landauer approach and the TD-NEGF method developed in the present thesis. Notice that the number of poles N_P used in the auxiliary-mode expansion depends on the mean temperature value.

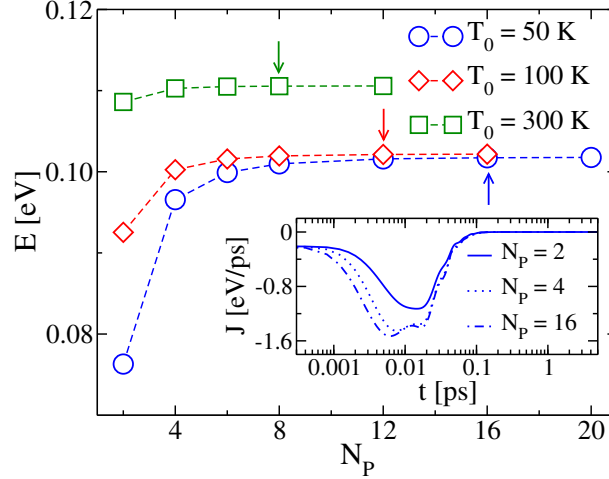


Figure 4.8: Energy of a diatomic chain vs number of poles N_P of the auxiliary-mode approach at different temperatures. The arrows indicates the convergence point for each temperature. Inset: Dynamics of the heat current for the diatomic chain at $T_0 = 50$ K.

Analysis of the thermal transport properties

Proceeding with the study, the time evolution of the thermal transport properties are analyzed in this section. Fig. 4.8 shows the total energy after thermal equilibration as a function of the number of poles used in the auxiliary mode expansion for the case of a dimer ($N = 2$). Although the heat flux tends to zero for each N_P (see the inset in Fig. 4.8), the energy in the steady state still grows as N_P increases. It converges for a given N_P value depending on the temperature, e.g., 16 and 8 poles are needed to reach convergence at 50 K and 300 K, respectively. This is related to the fact that only few poles are enough to describe high temperature effects in the auxiliary-mode approach [288]. The final energy values are close to those obtained for an ideal harmonic oscillator in thermal equilibrium, $E_C = \sum_{i=1}^N \hbar\omega_i (n(\omega_i) + 1/2)$ (see previous section). Thus, we expect to find $E_C = 8.83 \times 10^{-2}$ eV and $E_C = 9.56 \times 10^{-2}$ eV at 50 K and 300 K, respectively. The discrepancies observed in Fig. 4.8 relate to the coupling to the baths, i.e., they vanish in the weak coupling limit $\eta \rightarrow 0$, as previously discussed.

To gain further insight, an eigenvalue decomposition of the quantity $\mathcal{Z}(t) = (\hbar/2)\mathcal{K}_{\text{eff}}^T \cdot \mathcal{Q} \cdot \sigma(t)$ is performed. This matrix is related to the total energy of the central region after tracing out the bath degrees of freedom. To this end, the eigenvalue problem for the $N \times N$ matrix resulting from adding the diagonal blocks of $\mathcal{Z}(t)$ is solved. In Fig. 4.9(a), one can see the time evolution of the two eigenvalues for the diatomic chain at $T_0 = 300$ K. Both eigenvalues increase as a function of time and reach their time-independent limit once the system reaches equilibrium. Moreover, by analyzing the corresponding eigenvectors, one finds that the lower mode (E_1) corresponds to the case when the atoms vibrate with the same amplitude and in-phase (acoustic-like mode). This mode corresponds to the zero frequency translational mode of the isolated dimer; since translational symmetry is now broken due to the coupling to the baths, the mode acquires a

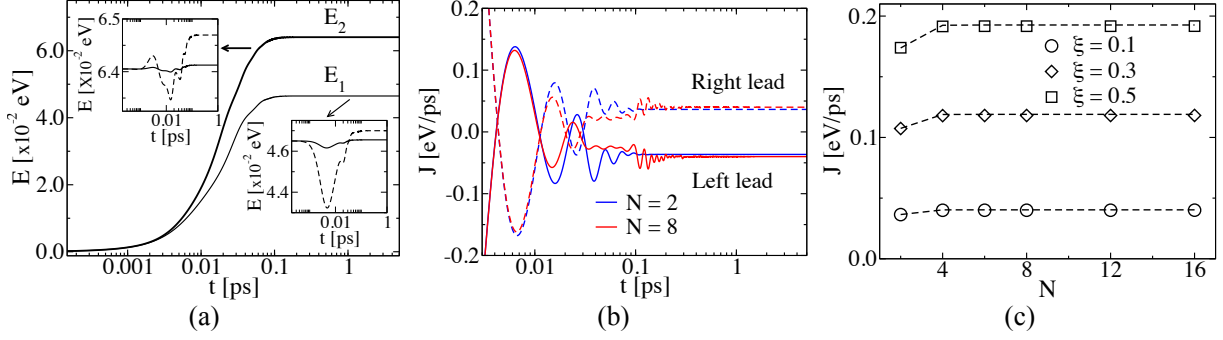


Figure 4.9: (a) Time evolution of the eigenvalues E_i for a diatomic chain at $T_0 = 300$ K. Inset: Their corresponding transient states after applying symmetric temperature bias around T_0 ($T_L = (1 + \xi)T_0$ and $T_R = (1 - \xi)T_0$), $\xi = 0.1$ ($\Delta T = 60$ K, solid lines) and $\xi = 0.3$ (180 K, dashed lines). (b) Dynamics of the heat flux from the left and right leads for atomic chains with 2 and 8 atoms with $\beta = 0.1$. (c) Variation of the steady heat flux after increasing the number of atoms in the atomic chain for different ξ . The mean temperature is 300 K. The dashed lines represent the values obtained by using Landauer approach.

finite frequency. The other mode (E_2) corresponds to the stretching mode of the dimer, where the atoms vibrate out of phase.

Consequently, in the insets of Fig. 4.9(a), the time evolution of the eigenvalues associated to the acoustic and optical modes of the diatomic chain are shown for two different values of the temperature bias, $\Delta T = 60$ K and 180 K. As ΔT increases, the fluctuations during the transient get larger because the central region exchanges a larger amount of energy with the heat baths in order to stabilize the entire system. As a function of time, the energy E_1 first decreases and then increases until reaching convergence, while the optical mode E_2 is stronger affected during the transient, and it displays larger fluctuations than E_1 . The time evolution of the heat current in both leads for linear chains containing two and eight sites is presented in Fig. 4.9(b). In both cases, the transients show similar features: the heat flux grows, oscillates and then saturates. One can also see that the time for reaching the steady state is longer for larger systems. The heat flux in the steady state for several chain sizes at 300 K and for different values of the temperature bias is shown in Fig. 4.9(c). Independently of the temperature bias, the heat flux increases with the number of sites, but it converges for $N > 8$. The flux values in the steady state are in agreement to those calculated by using the standard Landauer approach (see dashed lines in Fig. 4.9(c)).

4.2.2 Carbon-based molecular junctions

In the next step, it will be demonstrated that the TD-NEGF method developed in the present thesis can be efficiently combined with atomistic methods to address phonon dynamics in realistic nanoscale systems. Unlike the 1D atomic chain model, real nanomaterials display three different degree of freedom (x, y, and z direction) which means that the dimension of the

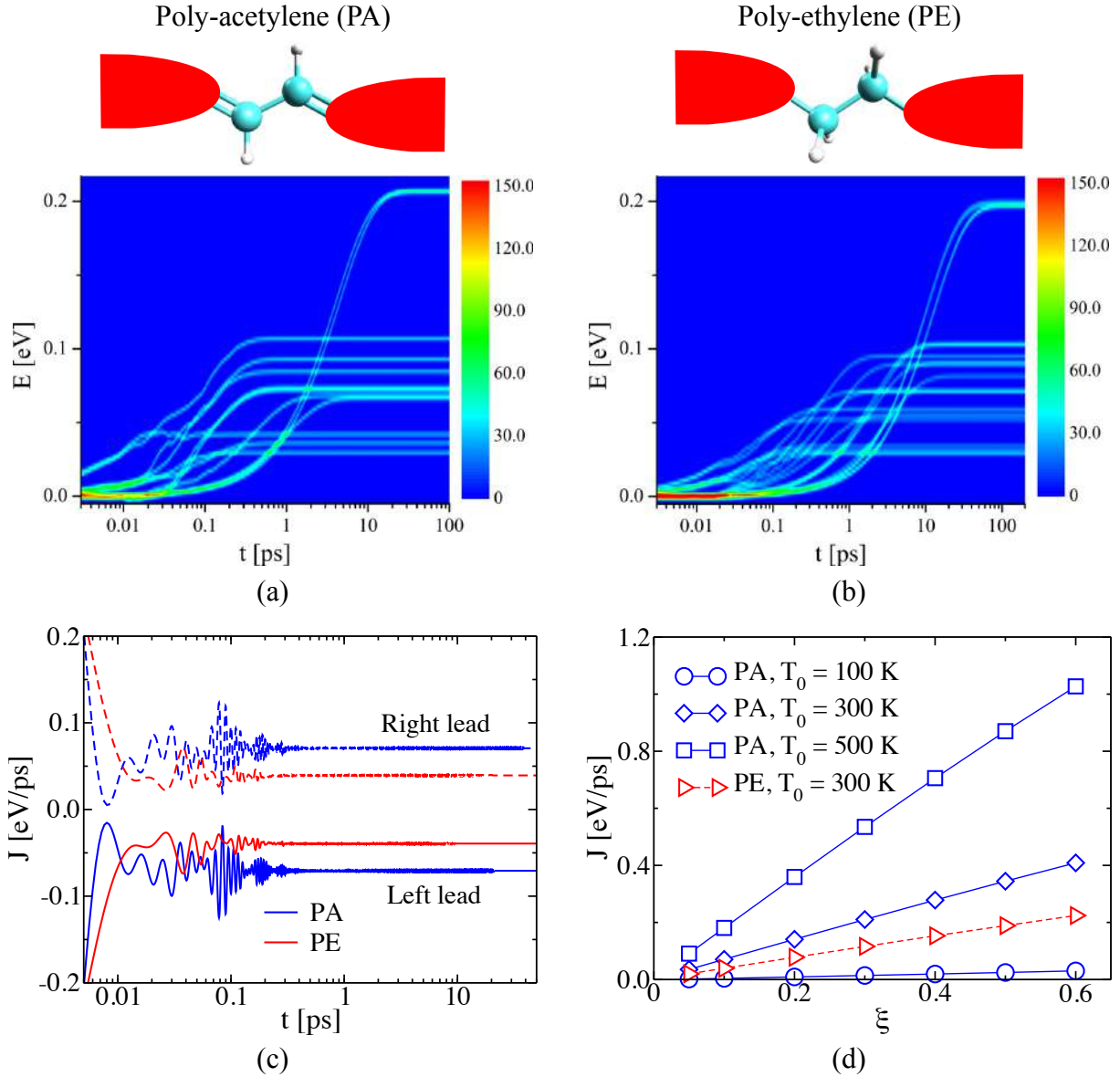


Figure 4.10: Energy density plot for molecular junctions made of (a) poly-acetylene (PA) and (b) poly-ethylene (PE) dimers. (c) Dynamics of the heat flux for both leads for PA and PE dimers after applying a temperature bias of $\Delta T = 60$ K at $T_0 = 300$ K. (d) Variation of the steady-state heat flux as a function of ξ for the PA dimer at different T_0 . The results for the corresponding PE dimer at $T_0 = 300$ K are also shown (dashed lines).

matrices will increase by a factor of three and, hence, the computational cost. As paradigmatic examples, this part of the study is focused on poly-acetylene (PA, 4 atoms) and poly-ethylene (PE, 6 atoms) dimers connected to two harmonic baths, as shown in Fig. 4.10(a,b). The main difference between them is the presence of double carbon bonds in the PA junction, while the PE junction only contains single carbon bonds. Structural optimizations are performed by using density functional theory as implemented in the Gaussian09 code [292]. For this purpose, B3LYP functionals are used together with the 6-31G basis set. Then, a finite difference method has been used to get the corresponding force constant matrices, which are the main input in TD-NEGF

method. To avoid spurious effects coming from the free ends, long enough molecular chains for structural optimization and force constant calculations have been considered. However, only the force constant matrix corresponding to a dimer located in the central part was taken to compute the phonon transport properties. Thus, $\Lambda_\alpha^{(0)}$ takes force constant values corresponding to realistic bonds connecting the end of the central region to the reservoirs. Thus, $\Lambda_\alpha^{(0)}$ will have the following structure,

$$\Lambda_\alpha^{(0)} \equiv \begin{pmatrix} 0 & \cdots & \cdots & \cdots & \cdots & 0 \\ & \ddots & & \vdots & & \\ \vdots & & K_{xx}^i & K_{xy}^i & K_{xz}^i & \vdots \\ 0 & \cdots & K_{yx}^i & K_{yy}^i & K_{yz}^i & \cdots & 0 \\ \vdots & & K_{zx}^i & K_{zy}^i & K_{zz}^i & \vdots \\ & & & \vdots & & \ddots & \\ 0 & \cdots & \cdots & \cdots & \cdots & & 0 \end{pmatrix}. \quad (4.47)$$

with $\{K^i\}$ as the force constant matrix associated to the atom i , which is making the coupling with the heat baths. For both molecular junctions, a Drude cut-off frequency of $\omega_c = 100$ THz is used. This value is around twice the maximum frequency corresponding to their vibrational spectrum. The number of poles in the auxiliary-mode expansion at 100 K, 300 K, and 500 K are 10, 8, and 4, correspondingly.

The variation of the energy density $D(E, t)$ during the thermal equilibration at $T_0 = 300$ K for PA and PE dimers is shown in Figs. 4.10(a,b), respectively. This density has been calculated as

$$D(E, t) = \sum_{i=1}^N (1/\gamma\sqrt{2\pi}) \exp[-((E - E_i)/\gamma\sqrt{2})^2] \quad (4.48)$$

with $\gamma = 0.001$ eV as the width of the Gaussian distribution and $\{E_i\}$ as the set of eigenvalues of $\mathcal{Z}(t)$. For both systems, all eigenmodes of the $\mathcal{Z}(t)$ matrix display very low energy at the beginning of the transient. Then, the lowest lying modes gain energy and achieve a maximum once the system reaches equilibrium. However, the eigenvalues in PE need a longer time to converge comparing to PA. This difference arises from the different coupling strengths to the leads (related to $\Lambda^{(0)}$). The coupling of the PA dimer takes place through double bonds which are stiffer than the coupling produced by single bonds (PE dimer). As a consequence, the magnitude of the oscillations in the heat flux during the transient after applying a temperature bias is different (larger for PA as shown in Fig. 4.10(c)). This difference in covalently bonded configurations also results in a larger heat flux for the PA dimer. This is better seen by comparing the heat flux as a function of ξ for both molecular junctions at $T_0 = 300$ K, see Fig. 4.10(d). Here, it was also found that the heat flux values for PE are very close to those found for the 1D atomic chain model, which is expected because of the similarity in configuration. Hydrogen atoms do not play an important role in the thermal transport of these molecular junctions. The heat flux displays a nearly linear dependence with respect to ξ for different mean temperatures T_0 as one can see in Fig. 4.10(d).

4.3 SUMMARY

In the present chapter, transient and steady-state phonon transport properties of nanoscale systems coupled to harmonic heat baths have been studied from a quantum point of view. This was done by developing a novel atomistic method which combines a time-dependent NEGF approach with DFT-based modeling. The time dependence of the transport properties were obtained by solving the equation of motion of the phonon density matrix $\sigma(t)$ with the help of an auxiliary-mode approach. As a result, the self-energies of the baths were expressed in terms of exponential functions and, hence, a set of ordinary differential equations was obtained. Two different spectral densities (wide-band limit and Drude regularization cases) were considered to represent the vibrational properties of the heat baths, however, convergence of transport properties with the number of poles in the auxiliary-mode expansion was only possible by using the Drude spectral density which considers a high-frequency cut-off.

As a first application, the thermal transport properties in the transient regime of an 1D atomic chain were studied. It was found a temperature dependence of the number of poles needed to reach convergence of the total energy and heat flux with the mean temperature of the system. In fact, few poles are sufficient to describe high temperature studies. By having a moderate coupling with the heat baths and a cut-off frequency which allow to conserve the main features of the system, the results for the steady-state heat flux are in agreement with those obtained by using the Landauer approach. In the weak coupling limit, the system nearly behaves like an isolated harmonic oscillator, showing their characteristics vibrational modes and energies.

Finally, by computing the force constant and coupling matrices using density-functional theory, the phonon dynamics of molecular junctions consisting of poly-acetylene and poly-ethylene dimers was described. Because of double carbon bond coupling between the PA dimer and the heat baths, the convergence of the eigenvalues is faster compared to the PE dimer case (single carbon bonds). This difference in coupling strength gives PA dimer a higher heat flux. Both dimers show a linear dependence of the heat flux with respect to the temperature bias. Although these examples were based on the Drude regularization of the spectral density, more realistic scenarios can be easily investigated.

5 CONCLUSIONS AND OUTLOOK

In the present thesis, classical and quantum computational methods have been used to investigate thermal transport in novel nanoscale systems such as 2D materials, nanotubes, and molecular junctions. Based on what was shown, we have here the possibility to perform a systematic study at the atomistic level addressing material-specific issues for the design of potential phononic devices. The methodologies employed in this work have been selected depending on the physical phenomena under interest and the desired accuracy of the results. Hence, the thesis was separated into three parts.

In the first part, thermal rectification effects were studied in nanoscale devices made of 2D materials. This research was carried out, from a classical point view, by using nonequilibrium molecular dynamics. The material targets were structurally asymmetric MoS₂ nanoribbons and coplanar hBN/graphene heterojunctions. As a result of this study, T-shaped nanoribbons displayed the largest rectification ratio (up to 30 %), when compared with trapezoidal and triangular structures, thus illustrating the strong sensitivity of thermal transport to the specific design of the lateral confinement. Our results clearly indicate that the thermal rectification effect is related to i) shape asymmetries, ii) interface material (planar stacking order), and ii) changes in the degree of spatial localization of high-frequency modes (under non-equilibrium heat transport conditions). The influence of substrate deposition on the thermal transport properties of coplanar hBN/graphene thermal rectifiers was also investigated by means of NEMD. Here, it was found that, independently of the substrate, the interface thermal resistance is reduced upon substrate deposition. This is mainly due to the suppression of out-of-plane modes at low frequencies that produces an increment of the spectral overlap between the power spectrum of the heat baths before and after reversing the temperature bias. Moreover, we have obtained that the thermal rectification effect is reduced for small degrees of structural asymmetry when hBN-G nanoribbons are deposited on a given substrate, but increases with increasing asymmetry, reaching values as large as $\sim 24\%$ for the highest asymmetric nanoribbon. We have also shown that the substrate temperature plays an important role in determining the magnitude of the thermal response in these nanomaterials, making possible to reach thermal rectification values of $> 50\%$

without altering their geometry. Therefore, these results thus provide a deeper insight into the role of structural asymmetry and substrate deposition in influencing the thermal response of 2D thermal rectifiers and thus open the possibility of atomic-scale and substrate engineering for controlling thermal transport in novel two-dimensional devices such as thermal memories and thermal cloaks.

In the second part of the thesis, we systematically studied quantum phonon transport at the nanoscale. We combined nonequilibrium Green's function formalism with density functional tight-binding theory to investigate quantum ballistic transport in 2D materials and nanotubes. This method is able to deal atomistically with large systems up to ~ 2000 atoms and it has been numerically implemented as a tool in the DFTB+ software (in-house version). Subsequently, we have rationalized the influence of intrinsic (structural anisotropy and grain boundaries) and external (molecular functionalization, strain engineering, and doping) factors altering the heat transport in these nanomaterials. Though these systems may be also accessible to simulations using classical force fields, they may require extensive parametrizations to study novel 2D materials. Hence, it is more suitable to address this issue within the NEGF-DFTB approach, where the chemistry of the problem is naturally included in the first-principle based computation of the force constants. Thus, it was found that 2D puckered materials (e.g., phosphorene, arsenene, and SnS monolayer) display a strong thermal anisotropy because of their peculiar atomic structure, being preferable heat transport along the zigzag direction. Among them, SnS monolayer showed the highest anisotropy in the thermal conductance which comes from the large difference between its phonon group velocity for zigzag and armchair transport directions. Grain boundaries have also been found to reduce the transmission probability of heat transport in graphene at certain vibrational frequencies. In fact, curved GBs showed lower thermal conductance than linear GBs, especially when out-of-plane distortions are added on the boundary which lead to a reduction of the in-plane contribution to the total phonon transmission. Moreover, additional structural distortions in the boundary strongly affects in-plane and out-of-plane mode contributions to the phonon transmission of graphene GBs. On the contrary, dynamical disorder only weakly affects in-plane modes. Hence, the thermal conductance of linear and curved GBs is reduced by effect of both types of disorder, the effect being stronger for linear GBs due to their higher degree of structural order. In short, dynamical effects on the phonon transport properties of graphene GBs have less impact comparing to structural disorder.

Tuning external parameters have offered the possibility to tailor the thermal transport properties of nanomaterials for the development of potential thermoelectric devices. Accordingly, by functionalizing graphene GBs with ad-atoms and small molecules, we obtained that their thermal conductance is reduced, although the intensity of the effect can be controlled in dependence of the structural symmetries of the grain boundary. Strain engineering of the transport setup (contact-device(scattering)-contact regions) has also been studied for hBN, phosphorene, and MoS₂ systems. We clearly demonstrated that the transport setup plays an important role for the control of the thermal conductance of the systems. Moreover, its influence becomes more dominant when materials with larger number of atomic layers are considered (hbn-1 layer,

Phosphorene-2 layers, MoS₂ monolayer-3 layers). Hereby, the thermal conductance of the three studied systems only decreases when the strain level in the device region increases. Whereas, for homogeneously strained systems, with the exception of MoS₂ monolayer, the results are only quantitatively different from those corresponding to the standard model of uniaxial strain. Then, the influence of BN concentration and the doping distribution pattern on the thermal transport properties of BNC heteronanotubes has been explored. Independently of the spatial atomic BN distribution, the phonon transmission function of the (6,6)-CNT is reduced at high frequencies after increasing the BN concentration. This effect is stronger for randomly doped BNC heteronanotubes. It was also found an anomalous concentration dependence of the phonon thermal conductance at 300 K, i.e., first decreases for BN concentrations < 30%, remains constant up to a concentration of $\sim 80\%$, and then increases. These studies have shown how different factors may have a positive or negative influence on the thermal transport properties and they suggest several ways to realize a nanosystem with a controlled thermal conductance, which is needed for technological applications in the energy-harvesting industry.

However, despite the interesting effects found by using the NEGF-DFTB method implemented in this work, we are still not able to explore novel out-of-equilibrium physical effects such as thermal rectification from a quantum point of view. As it was discussed before, one of the mechanisms to induce thermal rectification in a material is the structural asymmetry. Nonetheless, nonlinear interactions (e.g., phonon-phonon) are also necessary for displaying this effect because it provides a mechanism for phonons of different frequencies to interact between each other. On the other hand, some nanosystems also required the inclusion of nonlinear terms to have an appropriated description of their thermal transport properties, specially when the study is carried out at high temperatures where phonon-phonon interactions are more significant. Unlike the implementation for ballistic transport, in this approach, besides computing the dynamical matrix as the basic input for computing the heat flow, third and fourth order anharmonic coefficients are also needed. They appear as additional self-energies in the corresponding Green's function of the scattering region and involve convolutions in the frequency space of two- and three vibrational Green's functions. The type of processes that need to be included in the self-energies can be elucidated by using Feynmann diagrams. As a result, the problem needs to be solved self-consistently.

Finally, in the third part, we have developed a novel atomistic method which combines a time-dependent NEGF formalism with first-principle based modeling to study phonon dynamics in nanoscale junctions. The main idea of the method is to solve the equation of motion of the phonon density matrix with the help of an efficient auxiliary-mode approach. We have first applied the method to study thermal transport properties in the transient regime of an one-dimensional atomic chain. The results for the steady states are in agreement with those obtained by using the Landauer approach. By computing the force constant matrix and coupling matrices using density-functional theory, we have been able to describe the phonon dynamics of molecular junctions consisting of poly-acetylene and poly-ethylene dimers. Although our examples were

based on the Drude regularization of the spectral density, more realistic scenarios can be easily investigated. Our computational scheme is among the first attempts, up to now, to tackle time-dependent quantum phonon transport and allows it to study a variety of topical questions related to nanophononics, such as heat pumping, on an atomistic basis. Briefly, heat pumping can be implemented when a discrete vibrational system is coupled to hot and cold reservoirs and a time-dependent driving is applied to modulate the energetic position of the vibrational energy levels. This fine tuning modifies the strength of the coupling to the hot and cold reservoirs, effectively coupling and decoupling the system from each thermal bath over time scales related to the frequency of the external field.

In conclusion, we have here presented several mechanisms to deal and control heat transport in nanoscale systems. Besides suggesting possible experimental works and potential phononic devices, we think that the outcomes produced by this work can be used for the implementation of a machine learning-based code to predict and understand thermal transport properties of novel low-dimensional materials. Hence, addressing this possibility in connection with nanoscale thermal management will be the scope of future work.

A NEMD SIMULATIONS

A.1 BENCHMARKING OF THE HEAT BATH PARAMETERS

A first step before addressing the issue of thermal transport, was to implement a reliable force field for MoS₂ in LAMMPS code. Then, it was found the accurate simulation parameters to carry out the nonequilibrium molecular dynamics simulations presented in Chapter 2. To do this task, a systematic study of the parameters related to the heat baths was performed. The Nosé-Hoover thermostat was selected for the heat baths in order to have a good performance reproducing the canonical ensemble and avoid artifacts which have been reported by using, e.g., Berendsen thermostat [293].

After selecting the thermostat, the first fixed parameter was the length of the heat bath, L_{HB} . In our calculations, the mean temperature is 300 K and the temperature bias $\Delta T = 60$ K, i.e., $T_L = 330$ K and $T_R = 270$ K for the forward direction and $T_L = 270$ K and $T_R = 330$ K for the backward direction of the heat flux. Fig. A.1 shows the effect of the number of heat bath layers on the temperature profile of a symmetric MoS₂ nanoribbon ($W_{LR} = 1.0$). The bath relaxation time $\tau = 0.1$ was used for this study. A linear temperature gradient is observed in the inner part of the device region. The main difference in temperature profile between different heat bath conditions is the temperature jump between the heat bath and interior layers. With the number of heat bath layers increasing, the temperature jump is reduced as shown in Fig. A.1, this effect leading to an increase in the heat flux (see Table A.1). Further increase in the number of heat bath layers cannot eventually remove the temperature jump. The small remaining temperature jump is due to the thermal boundary resistance (TBR) between heat bath and the device region, which is the result of the mismatch in their corresponding phonon density of states [187]. A similar effect has been reported for carbon nanotubes [187], and silicon nanowires [293]. In addition, the sensitivity of the thermal rectification as a function of the heat bath length has been calculated. It turned out that for small lengths the thermal rectification for symmetric MoS₂ nanoribbons was different from zero but, after increasing L_{HB} , this value

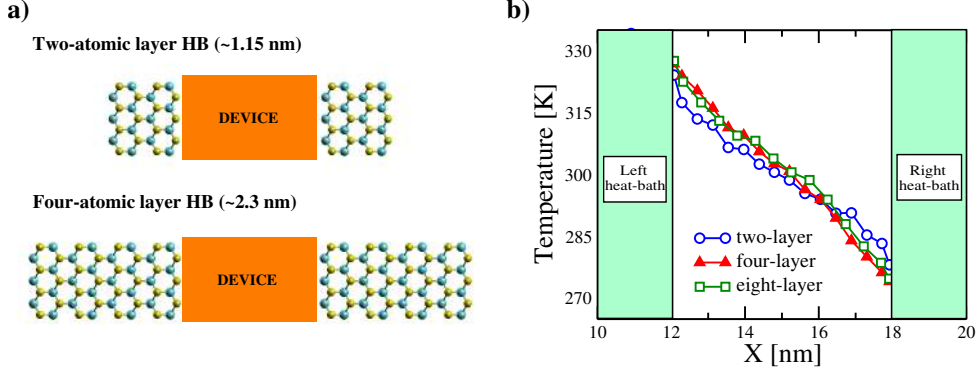


Figure A.1: a) Schematic of MoS₂ nanoribbons with different heat bath lengths. b) Variation of the temperature profile with the heat bath length for symmetric MoS₂ nanoribbons in the forward direction of the heat flux.

Table A.1: Values of the heat flux and thermal rectification for different length of the heat bath

		Length of the heat bath, L_{HB}		
		2-layer (~1.15 nm)	4-layer (~2.3 nm)	8-layer (~4.6 nm)
Heat flux [$\times 10^{-7}$ W]	forward	0.6856	0.8866	1.0367
	backward	0.6976	0.8937	1.0397
Thermal rectification, η		1.72 ± 0.1	0.79 ± 0.2	0.29 ± 0.1

converged to zero as expected for symmetric geometries. The threshold value for this behavior was $L_{HB} \sim 2.3$ nm. All the following calculations were thus carried out with this bath length.

Regarding the relaxation time, τ , it is well-known that the temperature profile has a strong dependence on the magnitude of this parameter. For instance, τ should not be too small compared to the time step because it can cause large oscillations in temperature. Such oscillations can lead to the accumulation of numerical errors, causing the system to deviate from the canonical distribution. Such numerical error accumulation can also happen if the relaxation time is very large because the total simulation time becomes very long. Here, L_{HB} is set to 2.3 nm (4 atomic layers) in order to perform this study. As it is shown in Fig. A.2, it was found that the temperature profile for MoS₂ nanoribbon with $W_{LR} = 1.0$ is strongly depended on this parameter. In fact, despite the heat bath reaching the target temperature and the temperature profile being well defined for $\tau = 0.001$, the heat flux for the hot and cold heat bath are rather different at steady state, which is not the correct thermodynamic behavior. In the case of large relaxation time, the MoS₂ nanoribbons display a wrong temperature profile for both directions of the heat flux. The heat baths do not reach the target temperature. Similar behaviors have been reported for other nanomaterials [187, 293]. Thus, these results indicate that the steady state temperature or heat current distribution do not depend on any particular value of the relaxation time in the range from 0.01 ps to 1 ps. Hence, in the present work, we chose $\tau = 0.1$ ps for the MD simulations, which is large enough to avoid high frequency temperature oscillations, and leads to a stabilization time (the time needed to reach the steady state in the simulation) of about 1.0 ns, which is short enough to avoid large numerical error accumulation. It is worth mentioning

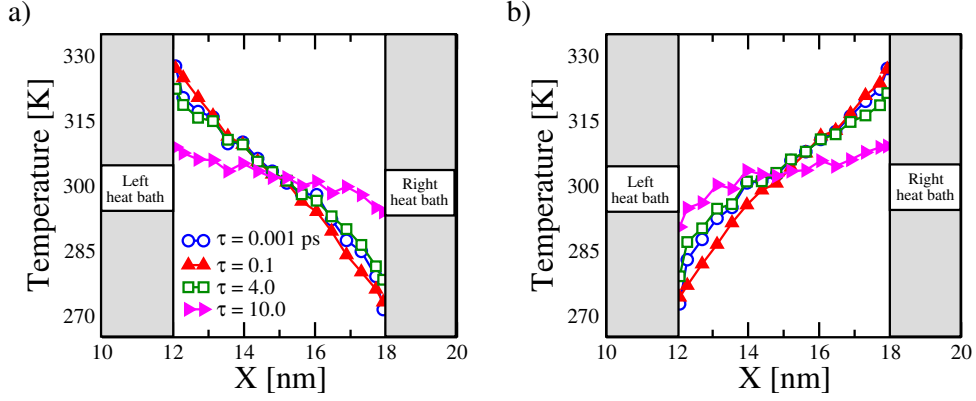


Figure A.2: Relaxation time dependence of the temperature profile for symmetric MoS₂ nanoribbons in the a) forward and b) backward direction of the heat flux.

Table A.2: Values of the heat flux and thermal rectification for different relaxation time of the heat bath

		Relaxation time of the heat bath, τ		
		0.1	4.0	10.0
Heat flux [$\times 10^{-7}$ W]	forward	0.8866	0.5132	0.3041
	backward	0.8937	0.5159	0.3063
Thermal rectification		0.79 ± 0.2	0.52 ± 0.1	0.72 ± 0.1

that despite the relaxation time dependence of the temperature profile in MoS₂ nanoribbons, the magnitude of the thermal rectification is only slightly affected because of the symmetry of the temperature profile when the temperature bias is reversed (see Table A.2).

A.2 REAL-SPACE VIBRATIONAL MODE ANALYSIS

Fig. A.3 complements the results presented in a similar figure in the Chapter 2 (see Fig. 2.6). Here, the spatial distribution of the vibrational modes, as given by the function $\phi_{i\alpha,\Lambda}$, is shown for the other two intervals of the participation ratio previously defined (see also the middle panel of Fig. A.3): I) $P > 0.4$ and II) $0.1 < P < 0.4$, for the forward and backward directions of the heat flux. For case I (Fig. A.3a,c), which corresponds to a subset of rather delocalized modes, it turns out that a major contribution to these modes is coming from atoms along the edges of the nanoribbon (both Mo and S atoms), while the bulk contributions are much weaker (values of $\phi_{i\alpha,\Lambda} \leq 2$). In case II (see Fig. A.3b,d) the behavior is more complex: sulfur atoms in the center and edges of the ribbon give the strongest contribution, while molybdenum atoms are basically "silent", a fact related to the previously found result that in the spectral range 230-370 cm^{-1} the Mo atoms do not appreciably contribute to the vibrational density of states. By comparing Fig. A.3a,b with Fig. A.3c,d, the spatial distribution of the vibrational modes in backward direction is similar to the obtained in the forward direction.

A rather similar behavior was found for trapezoidal MoS₂ nanoribbons of length $L = 5.9$ nm and $W_{LR} = 3.0$ as shown in Fig. A.4. Notice that the largest changes in the spatial distribution

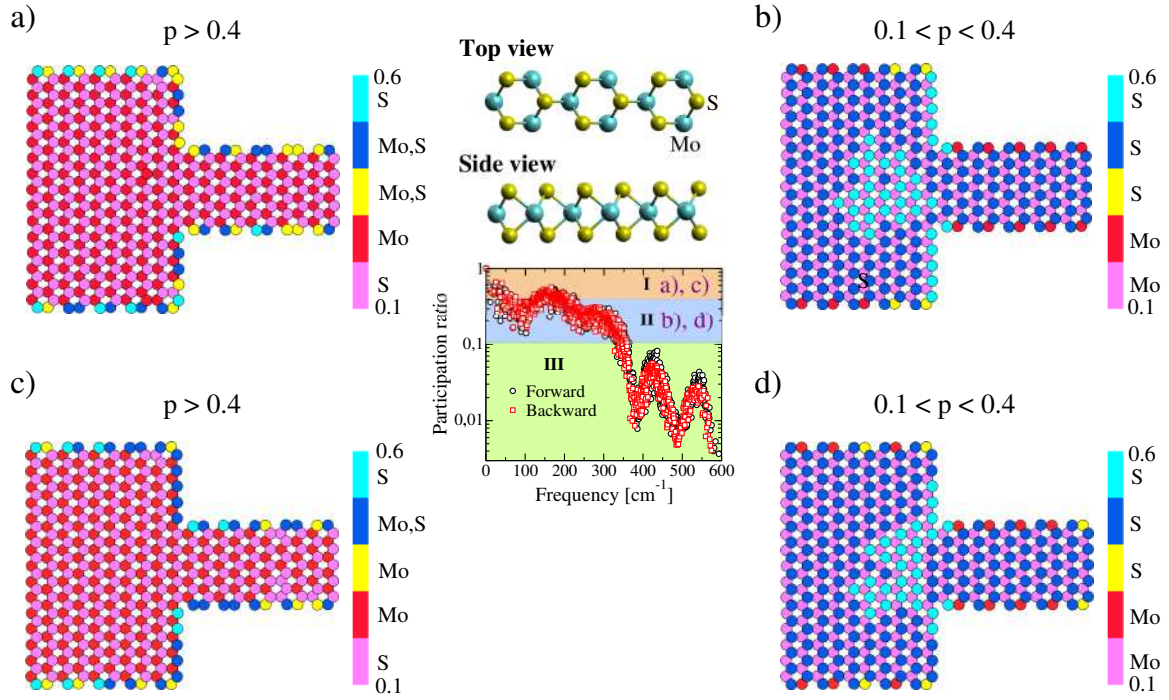


Figure A.3: Spatial distributions, ϕ , of vibrational modes for T-shaped MoS₂ nanoribbons of $L = 5.9$ nm and $W_{LR} = 3.0$ (XY plane). Two restrictions based on the magnitude of the participation ratio, P , have been considered: I) $P > 0.4$ and II) $0.1 < P < 0.4$ for the system obtained after NEMD simulation in the forward (a) and b)) and backward (c) and d)) direction. We have considered $\alpha = 0.1$ for this calculation. The color scale has the same meaning for all the cases, i.e., cyan balls mean highest contribution while pink balls lowest contribution for the vibrational modes. These pictures only show the contributions arising from the top S-layer as well as the Mo-layer.

of modes upon inversion of the heat flow direction takes place for the spectral range III with the smallest participation ratio. This behavior shows the same qualitative tendency as for the previously discussed T-shape nanoribbon. Hence, these results suggest that for the considered asymmetric nanoribbons, modes located within the spectral range from 350 cm⁻¹ to 600 cm⁻¹ are providing the main contribution to the thermal rectification, since they are the most affected by the inversion of the heat flow. On the other hand, the precise asymmetric shape of the ribbon seems to mainly determine the size of the thermal rectification.

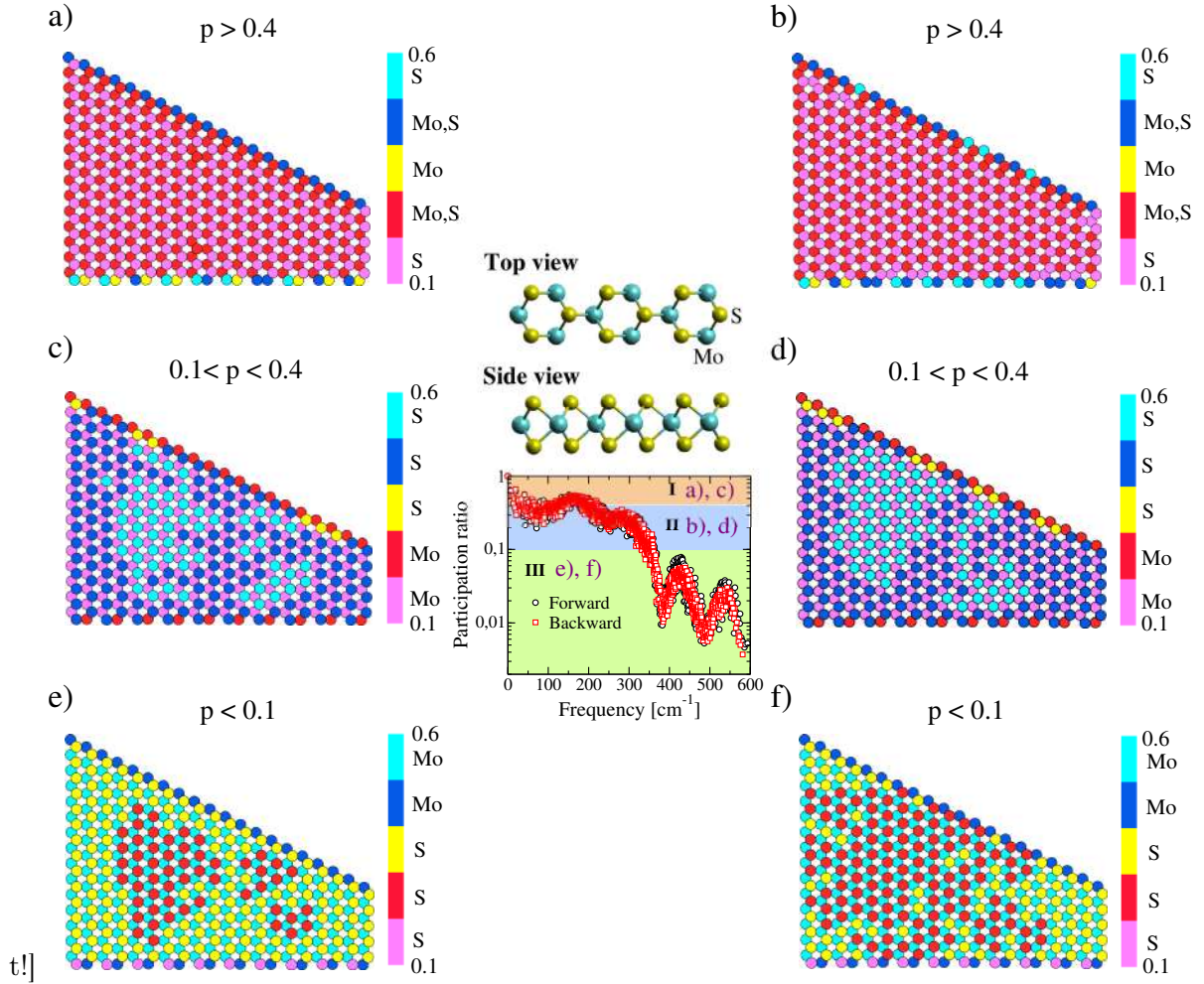


Figure A.4: Spatial distributions, ϕ , of vibrational modes for trapezoidal MoS_2 nanoribbons of $L = 5.9$ nm and $W_{\text{LR}} = 3.0$ (XY plane). Three restrictions based on the magnitude of the participation ratio, P , have been considered: I) $P > 0.4$, II) $0.1 < P < 0.4$, and III) $P < 0.1$ for the system obtained after NEMD simulation in the forward (a), c), and e)) and backward (b), d), and f)) direction. We have considered $\alpha = 0.1$ for this calculation. The color scale has the same meaning for all the cases, i.e., cyan balls mean highest contribution while pink balls lowest contribution for the vibrational modes. These pictures only show the contributions arising from the top S-layer as well as the Mo-layer.

B NEGF-DFTB IMPLEMENTATION

B.1 BASIC CONCEPTS OF DFTB

In DFTB, the KS orbitals are represented with a linear combination of atomic orbitals (LCAO) centered on the nuclei. Denoting the basis function by ϕ_μ and the expansion coefficients by $c_{\mu i}$, one can write the KS orbitals in the form

$$\psi_i(\mathbf{r}) = \sum_a \sum_{\mu \in a} c_{\mu i} \phi_\mu(\mathbf{r} - \mathbf{R}_a), \quad (\text{B.1})$$

where \mathbf{R}_a is the coordinate of the nucleus of atom a . Then, the first line of Eq. (3.51) can be written as

$$E^{H^0} = \sum_i n_i \sum_{ab} \sum_{\mu \in a} \sum_{\nu \in b} c_{\mu i} c_{\nu i} H_{\mu\nu}^0, \quad (\text{B.2})$$

with Hamilton matrix elements $H_{\mu\nu}^0 = \int \phi_\mu^* \hat{H}^0 \phi_\nu d\mathbf{r}$ being only dependent on the reference density. a and b are indices for atoms, μ and ν for atomic orbitals. The term in the second line of Eq. (3.51) consist of the DFT double-counting contributions, the nucleus-nucleus repulsion and exchange-correlation contributions. In tight-binding theory, they are usually approximated as a sum of one-center terms and short ranged two-center potentials V_{ab}^{rep} [244]

$$-\frac{1}{2} \int \int' \frac{\rho^{0'} \rho^0}{|\mathbf{r} - \mathbf{r}'|} - \int V^{xc}[\rho^0] \rho^0 + E^{xc}[\rho^0] + E^{nn} \approx \sum_a V_a^{rep}[\rho_a^0] + \frac{1}{2} \sum_{ab} V_{ab}^{rep}[\rho_a^0, \rho_b^0, r_{ab}]. \quad (\text{B.3})$$

With ρ_a^0 and ρ_b^0 as the atomic reference densities for atom a and b , respectively; and $r_{ab} = |\mathbf{R}_b - \mathbf{R}_a|$ is the interatomic distance. The atomic contributions sum up to a constant energy shift which cancels out when considering energy differences. For DFTB, the atomic contributions are neglected and a repulsive energy E^{rep} is defined as

$$E^{rep} = \frac{1}{2} \sum_{ab} V_{ab}^{rep}[\rho_a^0, \rho_b^0, r_{ab}]. \quad (\text{B.4})$$

The pair-potential V_{ab}^{rep} are fitted atom type and distance dependent to several systems (for details look Ref. [261]). Finally, the total non-scc DFTB energy can be written as

$$E^{nscs-DFTB} = \sum_{iab} \sum_{\mu \in a} \sum_{\nu \in b} n_i c_{\mu i} c_{\nu i} H_{\mu\nu}^0 + E^{rep}. \quad (\text{B.5})$$

To determine the molecular orbitals coefficients $c_{\mu i}$ (see Eq. (B.1)), Kohn-Sham equations are derived by taking the derivative of the total energy with respect to the normalization constraints

$$\int \psi_i^*(\mathbf{r}) \psi_i(\mathbf{r}) d\mathbf{r} = 1 \quad \forall i \quad (\text{B.6})$$

to get (δ is an index for an orbital, d for an atom):

$$\frac{\partial}{\partial c_{\delta i}} \left[E^{nscs-DFTB} - \sum_j n_j \epsilon_j \left(\sum_{ab} \sum_{\mu \in a} \sum_{\nu \in b} c_{\mu j} c_{\nu j} S_{\mu\nu} - 1 \right) \right] = 0 \quad \forall d, \delta \in d. \quad (\text{B.7})$$

The Kohn-Sham equations are approximate in the sense that an approximated energy $E^{nscs-DFTB}$ which depends on a reference density is considered. Inserting Eq. (B.5) yields a set of algebraic equations

$$\sum_b \sum_{\nu \in b} c_{\nu i} (H_{\mu\nu}^0 - \epsilon_i S_{\mu\nu}) = 0 \quad \forall a, \mu \in a, i. \quad (\text{B.8})$$

where $S_{\mu\nu} = \int \phi_\mu^*(\mathbf{r}) \phi_\nu(\mathbf{r}) d\mathbf{r}$ is the overlap matrix. Hence, the total energy in Eq. (B.5) can also be expressed in terms of ϵ_i as

$$E^{nscs-DFTB} = \sum_i n_i \epsilon_i + E^{rep}. \quad (\text{B.9})$$

Nevertheless, it is still missing how to calculate the pseudoatomic basis functions ϕ_μ . These are obtained by solving the Kohn-Sham equation for a spherical symmetric spin unpolarized neutral atom self-consistently

$$\left[-\frac{1}{2} \nabla^2 + V^{psat}(\mathbf{r}) \right] \phi_\mu(\mathbf{r}) = \epsilon_\mu^{psat} \phi_\mu(\mathbf{r}) \quad \forall \mu, \quad (\text{B.10})$$

where the pseudoatomic potential $V^{psat}(\mathbf{r})$ is given by

$$V^{psat}(\mathbf{r}) = V^{ne}(\mathbf{r}) + V^J[\rho(\mathbf{r})] + V^{xc}[\rho(\mathbf{r})] + \left(\frac{r}{r^c} \right)^p \quad (\text{B.11})$$

Here, the local density approximation (LDA) as parametrized by Perdew and Zunger or the PBE functional is often used as exchange-correlation potential. A contraction potential $(r/r^c)^p$ has been added as introduced by Eschrig [294] to form a more efficient basis set for molecular and solid-state systems. The parameter r^c is chosen to be about 1.85 times the atomic covalent

radius [283]. However, this parameter can also be determined using a variational principle for the total energy. The parameter p was found to have a rather small influence on the results and is usually chosen as $p = 2$. Then, the atomic orbital can be represented by linear combinations of Slater-type orbitals (STO)

$$\phi_{\mu}(\mathbf{r}) = \sum_{n,\alpha,l_{\mu},m_{\mu}} a_{n\alpha} r^{l_{\mu}+n} \exp(-\alpha r) Y_{l_{\mu}m_{\mu}}\left(\frac{\mathbf{r}}{r}\right), \quad (\text{B.12})$$

where $r = |\mathbf{r}|$, l and m are the angular momentum and the magnetic quantum numbers associated with the orbital μ , respectively. Extensive tests have shown that five different values of α and $n = 0, 1, 2, 3$ form a sufficiently accurate basis set [294]. From this procedure, an optimized atomic basis set ϕ_{μ} and its respective atomic potentials have been obtained per each atom-type

Consequently, the Hamiltonian matrix elements can be now computed by using two well established ways. The first and older way is the determination using an overlap of potentials in the form (in Dirac notation)

$$H_{\mu\nu}^0 = \begin{cases} \epsilon^{\text{free atom}} & \text{if } \mu = \nu \\ \langle \phi_{\mu} | \hat{T} + V[\rho_a^0] + V[\rho_b^0] | \phi_{\nu} \rangle & \text{if } a \neq b \\ 0 & \text{if } a = b, \mu \neq \nu. \end{cases} \quad (\text{B.13})$$

where $\hat{T} = -\nabla^2/2$ is the kinetic energy operator and $\epsilon^{\text{free atom}}$ is the eigenvalue of Eq. (B.10) when using the potential $V(r)$ of Eq. (B.11) without the additional term $(r/r^c)^p$ [262]. For the off-diagonal terms a two-center approximation is applied, crystal field and three-center terms are neglected. $V[\rho_a^0]$ is an atomic Kohn-Sham potential as given in Eq. (B.11) including the compressed density

$$\rho_a^0 = \sum_{\mu \in a} \phi_{\mu}(\mathbf{r}) \phi_{\mu}(\mathbf{r}) \quad (\text{B.14})$$

but without the additional term $(r/r^c)^p$. The second way to approximate the Hamiltonian matrix elements is similar to the first one but using density overlap of the term

$$H_{\mu\nu}^0 = \begin{cases} \epsilon^{\text{free atom}} & \text{if } \mu = \nu \\ \langle \phi_{\mu} | \hat{T} + V[\rho_a^0 + \rho_b^0] | \phi_{\nu} \rangle & \text{if } a \neq b \\ 0 & \text{if } a = b, \mu \neq \nu. \end{cases} \quad (\text{B.15})$$

The potential $V[\rho_a^0 + \rho_b^0]$ is identical to Eq. (B.11) but again without the additional term $(r/r^c)^p$. However, it has been shown for the self-consistent DFTB (described below) on small molecules, that for accurate and transferable two-center integrals ($a \neq b$) one parameter for the compression of ϕ_{μ} and ρ_a^0 is not sufficient [245, 261]. Thus, the overlap matrix elements $S_{\mu\nu}$ mentioned earlier and the Hamilton matrix elements $H_{\mu\nu}^0$ can be precomputed and tabulated (the two-center approximation simplifies this tabulation) for every atom type pair and a dense mesh

of interatomic distances. All this information can be found in the Slater-Koster files supplied by the DFTB+ community [283]. Therefore, it is not necessary to compute the matrix elements during the runtime of the calculation, but it is essential to account for the orientation of the orbitals within a molecule which is done using the Slater-Koster sin/cos-rules [245]. Hence, a lot of effort has been recently done to develop the Slater-Koster files for the most of chemical elements in the Periodic Table [295, 296].

To improve on the requirement of local charge neutrality, Elstner et al. [245] suggested to go beyond the first-order expansion of the Kohn-Sham energy functional and to include the second order corrections to the exchange-correlation energy. This new method is called self-consistent charge DFTB (scc-DFTB). For systems with sizable charge reorganization, the second order terms in the density fluctuations (see Eq. (3.51)) become important [245, 260]

$$E^{2nd} = \frac{1}{2} \int' \int \left(\frac{1}{|\mathbf{r} - \mathbf{r}'|} + \frac{\partial^2 E^{xc}}{\delta \rho \delta \rho'} \Big|_{\rho^0, \rho^{0'}} \right) \Delta \rho \Delta \rho'. \quad (\text{B.16})$$

To preserve computational efficiency, this term is approximated in a way that avoids explicit integration during the calculation. First, the density fluctuation is written as a superposition of atomic contributions

$$\Delta \rho = \sum_a \Delta \rho_a. \quad (\text{B.17})$$

The main approximation for this term consists of neglecting higher order multiple interactions, i.e., approximating the atomic density fluctuations $\Delta \rho_a$ by charge monopoles, truncating the expansion in spherical harmonics after the monopole term [245]

$$\Delta \rho_a \approx \Delta q_a F_a^{00} Y^{00}. \quad (\text{B.18})$$

In analogy to $\Delta \rho_a = \rho_a - \rho_a^0$, the charge fluctuation is the Mulliken charge $\Delta q_a = q_a - q_a^0$, where q_a^0 is the charge of the valence electrons of a neutral atom a , and q_a is the charge of that atom within the molecule which is calculated as

$$q_a = \sum_i n_i \sum_{\mu \in a} \sum_b \sum_{\nu \in b} c_{\mu i} c_{\nu i} S_{\mu \nu}. \quad (\text{B.19})$$

Therefore, the change of density in Eq. (B.18) is restricted to charge transfer between the atoms as estimated by the net charge Δq_a on atom a , and the deformation of the charge density is neglected in this approximation ($Y^{00} = \frac{1}{2} \sqrt{\frac{1}{\pi}}$). Inserting Eq. (B.18) and Eq. (B.17) into Eq. (B.16) and assuming exponentially decaying spherical charge densities with coefficients τ_a ,

$$\frac{F_a^{00}}{2\sqrt{\pi}} = \frac{\tau_a^3}{8\pi} \exp(-\tau_a |\mathbf{r} - \mathbf{R}_a|) \quad (\text{B.20})$$

an analytic function γ can be derived [245], which represents the interaction between the charge density fluctuations and further approximates the second order terms (see Eq. (B.16)). Then, the second order term becomes

$$E^{2nd} \approx E^\gamma = \frac{1}{2} \sum_{ab} \Delta q_a \Delta q_b \gamma_{ab}. \quad (\text{B.21})$$

Two main properties of γ_{ab} are highlighted which are described in detail in Ref. [245]. For large interatomic distances r_{ab} , γ_{ab} basically reduces to $1/r_{ab}$; i.e., it describes a pure Coulomb interaction of the partial charges Δq_a and Δq_b . For $a = b$, γ_{ab} describes the on-site self-repulsion,

$$\gamma_{ab} = U_a \quad (\text{B.22})$$

introducing the Hubbard parameter U_a which is the second derivative of the total energy of a neutral atom with respect to the occupation number of the highest occupied atomic orbital. In DFTB, it is estimated by using Janak's theorem [245]. The Hubbard parameter can also be related to the chemical hardness which is half of the difference of ionization potential and electron affinity. The exponential coefficient τ_a is determined by

$$\tau_a = \frac{16}{5} U_a, \quad (\text{B.23})$$

which imposes an inverse relationship between the Hubbard parameter and the covalent radius

$$U_a \propto \frac{1}{R_a^{cov}}. \quad (\text{B.24})$$

Therefore, the Hubbard parameter affects two physical properties, the electron-electron interaction within one atom, i.e., the diagonal elements γ_{aa} , and the size of the atoms for estimating the two-center terms γ_{ab} . This estimated atomic size determines the deviation of γ_{ab} from $1/r_{ab}$.

Furthermore, the coefficients $c_{\mu i}$ can be obtained by solving the Kohn-Sham equations in similar way as in Eqs. (B.7) and (B.8),

$$\sum_b \sum_{\nu \in b} c_{\nu i} (H_{\mu\nu} - \epsilon_i S_{\mu\nu}) = 0, \quad \forall a, \mu \in a, i. \quad (\text{B.25})$$

where the Hamilton matrix elements are

$$H_{\mu\nu} = H_{\mu\nu}^0 + \frac{1}{2} S_{\mu\nu} \sum_c \Delta q_c (\gamma_{ac} + \gamma_{bc}). \quad (\text{B.26})$$

Combining results, the scc-DFTB total energy finally reads [261]

$$\begin{aligned} E^{scc-DFTB} &= \sum_{iab} \sum_{\mu \in a} \sum_{\nu \in b} n_i c_{\mu i} c_{\nu i} H_{\mu\nu}^0 + \frac{1}{2} \sum_{ab} \Delta q_a \Delta q_b \gamma_{ab} + \frac{1}{2} \sum_{ab} V_{ab}^{rep} \\ &= \sum_i n_i \epsilon_i - \frac{1}{2} \sum_{ab} \Delta q_b (q_a \gamma_{ba} + q_a^0 \gamma_{ab}) + E^{rep}, \end{aligned} \quad (\text{B.27})$$

B.2 PHONON TOOL

As it was mentioned in Chapter 3, a new tool to study quantum thermal transport has been implemented in DFTB+ software (in-house version). The quantities that can be computed are phonon transmission function and, hence, the thermal conductance. Also, phonon dispersion of materials can be investigated by using this tool. For both type of study, the input file is called 'phonons_in.hsd'.

Phonon transport calculation

The steps to carry out this calculation are:

1. Build the structure file (GEN file) introducing first the coordinates of the central region, then the right heat bath and, finally, the corresponding to the left heat bath (see Fig. 3.2).
2. Compute the Hessian matrix for the entire system. The output file is "hessian.out".
3. Run the phonon calculation. To do this, the hessian and structure files must be in the same directory as the phonon-input file (phonons_in.hsd).

The phonon-input file presents the next structure,

```
geometry = genformat {
<<< "system.gen"
}

transport {
  device {
    AtomRange = 1 50
  }
  contact {
    Id = "Drain"
    ShiftAccuracy = 1e-4
    atomrange = 51 100
    temperature [K] = 300.0
  }
  contact {
    Id = "Source"
    ShiftAccuracy = 1e-4
    atomrange = 101 150
    temperature [K] = 300.0
  }
}
```

```

    }
}

Masses = { } # to study the influence of isotopes

Hessian {
  Cutoff = 100.0
  Type = total # or in-plane, out-of-plane
  Matrix = dftb{
    <<<hessian.out
  }
}

Analysis {
  TunnelingAndDOS{
    Verbosity = 91
    FreqRange = 1e-6 1e-2
    FreqStep = 4e-5
    Delta = 6e-4
  }

  Region = {
    Atoms = 1:50 # projected phonon DOS
  }

  Conductance{
    TempRange [K] = 1.0 802.0
    TempStep [K] = 1.0
  }
}

parseroptions = {
  WriteHSDInput = No
  WriteXMLInput = No
}

```

Phonon dispersion calculation

The steps to carry out this calculation are:

1. Build the structure file (GEN file) of a supercell. The supercell is composed by several replicas of the unit cell of the system under interest. The number of replicas may have an influence in the resolution of the phonon branches.
2. Compute the Hessian matrix for the supercell. The output file is "hessian.out".
3. Generate the k-point path for the phonon dispersion and save it in a file. The first line in that file must indicate the total number of k-points.
4. Run the phonon calculation. To do this, the hessian, k-points, and structure files must be in the same directory as the phonon-input file (phonons_in.hsd).

The phonon-input file presents the next structure,

```

geometry = genformat {
<<< scell.gen
}

PhononDispersion{
  nAtomUnitCell = 4
  KPoints {
    <<< kpath.dat
  }
}

Masses = {
# <<< mass.dat      # to study the influence of isotopes
}

Hessian {
  Cutoff = 60.0
  Type = total
  Matrix = dftb {
    <<<hessian.out
  }
}

parseroptions = {
  WriteHSDInput = No
  WriteXMLInput = No
  parserversion = 4
}

```


C TIME-DEPENDENT NEGF

Real-time advanced GF

The expression for the advanced GF, $\mathcal{G}^A(t, t')$, is also derived in a similar manner to this done for the retarded GF (see Chapter 4). In this case, the time derivative of the Eq. (4.5) is taken respect to the second argument τ' , i.e.,

$$\frac{\partial}{\partial \tau'} \mathcal{G}(\tau, \tau') = \delta(\tau, \tau') \mathcal{Q}^T + \mathcal{G} \cdot \mathcal{K}^T - \sum_k (-i) \mathcal{T}_C \begin{pmatrix} \mathbf{0} & \langle \mathbf{u}(\tau) \mathbf{V}_k^T u_k^T(\tau') \rangle \\ \mathbf{0} & \langle \mathbf{p}(\tau) \mathbf{V}_k^T u_k^T(\tau') \rangle \end{pmatrix}. \quad (\text{C.1})$$

Then, a mixed Green's function is defined as

$$\mathcal{G}'_k(\tau, \tau') = -i \mathcal{T}_C \begin{pmatrix} \mathbf{0} & \langle \mathbf{u}(\tau) u_k^T(\tau') \rangle \\ \mathbf{0} & \langle \mathbf{p}(\tau) u_k^T(\tau') \rangle \end{pmatrix},$$

The equation of motion for $\mathcal{G}(\tau, \tau')$ thus turns to be

$$\frac{\partial}{\partial \tau'} \mathcal{G}(\tau, \tau') = \delta(\tau, \tau') \mathcal{Q}^T + \mathcal{G} \cdot \mathcal{K}^T + \int d\tau'' \sum_k \mathcal{G}(\tau, \tau'') \cdot \begin{pmatrix} \mathbf{V}_k \mathcal{G}'_k(\tau'', \tau') \mathbf{V}_k^T & \mathbf{0} \\ \mathbf{0} & \mathbf{0} \end{pmatrix} \cdot \mathcal{Q}^T,$$

where $\Sigma(\tau, \tau') = \sum_k \mathbf{V}_k \mathcal{G}'_k(\tau, \tau') \mathbf{V}_k^T$ is the self-energy and \mathcal{G}'^0 represents the solution of the equation

$$\mathcal{Q} \cdot \partial_{\tau'} \mathcal{G}'^0(\tau, \tau') = \delta(\tau, \tau') \mathcal{I} + \mathcal{Q} \cdot \mathcal{G}'^0 \cdot \mathcal{K}^T.$$

Consequently, the new Dyson's equation for the central region Green's function is given by,

$$\mathcal{G}(\tau, \tau') = \mathcal{G}'^0(\tau, \tau') + \int d\tau_2 \int d\tau_3 \mathcal{G}(\tau, \tau_2) \cdot \begin{pmatrix} \Sigma(\tau_2, \tau_3) & \mathbf{0} \\ \mathbf{0} & \mathbf{0} \end{pmatrix} \cdot \mathcal{G}'^0(\tau_3, \tau'). \quad (\text{C.2})$$

Moreover, by using the Langreth's rules in Eq. (C.2), the real-time advanced Green's function is expressed as

$$\mathcal{G}^A(t, t') = \mathcal{G}'^{0,A}(t, t') + \int d\tau_2 \int d\tau_3 \mathcal{G}^A(t, \tau_2) \cdot \mathcal{S}^A(\tau_2, \tau_3) \cdot \mathcal{G}'^{0,A}(\tau_3, t'). \quad (\text{C.3})$$

Derivation of lesser self-energy

By using the normal mode representation of the real-space displacement $u_{\alpha S}(t)$, i.e.,

$$u_{\alpha S}(t) = \frac{1}{\sqrt{N}} \sum_k u_{\alpha k}(t) e^{ikx_S},$$

the lesser self-energy can be expressed as,

$$\Sigma_{\alpha nn'}^<(t, t') = -\frac{i}{\hbar} \sum_{kk'} V_{n, -k} V_{n', -k'} \langle u_{\alpha k'}(t') u_{\alpha k}(t) \rangle.$$

Here, due to the harmonic behavior of the heat baths, the normal mode amplitude is defined as:

$u_{\alpha k}(t) = \sqrt{\hbar/2m\omega_k} (b_{\alpha k}(t) + b_{\alpha, -k}^\dagger(t))$ with $b_{\alpha k}(t) = b_{\alpha k}(0) e^{-i\omega_k t}$. Thus,

$$\begin{aligned} \langle u_{\alpha k'}(t') u_{\alpha k}(t) \rangle &= \frac{\hbar}{2m\sqrt{\omega_k \omega_{k'}}} \langle b_{\alpha, -k'}^\dagger b_{\alpha, k} e^{-i\omega_k t + i\omega_{k'} t'} + b_{\alpha, k'} b_{\alpha, -k}^\dagger e^{-i\omega_{k'} t' + i\omega_{-k} t} \rangle \\ &= \frac{\hbar}{2\omega_k} \delta_{k', k} \left[\coth \frac{\omega_k}{2k_B T} \cos \omega_k(t - t') + i \sin \omega_k(t - t') \right] \end{aligned}$$

Finally, the lesser self-energy reads

$$\Sigma_{\alpha nn'}^<(t, t') = -i \int_0^\infty \frac{d\omega}{\pi} \Lambda_{\alpha nn'}(\omega) \left[\coth \frac{\omega}{2k_B T} \cos \omega(t - t') + i \sin \omega(t - t') \right]$$

with the Spectral Density $\Lambda_{\alpha nn'}(\omega)$ given by

$$\Lambda_{\alpha nn'}(\omega) = \pi \sum_k \frac{V_{nk}^* V_{n'k}}{2m\omega_k} \delta(\omega - \omega_{\alpha k})$$

Auxiliary-mode approach

Wide-band limit case

Here, the evaluation of the convolution of a lesser/greater Green's function and an advanced/retarded self-energy (see Eq. (4.15)) is shown in more details. Indeed, each term of the convolution will be independently treated. The first term is expressed as

$$\begin{aligned} \int d\tau \mathcal{G}^<(t, \tau) \mathcal{S}^A(\tau, t) &= \sum_\alpha \int_{t_0}^t d\tau \mathcal{G}^<(t, \tau) \cdot \mathcal{L}_\alpha^{(0)} [-2\partial_\tau \delta(\tau - t)] \\ &= \sum_\alpha \left[-2\delta(\tau - t) \mathcal{G}^<(t, \tau) \cdot \mathcal{L}_\alpha^{(0)} \right]_{\tau=t_0}^{\tau=t} + \sum_\alpha \partial_\tau \mathcal{G}^<(t, \tau)|_{\tau=t} \cdot \mathcal{L}_\alpha^{(0)} \\ &\equiv \sum_\alpha \partial_\tau \mathcal{G}^<(t, \tau)|_{\tau=t} \cdot \mathcal{L}_\alpha^{(0)} \end{aligned}$$

The boundary term at $\tau = t$, $-2\delta(0)\mathcal{G}^<(t, t) \cdot \mathcal{L}_\alpha^{(0)}$, cancels with the counter-term \mathbf{K}_{ct} initially defined. To explain this, let's start with the definition of the delta function which is,

$$\delta(t - t') = \int_0^\infty \frac{d\omega}{\pi} \cos \omega(t - t'). \quad (\text{C.4})$$

Next, the component of the boundary term is built,

$$\begin{aligned} -2\mathcal{L}_\alpha^{(0)}\delta(0) &= -2 \int_0^\infty \frac{d\omega}{\pi} \mathcal{L}_\alpha^{(0)} \cos \omega(0) \\ &= -2 \int_0^\infty \frac{d\omega}{\pi} \mathcal{L}_\alpha(\omega) \frac{\cos \omega(0)}{\omega}. \end{aligned} \quad (\text{C.5})$$

By replacing the initial form of the spectral density in the latter equation, it results

$$\begin{aligned} -2\mathcal{L}_\alpha^{(0)}\delta(0) &= -2 \sum_k \int_0^\infty d\omega \frac{\mathbf{V}_k^T \cdot \mathbf{V}_k}{2\omega\omega_k} \delta(\omega - \omega_{\alpha k}) \mathcal{I}' \\ &= - \sum_k \frac{\mathbf{V}_k^T \cdot \mathbf{V}_k}{\omega_k^2} \mathcal{I}' \end{aligned} \quad (\text{C.6})$$

with $\mathcal{I}' \equiv \text{diag}(\mathbf{I}, \mathbf{0})$. Therefore, one can see that this component is the same as the counter-term (previously defined). As consequence of this, the boundary term will be canceled with the renormalized term associated to $\mathcal{G}^<(t, t) \cdot \mathcal{K}_{\text{eff}}$. This is in agreement with the explanation given by Tuovinen et al. [63], whom state that the boundary terms can be neglected for long times. However, this approximation fails for short times while our approach is valid for all time scale. The boundary term at $\tau = t_0$ is neglected because when initial time goes to $-\infty$, this term is equal to zero. Then, to evaluate the derivative of $\mathcal{G}^<$, the equation of motion given above can be used. In the end, one finds

$$\int d\tau \mathcal{G}^<(t, \tau) \mathcal{S}^A(\tau, t) = \sum_\alpha \mathcal{G}^<(t, t) \cdot \mathcal{K}^T(t) \cdot \mathcal{L}_\alpha^{(0)}. \quad (\text{C.7})$$

The second term of the convolution reads

$$\begin{aligned} \int d\tau \mathcal{G}^R(t, \tau) \cdot \mathcal{S}^<(\tau, t) &= \sum_\alpha \int_{t_0}^t d\tau \mathcal{G}^R(t, \tau) \cdot \mathcal{L}_\alpha^{(0)} [C_\alpha(\tau - t) - \partial_\tau \delta(\tau - t)] \\ &= \sum_\alpha \int_{t_0}^t d\tau \mathcal{G}^R(t, \tau) \cdot \mathcal{L}_\alpha^{(0)} C_\alpha(\tau - t) \\ &\quad - \left[\sum_\alpha \delta(\tau - t) \mathcal{G}^R(t, \tau) \cdot \mathcal{L}_\alpha^{(0)} \right]_{\tau=t_0}^{\tau=t} + \sum_\alpha \frac{1}{2} \partial_\tau \mathcal{G}^R(t, \tau)|_{\tau=t} \cdot \mathcal{L}_\alpha^{(0)} \end{aligned}$$

These boundary terms will be canceled with similar terms rising from the evaluation of the convolution of its complex conjugate. Therefore, these can be removed from the final expression.

Accordingly, by using the equation of motion for the retarded Green's function, the third term of the previous equation turns into

$$\begin{aligned} \partial_\tau \mathcal{G}^R(t, \tau)|_{\tau=t} \cdot \mathcal{L}_\alpha^{(0)} &= \delta(t, \tau)|_{\tau=t} \mathcal{Q}^T \cdot \mathcal{L}_\alpha^{(0)} + \mathcal{G}^R(t, t) \cdot \mathcal{K}_{\text{eff}}^T \cdot \mathcal{L}_\alpha^{(0)} \\ &+ \int dt_2 \mathcal{G}^R(t, t_2) \cdot \mathcal{S}^A(t_2, t) \cdot \mathcal{Q}^T \cdot \mathcal{L}_\alpha^{(0)} \end{aligned} \quad (\text{C.8})$$

Here, the last term vanishes¹ and the same-time retarded Green's function can be obtained from its definition

$$\mathcal{G}^R(\tau, \tau') = -i\Theta(\tau - \tau') \begin{pmatrix} \left\langle \begin{matrix} [\mathbf{u}(\tau), \mathbf{u}^T(\tau')]_- \\ [\mathbf{p}(\tau), \mathbf{u}^T(\tau')]_- \end{matrix} \right\rangle & \left\langle \begin{matrix} [\mathbf{u}(\tau), \mathbf{p}^T(\tau')]_- \\ [\mathbf{p}(\tau), \mathbf{p}^T(\tau')]_- \end{matrix} \right\rangle \end{pmatrix}.$$

Namely,

$$\mathcal{G}^R(\tau, \tau) = -\frac{i}{2} \begin{pmatrix} \left\langle \begin{matrix} [\mathbf{u}(\tau), \mathbf{u}^T(\tau)]_- \\ [\mathbf{p}(\tau), \mathbf{u}^T(\tau)]_- \end{matrix} \right\rangle & \left\langle \begin{matrix} [\mathbf{u}(\tau), \mathbf{p}^T(\tau)]_- \\ [\mathbf{p}(\tau), \mathbf{p}^T(\tau)]_- \end{matrix} \right\rangle \end{pmatrix} = -\frac{i}{2} \begin{pmatrix} \mathbf{0} & i\mathbf{I} \\ -i\mathbf{I} & \mathbf{0} \end{pmatrix} = \frac{1}{2} \mathcal{Q}.$$

Thus, the second term of the convolution is finally given by

$$\begin{aligned} \int d\tau \mathcal{G}^R(t, \tau) \cdot \mathcal{S}^<(\tau, t) &= \sum_\alpha \int_{t_0}^t d\tau \mathcal{G}^R(t, \tau) \cdot \mathcal{L}_\alpha^{(0)} C_\alpha(\tau - t) \\ &+ \sum_\alpha \frac{1}{2} \left[\delta(t, \tau)|_{\tau=t} \mathcal{Q}^T \cdot \mathcal{L}_\alpha^{(0)} + \frac{1}{2} \mathcal{Q} \cdot \mathcal{K}^T \cdot \mathcal{L}_\alpha^{(0)} \right]. \end{aligned} \quad (\text{C.9})$$

Similar to the first term, the **third term** of the convolution becomes,

$$\begin{aligned} \int d\tau \mathcal{S}^R(t, \tau) \cdot \mathcal{G}^<(\tau, t) &= \sum_\alpha \int_{t_0}^t d\tau [-2\partial_\tau \delta(t - \tau)] \mathcal{L}_\alpha^{(0)} \cdot \mathcal{G}^<(\tau, t) \\ &= \sum_\alpha \left[-2\delta(t - \tau) \mathcal{L}_\alpha^{(0)} \cdot \mathcal{G}^<(\tau, t) \right]_{\tau=t_0}^{\tau=t} + \sum_\alpha \mathcal{L}_\alpha^{(0)} \cdot \partial_\tau \mathcal{G}^<(\tau, t)|_{\tau=t} \\ &= \sum_\alpha \mathcal{L}_\alpha^{(0)} \cdot \mathcal{K} \cdot \mathcal{G}^<(t, t) \end{aligned} \quad (\text{C.10})$$

To get the **fourth term**, the same procedure as performed for the second term must be done, i.e.,

$$\begin{aligned} \int d\tau \mathcal{S}^<(t, \tau) \cdot \mathcal{G}^A(\tau, t) &= \sum_\alpha \int_{t_0}^t d\tau \mathcal{L}_\alpha^{(0)} \cdot \mathcal{G}^A(\tau, t) C_\alpha(t - \tau) \\ &+ \left[\sum_\alpha \delta(t - \tau) \mathcal{L}_\alpha^{(0)} \cdot \mathcal{G}^A(t, \tau) \right]_{\tau=t_0}^{\tau=t} - \sum_\alpha \frac{1}{2} \mathcal{L}_\alpha^{(0)} \cdot \partial_\tau \mathcal{G}^A(\tau, t)|_{\tau=t} \end{aligned}$$

¹These relations are used in all the derivations

$$\mathcal{L}_\alpha^{(0)} \cdot \mathcal{Q}^T \cdot \mathcal{L}_\alpha^{(0)} = \mathcal{L}_\alpha^{(0)} \cdot \mathcal{Q} \cdot \mathcal{L}_\alpha^{(0)} = \begin{pmatrix} \mathbf{0} & \mathbf{0} \\ \mathbf{0} & \mathbf{0} \end{pmatrix}, \quad \mathcal{K}_{\text{eff}}^T \cdot \mathcal{L}_\alpha^{(0)} = \mathcal{K}^T \cdot \mathcal{L}_\alpha^{(0)} = \begin{pmatrix} \mathbf{0} & \mathbf{0} \\ \Lambda_\alpha^{(0)} & \mathbf{0} \end{pmatrix}.$$

As it was mentioned above, these boundaries terms will be canceled. Hence, the equation of motion for \mathcal{G}^A reads

$$\begin{aligned} \frac{\partial}{\partial t} \mathcal{L}_\alpha^{(0)} \cdot \mathcal{G}^A(t, t')|_{t'=t} &= \delta(t - t')|_{t'=t} \mathcal{L}_\alpha^{(0)} \cdot \mathcal{Q} + \mathcal{L}_\alpha^{(0)} \cdot \mathcal{K}_{\text{eff}}(t) \cdot \mathcal{G}^A(t, t) \\ &+ \mathcal{L}_\alpha^{(0)} \cdot \mathcal{Q} \cdot \int dt_2 \mathcal{S}^R(t, t_2) \cdot \mathcal{G}^A(t_2, t) \end{aligned}$$

Therefore,

$$\begin{aligned} \int d\tau \mathcal{S}^<(t, \tau) \cdot \mathcal{G}^A(\tau, t) &= \sum_\alpha \int_{t_0}^t d\tau C_\alpha(t - \tau) \mathcal{L}_\alpha^{(0)} \cdot \mathcal{G}^A(\tau, t) \\ &- \sum_\alpha \frac{1}{2} \left[\delta(t, \tau)|_{\tau=t} \mathcal{L}_\alpha^{(0)} \cdot \mathcal{Q} + \frac{1}{2} \mathcal{L}_\alpha^{(0)} \cdot \mathcal{K} \cdot \mathcal{Q}^T \right] \end{aligned} \quad (\text{C.11})$$

Replacing the four terms into the equation of motion for $\mathcal{G}^<(t, t)$ (see Eq. (4.15)), and taking in account that the boundary terms have been already canceled with the counter-terms associated to $\mathcal{K}_{\text{eff}} \cdot \mathcal{G}^<(t, t)$ and $\mathcal{G}^<(t, t) \cdot \mathcal{K}_{\text{eff}}^T$, this equation is written as

$$\begin{aligned} \frac{\partial}{\partial t} \mathcal{G}^<(t, t) &= \mathcal{K} \cdot \mathcal{G}^<(t, t) + \mathcal{G}^<(t, t) \cdot \mathcal{K}^T \\ &+ \mathcal{Q} \cdot \left[\mathcal{L}^{(0)} \cdot \mathcal{K} \cdot \mathcal{G}^<(t, t) + \sum_\alpha \int_{t_0}^t d\tau C_\alpha(t - \tau) \mathcal{L}_\alpha^{(0)} \cdot \mathcal{G}^A(\tau, t) - \frac{1}{4} \left(\mathcal{L}^{(0)} \cdot \mathcal{K} \cdot \mathcal{Q}^T \right) \right] \\ &+ \left[\mathcal{G}^<(t, t) \cdot \mathcal{K}^T \cdot \mathcal{L}^{(0)} + \sum_\alpha \int_{t_0}^t d\tau \mathcal{G}^R(t, \tau) \cdot \mathcal{L}_\alpha^{(0)} C_\alpha(\tau - t) + \frac{1}{4} \left(\mathcal{Q} \cdot \mathcal{K}^T \cdot \mathcal{L}^{(0)} \right) \right] \cdot \mathcal{Q}^T. \end{aligned} \quad (\text{C.12})$$

Drude regularization case

The imaginary component $C_\alpha(\tau)$ for the self-energies $c\mathcal{S}_\alpha^{<, >}$ can be also obtained when $\tau = t - t' < 0$. This reads as

$$C_\alpha(\tau) = -ik_B T_\alpha \omega_c e^{\omega_c \tau} - i \sum_{p=1}^{N_P} R_{\alpha, p} (\omega_c e^{\omega_c \tau} - \chi_{\alpha, p} e^{\chi_{\alpha, p} \tau})$$

where $R_{\alpha, p} = \frac{2k_B T_\alpha \omega_c^2}{\omega_c^2 - \chi_{\alpha, p}^2} \eta_p$ and $\chi_{\alpha, p} = -i2k_B T_\alpha \xi_p$. In the same way to $\tau = t - t' > 0$, $\mathcal{S}^{<, >}(t, t') =$

$\frac{\partial}{\partial t} \mathcal{N}^{<, >}(t, t')$ has also been set, where $\mathcal{N}^{<, >}(t, t')$ matrices are defined as

$$\mathcal{N}_\alpha^{<, >}(t, t') = \sum_{p=0}^{N_P} a_{\alpha, p}^{*, <, >} e^{b_{\alpha, p}^{*, <, >}(t-t')} \mathcal{L}_\alpha^{(0)} = \sum_{p=0}^{N_P} \mathcal{N}_{\alpha, p}(t, t') \quad (\text{C.13})$$

with

$$a_{\alpha,0}^{*,<,>} = \mp \frac{\omega_c}{2} - i \left(k_B T_\alpha + \sum_{p=1}^{N_P} R_{\alpha,p} \right), \quad b_{\alpha,0}^* = \omega_c,$$
$$a_{\alpha,p \geq 1}^{*,<,>} = i R_{\alpha,p}, \quad b_{\alpha,p \geq 1}^* = \chi_{\alpha,p}.$$

BIBLIOGRAPHY

- [1] A. L. Moore and L. Shi, Emerging challenges and materials for thermal management of electronics, *Mater. Today* 17, 163 (2014).
- [2] N. Li, J. Ren, L. Wang, G. Zhang, P. Hänggi, and B. Li, Colloquium: Phononics: Manipulating heat flow with electronic analogs and beyond, *Rev. Mod. Phys.* 84, 1045 (2012).
- [3] Y. Dubi and M. Di Ventra, Colloquium: heat flow and thermoelectricity in atomic and molecular junctions, *Rev. Mod. Phys.* 83, 131 (2011).
- [4] S. Volz et al., Nanophononics: state of the art and perspectives, *Eur. Phys. J. B* 89, 15 (2016).
- [5] A. A. Balandin and D. L. Nika, Phononics in low-dimensional materials, *Mater. Today* 15, 266 (2012).
- [6] S. R. Sklan, Splash, pop, sizzle: information processing with phononic computing, *AIP Advances* 5, 053302 (2015).
- [7] E. Pop, Energy dissipation and transport in nanoscale devices, *Nano Res.* 3, 147 (2010).
- [8] Z. Yan, G. Liu, J. M. Khan, and A. A. Balandin, Graphene quilts for thermal management of high-power GaN transistors, *Nat. Commun.* 3, 827 (2012).
- [9] G. J. Snyder and E. S. Toberer, Complex thermoelectric materials, *Nat. Mater.* 7, 105 (2008).
- [10] K. Biswas, J. He, I. D. Blum, C.-I. Wu, T. P. Hogan, D. N. Seidman, V. P. Dravid, and M. G. Kanatzidis, High-performance bulk thermoelectrics with all-scale hierarchical architectures, *Nature* 489, 414 (2012).
- [11] M. Aspelmeyer, T. J. Kippenberg, and F. Marquardt, Cavity optomechanics, *Rev. Mod. Phys.* 86, 1391 (2014).

- [12] R. P. G. McNeil, M. Kataoka, C. J. B. Ford, C. H. W. Barnes, D. Anderson, G. A. C. Jones, I. Farrer, and D. A. Ritchie, On-demand single-electron transfer between distant quantum dots, *Nature* 477, 439 (2011).
- [13] S. Hermelin, S. Takada, M. Yamamoto, S. Tarucha, A. D. Wieck, L. Saminadayar, C. Bäuerle, and T. Meunier, Electrons surfing on a sound wave as a platform for quantum optics with flying electrons, *Nature* 477, 435 (2011).
- [14] C. Rossignol, N. Chigarev, M. Ducouso, B. Audoin, G. Forget, F. Guillemot, and M. C. Durrieu, In-vitro picosecond ultrasonics in a single cell, *Appl. Phys. Lett.* 93, 123901 (2008).
- [15] L. G. C. Rego and G. Kirczenow, Quantized thermal conductance of dielectric quantum wires, *Phys. Rev. Lett.* 81, 232 (1998).
- [16] K. Schwab, E. A. Henriksen, J. M. Worlock, and M. L. Roukes, Measurement of the quantum of thermal conductance, *Nature* 404, 974 (2000).
- [17] L. Cui, W. Jeong, S. Hur, M. Matt, J. C. Klöckner, F. Pauly, P. Nielaba, J. C. Cuevas, E. Meyhofer, and P. Reddy, Quantized thermal transport in single-atom junctions, *Science* (2017).
- [18] N. Mosso, U. Drechsler, F. Menges, P. Nirmalraj, S. Karg, H. Riel, and B. Gotsmann, Heat transport through atomic contacts, *Nat. Nanotech.* (2017).
- [19] A. Sikora, H. Ftouni, J. Richard, C. Hébert, D. Eon, F. Omnés, and O. Bourgeois, Highly sensitive thermal conductivity measurements of suspended membranes (SiN and diamond) using a 3ω -Völklein method, *Rev. Sci. Instrum.* 83, 054902 (2012).
- [20] A. Sikora, H. Ftouni, J. Richard, C. Hébert, D. Eon, F. Omnés, and O. Bourgeois, Erratum: Highly sensitive thermal conductivity measurements of suspended membranes (SiN and diamond) using a 3ω -Völklein method [*Rev. Sci. Instrum.* 83, 054902 (2012)], *Rev. Sci. Instrum.* 84, 029901 (2013).
- [21] K. T. Regner, D. P. Sellan, Z. Su, C. H. Amon, A. J. H. McGaughey, and J. A. Malen, Broadband phonon mean free path contributions to thermal conductivity measured using frequency domain thermoreflectance, *Nat. Commun.* 4, 1640 (2013).
- [22] D. G. Cahill, W. K. Ford, K. E. Goodson, G. D. Mahan, A. Majumdar, H. J. Maris, R. Merlin, and S. R. Phillpot, Nanoscale thermal transport, *J. Appl. Phys.* 93, 793 (2003).
- [23] K. Kim, W. Jeong, W. Lee, and P. Reddy, Ultra-high vacuum scanning thermal microscopy for nanometer resolution quantitative thermometry, *ACS Nano* 6, 4248 (2012).
- [24] K. Kim, J. Chung, J. Won, O. Kwon, J. S. Lee, S. H. Park, and Y. K. Choi, Quantitative scanning thermal microscopy using double scan technique, *Appl. Phys. Lett.* 93, 203115 (2008).

- [25] Y. Zhou, Z. Fan, G. Qin, J.-Y. Yang, T. Ouyang, and M. Hu, Methodology perspective of computing thermal transport in low-dimensional materials and nanostructures: the old and the new, *ACS Omega* 3, 3278 (2018).
- [26] R. Kubo, Statistical-mechanical theory of irreversible processes. I. General theory and simple applications to magnetic and conduction problems, *J. Phys. Soc. Jap.* 12, 570 (1957).
- [27] F. Müller-Plathe, A simple nonequilibrium molecular dynamics method for calculating the thermal conductivity, *J. Chem. Phys.* 106, 6082 (1997).
- [28] P. Jund and R. Jullien, Molecular-dynamics calculation of the thermal conductivity of vitreous silica, *Phys. Rev. B* 59, 13707 (1999).
- [29] W. Li, J. Carrete, N. A. Katcho, and N. Mingo, ShengBTE: a solver of the Boltzmann transport equation for phonons, *Comp. Phys. Commun.* 185, 1747 (2014).
- [30] G. Fugallo, M. Lazzeri, L. Paulatto, and F. Mauri, Ab initio variational approach for evaluating lattice thermal conductivity, *Phys. Rev. B* 88, 045430 (2013).
- [31] M. Dove, M. Dove, M. Hochella, R. Liebermann, and A. Putnis, Introduction to lattice dynamics, *Cambridge Topics in Mineral Physics and Chemistry* (Cambridge University Press, , 1993).
- [32] N. Mingo and L. Yang, Phonon transport in nanowires coated with an amorphous material: An atomistic Green's function approach, *Phys. Rev. B* 68, 245406 (2003).
- [33] W. Zhang, T. S. Fisher, and N. Mingo, The atomistic Green's function method: an efficient simulation approach for nanoscale phonon transport, *Numer. Heat Tr. B-Fund* 51, 333 (2007).
- [34] W. Zhang, N. Mingo, and T. S. Fisher, Simulation of phonon transport across a non-polar nanowire junction using an atomistic Green's function method, *Phys. Rev. B* 76, 195429 (2007).
- [35] J.-S. Wang, B. K. Agarwalla, H. Li, and J. Thingna, Nonequilibrium Green's function method for quantum thermal transport, *Frontiers of Physics* 9, 673 (2014).
- [36] M. C. Wingert, S. Kwon, M. Hu, D. Poulikakos, J. Xiang, and R. Chen, Sub-amorphous thermal conductivity in ultrathin crystalline silicon nanotubes, *Nano Lett.* 15, 2605 (2015).
- [37] Y. Wang, A. Vallabhaneni, J. Hu, B. Qiu, Y. P. Chen, and X. Ruan, Phonon lateral confinement enables thermal rectification in asymmetric single-material nanostructures, *Nano Lett.* 14, 592 (2014).
- [38] Y. Zhou, X. Gong, B. Xu, and M. Hu, Decouple electronic and phononic transport in nanotwinned structures: a new strategy for enhancing the figure-of-merit of thermoelectrics, *Nanoscale* 9, 9987 (2017).

- [39] J. Wang and J.-S. Wang, Dimensional crossover of thermal conductance in nanowires, *Appl. Phys. Lett.* 90, 241908 (2007).
- [40] J. Hu, X. Ruan, and Y. P. Chen, Thermal conductivity and thermal rectification in graphene nanoribbons: a molecular dynamics study, *Nano Lett.* 9, 2730 (2009).
- [41] Y. Xu, X. Chen, J.-S. Wang, B.-L. Gu, and W. Duan, Thermal transport in graphene junctions and quantum dots, *Phys. Rev. B* 81, 195425 (2010).
- [42] A. Balandin and K. L. Wang, Effect of phonon confinement on the thermoelectric figure of merit of quantum wells, *J. Appl. Phys.* 84, 6149 (1998).
- [43] M. Kazan, G. Guisbiers, S. Pereira, M. R. Correia, P. Masri, A. Bruyant, S. Volz, and P. Royer, Thermal conductivity of silicon bulk and nanowires: effects of isotopic composition, phonon confinement, and surface roughness, *J. Appl. Phys.* 107, 083503 (2010).
- [44] W. Park et al., Phonon conduction in silicon nanobeam labyrinths, *Sci. Rep.* 7, 6233 (2017).
- [45] J. H. Seol et al., Two-dimensional phonon transport in supported graphene, *Science* 328, 213 (2010).
- [46] M. R. Wagner, B. Graczykowski, J. S. Reparaz, A. El Sachat, M. Sledzinska, F. Alzina, and C. M. Sotomayor Torres, Two-dimensional phononic crystals: disorder matters, *Nano Lett.* 16, 5661 (2016).
- [47] R. Anufriev, A. Ramiere, J. Maire, and M. Nomura, Heat guiding and focusing using ballistic phonon transport in phononic nanostructures, *Nat. Commun.* 8, 15505 (2017).
- [48] D. Segal and A. Nitzan, Molecular heat pump, *Phys. Rev. E* 73, 026109 (2006).
- [49] J. Ren, P. Hänggi, and B. Li, Berry-phase-induced heat pumping and its impact on the fluctuation theorem, *Phys. Rev. Lett.* 104, 170601 (2010).
- [50] M. Galperin, K. Saito, A. V. Balatsky, and A. Nitzan, Cooling mechanisms in molecular conduction junctions, *Phys. Rev. B* 80, 115427 (2009).
- [51] D. Segal and A. Nitzan, Spin-boson thermal rectifier, *Phys. Rev. Lett.* 94, 034301 (2005).
- [52] D. Segal, Heat flow in nonlinear molecular junctions: master equation analysis, *Phys. Rev. B* 73, 205415 (2006).
- [53] D. Wei, M. Obstbaum, M. Ribow, C. H. Back, and G. Woltersdorf, Spin Hall voltages from AC and DC spin currents, *Nat. Commun.* 5, 3768 (2014).
- [54] L. Bocklage, Coherent THz transient spin currents by spin pumping, *Phys. Rev. Lett.* 118, 257202 (2017).
- [55] A. Croy and U. Saalmann, Propagation scheme for nonequilibrium dynamics of electron transport in nanoscale devices, *Phys. Rev. B* 80, 245311 (2009).

- [56] B. Popescu, P. B. Woiczikowski, M. Elstner, and U. Kleinekathöfer, Time-dependent view of sequential transport through molecules with rapidly fluctuating bridges, *Phys. Rev. Lett.* 109, 176802 (2012).
- [57] B. S. Popescu and A. Croy, Efficient auxiliary-mode approach for time-dependent nano-electronics, *New J. Phys.* 18, 093044 (2016).
- [58] S. Kurth, G. Stefanucci, C.-O. Almbladh, A. Rubio, and E. K. U. Gross, Time-dependent quantum transport: a practical scheme using density functional theory, *Phys. Rev. B* 72, 035308 (2005).
- [59] X. Zheng, F. Wang, C. Y. Yam, Y. Mo, and G. Chen, Time-dependent density-functional theory for open systems, *Phys. Rev. B* 75, 195127 (2007).
- [60] C. Oppenländer, B. Korff, and T. A. Niehaus, Higher harmonics and ac transport from time dependent density functional theory, *J. Comput. Electron.* 12, 420 (2013).
- [61] R. Biele, R. D'Agosta, and A. Rubio, Time-dependent thermal transport theory, *Phys. Rev. Lett.* 115, 056801 (2015).
- [62] M. I. Sena-Junior, L. R. F. Lima, and C. H. Lewenkopf, Phononic heat transport in nanomechanical structures: steady-state and pumping, *J. Phys. A-Math. Theor.* 50, 435202 (2017).
- [63] R. Tuovinen, N. Säkkinen, D. Karlsson, G. Stefanucci, and R. van Leeuwen, Phononic heat transport in the transient regime: an analytic solution, *Phys. Rev. B* 93, 214301 (2016).
- [64] G. Cuniberti, G. Fagas, and K. Richter, *Introducing molecular electronics*, Lecture Notes in Physics (Springer Berlin Heidelberg, , 2006).
- [65] L. Cui, R. Miao, K. Wang, D. Thompson, L. A. Zotti, J. C. Cuevas, E. Meyhofer, and P. Reddy, Peltier cooling in molecular junctions, *Nat. Nanotechnol.* 13, 122 (2018).
- [66] W. Lee, K. Kim, W. Jeong, L. A. Zotti, F. Pauly, J. C. Cuevas, and P. Reddy, Heat dissipation in atomic-scale junctions, *Nature* 498, 209 (2013).
- [67] B. Li, L. Wang, and G. Casati, Thermal diode: Rectification of heat flux, *Phys. Rev. Lett.* 93, 184301 (2004).
- [68] J. Zhu, K. Hippalgaonkar, S. Shen, K. Wang, Y. Abate, S. Lee, J. Wu, X. Yin, A. Majumdar, and X. Zhang, Temperature-gated thermal rectifier for active heat flow control, *Nano Lett.* 14, 4867 (2014).
- [69] C. W. Chang, D. Okawa, A. Majumdar, and A. Zettl, Solid-state thermal rectifier, *Science* 314, 1121 (2006).
- [70] H. Tian, D. Xie, Y. Yang, T.-L. Ren, G. Zhang, Y.-F. Wang, C.-J. Zhou, P.-G. Peng, L.-G. Wang, and L.-T. Liu, A novel solid-state thermal rectifier based on reduced graphene oxide, *Sci. Rep.* 2, (2012).

- [71] J. Lee, V. Varshney, A. K. Roy, J. B. Ferguson, and B. L. Farmer, Thermal rectification in three-dimensional asymmetric nanostructure, *Nano Lett.* 12, 3491 (2012).
- [72] T. S. Komatsu and N. Ito, Thermal diode utilizing asymmetric contacts to heat baths, *Phys. Rev. E* 81, 010103 (2010).
- [73] N. Yang, G. Zhang, and B. Li, Thermal rectification in asymmetric graphene ribbons, *Appl. Phys. Lett.* 95, 033107 (2009).
- [74] W. Kobayashi, Y. Teraoka, and I. Terasaki, An oxide thermal rectifier, *Appl. Phys. Lett.* 95, 171905 (2009).
- [75] J. Lan and B. Li, Thermal rectifying effect in two-dimensional anharmonic lattices, *Phys. Rev. B* 74, 214305 (2006).
- [76] W.-R. Zhong, D.-Q. Zheng, and B. Hu, Thermal control in graphene nanoribbons: thermal valve, thermal switch and thermal amplifier, *Nanoscale* 4, 5217 (2012).
- [77] Q.-X. Pei, Y.-W. Zhang, Z.-D. Sha, and V. B. Shenoy, Carbon isotope doping induced interfacial thermal resistance and thermal rectification in graphene, *Appl. Phys. Lett.* 100, 101901 (2012).
- [78] G. Zhang and H. Zhang, Thermal conduction and rectification in few-layer graphene Y junctions, *Nanoscale* 3, 4604 (2011).
- [79] S. Pal and I. K. Puri, Thermal AND gate using a monolayer graphene nanoribbon, *Small* 11, 2910 (2015).
- [80] S. Z. Butler et al., Progress, challenges, and opportunities in two-dimensional materials Beyond Graphene, *ACS Nano* 7, 2898 (2013).
- [81] M. Chhowalla, H. S. Shin, G. Eda, L.-J. Li, K. P. Loh, and H. Zhang, The chemistry of two-dimensional layered transition metal dichalcogenide nanosheets, *Nat. Chem.* 5, 263 (2013).
- [82] P. Miro, M. Audiffred, and T. Heine, An atlas of two-dimensional materials, *Chem. Soc. Rev.* 43, 6537 (2014).
- [83] S. Zhang, S. Guo, Z. Chen, Y. Wang, H. Gao, J. Gomez-Herrero, P. Ares, F. Zamora, Z. Zhu, and H. Zeng, Recent progress in 2D group-VA semiconductors: from theory to experiment, *Chem. Soc. Rev.* 47, 982 (2018).
- [84] L. Li, Y. Yu, G. J. Ye, Q. Ge, X. Ou, H. Wu, D. Feng, X. H. Chen, and Y. Zhang, Black phosphorus field-effect transistors, *Nat. Nanotechnol.* 9, 372 (2014).
- [85] H. Liu, A. T. Neal, Z. Zhu, Z. Luo, X. Xu, D. Tomanek, and P. D. Ye, Phosphorene: an unexplored 2D semiconductor with a high hole mobility, *ACS Nano* 8, 4033 (2014).

- [86] H. Du, X. Lin, Z. Xu, and D. Chu, Recent developments in black phosphorus transistors, *J. Mater. Chem. C* 3, 8760 (2015).
- [87] Y. Pan, Y. Wang, M. Ye, R. Quhe, H. Zhong, Z. Song, X. Peng, D. Yu, J. Yang, J. Shi, and J. Lu, Monolayer phosphorene-metal contacts, *Chem. Mater.* 28, 2100 (2016).
- [88] Z. Luo, J. Maassen, Y. Deng, Y. Du, R. P. Garrelts, M. S. Lundstrom, P. D. Ye, and X. Xu, Anisotropic in-plane thermal conductivity observed in few-layer black phosphorus, *Nat. Commun.* 6, 8572 (2015).
- [89] A. Jain and A. J. H. McGaughey, Strongly anisotropic in-plane thermal transport in single-layer black phosphorene, *Sci. Rep.* 5, (2015).
- [90] T.-H. Liu and C.-C. Chang, Anisotropic thermal transport in phosphorene: effects of crystal orientation, *Nanoscale* 7, 10648 (2015).
- [91] Z.-Y. Ong, Y. Cai, G. Zhang, and Y.-W. Zhang, Strong thermal transport anisotropy and strain modulation in single-layer phosphorene, *J. Phys. Chem. C* 118, 25272 (2014).
- [92] F. Xia, H. Wang, and Y. Jia, Rediscovering black phosphorus as an anisotropic layered material for optoelectronics and electronics, *Nat. Commun.* 5, 4458 (2014).
- [93] Z. Sofer, D. Sedmidubský, S. Huber, J. Luxa, D. Bousa, C. Boothroyd, and M. Pumera, Layered black phosphorus: strongly anisotropic magnetic, electronic, and electron-transfer properties, *Angew. Chem. Int. Edit.* 55, 3382 (2016).
- [94] R. Fei, A. Faghaninia, R. Soklaski, J.-A. Yan, C. Lo, and L. Yang, Enhanced thermoelectric efficiency via orthogonal electrical and thermal conductances in phosphorene, *Nano Lett.* 14, 6393 (2014).
- [95] Z. Shengli, Y. Zhong, L. Yafei, C. Zhongfang, and Z. Haibo, Atomically thin arsenene and antimonene: semimetal-semiconductor and indirect-direct band-gap transitions, *Angew. Chem. Inter. Ed.* 54, 3112 (2015).
- [96] C. Kamal and M. Ezawa, Arsenene: two-dimensional buckled and puckered honeycomb arsenic systems, *Phys. Rev. B* 91, 085423 (2015).
- [97] Z. Zhu, J. Guan, D. Liu, and D. Tománek, Designing isoelectronic counterparts to layered group V semiconductors, *ACS Nano* 9, 8284 (2015).
- [98] M. Zeraati, S. M. Vaez Allaei, I. Abdolhosseini Sarsari, M. Pourfath, and D. Donadio, Highly anisotropic thermal conductivity of arsenene: an ab-initio study, *Phys. Rev. B* 93, 085424 (2016).
- [99] J. R. Brent, D. J. Lewis, T. Lorenz, E. A. Lewis, N. Savjani, S. J. Haigh, G. Seifert, B. Derby, and P. O'Brien, Tin(II) sulfide (SnS) nanosheets by liquid-phase exfoliation of herzenbergite: IV-VI main group two-dimensional atomic crystals, *J. Am. Chem. Soc.* 137, 12689 (2015).

- [100] R. Fei, W. Li, J. Li, and L. Yang, Giant piezoelectricity of monolayer group IV monochalcogenides: SnSe, SnS, GeSe, and GeS, *Appl. Phys. Lett.* 107, (2015).
- [101] J. Xia, X.-Z. Li, X. Huang, N. Mao, D.-D. Zhu, L. Wang, H. Xu, and X.-M. Meng, Physical vapor deposition synthesis of two-dimensional orthorhombic SnS flakes with strong angle/temperature-dependent Raman responses, *Nanoscale* 8, 2063 (2016).
- [102] R. Guo, X. Wang, Y. Kuang, and B. Huang, First-principles study of anisotropic thermoelectric transport properties of IV-VI semiconductor compounds SnSe and SnS, *Phys. Rev. B* 92, 115202 (2015).
- [103] L.-D. Zhao, S.-H. Lo, Y. Zhang, H. Sun, G. Tan, C. Uher, C. Wolverton, V. P. Dravid, and M. G. Kanatzidis, Ultralow thermal conductivity and high thermoelectric figure of merit in SnSe crystals, *Nature* 508, 373 (2015).
- [104] R. Kappera, D. Voiry, S. E. Yalcin, B. Branch, G. Gupta, A. D. Mohite, and M. Chhowalla, Phase-engineered low-resistance contacts for ultrathin MoS₂ transistors, *Nat. Mater.* 1128 (2014).
- [105] B. Radisavljevic, A. Radenovic, J. Brivio, V. Giacometti, and A. Kis, Single-layer MoS₂ transistors, *Nat. Nanotechnol.* 6, 147 (2011).
- [106] X. Liu, G. Zhang, Q.-X. Pei, and Y.-W. Zhang, Phonon thermal conductivity of monolayer MoS₂ sheet and nanoribbons, *Appl. Phys. Lett.* 103, 133113 (2013).
- [107] J. Wu, H. Schmidt, K. K. Amara, X. Xu, G. Eda, and B. Izyilmaz, Large thermoelectricity via variable range hopping in chemical vapor deposition grown single-layer MoS₂, *Nano Lett.* 14, 2730 (2014).
- [108] R. Yan, J. R. Simpson, S. Bertolazzi, J. Brivio, M. Watson, X. Wu, A. Kis, T. Luo, A. R. Hight Walker, and H. G. Xing, Thermal conductivity of monolayer molybdenum disulfide obtained from temperature-dependent raman spectroscopy, *ACS Nano* 8, 986 (2014).
- [109] S. Sahoo, A. P. S. Gaur, M. Ahmadi, M. J.-F. Guinel, and R. S. Katiyar, Temperature-dependent raman studies and thermal conductivity of few-Layer MoS₂, *J. Phys. Chem. C* 117, 9042 (2013).
- [110] J. Liu, G.-M. Choi, and D. G. Cahill, Measurement of the anisotropic thermal conductivity of molybdenum disulfide by the time-resolved magneto-optic Kerr effect, *J. Appl. Phys.* 116, 233107 (2014).
- [111] A. A. Balandin, S. Ghosh, W. Bao, I. Calizo, D. Teweldebrhan, F. Miao, and C. N. Lau, Superior thermal conductivity of single-layer graphene, *Nano Lett.* 8, 902 (2008).
- [112] A. Taube, J. Judek, A. Lapińska, and M. Zdrojek, Temperature-dependent thermal properties of supported MoS₂ monolayers, *ACS Appl. Mater. Inter.* 7, 5061 (2015).

- [113] A. Cepellotti, G. Fugallo, L. Paulatto, M. Lazzeri, F. Mauri, and N. Marzari, Phonon hydrodynamics in two-dimensional materials, *Nat. Commun.* 6, 6400 (2015).
- [114] J.-W. Jiang, X. Zhuang, and T. Rabczuk, Orientation dependent thermal conductance in single-layer MoS₂, *Sci. Rep.* 3, 2209 (2013).
- [115] W. Li, J. Carrete, and N. Mingo, Thermal conductivity and phonon linewidths of monolayer MoS₂ from first principles, *Appl. Phys. Lett.* 103, 253103 (2013).
- [116] X. Wei, Y. Wang, Y. Shen, G. Xie, H. Xiao, J. Zhong, and G. Zhang, Phonon thermal conductivity of monolayer MoS₂: a comparison with single layer graphene, *Appl. Phys. Lett.* 105, 103902 (2014).
- [117] Y. Cai, J. Lan, G. Zhang, and Y.-W. Zhang, Lattice vibrational modes and phonon thermal conductivity of monolayer MoS₂, *Phys. Rev. B* 89, 035438 (2014).
- [118] A. Enyashin, S. Gemming, and G. Seifert, Nanosized allotropes of molybdenum disulfide, *Eur. Phys. J.-Spec. Top.* 149, 103 (2007).
- [119] H. Guo, N. Lu, J. Dai, X. Wu, and X. C. Zeng, Phosphorene nanoribbons, phosphorus nanotubes, and van der Waals multilayers, *J. Phys. Chem. C* 118, 14051 (2014).
- [120] T. Niu and A. Li, From two-dimensional materials to heterostructures, *Prog. Surf. Sci.* 90, 21 (2015).
- [121] H. Wang, F. Liu, W. Fu, Z. Fang, W. Zhou, and Z. Liu, Two-dimensional heterostructures: fabrication, characterization, and application, *Nanoscale* 6, 12250 (2014).
- [122] Y. Chen, Y. Zhang, K. Cai, J. Jiang, J.-C. Zheng, J. Zhao, and N. Wei, Interfacial thermal conductance in graphene/black phosphorus heterogeneous structures, *Carbon* 117, 399 (2017).
- [123] Y. Liu, Z.-Y. Ong, J. Wu, Y. Zhao, K. Watanabe, T. Taniguchi, D. Chi, G. Zhang, J. T. L. Thong, C.-W. Qiu, and K. Hippalgaonkar, Thermal conductance of the 2D MoS₂/h-BN and graphene/h-BN interfaces, *Sci. Rep.* 7, (2017).
- [124] Z. Yan, L. Chen, M. Yoon, and S. Kumar, Phonon transport at the interfaces of vertically stacked graphene and hexagonal boron nitride heterostructures, *Nanoscale* 8, 4037 (2016).
- [125] L. Ci, L. Song, C. Jin, D. Jariwala, D. Wu, Y. Li, A. Srivastava, Z. F. Wang, K. Storr, L. Balicas, F. Liu, and P. M. Ajayan, Atomic layers of hybridized boron nitride and graphene domains, *Nat. Mater.* 9, 430 (2010).
- [126] Y. Gao, Y. Zhang, P. Chen, Y. Li, M. Liu, T. Gao, D. Ma, Y. Chen, Z. Cheng, X. Qiu, W. Duan, and Z. Liu, Toward single-layer uniform hexagonal boron nitride-graphene patchworks with zigzag linking edges, *Nano Lett.* 13, 3439 (2013).

- [127] J. E. Barrios-Vargas, B. Mortazavi, A. W. Cummings, R. Martinez-Gordillo, M. Pruneda, L. Colombo, T. Rabczuk, and S. Roche, Electrical and thermal transport in coplanar polycrystalline graphene-hBN heterostructures, *Nano Lett.* 17, 1660 (2017).
- [128] J. Lu, L. C. Gomes, R. W. Nunes, A. H. Castro Neto, and K. P. Loh, Lattice relaxation at the interface of two-dimensional crystals: graphene and hexagonal boron-nitride, *Nano Lett.* 14, 5133 (2014).
- [129] G. Seol and J. Guo, Bandgap opening in boron nitride confined armchair graphene nanoribbon, *Appl. Phys. Lett.* 98, 143107 (2011).
- [130] Y. An, M. Zhang, D. Wu, T. Wang, Z. Jiao, C. Xia, Z. Fu, and K. Wang, The rectifying and negative differential resistance effects in graphene/h-BN nanoribbon heterojunctions, *Phys. Chem. Chem. Phys.* 18, 27976 (2016).
- [131] S. Jiuxu, Y. Yintang, L. Hongxia, and G. Lixin, Negative differential resistance in an (8, 0) carbon/boron nitride nanotube heterojunction, *J. Semicond.* 32, 042003 (2011).
- [132] Z.-Y. Zhang, C. Miao, and W. Guo, Nano-solenoid: helicoid carbon-boron nitride heteronanotube, *Nanoscale* 5, 11902 (2013).
- [133] A. C. M. Carvalho, C. G. Bezerra, J. A. Lawlor, and M. S. Ferreira, Density of states of helically symmetric boron carbon nitride nanotubes, *J. Phys.-Condens. Mat.* 26, 015303 (2014).
- [134] T. Zhu and E. Ertekin, Resolving anomalous strain effects on two-dimensional phonon flows: the cases of graphene, boron nitride, and planar superlattices, *Phys. Rev. B* 91, 205429 (2015).
- [135] X.-K. Chen, Z.-X. Xie, W.-X. Zhou, and K.-Q. Chen, The thermal conductivity in hybridised graphene and boron nitride nanoribbons modulated with strain, *J. Phys. D: Appl. Phys.* 49, 115301 (2016).
- [136] Y. Hong, J. Zhang, and X. C. Zeng, Thermal contact resistance across a linear heterojunction within a hybrid graphene/hexagonal boron nitride sheet, *Phys. Chem. Chem. Phys.* 18, 24164 (2016).
- [137] X.-K. Chen, Z.-X. Xie, W.-X. Zhou, L.-M. Tang, and K.-Q. Chen, Thermal rectification and negative differential thermal resistance behaviors in graphene/hexagonal boron nitride heterojunction, *Carbon* 100, 492 (2016).
- [138] C. da Silva, F. Saiz, D. A. Romero, and C. H. Amon, Coherent phonon transport in short-period two-dimensional superlattices of graphene and boron nitride, *Phys. Rev. B* 93, 125427 (2016).
- [139] A. Kinaci, J. B. Haskins, C. Sevik, and T. Cagin, Thermal conductivity of BN-C nanostructures, *Phys. Rev. B* 86, 115410 (2012).

- [140] T. Zhu and E. Ertekin, Phonon transport on two-dimensional graphene/boron nitride superlattices, *Phys. Rev. B* 90, 195209 (2014).
- [141] J.-W. Jiang, J.-S. Wang, and B.-S. Wang, Minimum thermal conductance in graphene and boron nitride superlattice, *Appl. Phys. Lett.* 99, 043109 (2011).
- [142] Z.-Y. Ong, G. Zhang, and Y.-W. Zhang, Controlling the thermal conductance of graphene/h-BN lateral interface with strain and structure engineering, *Phys. Rev. B* 93, 075406 (2016).
- [143] H. Sevinçli, W. Li, N. Mingo, G. Cuniberti, and S. Roche, Effects of domains in phonon conduction through hybrid boron nitride and graphene sheets, *Phys. Rev. B* 84, 205444 (2011).
- [144] C. Lin, X. Zhang, and Z. Rao, Theoretical prediction of thermal transport in BC_2N monolayer, *Nano Energy* 38, 249 (2017).
- [145] K. Yang, Y. Chen, R. D'Agosta, Y. Xie, J. Zhong, and A. Rubio, Enhanced thermoelectric properties in hybrid graphene/boron nitride nanoribbons, *Phys. Rev. B* 86, 045425 (2012).
- [146] D. Lloyd, X. Liu, J. W. Christopher, L. Cantley, A. Wadehra, B. L. Kim, B. B. Goldberg, A. K. Swan, and J. S. Bunch, Band gap engineering with ultralarge biaxial strains in suspended monolayer MoS_2 , *Nano Lett.* 16, 5836 (2016).
- [147] N. Wei, L. Xu, H.-Q. Wang, and J.-C. Zheng, Strain engineering of thermal conductivity in graphene sheets and nanoribbons: a demonstration of magic flexibility, *Nanotechnol.* 22, 105705 (2011).
- [148] Y. Wang, C. Cong, R. Fei, W. Yang, Y. Chen, B. Cao, L. Yang, and T. Yu, Remarkable anisotropic phonon response in uniaxially strained few-layer black phosphorus, *Nano Res.* 8, 3944 (2015).
- [149] H. J. Conley, B. Wang, J. I. Ziegler, J. Richard F. Haglund, S. T. Pantelides, and K. I. Bolotin, Bandgap engineering of strained monolayer and bilayer MoS_2 , *Nano Lett.* 13, 3626 (2013).
- [150] Q.-X. Pei, Y.-W. Zhang, Z.-D. Sha, and V. B. Shenoy, Tuning the thermal conductivity of silicene with tensile strain and isotopic doping: a molecular dynamics study, *J. Appl. Phys.* 114, 033526 (2013).
- [151] J.-W. Jiang, Phonon bandgap engineering of strained monolayer MoS_2 , *Nanoscale* 6, 8326 (2014).
- [152] Y. D. Kuang, L. Lindsay, S. Q. Shi, and G. P. Zheng, Tensile strains give rise to strong size effects for thermal conductivities of silicene, germanene and stanene, *Nanoscale* 8, 3760 (2016).

- [153] M. Ghorbani-Asl, S. Borini, A. Kuc, and T. Heine, Strain-dependent modulation of conductivity in single-layer transition-metal dichalcogenides, *Phys. Rev. B* 87, 235434 (2013).
- [154] M. A. Bissett, M. Tsuji, and H. Ago, Strain engineering the properties of graphene and other two-dimensional crystals, *Phys. Chem. Chem. Phys.* 16, 11124 (2014).
- [155] A. Castellanos-Gomez, V. Singh, H. S. J. van der Zant, and G. A. Steele, Mechanics of freely-suspended ultrathin layered materials, *Ann. Phys.* 527, 27 (2015).
- [156] Y. Li, Z. Hu, S. Lin, S. K. Lai, W. Ji, and S. P. Lau, Giant anisotropic raman response of encapsulated ultrathin black phosphorus by uniaxial strain, *Adv. Funct. Mater.* 27, (2016).
- [157] Y. Wang, C. Cong, W. Yang, J. Shang, N. Peimyoo, Y. Chen, J. Kang, J. Wang, W. Huang, and T. Yu, Strain-induced direct–indirect bandgap transition and phonon modulation in monolayer WS₂, *Nano Res.* 8, 2562 (2015).
- [158] J.-W. Jiang, H. S. Park, and T. Rabczuk, Molecular dynamics simulations of single-layer molybdenum disulphide (MoS₂): Stillinger-Weber parametrization, mechanical properties, and thermal conductivity, *J. Appl. Phys.* 114, 064307 (2013).
- [159] M. Bürkle, T. J. Hellmuth, F. Pauly, and Y. Asai, First-principles calculation of the thermoelectric figure of merit for [2,2]paracyclophane-based single-molecule junctions, *Phys. Rev. B* 91, 165419 (2015).
- [160] P. Reddy, S.-Y. Jang, R. A. Segalman, and A. Majumdar, Thermoelectricity in molecular junctions, *Science* 315, 1568 (2007).
- [161] K. Baheti, J. A. Malen, P. Doak, P. Reddy, S.-Y. Jang, T. D. Tilley, A. Majumdar, and R. A. Segalman, Probing the chemistry of molecular heterojunctions using thermoelectricity, *Nano Lett.* 8, 715 (2008).
- [162] D. Manzano, M. Tiersch, A. Asadian, and H. J. Briegel, Quantum transport efficiency and Fourier’s law, *Phys. Rev. E* 86, 061118 (2012).
- [163] M. Buerkle and Y. Asai, Thermal conductance of teflon and polyethylene: insight from an atomistic, single-molecule level, *Sci. Rep.* 7, (2017).
- [164] J. C. Klöckner, M. Bürkle, J. C. Cuevas, and F. Pauly, Length dependence of the thermal conductance of alkane-based single-molecule junctions: an ab initio study, *Phys. Rev. B* 94, 205425 (2016).
- [165] A. Pecchia, G. Romano, and A. Di Carlo, Theory of heat dissipation in molecular electronics, *Phys. Rev. B* 75, 035401 (2007).
- [166] Z. Wang, J. A. Carter, A. Lagutchev, Y. K. Koh, N.-H. Seong, D. G. Cahill, and D. D. Dlott, Ultrafast flash thermal conductance of molecular chains, *Science* 317, 787 (2007).

- [167] S. Plimpton, Fast parallel algorithms for short-range molecular dynamics, *J. Comp. Phys.* 117, 1 (1995).
- [168] R. Parr and Y. Weitao, Density-functional theory of atoms and molecules, International Series of Monographs on Chemistry (Oxford University Press, , 1994).
- [169] D. Rapaport, The art of molecular dynamics simulation (Cambridge University Press, , 1997).
- [170] K. Varga and J. Driscoll, Computational nanoscience: applications for molecules, clusters, and solids (Cambridge University Press, , 2011).
- [171] Z. Gang, Nanoscale energy transport and harvesting: a computational study (Pan Stanford, , 2015).
- [172] D. Frenkel and B. Smit, Understanding molecular simulation: from algorithms to applications, Computational science series (Elsevier Science, , 2001).
- [173] L. Verlet, Computer "experiments" on classical fluids. I. Thermodynamical properties of Lennard-Jones molecules, *Phys. Rev.* 159, 98 (1967).
- [174] W. C. Swope, H. C. Andersen, P. H. Berens, and K. R. Wilson, A computer simulation method for the calculation of equilibrium constants for the formation of physical clusters of molecules: application to small water clusters, *J. Chem. Phys.* 76, 637 (1982).
- [175] F. Gatti, Molecular quantum dynamics: from theory to applications, Physical Chemistry in Action (Springer Berlin Heidelberg, , 2014).
- [176] J. Chen, G. Zhang, and B. Li, Substrate coupling suppresses size dependence of thermal conductivity in supported graphene, *Nanoscale* 5, 532 (2013).
- [177] J. Tersoff, New empirical approach for the structure and energy of covalent systems, *Phys. Rev. B* 37, 6991 (1988).
- [178] J. Tersoff, Empirical interatomic potential for carbon, with applications to amorphous carbon, *Phys. Rev. Lett.* 61, 2879 (1988).
- [179] H. A. Lorentz, Ueber die Anwendung des Satzes vom Virial in der kinetischen Theorie der Gase, *Ann. Phys.* 248, 127 (1881).
- [180] A. Dhar, Heat transport in low-dimensional systems, *Adv. Phys.* 57, 457 (2008).
- [181] H. J. C. Berendsen, J. P. M. Postma, W. F. van Gunsteren, A. DiNola, and J. R. Haak, Molecular dynamics with coupling to an external bath, *J. Chem. Phys.* 81, 3684 (1984).
- [182] E. Rosta, N.-V. Buchete, and G. Hummer, Thermostat artifacts in replica exchange molecular dynamics simulations, *J. Chem. Theory Comput.* 5, 1393 (2009).

- [183] P. H. Hünenberger, in *Advanced computer simulation: approaches for soft matter sciences I*, edited by C. Dr. Holm and K. Prof. Dr. Kremer (Springer Berlin Heidelberg, Berlin, Heidelberg, 2005), pp. 105–149.
- [184] P. K. Schelling, S. R. Phillpot, and P. Keblinski, Comparison of atomic-level simulation methods for computing thermal conductivity, *Phys. Rev. B* 65, 144306 (2002).
- [185] J. R. Lukes, D. Y. Li, X. G. Liang, and C. L. Tien, Molecular dynamics study of solid thin-film thermal conductivity, *J. Heat Transf.* 122, 536 (2000).
- [186] A. Tenenbaum, G. Ciccotti, and R. Gallico, Stationary nonequilibrium states by molecular dynamics. Fourier's law, *Phys. Rev. A* 25, 2778 (1982).
- [187] J. Shiomi and S. Maruyama, Molecular dynamics of diffusive-ballistic heat conduction in single-walled carbon nanotubes, *Jpn. J. Appl. Phys.* 47, 2005 (2008).
- [188] P. B. Allen, J. L. Feldman, J. Fabian, and F. Wooten, Diffusons, locons and propagons: character of atomic vibrations in amorphous Si, *Philos. Mag. B* 79, 1715 (1999).
- [189] A. Bodapati, P. K. Schelling, S. R. Phillpot, and P. Keblinski, Vibrations and thermal transport in nanocrystalline silicon, *Phys. Rev. B* 74, 245207 (2006).
- [190] J. M. Dickey and A. Paskin, Computer simulation of the lattice dynamics of solids, *Phys. Rev.* 188, 1407 (1969).
- [191] J. M. Haile, *Molecular dynamics simulation: elementary methods*, A Wiley-Interscience publication (Wiley, , 1997).
- [192] J. Chen, G. Zhang, and B. Li, Remarkable reduction of thermal conductivity in silicon nanotubes, *Nano Lett.* 10, 3978 (2010).
- [193] P. K. Schelling and S. R. Phillpot, Mechanism of thermal transport in zirconia and yttria-stabilized zirconia by molecular-dynamics simulation, *J. Am. Chem. Soc.* 84, 2997 (2001).
- [194] L. Medrano Sandonas, R. Gutierrez, A. Dianat, and G. Cuniberti, Engineering thermal rectification in MoS₂ nanoribbons: a non-equilibrium molecular dynamics study, *RSC Adv.* 5, 54345 (2015).
- [195] L. Medrano Sandonas, G. Cuba-Supanta, R. Gutierrez, A. Dianat, C. V. Landauro, and G. Cuniberti, Enhancement of thermal transport properties of asymmetric Graphene/hBN nanoribbon heterojunctions by substrate engineering, *Carbon* 124, 642 (2017).
- [196] T.-H. Liu, Y.-C. Chen, C.-W. Pao, and C.-C. Chang, Anisotropic thermal conductivity of MoS₂ nanoribbons: chirality and edge effects, *Appl. Phys. Lett.* 104, 201909 (2014).
- [197] V. Varshney, S. S. Patnaik, C. Muratore, A. K. Roy, A. A. Voevodin, and B. L. Farmer, MD simulations of molybdenum disulphide (MoS₂): force-field parameterization and thermal transport behavior, *Comp. Mater. Sci.* 48, 101 (2010).

- [198] M. Buscema, M. Barkelid, V. Zwiller, H. S. J. van der Zant, G. A. Steele, and A. Castellanos-Gomez, Large and tunable photothermoelectric effect in single-layer MoS₂, *Nano Lett.* 13, 358 (2013).
- [199] T. Onodera et al., A computational chemistry study on friction of h-MoS₂. Part I. Mechanism of single sheet lubrication, *J. Phys. Chem. B* 113, 16526 (2009).
- [200] T. Onodera et al., A computational chemistry study on friction of h-MoS₂. Part II. Friction anisotropy, *J. Phys. Chem. B* 114, 15832 (2010).
- [201] B. J. van Wees, H. van Houten, C. W. J. Beenakker, J. G. Williamson, L. P. Kouwenhoven, D. van der Marel, and C. T. Foxon, Quantized conductance of point contacts in a two-dimensional electron gas, *Phys. Rev. Lett.* 60, 848 (1988).
- [202] L. Zhu and B. Li, Low thermal conductivity in ultrathin carbon nanotube (2, 1), *Sci. Rep.* 4, 4917 (2014).
- [203] B. Liu, J. A. Baimova, C. D. Reddy, S. V. Dmitriev, W. K. Law, X. Q. Feng, and K. Zhou, Interface thermal conductance and rectification in hybrid graphene/silicene monolayer, *Carbon* 79, 236 (2014).
- [204] W. Cai, A. L. Moore, Y. Zhu, X. Li, S. Chen, L. Shi, and R. S. Ruoff, Thermal transport in suspended and supported monolayer graphene grown by chemical vapor deposition, *Nano Lett.* 10, 1645 (2010).
- [205] X. Zhang, H. Bao, and M. Hu, Bilateral substrate effect on the thermal conductivity of two-dimensional silicon, *Nanoscale* 7, 6014 (2015).
- [206] J. Zhang, Y. Hong, Z. Tong, Z. Xiao, H. Bao, and Y. Yue, Molecular dynamics study of interfacial thermal transport between silicene and substrates, *Phys. Chem. Chem. Phys.* 17, 23704 (2015).
- [207] Z. Wang, T. Feng, and X. Ruan, Thermal conductivity and spectral phonon properties of free-standing and supported silicene, *J. Appl. Phys.* 117, 084317 (2015).
- [208] G. C. Correa, C. J. Foss, and Z. Aksamija, Interface thermal conductance of van der Waals monolayers on amorphous substrates, *Nanotechnol.* 28, 135402 (2017).
- [209] J. Zhang, Y. Hong, M. Liu, Y. Yue, Q. Xiong, and G. Lorenzini, Molecular dynamics simulation of the interfacial thermal resistance between phosphorene and silicon substrate, *Int. J. Heat Mass Tran.* 104, 871 (2017).
- [210] S. Munetoh, T. Motooka, K. Moriguchi, and A. Shintani, Interatomic potential for Si-O systems using Tersoff parameterization, *Comp. Mater. Sci.* 39, 334 (2007).
- [211] T. Kumagai, S. Izumi, S. Hara, and S. Sakai, Development of bond-order potentials that can reproduce the elastic constants and melting point of silicon for classical molecular dynamics simulation, *Comp. Mater. Sci.* 39, 457 (2007).

- [212] J. Tersoff, Modeling solid-state chemistry: Interatomic potentials for multicomponent systems, *Phys. Rev. B* 39, 5566 (1989).
- [213] M. Neek-Amal and F. M. Peeters, Graphene on boron-nitride: Moiré pattern in the van der Waals energy, *Appl. Phys. Lett.* 104, 041909 (2014).
- [214] E. P. Bellido and J. M. Seminario, Molecular dynamics simulations of folding of supported graphene, *J. Phys. Chem. C* 114, 22472 (2010).
- [215] K. Gordiz and S. M. V. Allaei, Thermal rectification in pristine-hydrogenated carbon nanotube junction: a molecular dynamics study, *J. Appl. Phys.* 115, 163512 (2014).
- [216] B. Li, J. Lan, and L. Wang, Interface thermal resistance between dissimilar anharmonic lattices, *Phys. Rev. Lett.* 95, 104302 (2005).
- [217] M. Alaghemandi, F. Leroy, F. Müller-Plathe, and M. C. Böhm, Thermal rectification in nanosized model systems: a molecular dynamics approach, *Phys. Rev. B* 81, 125410 (2010).
- [218] L. Medrano Sandonas, D. Teich, R. Gutierrez, T. Lorenz, A. Pecchia, G. Seifert, and G. Cuniberti, Anisotropic thermoelectric response in two-dimensional puckered structures, *J. Phys. Chem. C* 120, 18841 (2016).
- [219] L. Medrano Sandonas, H. Sevincli, R. Gutierrez, and G. Cuniberti, First-principle-based phonon transport properties of nanoscale graphene grain boundaries, *Adv. Sci.* 1700365 (2018).
- [220] L. Medrano Sandonas, R. Gutierrez, A. Pecchia, A. Dianat, and G. Cuniberti, Thermoelectric properties of functionalized graphene grain boundaries, *J. Self-Assem. Mol. Electron.* 3, 1 (2015).
- [221] L. Medrano Sandonas, R. Gutierrez, A. Pecchia, G. Seifert, and G. Cuniberti, Tuning quantum electron and phonon transport in two-dimensional materials by strain engineering: a Green's function based study, *Phys. Chem. Chem. Phys.* 19, 1487 (2017).
- [222] S. Volz, Thermal nanosystems and nanomaterials, *Topics in Applied Physics* (Springer Berlin Heidelberg, , 2009).
- [223] J.-S. Wang, J. Wang, and J. T. Lü, Quantum thermal transport in nanostructures, *Eur. Phys. J. B* 62, 381 (2008).
- [224] G. Stefanucci and R. van Leeuwen, Nonequilibrium many-body theory of quantum systems: A modern introduction (Cambridge University Press, , 2013).
- [225] P. C. Martin and J. Schwinger, Theory of many-particle systems. I, *Phys. Rev.* 115, 1342 (1959).
- [226] L. Kadanoff and G. Baym, Quantum statistical mechanics: Green's function methods in equilibrium and nonequilibrium problems, *Frontiers in physics* (W.A. Benjamin, , 1962).

- [227] L. V. Keldysh, Diagram technique for nonequilibrium processes, *Zh. Eksp. Teor. Fiz.* 47, 1515 (1964), [*Sov. Phys. JETP*20,1018(1965)].
- [228] M. Wagner, Expansions of nonequilibrium Green's functions, *Phys. Rev. B* 44, 6104 (1991).
- [229] A.-P. Jauho, N. S. Wingreen, and Y. Meir, Time-dependent transport in interacting and noninteracting resonant-tunneling systems, *Phys. Rev. B* 50, 5528 (1994).
- [230] S. Datta, *Electronic transport in mesoscopic systems*, Cambridge Studies in Semiconductor Physi (Cambridge University Press, , 1997).
- [231] A. Ozpineci and S. Ciraci, Quantum effects of thermal conductance through atomic chains, *Phys. Rev. B* 63, 125415 (2001).
- [232] T. Yamamoto and K. Watanabe, Nonequilibrium Green's function approach to phonon transport in defective carbon nanotubes, *Phys. Rev. Lett.* 96, 255503 (2006).
- [233] J.-S. Wang, J. Wang, and N. Zeng, Nonequilibrium Green's function approach to mesoscopic thermal transport, *Phys. Rev. B* 74, 033408 (2006).
- [234] J.-S. Wang, N. Zeng, J. Wang, and C. K. Gan, Nonequilibrium Green's function method for thermal transport in junctions, *Phys. Rev. E* 75, 061128 (2007).
- [235] N. Mingo, Anharmonic phonon flow through molecular-sized junctions, *Phys. Rev. B* 74, 125402 (2006).
- [236] M. Galperin, A. Nitzan, and M. A. Ratner, Heat conduction in molecular transport junctions, *Phys. Rev. B* 75, 155312 (2007).
- [237] X. Wang, G. Sun, P. Routh, D.-H. Kim, W. Huang, and P. Chen, Heteroatom-doped graphene materials: syntheses, properties and applications, *Chem. Soc. Rev.* 43, 7067 (2014).
- [238] R. Kubo, The fluctuation-dissipation theorem, *Rep. Prog. Phys.* 29, 255 (1966).
- [239] J. Velez and W. Butler, On the equivalence of different techniques for evaluating the Green function for a semi-infinite system using a localized basis, *J. Phys.-Condens. Mat.* 16, R637 (2004).
- [240] M. P. L. Sancho, J. M. L. Sancho, J. M. L. Sancho, and J. Rubio, Highly convergent schemes for the calculation of bulk and surface Green functions, *J. Phys. F Met. Phys.* 15, 851 (1985).
- [241] A. Urban, Environment-dependent crystal-field tight-binding based on density-functional theory (Friedrich-Alexander-Universität, , 2012).
- [242] T. Walter, Semiempirical quantum-chemical methods, *Wires. Comput. Mol. Sci.* 4, 145 (2013).

- [243] G. Seifert, H. Eschrig, and W. Bierger, An approximation variant of LCAO-X-ALPHA methods, *Z. Phys. Chem.* 267, 529 (1986).
- [244] W. M. C. Foulkes and R. Haydock, Tight-binding models and density-functional theory, *Phys. Rev. B* 39, 12520 (1989).
- [245] M. Elstner, D. Porezag, G. Jungnickel, J. Elsner, M. Haugk, T. Frauenheim, S. Suhai, and G. Seifert, Self-consistent-charge density-functional tight-binding method for simulations of complex materials properties, *Phys. Rev. B* 58, 7260 (1998).
- [246] D. Riccardi, P. König, X. Prat-Resina, H. Yu, M. Elstner, T. Frauenheim, and Q. Cui, "Proton holes" in long-range proton transfer reactions in solution and enzymes: a theoretical analysis, *J. Am. Chem. Soc.* 128, 16302 (2006).
- [247] E. Erdogan, I. H. Popov, A. N. Enyashin, and G. Seifert, Transport properties of MoS₂ nanoribbons: edge priority, *Eur. Phys. J. B* 85, 33 (2012).
- [248] H. Sevincli, C. Sevik, T. Cagin, and G. Cuniberti, A bottom-up route to enhance thermoelectric figures of merit in graphene nanoribbons, *Sci. Rep.* 3, (2013).
- [249] E. Erdogan, I. Popov, C. G. Rocha, G. Cuniberti, S. Roche, and G. Seifert, Engineering carbon chains from mechanically stretched graphene-based materials, *Phys. Rev. B* 83, 041401 (2011).
- [250] H. A. Witek and K. Morokuma, Systematic study of vibrational frequencies calculated with the self-consistent charge density functional tight-binding method, *J. Comput. Chem.* 25, 1858 (2004).
- [251] M. B. Oviedo, C. F. A. Negre, and C. G. Sanchez, Dynamical simulation of the optical response of photosynthetic pigments, *Phys. Chem. Chem. Phys.* 12, 6706 (2010).
- [252] R. Scholz, R. Lushtinets, G. Seifert, T. Jägeler-Hoheisel, C. Körner, K. Leo, and M. Rappacioli, Quantifying charge transfer energies at donor-acceptor interfaces in small-molecule solar cells with constrained DFTB and spectroscopic methods, *J. Phys. Condens. Mat.* 25, 473201 (2013).
- [253] V. Barone, I. Carnimeo, and G. Scalmani, Computational spectroscopy of large systems in solution: the DFTB/PCM and TD-DFTB/PCM approach, *J. Chem. Theory Comput.* 9, 2052 (2013).
- [254] G. Seifert and J.-O. Joswig, Density-functional tight binding - an approximate density-functional theory method, *Wires. Comput. Mol. Sci.* 2, 456 (2012).
- [255] M. Elstner and G. Seifert, Density functional tight binding, *Philos. T. Roy. Soc. A* 372, (2014).

- [256] M. Gaus, Q. Cui, and M. Elstner, Density functional tight binding: application to organic and biological molecules, *Wires. Comput. Mol. Sci.* 4, 49 (2014).
- [257] P. Hohenberg and W. Kohn, Inhomogeneous electron gas, *Phys. Rev.* 136, B864 (1964).
- [258] M. Born and R. Oppenheimer, Zur Quantentheorie der Molekeln, *Ann. Phys.* 389, 457 (1927).
- [259] W. Kohn and L. J. Sham, Self-consistent equations including exchange and correlation effects, *Phys. Rev.* 140, A1133 (1965).
- [260] M. Elstner, SCC-DFTB: What is the proper degree of self-consistency?, *J. Phys. Chem. A* 111, 5614 (2007).
- [261] M. Gaus, Q. Cui, and M. Elstner, DFTB3: extension of the self-consistent-charge density-functional tight-binding method (SCC-DFTB), *J. Chem. Theory Comput.* 7, 931 (2011).
- [262] D. Porezag, T. Frauenheim, T. Köhler, G. Seifert, and R. Kaschner, Construction of tight-binding-like potentials on the basis of density-functional theory: application to carbon, *Phys. Rev. B* 51, 12947 (1995).
- [263] S. Hazebroucq, G. S. Picard, C. Adamo, T. Heine, S. Gemming, and G. Seifert, Density-functional-based molecular-dynamics simulations of molten salts, *J. Chem. Phys.* 123, 134510 (2005).
- [264] R. Liang, J. M. J. Swanson, and G. A. Voth, Benchmark study of the SCC-DFTB approach for a biomolecular proton channel, *J. Chem. Theory Comput.* 10, 451 (2014).
- [265] P. Huang, H. Zhu, L. Jing, Y. Zhao, and X. Gao, Graphene covalently binding aryl groups: conductivity increases rather than decreases, *ACS Nano* 5, 7945 (2011).
- [266] R. Erni, M. D. Rossell, M.-T. Nguyen, S. Blankenburg, D. Passerone, P. Hartel, N. Alem, K. Erickson, W. Gannett, and A. Zettl, Stability and dynamics of small molecules trapped on graphene, *Phys. Rev. B* 82, 165443 (2010).
- [267] A. Du, Y. Chen, Z. Zhu, G. Lu, and S. C. Smith, C-BN single-walled nanotubes from hybrid connection of BN/C nanoribbons: prediction by ab initio density functional calculations, *J. Am. Chem. Soc.* 131, 1682 (2009).
- [268] Q. Yu et al., Control and characterization of individual grains and grain boundaries in graphene grown by chemical vapour deposition, *Nat. Mater.* 10, 443 (2011).
- [269] O. V. Yazyev and S. G. Louie, Electronic transport in polycrystalline graphene, *Nat. Mater.* 9, 806 (2010).
- [270] G. Qin, Q.-B. Yan, Z. Qin, S.-Y. Yue, M. Hu, and G. Su, Anisotropic intrinsic lattice thermal conductivity of phosphorene from first principles, *Phys. Chem. Chem. Phys.* 17, 4854 (2015).

- [271] C. Kamal, A. Chakrabarti, and M. Ezawa, Direct band gaps in group IV-VI monolayer materials: binary counterparts of phosphorene, *Phys. Rev. B* 93, 125428 (2016).
- [272] Y. Tison, J. Lagoute, V. Repain, C. Chacon, Y. Girard, F. Joucken, R. Sporken, F. Gargiulo, O. V. Yazyev, and S. Rousset, Grain boundaries in graphene on SiC(0001) substrate, *Nano Lett.* 14, 6382 (2014).
- [273] T. Lehmann, D. A. Ryndyk, and G. Cuniberti, Enhanced thermoelectric figure of merit in polycrystalline carbon nanostructures, *Phys. Rev. B* 92, 035418 (2015).
- [274] H. Sevinçli and M. Brandbyge, Phonon scattering in graphene over substrate steps, *Appl. Phys. Lett.* 105, 153108 (2014).
- [275] A. Y. Serov, Z.-Y. Ong, and E. Pop, Effect of grain boundaries on thermal transport in graphene, *Appl. Phys. Lett.* 102, 033104 (2013).
- [276] S. Hu, J. Chen, N. Yang, and B. Li, Thermal transport in graphene with defect and doping: phonon modes analysis, *Carbon* 116, 139 (2017).
- [277] P. Yasaei, A. Fathizadeh, R. Hantehzadeh, A. K. Majee, A. El-Ghandour, D. Estrada, C. Foster, Z. Aksamija, F. Khalili-Araghi, and A. Salehi-Khojin, Bimodal phonon scattering in graphene grain boundaries, *Nano Lett.* 15, 4532 (2015).
- [278] S. Irle, G. Zheng, M. Elstner, and K. Morokuma, From C₂ molecules to self-assembled fullerenes in quantum chemical molecular dynamics, *Nano Lett.* 3, 1657 (2003).
- [279] H. Zhang, G. Lee, C. Gong, L. Colombo, and K. Cho, Grain boundary effect on electrical transport properties of graphene, *J. Phys. Chem. C* 118, 2338 (2014).
- [280] X. Mu, X. Wu, T. Zhang, D. B. Go, and T. Luo, Thermal transport in graphene oxide - From ballistic extreme to amorphous limit, *Sci. Rep.* 4, 1 (2014).
- [281] Q. Peng, W. Ji, and S. De, First-principles study of the effects of mechanical strains on the radiation hardness of hexagonal boron nitride monolayers, *Nanoscale* 5, 695 (2013).
- [282] Z.-D. Sha, Q.-X. Pei, Z. Ding, J.-W. Jiang, and Y.-W. Zhang, Mechanical properties and fracture behavior of single-layer phosphorene at finite temperatures, *J. Phys. D: Appl. Phys.* 48, 395303 (2015).
- [283] T. Frauenheim, G. Seifert, M. Elstner, Z. Hajnal, G. Jungnickel, D. Porezag, S. Suhai, and R. Scholz, A Self-consistent charge density-functional based tight-binding method for predictive materials simulations in physics, chemistry and biology, *Phys. Status Solidi B* 217, 41 (2000).
- [284] G. Seifert, Tight-binding density functional theory: An approximate Kohn-Sham DFT scheme, *J. Phys. Chem. A* 111, 5609 (2007).

- [285] M. Machado, T. Kar, and P. Piquini, The influence of the stacking orientation of C and BN stripes in the structure, energetics, and electronic properties of BC₂N nanotubes, *Nanotechnol.* 22, 205706 (2011).
- [286] J. P. Guedes, F. de Brito Mota, S. Azevedo, and C. M. C. de Castilho, Structure, energetic stability and tunable electronic properties of B_xC_yN_z armchair nanotubes: a theoretical study on the influence of diameter and local carbon concentration, *Eur. Phys. J. B* 88, 236 (2015).
- [287] W. Ulrich, *Quantum dissipative systems* (2nd Edition), Series in Modern Condensed Matter Physics (World Scientific Publishing Company, , 1999).
- [288] G. Ritschel and A. Eisfeld, Analytic representations of bath correlation functions for ohmic and superohmic spectral densities using simple poles, *J. Chem. Phys.* 141, 094101 (2014).
- [289] C. Meier and D. J. Tannor, Non-Markovian evolution of the density operator in the presence of strong laser fields, *J. Chem. Phys.* 111, 3365 (1999).
- [290] J. Hu, R.-X. Xu, and Y. Yan, Communication: Padé spectrum decomposition of Fermi function and Bose function, *J. Chem. Phys.* 133, 101106 (2010).
- [291] J.-S. Wang, Quantum thermal transport from classical molecular dynamics, *Phys. Rev. Lett.* 99, 160601 (2007).
- [292] M. J. Frisch et al., *Gaussian—09 Revision E.01*, 2009.
- [293] J. Chen, G. Zhang, and B. Li, Molecular dynamics simulations of heat conduction in nanostructures: effect of heat bath, *J. Phys. Soc. Jpn.* 79, 074604 (2010).
- [294] H. Eschrig, *Optimized LCAO method and the electronic structure of extended systems*, Research reports in physics (Springer-Verlag, , 1989).
- [295] Z. Bodrog, B. Aradi, and T. Frauenheim, Automated repulsive parametrization for the DFTB method, *J. Chem. Theory Comput.* 7, 2654 (2011).
- [296] M. Wahiduzzaman, A. F. Oliveira, P. Philippen, L. Zhechkov, E. van Lenthe, H. A. Witek, and T. Heine, DFTB parameters for the periodic table: Part 1, electronic structure, *J. Chem. Theory Comput.* 9, 4006 (2013).

Scientific output

List of publications related to the thesis

Chapter 2

- L. Medrano Sandonas, R. Gutierrez, A. Dianat, and G. Cuniberti. Engineering thermal rectification in MoS₂ nanoribbons: a non-equilibrium molecular dynamics study. *RSC Advances*, 5, 54345, (2015).
- L. Medrano Sandonas, G. Cuba-Supanta, R. Gutierrez, A. Dianat, C. V. Landauro, and G. Cuniberti. , Enhancement of thermal transport properties of asymmetric Graphene/hBN nanoribbon heterojunctions by substrate engineering. *Carbon*, 124, 642-650, (2017).

Chapter 3

- L. Medrano Sandonas, R. Gutierrez, A. Pecchia, A. Dianat, and G. Cuniberti. Thermoelectric properties of functionalized graphene grain boundaries. *Journal of Self-Assembly and Molecular Electronics*, 3, 5, (2015).
- L. Medrano Sandonas, D. Teich, R. Gutierrez, T. Lorenz, A. Pecchia, G. Seifert, and G. Cuniberti. Anisotropic thermoelectric response in two-dimensional puckered structures. *The Journal of Physical Chemistry C*, 120, 18841-18849, (2016).
- L. Medrano Sandonas, R. Gutierrez, A. Pecchia, G. Seifert, and G. Cuniberti. Tuning quantum electron and phonon transport in two-dimensional materials by strain engineering: a Green's function based study. *Physical Chemistry Chemical Physics*, 19, 1487-1495, (2017).

- L. Medrano Sandonas, H. Sevincli, R. Gutierrez, and G. Cuniberti. , First-principle-based phonon transport properties of nanoscale graphene grain boundaries. *Advanced Science*, 5, 1700365, (2018).
- L. Medrano Sandonas, G. Cuba-Supanta, R. Gutierrez, C. V. Landauro, J. Rojas-Tapia, and G. Cuniberti. Tunable thermoelectric transport in helical BNC heteronanotubes. Submitted, (2018).

Chapter 4

- L. Medrano Sandonas, A. Croy, R. Gutierrez, and G. Cuniberti. Atomistic framework for time-dependent thermal transport. *The Journal of Physical Chemistry C*, 122, 21062-21068, (2018).

Other publications

- A.S. Bonilla, R. Gutierrez, L. Medrano Sandonas, D. Nozaki, A.P. Bramanti, and G. Cuniberti. Structural distortions in molecular-based quantum cellular automata: a minimal model based study. *Physical Chemistry Chemical Physics*, 16, 17777-17785, (2014).
- L. R. Medrano, C. V. Landauro, and J. Rojas-Tapia. Implementation of an alternative method to determine the critical cooling rate: application in silver and copper nanoparticles. *Chemical Physics Letters*, 612, 273-279, (2014).
- Z. Liao, L. Medrano Sandonas, T. Zhang, M. Gall, A. Dianat, R. Gutierrez, U. Mühle, J. Gluch, R. Jordan, G. Cuniberti, and E. Zschech. In-situ stretching patterned graphene nanoribbons in the transmission electron microscope. *Scientific Reports*, 7, 211, (2017).
- L. Medrano Sandonas and C. V. Landauro. Disorder-induced metal-insulator transition in cooled silver and copper nanoparticles: A statistical study. *Chemical Physics Letter*, 681, 22-28, (2017).
- E. Mervinetsky, I. Alshanski, Y. Hamo, L. Medrano Sandonas, A. Dianat, J. Buchwald, R. Gutierrez, G. Cuniberti, M. Hurevich, and S. Yitzchaik. Copper induced conformational changes of tripeptide monolayer based impedimetric biosensor. *Scientific Reports*, 7, 9498, (2017).
- A. Gankin, R. Sfez, E. Mervinetsky, J. Buchwald, A. Dianat, L. Medrano Sandonas, R. Gutierrez, G. Cuniberti, and S. Yitzchaik. Molecular and ionic dipole effects on the electronic properties of Si-/SiO₂-grafted alkylamine monolayers. *ACS Applied Materials & Interfaces*, 9, 44873-44879, (2017).

- T. Zhang, Z. Liao, L. Medrano Sandonas, A. Dianat, X. Liu, P. Xiao, I. Amin, R. Gutierrez, T. Chen, E. Zschech, G. Cuniberti, and R. Jordan. Polymerization-driven monomer passage through monolayer chemical vapour deposition graphene. *Nature Communications*, 9, 4051, (2018).
- A. Santana-Bonilla, L. Medrano Sandonas, R. Gutierrez, and G. Cuniberti. Exploring the write-in process in molecular quantum cellular automata: a combined modelling and first-principle approach. Submitted, (2018).

Participation in conferences

Oral communication

- DPG spring meeting 2015, Berlin, Germany, (2015).
- PHONONICS 2015: 3rd International Conference on Phononic Crystals/Metamaterials, Phonon Transport and Phonon Coupling, Paris, France, (2015).
- DPG spring meeting 2016, Regensburg, Germany, (2016).
- SINAPSIS 2016: First meeting of Peruvian researchers in Europe, Paris, France, (2016).
- Flatlands beyond graphene 2016, Bled, Slovenia, (2016).
- DPG Spring meeting 2017, Dresden, Germany, (2017).
- Joint IMPRS Workshop on Condensed Matter, Quantum Technology and Quantum Materials, Dresden, Germany, (2017).
- 18th Trends in Nanotechnology International Conference, Dresden, Germany, (2017).
- 14th European Conference on Molecular electronics, Dresden, Germany, (2017).
- DPG Spring meeting 2018, Berlin, Germany, (2018).
- 8th European conference & Exhibitions in Graphene and 2D Materials-GRAPHENE 2018, Dresden, Germany, (2018).

Poster presentation

- 7th European conference & Exhibitions in Graphene and 2D Materials-GRAPHENE 2017, Barcelona, Spain, (2017).
- NIM Conference "Nanostructured functional Materials for sustainable Energy Provision", Munich, Germany, (2017).

Schools

- IMPRS Summer School on Photoinduced Dynamics, Prague, Czech Republic, (2015).
- 47th IFF Spring School: Memristive Phenomena- From Fundamental Physics to Neuromorphic Computing, Jülich, Germany, (2016).

ACKNOWLEDGMENTS

As far I can remember, this story started in September 2013 when I came to Dresden for an interview to take part at the "International Max Planck Research School" (IMPRS) for doctoral studies. Similar to all story, this one also has an end which, in this case, is the present work that you have just read. It has been a long way to reach this moment but, with effort and perseverance, I managed to give a proper end to my doctoral life. However, this period of my existence would not have been possible to overcome without the help of many people. Therefore, I would like to thank many of them.

Firstly, I express my gratitude to my supervisor Prof. Dr. Gianaurelio Cuniberti for the support, guidance and, specially, for giving me the opportunity of being part of the Chair of Material Sciences and Nanotechnology at TU Dresden, where I carried out the doctoral research and met my first friends in Europe.

I would also like to thank my day-to-day supervisor Prof. Dr. rer. nat. et Ing. habil. Rafael Gutierrez Laliga for the constant mentoring and for allowing me to work in research topics which helped me to develop new scientific skills and to grow as a research scientist. Despite all the hard work that he "nicely" offered me to do, I think I was lucky meeting him. MUCHAS GRACIAS RAFAEL!

The research presented in this thesis had not been able to be performed without the help of my collaborators. In this sense, I would like to express my gratitude to Dr. Arezoo Dianat (and Mutti), Dr. Alessandro Pecchia (and the boat), Dr. Alexander Croy, Prof. Dr. Gottard Seifert, and Prof. Dr. Haldun Sevincli. Special thanks to Dr. Carlos Landauro Sáenz who is always supporting in my academic life as a friend and former supervisor. Here, I also thank Sylvi, Grit, Nicole, and Manuela for helping with all the administrative part and making my research stay in Dresden easier.

A special thanks to my family. Hasta el momento no logro conseguir las palabras adecuadas para agradecer todo lo que mis padres han realizado por mi. Sino fuera por su esfuerzo nunca

hubiese podido llegar hasta donde estoy ahora. Así que, por favor, "vieja y viejo" acepten estas sinceras palabras de agradecimiento por todo el amor incondicional y apoyo que me han otorgado. También me gustaría agradecer a mis hermanos Jhonny y Cristiam por su apoyo moral y, especialmente, por cuidar de mis padres en mi ausencia. A mis sobrinas les agradezco por todas las alegrías que me dan cuando hablamos por Skype. MUCHAS GRACIAS FAMILIA!

Here, I also thank Mirtha for all the help and support that she has offered me since the day we met in Peru. It has been a very tough road but we are making it possible. GRACIAS AMORCITO!

This paragraph has been specially selected to thank my awesome friends who made my life in Dresden more interesting and entertaining. I would like to start with some memorable mentions such as T. Alejandro Santana, P. Nacho González, and Sarinha Vanessa Teixeira. Muchas gracias and Muito Obrigado for all the help since my first months in Germany! I also thank very much to my beloved people from the WA group "What is love" (Marisinha, Anita, Michael, Sundy Sundy, Claudia, Yin-yang, David, Andreita, Giulia, Marianna, DJ Joao, Hagen, Jan, Kedar, Lena, Lili, Luchin, Toño, Mitra, Sandro, Santi, and God Goran), GUYS without you I would have never got the motivation to finish this thesis! Thanks for all the amazing nights, mornings, and sometimes afternoons that made me feel at home. Special thanks to Thomas, Daijiro, Alvaro, Nadia, and Andrii for making the office and coffee hours much happier as they must be. Also, I am very grateful to Marisinha, Ngazinha, and Alvaro for all the help during the last weeks before ending this period. GRACIAS for everything AMIG@S!!!

Finally but very important, I would like to thank the Max Planck Society (IMPRS in Dresden) and the Deutscher Akademischer Austauschdienst (DAAD, Doctoral programmes 2015/16) for the financial support to carry out the doctoral research without any problem.

Meinen herzlichen Dank für alles! — Many thanks to all! — Muchas gracias a todos!